



Forschungszentrum Karlsruhe
in der Helmholtz-Gemeinschaft

Wissenschaftliche Berichte
FZKA 6829

Results of the QUENCH-09 Experiment with a B₄C Control Rod

**M. Steinbrück, A. Miassoedov, G. Schanz,
L. Sepold, U. Stegmaier, H. Steiner,
J. Stuckert**

**Institut für Materialforschung
Institut für Kern- und Energietechnik
Programm Nukleare Sicherheitsforschung**

Dezember 2004

Forschungszentrum Karlsruhe

in der Helmholtz-Gemeinschaft

Wissenschaftliche Berichte

FZKA 6829

Results of the QUENCH-09 Experiment

with a B_4C Control Rod

M. Steinbrück, A. Miassoedov, G. Schanz, L. Sepold,
U. Stegmaier, H. Steiner, J. Stuckert

Institut für Materialforschung
Institut für Kern- und Energietechnik
Programm Nukleare Sicherheitsforschung

Forschungszentrum Karlsruhe GmbH, Karlsruhe

2004

Für diesen Bericht behalten wir uns alle Rechte vor

Forschungszentrum Karlsruhe GmbH
Postfach 3640, 76021 Karlsruhe

Mitglied der Hermann von Helmholtz-Gemeinschaft
Deutscher Forschungszentren (HGF)

ISSN 0947-8620

Zusammenfassung

Ergebnisse des Versuchs QUENCH-09 mit einem B₄C-Steuerstab

Die Experimente der QUENCH-Serie dienen der Bestimmung des Wasserstoff-Quellterms als Folge der Wasser- oder Dampf-Einspeisung in den freigelegten Kern eines Leichtwasserreaktors (LWR). Eng damit verknüpfte Ziele sind die Untersuchung des wesentlich vom Szenario abhängigen Fortschreitens der Kernschädigung und der unvollständig verstandenen Mechanismen der Kernabkühlung im Flutvorgang, sowie die Gewinnung von Informationen für eine fortgeschrittene Behandlung der Phänomene in Codes. Das experimentelle Programm stützt sich auf eine parametrisierte Out-of-pile-Simulation der Bedingungen im Kern unter Einsatz eines Bündels elektrisch beheizter Brennstabsimulatoren. Wesentliche Informationen können erzielt werden, jedoch wird die Übertragung auf vollständig realistische Bedingungen eines Kerns als separate Verifizierungs-Aufgabe angesehen, die eine Unterstützung durch In-pile-Experimente und Code-Analysen erfordert.

Die QUENCH-Testbündel bestehen aus einem zentralen Stab und 20 umgebenden Brennstabsimulatoren, die über eine Länge von 1024 mm beheizt sind. Die Brennstabhüllrohre (Zircaloy-4; Zry) und die Abstandshaltergitter sind identisch zu den in Druckwasserreaktoren verwendeten, während der Brennstoff durch ZrO₂-Pellets repräsentiert wird. Die Teststrecke ist instrumentiert durch Thermoelemente (TE), die an den Hüllrohren, dem Shroud und dem doppelwandigen Kühlmantel in Ebenen zwischen -50 mm und 1350 mm angebracht sind. Zentrale TEs sind in drei der vier Eckstäbe montiert. Die Experimente werden in einer strömenden Atmosphäre aus überhitztem Dampf und Argon-Trägergas durchgeführt. Das abgeführte Gas wird hauptsächlich mittels eines Massenspektrometers analysiert.

QUENCH-09 wurde am 3. Juli 2002 durchgeführt und ist nach QUENCH-07 das zweite Experiment mit einer Kontrollstab-Einheit im Bündelzentrum, die aus einem Absorberstab (B₄C-Pellets / Edelstahlhüllrohr) und einem Zry Führungsrohr besteht. Das Massenverhältnis Stahl / B₄C von 3,5 war identisch zu dem im künftigen PHEBUS FPT3-Experiment vorgesehenen Kontrollstab. Zusätzlich zur üblichen TE-Instrumentierung wurden drei TE in Nuten der Absorberstab-Hülle eingebettet. QUENCH-09 wurde ähnlich zu QUENCH-07 durchgeführt, mit Ausnahme zweier Punkte: Der Dampfdurchsatz wurde während einer „B₄C-Oxidationsphase“ von 3,4 auf 0,4 g/s reduziert, um Dampfangelbedingungen im Bündel einzustellen und eine bessere Vergleichbarkeit mit den Bedingungen im PHEBUS FPT3 Experiment zu erzielen. Außerdem wurde mit der Einspeisung von 50 g/s Satttdampf (anstelle von 15 g/s in QUENCH-07) angestrebt, das Bündel so schnell wie möglich abzukühlen, um seinen Zustand vor der Abkühlung zu erhalten. In beiden Tests soll das Kontrollstabversagen und dessen Einfluss auf die Schädigung des umgebenden Bündels untersucht werden. Hinsichtlich der Chemie der flüchtigen Spaltprodukte waren die B₄C-Oxidation und die Kontrollstab-Zerstörung zu untersuchen. Die Experimente wurden innerhalb des „COLOSS“-Projekts durch die Europäische Gemeinschaft mitfinanziert.

Eine Kontrollstab-Leckage wurde aus dem in der Abgasstrecke nachgewiesenen Füllgas-Signal bei ~1555 K abgeleitet, bei ungefähr der gleichen Absorberstab-Temperatur wie in QUENCH-07 (~1585 K). Jedoch wurden danach und bis zur Abkühlphase im Vergleich zu QUENCH-07 unerwartet schwache Signale flüchtiger Reaktionsprodukte der Kontrollstab-

schädigung mittels Massenspektrometrie registriert. In der Abkühlphase wurde die heftige Freisetzung von Wasserstoff von starken Anstiegen der Erzeugung von CO und CO₂ begleitet. Weiterhin wurde die Bildung von Borsäure identifiziert und eine geringe Menge gebildeten Methans nachgewiesen. Die Auswertung der Massenspektrometer-Daten auf der Basis der gesamten Mengen an CO und CO₂ sowie metallographische Nachuntersuchungen des Bündels ergab einen errechneten oxidativen Umsatz von etwa 50 % der verfügbaren Menge an B₄C (im Vergleich zu etwa 20 % für QUENCH-07). Der nominale Beitrag der B₄C-Oxidation zum H₂-Signal von 2,2 % ist vergleichbar mit den 2,4 % für QUENCH-07; aber diese Zahlen lassen die sekundären Einflüsse auf die Schädigung der beiden Bündel nicht erkennen. Die insgesamt erzeugte Wasserstoffmenge von 460 g in QUENCH-09 ist der bisher höchste in einem QUENCH-Versuch nachgewiesene Wert, und das gilt auch für den während der Abkühlphase freigesetzten Anteil von 87 %.

Der Bericht enthält eine zusammenfassende Auswertung der Daten aus der Test-Instrumentierung, insbesondere zur Temperaturmessung und einschließlich der abgeleiteten Ereignis-Sequenz. Die Nachuntersuchung wird im Detail dargelegt, interpretiert und separat zusammengefasst. Es wird hier erwähnt, dass die Umwandlung des Bündels in eine Konfiguration aus einer Blockade und Strömungskanälen weiter fortgeschritten ist als bei allen vorher durchgeführten Versuchen. Ein analytischer Beitrag unterstützt die Interpretation der experimentellen Ergebnisse. Beiträge zum Anhang betreffen experimentelle Beschränkungen und Hinweise auf ihre Berücksichtigung.

Abstract

The QUENCH experiments series is focused on the determination of the hydrogen source term resulting from the water or steam injection into an uncovered core of a light water reactor (LWR). Closely connected aims are to study the scenario strongly dependent on core damage progression and the insufficiently understood mechanisms related to re-flooding and core recovery, as well as to provide information for an advanced treatment of the phenomena in codes. The experimental program relies on out-of-pile simulation of core conditions in parametric manner by use of electrically heated fuel rod simulator bundles. Essential information can be obtained, but transcription to fully realistic core conditions is seen as separate verification task requiring support from in-pile experiments and code analysis.

The QUENCH test bundles consist of a central rod and 20 surrounding fuel rod simulators heated over a length of 1024 mm. The Zircaloy-4 (Zry) fuel rod claddings and the grid spacers are identical to those used in pressurized water reactors, whereas the fuel is represented by ZrO_2 pellets. The test section is instrumented with thermocouples (TC) attached to the rod cladding, the shroud, and the double-walled cooling jacket at levels between -50 mm and 1350 mm. Centerline TCs are mounted inside three of the four corner rods. The experiments are performed in flowing superheated steam / argon carrier gas atmosphere. The off-gas is mainly analyzed by a mass spectrometer.

QUENCH-09, performed at Karlsruhe Research Center on 03 July, 2002, was the second experiment after QUENCH-07 with a control rod arrangement in the bundle center, consisting of absorber rod (B_4C pellets / stainless steel cladding) and Zry guide tube. The steel to B_4C mass ratio of 3.5 was identical to that in the future PHEBUS FPT3 experiment. In addition to the usual TC instrumentation three TCs were embedded in a groove of the absorber rod cladding. QUENCH-09 was conducted similarly to QUENCH-07, except for two items: First, the steam flow was reduced from 3.4 to 0.4 g/s during the " B_4C oxidation phase" to reach steam starvation in the bundle and thus to provide closer comparison with the PHEBUS FPT3 experiment. Second, cooling was achieved with 50 g/s of saturated steam (instead of 15 g/s in QUENCH-07) in order to cool down the bundle as fast as possible to preserve its state before cooling initiation. Both tests are to investigate the control rod failure and the effect on the degradation of the surrounding fuel rod bundle. With respect to volatile fission products chemistry the gaseous species from B_4C oxidation and control rod degradation were determined. The experiments were co-sponsored by the European Community within the "COLOSS" project.

Control rod leakage was deduced from filling gas signal detection in the off-gas pipe at ~1555 K, roughly the same absorber rod temperature as in QUENCH-07 (~1585 K). In spite of this, mass spectrometry has determined then and until the cooling phase only unexpectedly faint signals of volatile control rod degradation products compared to QUENCH-07. In the cooling phase the violent H_2 release was accompanied by large increases in the generation of CO and CO_2 . Further, boric acid generation was identified as well as a small amount of methane formation detected. Mass spectrometer data evaluation on basis of the combined amounts of CO and CO_2 as well as metallographic post-test examinations of the bundle resulted in a calculated oxidative conversion of roughly 50 % of the available B_4C mass (compared to roughly 20 % in QUENCH-07). The nominal contribution of B_4C oxidation to the H_2

signal, i.e. 2.2 % is comparable to 2.4 %, the respective percentage determined for QUENCH-07, but those figures do not indicate the secondary influences on the degradation of both bundles. The total hydrogen generation of 460 g in QUENCH-09 is the highest amount recorded up to now in a QUENCH experiment, as well as the fraction released during the cooling phase, 87 %.

The report gives a summarizing evaluation of the instrumentation data, especially on temperature measurements, and includes the deduced sequence of events. The post-test examination is covered in detail, interpreted, and separately summarized. It is mentioned that the transformation of the bundle to a blockage/flow channel configuration is found more advanced than for any previous QUENCH experiment. An analytical contribution supports the interpretation of the experimental results. Appendix contributions give brief information on experimental constraints and counteractions.

Contents

List of Tables.....	1
List of Figures.....	2
Introduction	9
1. Description of the Test Facility.....	11
2. Test Bundle Instrumentation	13
3. Gas Measurement Devices	13
4. Data Acquisition and Process Control.....	15
5. Test Conduct and Pertinent Results	16
6. Posttest Examination.....	19
6.1 Posttest Appearance Prior to Bundle Sectioning.....	19
6.2 Sectioning of the Test Bundle	20
6.3 Investigation Procedures of the Metallographic Examination.....	20
6.4 Results of Bundle Documentation and Microstructure Interpretation	21
6.5 Lateral Oxide Scale Thickness Distribution and Axial Profile	26
6.6 SEM/EDX Analysis of Special Components and Products	27
6.7 Hydrogen Absorption by Zircaloy	30
6.8 Summary and Conclusions	30
7. Analytical support by the Bundle Code CALUMO	31
8. Summary.....	37
References.....	39
Acknowledgments	41
Appendix 1	175
Posttest measurement of the total argon flow through the QUENCH-09 bundle with the perforated inner cooling jacket	175
Appendix 2	181
Errors in the temperature measurement by the “hot-zone effect”.....	181
References.....	182

List of Tables

- Table 1: QUENCH test matrix
- Table 2: Design characteristics of the QUENCH-09 test bundle
- Table 3: List of instrumentation for the QUENCH-09 test
- Table 4: QUENCH-09; Failure of thermocouples
- Table 5: QUENCH-09; Sequence of events
- Table 6: QUENCH-09; Excursion temperatures
- Table 7: QUENCH-09; Maximum measured test rod temperature of each elevation
- Table 8: QUENCH-09; Maximum measured shroud temperature of each elevation
- Table 9: QUENCH-09; Onset of cooling based on cladding TCs (TFS and TCR), central rod centerline TC (TCRC 13), corner rod TCs (TIT), and shroud TCs (TSH)
- Table 10: QUENCH-07 and-09; Comparison of hydrogen data and results on the B₄C oxidation products
- Table 11: QUENCH-09; Chemical analysis of condensate samples from the MS off-gas pipe
- Table 12: QUENCH-09; Chemical analysis of the debris taken posttest from bundle elevation 1300 – 1400 mm
- Table 13: QUENCH-09; Cross sections for the metallographic examination
- Table A2-1. Questionable thermocouple readings of tests QUENCH-01 through -09

List of Figures

- Fig. 1: Flow diagram of the QUENCH test facility
- Fig. 2: QUENCH Facility; Main components
- Fig. 3: QUENCH Facility; Containment and test section
- Fig. 4: QUENCH test section; Flow lines
- Fig. 5: QUENCH-09; Fuel rod simulator bundle (cross section) with control rod simulator in the center
- Fig. 6: Heated fuel rod simulator
- Fig. 7: Control rod simulator (unheated)
- Fig. 8: QUENCH-09; Test bundle instrumentation (azimuthal orientation) and rod designation (top view)
- Fig. 9: Axial temperature measurement locations in the QUENCH test section
- Fig. 10: QUENCH-09; Arrangement of the thermocouples inside the corner rods
- Fig. 11: QUENCH; High-temperature thermocouple
- Fig. 12: TC fastening concept for the QUENCH test rod
- Fig. 13: QUENCH facility; H₂ measurement with the GAM 300 mass spectrometer
- Fig. 14: Mass spectrometer sampling position at the off-gas pipe
- Fig. 15: Hydrogen measurement with the CALDOS analyzer
- Fig. 16: QUENCH-09; Test as performed
- Fig. 17: QUENCH-09; Test phases illustrated with help of the temperature measured by the thermocouple TFS 2/12 B together with the heatup rate, top, and total electric power vs. time, bottom
- Fig. 18: QUENCH-09; Temperature histories of rod cladding thermocouples (TFS) at the lower elevations for the entire test time, top, and of the various thermocouples between 2000 and 3500 s, bottom.
- Fig. 19: QUENCH-09; Overview of shroud temperature (TSH) histories, top, and the histories of the TCI (inner cooling jacket) temperatures, bottom
- Fig. 20: QUENCH-09; Absorber rod cladding temperatures at 750, 850, and 950 mm elevation, top, and helium concentration, bottom, to demonstrate initiation of control rod failure
- Fig. 21: QUENCH-09; Selected times for the axial temperature profiles (illustrated with help of thermocouple TFS 2/12 B)

-
- Fig. 22: QUENCH-09; Axial temperature profile TFS 2, TFS 5, TSH, left, and axial temperature profile of all TFS, right, at 2280 s (absorber rod failure)
- Fig. 23: QUENCH-09; Axial temperature profile TFS 2, TFS 5, TSH, left, and axial temperature profile of all TFS, right, at 2582 s (beginning of temperature excursions)
- Fig. 24: QUENCH-09; Axial temperature profile TFS 2, TFS 5, TSH, left, and axial temperature profile of all TFS, right, at 2636 s (beginning of steam flow reduction)
- Fig. 25: QUENCH-09; Steam flow rate based on flow meters F 205 and F 206 (before cooldown) and F 204 (cooldown), top, and qualitative flow rate of the offgas pipe (F 601) during the cooling phase, bottom
- Fig. 26: QUENCH-09; Coolant temperatures T 511 (bundle inlet), TFS 2/1 (-250 mm), TFS 5/4/0 (-50 mm), TFS 2/6 (250 mm), TFS 2/17 (1350 mm), and T 512 (bundle outlet, ~1350 mm), top, and system pressure at test section inlet (P 511), at outlet (P 512), and in the off-gas pipe (P 601) before and during the cooldown phase, bottom
- Fig. 27: QUENCH-09; Rod internal pressure (P 411) together with the pressure at the test section inlet (P 511), and the krypton concentration to demonstrate rod cladding failure, top, and shroud insulation pressure (P 406) together with the pressure at the test section inlet (P 511) to demonstrate shroud failure, bottom
- Fig. 28: QUENCH-09; Argon coolant pressure of the cooling jacket (P 403) together with the pressure at the test section inlet (P 511) indicating failure of the inner cooling jacket
- Fig. 29: QUENCH-09; Hydrogen release rate together with the total H₂ measured by MS GAM 300
- Fig. 30: QUENCH-09; Boron carbide oxidation products CH₄, CO₂, and CO, top, and boric acids vs. time, bottom
- Fig. 31: QUENCH-09; Boron concentration in the MS off-gas condensate together with the mass spectrometer signals at atomic masses 43 and 62
- Fig. 32: QUENCH-09; Posttest view into the off-gas pipe demonstrating debris transported from the upper bundle region
- Fig. 33: QUENCH-09; Debris taken posttest from bundle elevation 1300 – 1400 mm. Two views of the heaviest sample with weight of approx. 55 g
- Fig. 34: QUENCH-09; Posttest appearance of bundle and shroud from around 500 mm upward, 0° (left) and 270° (right) orientation
- Fig. 35: QUENCH-09; Posttest appearance of bundle and shroud from about 500 mm upward, 90° orientation
- Fig. 36: QUENCH-09; Posttest appearance of bundle and shroud at 180° orientation from about 500 mm upward, left, and of the topmost zone, right
- Fig. 37: QUENCH-09; Posttest photographs from inside the test bundle at axial levels of approx. 450 mm, bottom, and 550 mm, top
- Fig. 38: QUENCH-09; Posttest photographs from inside the test bundle demonstrating rod cladding rupture at approx. 490 mm, bottom, and 500 mm, top

- Fig. 39: QUENCH-09; Posttest photographs from inside the test bundle at 540 mm elevation
- Fig. 40: QUENCH-09; Photographs of the failure location at the inner cooling jacket
- Fig. 41: QUENCH-09; Sectioning of the test bundle
- Fig. 42: QUENCH-09; Cross sections at 60 mm, 73 mm, 444 mm, and 460 mm
- Fig. 43: QUENCH-09; Cross sections at 507 mm, 520 mm, 577 mm, and 590 mm
- Fig. 44: QUENCH-09; Cross sections at 637 mm, 650 mm, 687 mm, and 700 mm
- Fig. 45: QUENCH-09; Cross sections at 937 mm, 950 mm, 1480 mm, and 1510 mm
- Fig. 46: QUENCH-09; Cross sections at 73 mm bundle elevation (QUE-09-1); overview from top
- Fig. 47: QUENCH-09; Cross section at 460 mm bundle elevation (QUE-09-18); overview from top
- Fig. 48: QUENCH-09; Cross section at 460 mm bundle elevation (QUE-09-18); melt relocation at bundle corners
- Fig. 49: QUENCH-09; Cross section at 460 mm bundle elevation (QUE-09-18); small melt lumps
- Fig. 50: QUENCH-09; Cross section at 520 mm bundle elevation (QUE-09-2); overview from top
- Fig. 51: QUENCH-09; Cross section at 520 mm bundle elevation (QUE-09-2); melt accumulation (left) and shroud melting (right) related to external shroud thermocouples
- Fig. 52: QUENCH-09; Cross section at 520 mm bundle elevation (QUE-09-2); interaction and melting of control rod components
- Fig. 53: QUENCH-09; Cross section at 520 mm bundle elevation (QUE-09-2); examples for rods in various degradation states
- Fig. 54: QUENCH-09; Cross section at 520 mm bundle elevation (QUE-09-2); common melt pool of rods #2 (top) and #9 (bottom), indicating control rod components transfer via melt relocation from above
- Fig. 55: QUENCH-09; Cross section at 520 mm bundle elevation (QUE-09-2); melt accumulation and relocation, involving rod #19 and destroying NW corner rod
- Fig. 56: QUENCH-09; Cross section at 590 mm bundle elevation (QUE-09-4); overview from top
- Fig. 57: QUENCH-09; Cross section at 590 mm bundle elevation (QUE-09-4); central part, top view; EDX-analysis positions are indicated
- Fig. 58: QUENCH-09; Cross section at 590 mm bundle elevation (QUE-09-4); examples for fuel rod simulators in relatively fair preservation; all at the SW part of the bundle, and in contact with blockage by dense melt
- Fig. 59: QUENCH-09; Cross section at 590 mm bundle elevation (QUE-09-4); Blockage, adjacent to rod #5, shows (in polarized light) dense character and equiaxed grains. Pellet indicated by coarser grains, flow channel identified by growth of columnar scale

-
- Fig. 60: QUENCH-09; Cross section at 590 mm bundle elevation (QUE-09-4); some information on the history of the blockage at the SW part of the bundle: embedding of rods, in-situ oxidation, re-solidification
- Fig. 61: QUENCH-09; Cross section at 590 mm bundle elevation (QUE-09-4); examples for fuel rod simulators in partial preservation; locally remaining pellet, elsewhere heater rod destruction
- Fig. 62: QUENCH-09; Cross section at 590 mm bundle elevation (QUE-09-4); examples for strongly damaged fuel rod simulators, and tungsten heater rod degradation via melt formation
- Fig. 63: QUENCH-09; Cross section at 590 mm bundle elevation (QUE-09-4); microstructure of melt, accumulated around tungsten heater of fuel rod simulator #2, resulting from heater rod degradation at the relocation sources (see other figures for analysis)
- Fig. 64: QUENCH-09; Cross section at 590 mm bundle elevation (QUE-09-4); a steam flow channel at the bundle periphery and the shroud at a position of crack formation during quenching
- Fig. 65: QUENCH-09; Cross section at 590 mm bundle elevation (QUE-09-4); metallic melt at S to SE position of the shroud, resulting from stainless steel cooling jacket attack
- Fig. 66: QUENCH-09; Cross section at 650 mm bundle elevation (QUE-09-6); overview from top
- Fig. 67: QUENCH-09; Cross section at 650 mm bundle elevation (QUE-09-6); central part, top view
- Fig. 68: QUENCH-09; Cross section at 650 mm bundle elevation (QUE-09-6); examples for fuel rod simulators in fair preservation, relative to the advanced bundle destruction
- Fig. 69: QUENCH-09; Cross section at 650 mm bundle elevation (QUE-09-6); examples for fuel rod simulators in the advanced degradation, characteristic for the elevation
- Fig. 70: QUENCH-09; Cross section at 650 mm bundle elevation (QUE-09-6); examples for fuel rod simulators in bad condition
- Fig. 71: QUENCH-09; Cross section at 700 mm bundle elevation (QUE-09-8); overview from top
- Fig. 72: QUENCH-09; Cross section at 700 mm bundle elevation (QUE-09-8); central part, top view
- Fig. 73: QUENCH-09; Cross section at 700 mm bundle elevation (QUE-09-8); examples for fuel rod simulators in better condition, compared to the elevation QUE-09-6 (650 mm)
- Fig. 74: QUENCH-09; Cross section at 700 mm bundle elevation (QUE-09-8); examples for fuel rod simulators in the characteristic degradation state of the elevation
- Fig. 75: QUENCH-09; Cross section at 700 mm bundle elevation (QUE-09-8); examples for fuel rod simulators in relatively bad condition
- Fig. 76: QUENCH-09; Cross section at 950 mm bundle elevation (QUE-09-14); overview from top

- Fig. 77: QUENCH-09; Cross section at 950 mm bundle elevation (QUE-09-14); bundle center in closer view, state of fuel rod simulator #6, and details of melt in connection
- Fig. 78: QUENCH-09; Cross section at 950 mm bundle elevation (QUE-09-14); fuel rod simulator #21 in SW direction, showing previous interaction of the cladding with the pellet and complete conversion to zirconia during free steam exposure
- Fig. 79: QUENCH-09; Cross section at 950 mm bundle elevation (QUE-09-14); fuel rod simulator #9 in SE direction, showing earlier internal cladding melting, adhering external melt, and considerable heater rod dissolution
- Fig. 80: QUENCH-09; Cross section at 950 mm bundle elevation (QUE-09-14); examples for fuel rod simulators of the inner ring
- Fig. 81: QUENCH-09; Cross section at 950 mm bundle elevation (QUE-09-14); examples for fuel rod simulators of the outer ring
- Fig. 82: QUENCH-09; Cross section at 1480 mm bundle elevation (QUE-09-16 bottom); overview from top
- Fig. 83: QUENCH-09; Cross section at 1480 mm bundle elevation (QUE-09-16 bottom); oxidation state of fuel rod simulator #19, consisting of molybdenum electrode rod, plasma-coated by zirconia layer, and Zry cladding
- Fig. 84: QUENCH-09; Cross section at 1480 mm bundle elevation (QUE-09-16 bottom); state of selected fuel rod simulators in fair condition
- Fig. 85: QUENCH-09; Cross section at 1480 mm bundle elevation (QUE-09-16 bottom); selected fuel rod simulators with intact molybdenum electrode and zirconia coating, but strongly damaged cladding
- Fig. 86: QUENCH-09; Oxide layer thickness at bundle elevation 460 mm (Cross section QUE-09-18)
- Fig. 87: QUENCH-09; Oxide layer thickness at bundle elevation 520 mm (Cross section QUE-09-2)
- Fig. 88: QUENCH-09; Oxide layer thickness at bundle elevation 950 mm (Cross section QUE-09-14)
- Fig. 89: QUENCH-09; Oxide layer thickness at bundle elevation 1480 mm (Cross section QUE-09-16)
- Fig. 90: QUENCH-09; Oxide layer thickness at bundle elevation 1510 mm (Cross section QUE-09-16)
- Fig. 91: QUENCH-09; Axial distribution of the oxide scale thickness
- Fig. 92: QUENCH-09; Cross section at 520 mm bundle elevation (QUE-09-2); SEM/EDX analysis of melt within peripheral zones of the control rod (compare with next figure and Fig. 52)
- Fig. 93: QUENCH-09; Cross section at 520 mm bundle elevation (QUE-09-2); SEM/EDX analysis of melt, close to and within the absorber pellet (compare with previous figure and Fig 52)

-
- Fig. 94: QUENCH-09; Cross section at 520 mm bundle elevation (QUE-09-2); SEM/EDX analysis of melt within rod #2, verifying spreading and mixing of CR melt during downward relocation in damaged rods (see Fig. 54)
- Fig. 95: QUENCH-09; Cross section at 520 mm bundle elevation (QUE-09-2); SEM/EDX analysis of melt within rod #8, indicating presence of control rod degradation products
- Fig. 96: QUENCH-09; Cross section at 520 mm bundle elevation (QUE-09-2); SEM/EDX analysis of melt within rods #5 and #14, indicating presence of control rod degradation products
- Fig. 97: QUENCH-09; Cross section at 590 mm bundle elevation (QUE-09-4); non porous melt pool, penetrated by steam flow channels, after complete conversion to ceramic state by pool oxidation mechanism; no control rod components detected in SEM/EDX analysis
- Fig. 98: QUENCH-09; Cross section at 590 mm bundle elevation (QUE-09-4); SEM/EDX analysis of porous melt in the bundle centre, resulting from fuel rod dissolution by control rod melt (left), and tungsten-rich melt, formed by dissolution of uncovered heater rod (right); (for W-dissolution see also Fig. 99)
- Fig. 99: QUENCH-09; Cross section at 590 mm bundle elevation (QUE-09-4); SEM/EDX analysis of the heater rod of fuel rod simulator #2 and of the tungsten-rich melt around; (for dissolution of tungsten see also Fig. 98)
- Fig. 100: QUENCH-09; Cross section at 950 mm bundle elevation (QUE-09-14); SEM/EDX analysis positions and element spectra, obtained for melts and rubble fragments
- Fig. 101: QUENCH-09; Cross section at 950 mm bundle elevation (QUE-09-14); SEM/EDX analysis positions and element spectra, obtained for melts and rubble fragments in bundle centre
- Fig. 102: QUENCH-09; Analysis of hydrogen absorbed in the residual metallic parts of the rods and shroud
- Fig. 103: QUENCH-09; Evolution of rod and shroud temperatures of QUENCH-09 at different axial locations, CALUMO-calculated data in comparison with experimental values
- Fig. 104: QUENCH-09; Evolution of rod and shroud temperatures of QUENCH-09 at different axial locations, CALUMO-calculated data in comparison with experimental values
- Fig. 105: QUENCH-09; Evolution of rod and shroud temperatures of QUENCH-09 at different axial locations, CALUMO-calculated data in comparison with experimental values
- Fig. 106: QUENCH-09; Axial distributions of the steam flow rate at different times during steam reduction
- Fig. 107: QUENCH-09; Evolution of the hydrogen production rate and the overall produced hydrogen for QUENCH-09 calculated with CALUMOqx
- Fig. 108: QUENCH-09; Axial distribution of the oxide scale thickness in the upper part of the test section during steam reduction
- Fig. 109: QUENCH-09; Axial distribution of the oxide scale thickness at the beginning and end of steam flow reduction and the end of QUENCH-09

- Fig. 110: QUENCH-09; CALUMO calculated data and measured values for the oxide scale thickness of the experiment QUENCH-09 (Prater/Courtright trans. temp 1880 K)
- Fig. A1-1 QUENCH-09; Posttest arrangement of the bypass tube to simulate the cooling jacket break
- Fig. A1-2 Posttest argon flow and pressure measurements to simulate the break of the inner cooling jacket during the QUENCH-09 test
- Fig. A1-3 Pressure histories of P 403 (annulus of the cooling jacket) and P 601 (off-gas pipe) during test QUENCH-09 together with the argon bundle flow rate measured posttest (corrected from the time of "jacket break" as indicated)
- Fig. A2-1 QUENCH-09; Measured and calculated oxide layer thickness at levels 750 and 950 mm showing significant differences at 750 mm due to uncertainties in the temperature measurement, i.e. hot zone-effect of the rod cladding thermocouples
- Fig. A2-2 QUENCH-09; Design of the duplex-sheathed thermocouple, left, and posttest photograph, right
- Fig. A2-3 QUENCH-09; Test with two duplex-sheathed thermocouples routed to opposite directions, TC tips slightly overlapping, along the axis of the light furnace KALIO
- Fig. A2-4 QUENCH-09; Different temperature readings from thermocouples fastened at the same level of the fuel rod simulator, bottom, and on the shroud surface, top

Introduction

The most important accident management measure to terminate a severe accident transient in a light water reactor (LWR) is the injection of water to cool the uncovered degraded core. Analysis of the TMI-2 [1] accident and the results of integral out-of-pile (CORA [2, 3]) and in-pile experiments (LOFT [4], PHEBUS, PBF) have shown that before the water succeeds in cooling the fuel pins there could be an enhanced oxidation of the Zircaloy cladding that in turn causes a sharp rise in temperature, hydrogen production, and fission product release.

Besides, quenching is considered a worst-case accident scenario regarding hydrogen release to the containment. For in- and ex-vessel safety analyses one has to prove that the hydrogen release rate and total amount do not exceed limits for the considered power plant. The hydrogen generation rate must be known to design appropriately accident mitigation measures as passive autocatalytic recombiners and igniters.

The physical and chemical phenomena of the hydrogen release are, however, not sufficiently well understood. The increased hydrogen production during quenching cannot be determined on the basis of the available Zircaloy/steam oxidation correlations. Presently it is assumed that the following phenomena lead to an enhanced oxidation and hydrogen generation [5]:

- Melt oxidation,
- Double-sided cladding oxidation
- Interim steam starvation conditions,
- Crack surfaces oxidation (to a less extent).

In most of the code systems describing severe fuel damage, these phenomena are either not considered or only modeled in a simplified empirical manner.

In addition, no models are yet available to predict correctly the thermal-hydraulic or the clad behavior of the quenching processes in the CORA and LOFT LP-FP-2 tests. An extensive experimental database is therefore needed as a basis for model development and code improvement.

The Forschungszentrum Karlsruhe is therefore performing the QUENCH program on the investigation of coolability and determination of the hydrogen source term. The main objectives of this program are:

- The provision of an extensive experimental database for the development of detailed mechanistic fragmentation models,
- The examination of the physico-chemical behavior of overheated fuel elements under different flooding conditions,
- The provision of an improved understanding of the effects of water injection at different stages of a degraded core,
- The determination of cladding failure criteria, cracking of oxide layers, exposure of new metallic surfaces to steam

- The investigation of the oxide layer degradation under steam starvation conditions and influence of this phenomenon on subsequent flooding,
- The investigation of the melt oxidation process,
- The determination of the hydrogen source term.

The experimental part of the QUENCH program began with small-scale experiments with short Zircaloy fuel rod segments [6-8]. On the basis of these results well-instrumented large-scale bundle experiments with fuel rod simulators under nearly adiabatic conditions are performed in the QUENCH facility at the Forschungszentrum Karlsruhe. The large-scale bundle experiments are more representative of prototypic reactor accident conditions than are the single-rod experiments. Important parameters of the bundle test program (see [Table 1](#)) are: quench medium, i.e. water or steam, fluid injection rate, cladding oxide layer thickness, and the temperature at onset of flooding.

The QUENCH-09 bundle experiment, was performed at the Forschungszentrum Karlsruhe on 03 July, 2002. This report describes the test facility and the test bundle, and the main results of the QUENCH-09 experiment including the posttest examination. In addition, a section is dedicated to the computational support performed with the CALUMO oxidation behavior code. Further analytical support for the test preparation and evaluation is published elsewhere [11].

Both bundle tests, QUENCH-07 and -09, were conducted as part of the program on the investigation of severe fuel damage at FZK consisting of integral tests, separate-effects tests, modeling, and code application. Most of the results were obtained within the frame of the "Fifth framework programme of the European Community for research, technological development and demonstration activities (1998 to 2002)", particularly in the COLOSS program in the years 2000-2002. Extensive work has been done on the oxidation of boron carbide and absorber melts as well as on the degradation of B₄C/SS/Zry control rods, which has been reported elsewhere [9, 10].

1. Description of the Test Facility

The QUENCH test facility consists of the following component systems:

- The test section with 21 fuel rod simulators (in QUENCH-09: 20 fuel rod simulators and one control rod simulator),
- the electric power supply for the test bundle heating,
- the water and steam supply system,
- the argon gas supply system,
- the hydrogen measurement devices,
- the process control system,
- the data acquisition system.

A simplified flow diagram of the QUENCH test facility is given in [Fig. 1](#), a three-dimensional schematic of the components in [Fig. 2](#). The main component of the facility is the test section with the test bundle ([Figs. 3 and 4](#)). The superheated steam from the steam generator and superheater together with argon as the carrier gas for the gas analysis systems enter the test bundle at the bottom end. The steam that is not consumed, the argon, the hydrogen, and the carbon and boron containing gases produced in the zirconium-steam and B_4C -steam reactions flow from the bundle outlet through a water-cooled off-gas pipe to the condenser ([Figs. 1 and 2](#)). Here the steam is separated from the non-condensable gases. The cooldown phase with steam is initiated by turning off the superheated steam of 3 g/s and injecting the saturated steam with 50 g/s whereas the argon mass flow rate remains unchanged.

The design characteristics of the test bundle are given in [Table 2](#). The test bundle is made up of 20 fuel rod simulators, each with a total length of approximately 2.5 m, of one central control rod, and of four corner rods (see cross section in [Fig. 5](#)). Twenty fuel rod simulators are heated electrically over a length of 1024 mm. The fuel rod simulators are held in their positions by five grid spacers, four of zircaloy, and one of inconel in the lower bundle zone ([Figs. 6, 7, and 9](#)). The cladding of the fuel rod simulators is identical to that used in PWRs with respect to material and dimensions, i.e. Zircaloy-4, 10.75 mm outside diameter, 0.725 mm wall thickness (see also [Table 2](#)). The rods are filled with a mixture of 95 % argon and 5 % krypton to approx. 0.22 MPa, i.e. a pressure slightly above the system pressure. The gas filling of the heated rods is realized by a channel-like connection system inside the lower sealing plate. The krypton additive allows detecting rod failure of the heated rods during the experiment with help of the mass spectrometer.

In this experiment the central rod contains boron carbide (B_4C) pellets with a stack length of ~1 m (to represent the neutron absorber), stainless steel cladding, and is surrounded by a Zircaloy-4 guide tube. The steel to B_4C mass ratio of 3.5 is identical to that in the future PHEBUS FPT3 experiment. The filling gas for the central rod is helium with a pressure of 0.12 MPa to detect absorber rod failure. To allow steam access to the gap between absorber rod cladding and guide tube, the guide tube holds four holes of 4 mm diameter each at the bottom (-34 mm) and the top (1179 mm).

Heating of the 20 fuel rod simulators is electrical. The total heating power available is 70 kW, distributed among the two groups of heated rods with 35 kW each. The first group consists of the inner eight rods (rod numbers 2-9), the second group consists of the outer twelve rods (rod numbers 10-21). The rod designation can be taken from [Fig. 8](#). Tungsten heating elements of 6 mm diameter are installed in the center of the rods and are surrounded by annular ZrO₂ pellets ([Fig. 6](#)). The tungsten heaters are connected to electrodes made of molybdenum and copper at each end of the heater. The molybdenum and copper electrodes are joined by high-frequency/high-temperature brazing performed under vacuum. For electrical insulation the surfaces of the brazed electrodes are plasma-coated with 0.2 mm ZrO₂. To protect the copper electrodes and the O-ring-sealed wall penetrations against excessive heat they are water-cooled (lower and upper cooling chamber). The copper electrodes are connected to the DC electric power supply by means of special sliding contacts at the top and bottom.

The four corner positions of the bundle are occupied either by solid zircaloy rods with a diameter of 6 mm or by solid rods (upper part) and zircaloy tubes (lower part) of $\varnothing 6 \times 0.5$ mm for thermocouple instrumentation at the inside ([Fig. 8](#)). The positioning of the four corner rods avoids an atypically large flow cross section at the outer positions and hence helps to obtain a rather uniform radial temperature profile. A solid zircaloy rod (rod B) can be pulled out during the test, e.g. at the end of the pre-oxidation phase, to determine the axial oxide layer thickness at that time.

The lower boundary for the lower cooling chamber is a sealing plate made of stainless steel with plastic inlays for electrical insulation, sealed to the system by O-shaped rings. The upper boundary of the lower cooling chamber is a sealing plate of stainless steel. An insulation plate made of plastic (PEEK) forms the top of the upper cooling chamber, and a sealing plate of Al₂O₃ (heat-protection shield) is the lower boundary of the upper cooling chamber (see [Fig. 6](#)).

In the region below the upper Al₂O₃ plate the copper electrode is connected firmly to the cladding. This is done by hammering the cladding onto the electrode with a sleeve of boron nitride put between electrode and cladding for electrical insulation. The axial position of the fuel rod simulator in the test bundle is fixed by a groove and a locking ring in the upmost region of the Cu electrodes. Referred to the test bundle the fixation of the fuel rod simulators is located directly above the upper edge of the upper insulation plate. So, during operation the fuel rod simulators are allowed to expand downwards. Clearance for expansion of the test rods is provided in the region of the lower sealing plate. Also in this region relative movement between cladding and internal heater/electrode can take place.

The test bundle is surrounded by a 2.38 mm thick shroud (80 mm ID) made of zircaloy with a 37 mm thick ZrO₂ fiber insulation and an annular cooling jacket made of stainless steel ([Figs. 4 and 5](#)). The 6.7 mm annulus of the cooling jacket is cooled by an argon flow. Above the heated zone, i.e. above the 1024 mm elevation there is no ZrO₂ fiber insulation to allow for higher radial heat losses. This region of the cooling jacket is cooled by a water flow ([Figs. 3 and 4](#)). Both, the lack of ZrO₂ insulation above the heated region and the water cooling force the axial temperature maximum downward.

2. Test Bundle Instrumentation

The test bundle was instrumented with sheathed thermocouples attached to the rod claddings at 17 different elevations between -250 mm and 1350 mm and at different orientations (Figs. 8 and 9). The elevations of the surface-mounted shroud thermocouples are from -50 mm to 1250 mm. In the lower bundle region, i.e. up to the 550 mm elevation, NiCr/Ni thermocouples (1 mm diameter, stainless steel sheath, MgO insulation) are used for temperature measurement of rod cladding and shroud as is illustrated in Fig. 9. The thermocouples of the hot zone, i.e. from 650 mm upward, are high-temperature thermocouples with W-5Re/W-26Re wires, HfO₂ insulation, and a duplex sheath of tantalum (internal)/zirconium with an outside diameter of 2.1 mm (Fig. 11). The leads of the thermocouples from -250 mm to 650 mm leave the test section at the bottom whereas most of the TCs above 650 mm are routed to the top. Problems resulting from those thermocouples when TC cables pass through the hot zone are discussed in the appendix of this report.

The thermocouple attachment technique for the surface-mounted high-temperature TCs is illustrated in Fig. 12. The TC tip is held in place by two clamps of zirconium. As these clamps are prone to oxidation and embrittlement in a steam environment an Ir-Rh wire of 0.25 mm diameter is additionally used in the experiments with pre-oxidation as was also in test QUENCH-09.

The thermocouples attached to the outer surface of the rod cladding and shroud are designated “TFS” and “TSH” for the heated rods and shroud, respectively. “TCRI” is the designation for the NiCr/Ni-type thermocouples (SS sheath, 0.36 mm diameter at the tip) embedded in grooves of 0.4 mm at the outer surface of the B₄C absorber rod cladding at the 750, 850, and 950 mm elevation.

The wall of the inner tube of the cooling jacket is instrumented between -250 mm and 1150 mm with 22 NiCr/Ni thermocouples (designation “TCI”). Five NiCr/Ni thermocouples are fixed at the outer surface of the outer cooling jacket (“TCO”). The designation of the thermocouples inside the Zircaloy instrumentation rods (corner positions) is “TIT” (Fig. 10). Three of the four corner rods of the QUENCH-09 test bundle were instrumented as follows:

- Rod A: W/Re, 2.1 mm diameter, Zr/Ta duplex sheath, 950 mm elevation (TIT A/13)
- Rod C: NiCr/Ni, 1 mm diameter, stainless steel sheath, 550 mm elevation (TIT C/9)
- Rod D: W/Re, 2.1 mm diameter, Zr/Ta duplex sheath, 850 mm elevation (TIT D/12).

A list of the instruments for experiment QUENCH-09 installed in the test section and at the test loop are given in Table 3. The thermocouples that failed prior or during the test are listed in Table 4.

3. Gas Measurement Devices

The hydrogen and other gases are analyzed by three different measurement systems: (1) a Balzers mass spectrometer (MS) “GAM 300” (Fig. 13) located at the off-gas pipe between

the test section and the condenser, (2) a hydrogen detection system "Caldos 7 G" (Fig. 15) located downstream the condenser, (3) a second, simpler mass spectrometer "Prisma" made by Balzers installed close to the Caldos device (see Fig. 2). So, the non-condensable off-gas passes at first the "GAM 300" MS, then the condenser, the "Prisma" MS, and eventually the Caldos analyzer before it exits to the outside. Due to their different locations in the facility the mass spectrometer "GAM 300" responds almost immediately (less than 5 s) to a change in the gas composition in the bundle whereas the mass spectrometer "Prisma" and the Caldos device have a delay time of about 20-30 s.

The mass spectrometer "BALZERS GAM 300" is a completely computer-controlled quadrupole MS with an 8 mm rod system which allows quantitative measurement of gas concentrations down to about 10 ppm. For the MS measurement a sampling tube is inserted in the off-gas pipe (Fig. 14). It has several holes at different elevations to guarantee that the sampling of the gas to be analyzed is representative. The temperature and pressure of the analyzed gas are measured near the inlet valve of the MS. To avoid steam condensation in the gas pipes between the sampling position and the MS the gas pipe is heated to be between 110 °C and 150 °C (the upper operating temperature of the MS inlet valves). This allows the MS to analyze the steam production rate assuming that no significant condensation takes place in the off-gas pipe upstream the sampling position. Besides, the concentrations of the following species were continuously measured by the mass spectrometer during all test phases: argon, hydrogen, CO, CO₂, CH₄, oxygen, as well as krypton and helium.

The absorber rod was filled with helium allowing the detection of the first failure of the control rod cladding. The MS is calibrated for H₂, CO, CO₂, and CH₄ with well-defined argon/gas mixtures and for steam with mixtures of argon and steam supplied by the steam generator of a Bronkhorst controlled evaporator mixing (CEM) system. He, Kr as well as boric acids are only qualitatively measured. As the fuel rod simulators are filled with a mixture of argon and 5% krypton, the measurement of krypton can be used as an indicator for a cladding failure. The MS off-gas is released into the atmosphere because the amount of the gases taken out of the system is negligible.

The MS cannot distinguish between CO and N₂ (both at atomic mass 28). Thus, it has to be assumed that the test section is free of nitrogen and the whole intensity at amu 28 is due to CO release. Nevertheless, one should have in mind that under special circumstances (e.g. shroud failure) N₂ can also enter the test section.

The principle of measurement of the Caldos system is based on the different heat conductivities of different gases. To avoid any moisture the analyzed gas passes a gas cooler, which is controlled at 296 K (Fig. 15). The response time of the gas analyzer is documented in the manufacturer's manual to be 2 s, i.e. a time in which 90 % of the final value should be reached. As the Caldos analyzer is calibrated for an argon/hydrogen mixture, the accuracy of the hydrogen measurement is affected by the presence of additional gases, e.g. reaction products from the B₄C oxidation during the QUENCH-09 experiment.

4. Data Acquisition and Process Control

A computer-based control and data acquisition system is used in the QUENCH facility. Data acquisition, data storage, online visualization as well as process control, control engineering and system protection are accomplished by four computer systems that are linked in a network.

The data acquisition system allows recording of about 200 measurement channels at a maximum frequency of 25 Hz per channel. The experimental data and the date and time of the data acquisition are stored as raw data in binary format. After the experiment the raw data are converted into SI units and stored as ASCII data.

For process control, a system flow chart with the most important actual measurement values is displayed on the computer screen. Furthermore, the operating mode of the active components (pumps, steam generator, superheater, DC power system, valves) is indicated. Blocking systems and limit switches ensure safe plant operation. Operating test phases, e.g. heat-up or quenching phases, are pre-programmed and can be started on demand during the experiment. The parameter settings of the control circuits and devices can be modified online.

Online visualization allows to observe and to document the current values of selected measurement positions in the form of tables or plots. Eight diagrams with six curves each can be displayed as graphs. This means that altogether 48 measurement channels can be selected and displayed online during the course of the experiment.

The data of the main data acquisition system and of the mass spectrometers were stored on different computers. Both computers were synchronized by radio-controlled clocks.

The data of the main acquisition system were stored at the following frequencies:

0–440 s	0.25 Hz
440–2798 s	1 Hz
2798–3256	2.5 Hz
3256–3646 s	5 Hz
3646–4011 s	1 Hz
4011–4551 s	0.25 Hz

The mass spectrometer data were recorded at a frequency of around 0.2 Hz during the entire test.

5. Test Conduct and Pertinent Results

In general, a QUENCH experiment consists of the following test phases: Heatup, pre-oxidation (optional), transient, and cooling. During all phases except cooling, superheated steam and argon as carrier gas enter the test bundle at the bottom and leave it at the top together with the hydrogen that is produced in the zirconium-steam reaction. Cooling is accomplished by injecting water or saturated steam at the bottom of the test section. For both cases superheated steam is turned off upon injection.

The conduct of the QUENCH-09 test ([Figs. 16 and 17](#)) was planned to be as for QUENCH-07, but after the temperature plateau steam flow should be reduced to 0.4 g/s¹ to reach steam starvation in the bundle, and cooling should be achieved with 50 g/s of saturated steam instead of 15 g/s having been injected during the QUENCH-07 test. The investigation of steam starvation conditions (0.4 g/s) was to widen the database and to provide closer comparison with the PHEBUS FPT3 experiment whereas the high steam mass flow rate was to cool down the bundle as fast as possible and so to try to preserve the bundle status prior to cooling initiation.

The sequence of events is listed in [Table 5](#). The bundle was heated by a series of stepwise increases of electrical power from room temperature to ~873 K in an atmosphere of flowing argon (3 g/s) and preheated steam (3.4 g/s). The bundle was stabilized at this temperature, the electrical power being 4 kW. During this time the operation of the various systems was checked. Afterwards the power was ramped smoothly to 13.3 kW, corresponding to a maximum temperature of ~1340 K, and then kept constant in order to reach the target temperature of 1773 K.

The QUENCH-09 test results are shown in [Figs. 18-31](#). Local perturbation of the control rod temperature was first detected at 2280 s indicating initial control rod failure at ~1555 K. This was confirmed a few seconds afterwards by the helium detection in the off-gas ([Fig. 20](#)). In both experiments, QUENCH-07 and -09, the control rods failed at nearly the same temperature and a time when each bundle approached the B₄C oxidation phase temperature.

The target temperature of 1773 K at the hottest location, i.e. 950 mm above the bottom of the heated length, was reached at 2581 s, and a power reduction maneuver was initiated. (For QUENCH-07 it was decided during the test to reduce the power when the temperatures at the elevation 950 mm had reached 1723 K, i.e. 50 K lower, in order to definitively exclude early temperature escalation.) Simultaneously, temperature escalations occurred at the same elevation. This early escalation did not occur during QUENCH-07. Increases in temperature were observed during the next few seconds at elevations 850 and 750 mm. Due to the temperature excursion and possible melt formation corner rod B was not withdrawn as was planned prior to the test so that there are no oxidation data available before the start of the cooling phase.

¹ The reduced steam flow actually should be 0.3 g/s. Post-test analyses of the MS data indicated that the real steam flow rate in this phase was rather 0.4 g/s.

At 2633 s the steam flow of 3.4 g/s was turned off and at 2636 s the signal of the F 206 flow meter indicated the steam flow to be constant at ~0.4 g/s until 3316 s when the superheated steam flow was terminated and the flow of 50 g/s was initiated and established at 3358 s according to the F 204 flow meter measurement.

The power reduction to 8 kW was completed at 2602 s ([Fig. 17, bottom](#)). Just at that time (2600 s) krypton was detected in the off-gas pipe, indicating failure of at least one of the fuel rod simulators ([Fig. 27, top](#)). Also at this time the maximum temperature was ~2050 K. Despite the lower power the temperature escalation continued, reaching a peak of 2283 K at ~2630 s (TFS 4/13). At about the same time, i.e. at 2623 s, the shroud failed ([Fig. 27, bottom](#)) indicated by the pressure drop of P 406 (pressure in the annulus between shroud and inner cooling jacket). The hydrogen generation increased sharply to a peak of 0.24 g/s at 2648 s (peak duration ~2590-2710 s), shown in [Fig. 29](#). At the same time very small amounts of CO and metaboric acid were detected in the offgas ([Fig. 30](#)).

Prior to the test it had been decided that in case of a premature escalation the steam flow would be reduced to 0.4 g/s to limit the oxidation power and hence to stabilize the bundle temperatures. This was effected at 2637 s. At that time some temperatures at higher elevations began already to decrease. During the next eleven minutes the conditions in the bundle were essentially steam-starved, as indicated by the mass spectrometer measurements. In this period of time the power was increased in a stepwise manner to stabilize the maximum bundle temperature at 2073 K ([Fig. 17](#)). The location of the escalation moved downward, and at the upper elevations the bundle temperature generally decreased because the steam was already consumed there and no more oxidation was possible. Evaluated excursion temperatures are listed in [Table 6](#). Thermocouple failures began with the first temperature excursions, so that the maximum bundle temperature cannot be determined. The maximum measured test rod temperature amounts to 2473 K during the steam-starvation phase at the 750 mm bundle elevation (TFS 2/11, see [Table 7](#)). The shroud temperatures had their maximum at around cooling initiation ([Table 8](#)).

In contrast to QUENCH-07, almost no CO, CO₂ or CH₄ was observed up to cooling initiation ([Fig. 30](#)). Only a small intermediate CO peak (< 0.1 g) was seen by the MS between 2593 and 2666 s, whereas in QUENCH-07 2.5 g CO and 3.6 g CO₂ were produced up to initiation of cool-down. The total hydrogen generation up to the end of the steam-starved phase was measured to be ~60 g (QUENCH-07: 62 g during pre-oxidation).

Cooling was initiated at 3316 s by switching the injection to cold steam (~440-500 K) at a rate of 50 g/s. The power was kept at 15 kW for ~25 s, reduced to 4 kW in 16 s and kept constant for ~70 s. The electrical power was then shut off, but the steam injection continued until cooling to ~470 K had been achieved. The temperatures measured at initiation of cooling are provided in [Fig. 9](#).

The escalation that had moved into the lower half of the bundle during the steam starvation period was immediately terminated for the lower bundle elevations at the beginning of the cooling phase. However, several locations toward the top of and above the heated zone which had exhibited stable or even decreasing temperatures prior to the initiation of cooling experienced a strong escalation which clearly began immediately after increase of the steam

flow. According to the posttest photographs in [Fig. 40](#), an interaction of a metallic strip for fixing the ZrO₂ fiber insulation (changed to plastics ones in future tests) with stainless steel led to the failure of the inner cooling jacket at 3343 s. This was additionally indicated by a drop of the argon pressure P 403, i.e. the pressure in the annulus inner/outer cooling jacket (see [Fig. 28](#)). At about the same time an increased release of all gaseous species was observed. A large amount of hydrogen (400 g) and significant quantities of CO (33 g) and CO₂ (22 g) were produced during the cooling phase for a period of about 3 minutes, i.e. even after the electrical power was shut down ([Figs 29 and 30, top](#)). The detection of boric acids persisted for a further two minutes ([Fig. 30, bottom](#)). Methane production was much smaller and lasted for a shorter period of time. Even at the location of the mass spectrometer sampling tube the temperature T 601 increased from ~345 to ~940 K within one minute after cooling initiation.

The observation in QUENCH-09, that no significant amount of reaction products of the B₄C oxidation was generated before cooling initiation and that the total amount of CO and CO₂ was almost completely produced during the cooling phase, could be explained in the following ways. 1) Steam had only very shortly direct access to the B₄C pellets for oxidation at the time when the first local breach of the steel cladding occurred, i.e. at ~1550 K. Then, the gap between cladding and guide tube was closed by relocated melt preventing further oxidation of B₄C. The eutectic B₄C-SS-Zr melt remained localized due to a protective ZrO₂ scale. With the failure of the oxide scale of the guide tube, which occurred during flooding, the melt is released and oxidized immediately. This scenario would explain the observed rapid increase of CO₂ and CO release being favored by steam excess during cooling. 2) Another explanation is based on results of pre-test calculations and MS measurements [20]. The just started release of CO due to the interaction between steam and B₄C stopped after reduction of the steam flow from 3.4 to 0.4 g/s. Most likely, the location of the first absorber rod failure was in the hottest elevation. Here, steam starvation conditions established and the oxidation of B₄C was interrupted.

Regarding the gas measurement by the mass spectrometer it has to be noted that the measured values of all gas species are most reliable up to the cooling phase, i.e. at 3315 s. After the initiation of the cooling phase the argon concentration was analyzed to be almost zero for a period of about 30 s. The small Ar concentration complicates the quantitative evaluation using the measured concentrations of the species and the given Ar flow rate according to equation (1).

$$\dot{m}_{gas} = \dot{m}_{Ar} \cdot \frac{M_{gas}}{M_{Ar}} \cdot \frac{c_{gas}}{c_{Ar}} \quad (1)$$

with \dot{m} , M , and c as mass flow rate, molecular mass, and concentration, respectively.

Therefore, the steam flow rate is used when the argon concentration is too small. The failure of the inner cooling jacket in test QUENCH-09 at 3343 s caused an additional difficulty due to an increased argon bundle flow. After the failure of the cooling jacket "FM 401 modified" is used in equation (1) instead of the argon bundle flow FM 401. The correction procedure for

the argon flow through the test bundle after failure of the cooling jacket is described in Appendix 1. Furthermore, MS data were evaluated with reference to the steam inlet data as cross-check.

Based on the total amounts of CO and CO₂ (33 and 22 g, respectively) the contribution of hydrogen by the B₄C oxidation in QUENCH-09 was evaluated to 2.2 %, compared to 2.4 % in QUENCH-07. The percentage of the B₄C mass that was oxidized during the QUENCH-09 test was evaluated with help of the posttest examination and amounts to roughly 50 % (20 % in QUENCH-07). The QUENCH-09 hydrogen release in total resulted in 460 g, 87 % of which was produced during cooling. [Table 10](#) compares the results of QUENCH-07 and -09.

During the test samples of fluid condensed behind the sampling line of the mass-spectrometer were taken. The samples were collected in flasks at regular time interval. After the test the samples were chemically analyzed. The results of the boron concentration are listed in [Table 11](#).

With respect to the second period of escalation in the upper bundle region of QUENCH-09 in which cooling was effected with 50 g/s steam flow, it is conjectured that the long period of steam starvation caused a reduction in thickness of the protective ZrO₂ scale so that upper regions of the bundle became particularly susceptible to oxygen uptake and an enhanced zirconium oxidation led to the second escalation period. Therefore, an enhanced oxygen uptake took place when the high steam flow was supplied to the test bundle.

6. Posttest Examination

6.1 Posttest Appearance Prior to Bundle Sectioning

In the region between ~520 and 840 mm the shroud and the bundle were partially molten, and the shroud was shaped to a large “bubble”, similar to the QUENCH-07 bundle. Furthermore the shroud is severely oxidized in this region and reacted with the ZrO₂ fiber insulation ([Fig. 34-36](#)). A large number of once-molten fragments of black color were found at the opening of the test train exit and were seen to have been transported for over one meter into the off-gas pipe ([Figs. 32 and 33](#)). Some of these fragments were collected and investigated on the chemical composition ([Table 12](#)). During dismantling the heated rods with the upper electrodes broke off so that the upper bundle end is then at around 1000 mm elevation. After dismantling, the test bundle and shroud appear severely damaged in the region from ~520 mm elevation upward.

3-D posttest information on the inside of the bundle is provided in [Figs. 37–39](#). The photos were obtained with help of an OLYMPUS endoscope. [Fig. 37](#) shows the failures of sheathed thermocouples. On the upper photo one can see a longitudinal crack in the oxidized Zircaloy sheath of the high-temperature TC, caused by thermo-mechanical stress. The lower photograph presents the result of the eutectic interaction (~1570 K) between the Zircaloy shroud and stainless steel sheath of the NiCr/Ni thermocouple.

Fig. 38 exhibits a longitudinal crack at rod 16 and a rupture formation at the oxidized cladding of rod 17. Crack formation in oxidized claddings was studied in detail in the single rod experiments. The appearance of the rupture at the cladding of rod 17, however, was not observed in single rod tests. Fig. 39 shows the slightly-deformed lower part of the Zircaloy spacer grid at the 550 mm elevation. There is some relocated melt located between the spacer and the shroud.

6.2 Sectioning of the Test Bundle

The encapsulation of the test bundle was performed in three steps. First, a cap was placed over the bottom of the copper electrodes and a low-melting metal alloy (containing Pb, Bi, Sn, and In; density of $\sim 10 \text{ kg/dm}^3$; melting point of 331 K) was used to seal the bottom of the bundle. Secondly, a small amount of the same resin to be used for the encapsulation of the bundle was placed on top of the metal to generate an interface of around 0.2 m that prevents the metal from being liquefied after starting to epoxy the bundle together with its shroud. The test bundle was evacuated before charging it with resin to allow filling of pores and cracks. Due to the “ballooned” shape of the shroud in the hot region, the mould for filling the bundle from the bottom with epoxy resin had an inner diameter of 190 mm so that approx. 34 kg of resin and hardener were needed. The epoxy system Rütapox 0273 with the hardener designated LC (manufactured by Bakelite GmbH, Iserlohn) was chosen based on the experience with the CORA test bundles. After epoxying the bundle the resin is allowed to harden for one week. After hardening the epoxied bundle showed large cracks in the upmost region due to the large amount of resin used.

The cross sections of the QUENCH-09 test bundle were chosen according to the sectioning map given as an overview in Fig. 41. The exact elevations are listed in Table 13. The cross sections that were polished for metallographic examination can also be taken from Table 13.

Figs. 42-45 present an overview of the cross sections available. They are described and interpreted in section 6.4.

6.3 Investigation Procedures of the Metallographic Examination

The post-test examination of the bundle is based on the metallographic preparation of cross section slabs by careful grinding and polishing, comprehensive investigation and photo documentation. The evaluation uses a selection of available examples for illustration. The interpretation of the bundle behavior is explained by composing micrographs into thematic figures. The final bundle state is thus described, and the mechanisms of physico-chemical components' interaction and of the oxidation are deduced as far as possible. For this it was helpful to proceed upwards from the lower bundle elevations, in the direction of increasing temperatures, and thus increasing extent of interaction. Thus, the state at lower elevations could be used to understand intermediate states of the higher elevations. Special attention was paid to the quench and control rod related phenomena.

Additional information was gained in a separate study by scanning electron microscopy (SEM) and energy-dispersive element analysis (EDX). Certain polished cross sections and

positions therein were selected in order to verify suspected bundle components interactions, especially the resulting distribution of control rod components. Results are given in the respective section together with examples for micrographs, spectra and analyzed compositions.

For all prepared cross sections the scale thickness on simulator and corner rod surfaces as well as inner shroud surfaces was measured as far as possible. This was done in four directions around rods and shroud. The results are collected in [Figs. 86-90](#) and an axial profile is provided in [Fig. 91](#).

6.4 Results of Bundle Documentation and Microstructure Interpretation

Cross section QUE-09-01, bundle elevation 73 mm

The cross section overview of bundle, shroud and spacer grid is depicted in [Fig. 46](#). This figure can serve as reference for the non-damaged bundle since no change by the test is detected. An eccentricity of the control rod versus its guide tube is mentioned. The bottom of slab QUE-09-01 at cross section elevation 60 mm is depicted as smaller insert to the right of the figure. Note that this picture has been mirror-inverted (converted to top view) in order to facilitate the comparison.

Cross section QUE-09-18, bundle elevation 460 mm

During the preparation of the cross section slab the central control rod stub was lost, unfortunately. The other 20 fuel rod simulators are found in a distorted arrangement, reflecting their individual movement due to bending ([Fig. 47](#)). The shroud is intact, but at the south-east (SE) and NW positions some external thermocouples (TCs) are seen connected to the shroud wall by melt relocation from above. Within the bundle two melt lumps, one between rods #2 and #9, the other between rod #15 and the shroud are found; details and interpretation are given later. Different from the massive corner rod B, the three instrumented corner rods were initially hollow. Obviously, they got filled by internal melt relocation. Incomplete tube filling and wetting of the TC sheath is seen for the corner rod at NE. An observed rubble fragment is a strongly damaged TC. The insert to the right of [Fig. 47](#) depicts the bottom of the slab, the cross section elevation 444 mm, given in inverted view for comparison.

[Fig. 48](#) illustrates three corner rods together with adjacent fuel rods, on top of the figure the corner rods A and C position. Both corner rods are filled by internally relocated melt, as already mentioned. The bottom viewgraphs show the partial filling of corner tube B and TC wetting (left), and the void formation within rod #21 due to partial cladding melt relocation (right). A peak temperature of ~2050 K for the cladding of the rod is deduced. [Fig. 49](#) depicts the melt lump between rods #2 and #9 in detail, together with the lump between rod #15 and the shroud. Both lumps have relocated from higher elevations.

Cross section QUE-09-02, bundle elevation 520 mm

At this cross section considerable damage to the bundle and the shroud is most obvious in the overview macrograph ([Fig. 50](#)), which includes as insert the inverted view on the slab bottom at 507 mm. The corner rods A and B are found attached to the shroud by "necks", which were formed during steam oxidation of the contacting structural components. In contrast, the corner rods C and D, which had moved inwards, got contact to rods #10 and #21,

or #7 and #19, respectively. Finally, for the corner rod C only the TC can be distinguished. Some fuel rod simulators have a distorted but still closed contour, others show more or less wide-split openings. Several of them form pairs and contain common melt pools. The central control rod (CR) indicates interactions between its components. More information is given together with illustrations in higher magnification:

Fig. 51 depicts the melt accumulation at all external shroud TC positions, by which bridges between the TCs and the shroud surface have formed. For two of them the melting process included even the shroud wall, so that on SW position the close rod (#15) is included into the common melt pool. Fig. 52 shows the CR with the B₄C pellet at eccentric position. Besides a large and several small voids the original contour of the CR contains re-solidified “absorber melt”, as shown on the right side of the figure. As the guide tube (Zry) and the cladding (SS) of the CR did not remain as solid structures, one has to assume that the guide tube scale did stabilize the CR contour of the melt for rather long time. The fact, however, that this scale is finally absent, indicates its late failure, possibly by spalling and transfer of fragments with the medium during quenching. It is well known that scales, grown on melts of mixed composition are less stable than scales on pure cladding material.

Fig. 53 gives a selection of rods showing examples for a closed scale, a split scale, and connections with other rods. The closed contour of rod #14 provided protection from steam ingress, which took place through the breach of rod #17. After relocation of the melt between rods #3 and #12 the common scale did not remain tight, whereas the melt pool between rods #20 and #8 retained its barrier function, as indicated by the non-oxidized void surface. Fig. 54 depicts the overview on rods #2 and #9 (left) and respective melts (right). The more regular (rod #2, top) or more irregular (rod #9, bottom) microstructures of the melts indicate smaller or larger fractions of CR interaction products, transferred from the CR to the surrounding rods. This transfer should have taken place at higher elevation. So, local differences in composition and related variations of oxidation and re-solidification behavior arose, even within the same connected melt pool.

Fig. 55 illustrates the distribution of metallic materials around rod #19, together with metallic corner rod residues around the TC. The void to the right of the TC had contact to steam according to its ceramic contour, whereas the void to the left of the TC remained isolated from steam within an intact scale, ranging from rod #19 to #7. These details are mentioned to draw the attention to the change from the original arrangement “rod bundle / interconnected flow channel” towards a “blockage / flow channels” configuration, which went on during the experiment and can be distinguished at many positions. The wedge-shaped melt accumulation at rod #19 shows at closer look (right side of the figure) the typical cladding-type melt microstructure with dendritic ZrO₂ precipitates, formed during cool-down. Further, even the gap between ZrO₂ pellet and tungsten heater rod is filled by melt, which might have penetrated through a crack of the annular fuel simulator pellet. Damage of that kind occurred at rather low level in this experiment, which leads over to the next higher elevation.

Cross section QUE-09-04, bundle elevation 590 mm

Only 70 mm higher, the bundle shows a strikingly different state (Fig. 56). This is compared to that of the bottom of the cross section slab (elevation 577 mm), which is given as insert to the right of the figure. To a first impression the bundle seems to be completely blocked, since porous masses cover most of the area. The shroud is converted to a thick and porous wall with quite defined outer contour, whereas its inner limit is seen mainly at NW direction. Here,

flow channels between the shroud and the spacer grid structure remained open. The expansion of the outer shroud contour is understood as the result of reductive consumption of ZrO_2 fibers of the insulation package. Therefore, the bundle itself, the most important part of the test insert, is given in [Fig. 57](#) as basis for the following detailed description of the bundle interior.

It is helpful to start the interpretation of the bundle state as depicted in [Fig. 57](#) by trying to identify the damage progression history. At the considered elevation and above, violent control rod degradation has taken place (see CR remnants in insert of [Fig. 56](#) and absence at the described top elevation). Distribution of “absorber melt” in the bundle and initiation of fuel rod degradation are the plausible reasons for inhomogeneous damage progression during dispersion, dilution and steam oxidation of absorber melt. Partial contact with absorber melt must have contributed to fuel rod simulator cladding perforation and splitting failures. Cladding melt dispersion and steam oxidation have followed. The metallic melts have enclosed some empty volumes during relocation and in addition the melt, which got “contaminated” by fractions of CR descent, has formed some internal porosity due to enclosed gaseous oxidation products. Both mechanisms are understood to have contributed to the finally observed melt distribution and porosity.

With respect to the here observed melt porosity an experimental study by A. de Bremaecker is mentioned, in which violent interaction between yttria-stabilized zirconia and oxidation products of boron carbide took place: The observed foaming (“bloating”) of generated melt has been interpreted to accompany formation of YBO_3 mixed oxide [19].

The metallic melts have continuously gained properties of viscous magma and were stabilized in final position during completion of their conversion to re-solidified ceramic masses, which are observed now. In support of this anticipated interpretation the first items to be explained are the finally open and thus active steam flow channels through the magma. Fortunately, most of them can be distinguished by their lighter gray tint (see positions, indicated in [Fig. 57](#)): Direct steam contact led to conversion to stoichiometric ZrO_2 , which is known to reflect and scatter the illuminating light more than substoichiometric scale. The blockage at S to SW position, which is otherwise dense, is penetrated by several relatively narrow steam flow channels. This blockage should not contain CR components; SEM/EDX analysis, reported below, will give the definitive answer. Besides the above mentioned large channels between shroud and spacer in NE orientation, different cross section forms of various active flow channels are observed. Less obvious is the interpretation of other empty areas as finally blocked former flow channels, which were not active until the end of the test termination phase. Two of them are indicated in [Fig. 57](#) as well, as they show the typical continuous contour layer around. Naturally, the failure of flow channel walls and the steam exposure of previously protected metallic material can hardly be distinguished in the oxidized state of the bundle elevation. In total, most of the smaller voids are interpreted as closed pores.

This leads over to the description of the individual fuel rod remnants. The rod cladding remained nowhere metallic, and even its products of steam oxidation and pellet interaction are only found fragmented or incomplete. [Fig. 58](#) depicts fuel rods within the above mentioned partial blockage of the bundle at SW. The rods are found in fair condition, rod # 5 shows still a near fragment of oxidized cladding. After having lost the protection from the cladding, the ZrO_2 pellets were exposed to steam or metallic melt (#16), and underwent recrystallization in

contact to the hot tungsten heaters. The heater rods are still surrounded by the pellet remnants and were protected from steam oxidation.

Fuel rod #5, depicted already in the previous figure, is inspected with respect to the surrounding melt in [Fig. 59](#). Pellet and surrounding melt cannot be distinguished easily at first glance. However, micrographs, taken in polarized light, help to draw the attention to informative features. Whereas the pellet is found relatively coarse-grained, the surrounding melt consists of finer grains of regular form. This microstructure is in agreement with an in-situ conversion of the melt to the ceramic state, according to the pool oxidation mechanism, supported and described in [8]. In contrast, the grains at the border of a steam flow channel (top, left in the figure) correspond to the zirconia scale growth around the previously still metallic melt. Within the same melt pool, N from rod #15, crack formation in relation to a small void is illustrated in [Fig. 60](#). During melt accumulation, the void, which can be a pore or eventually a steam flow channel, has formed and remained at the original pellet surface. Oxidative conversion and re-solidification of the melt followed, in a final phase stress relief by crack growth took place. The crack system followed boundaries of elongated grains through the pellet, into the melt, and along the former pellet contour.

Continuing with the description of the fuel rods, [Fig. 61](#) gives a selection of fuel rods, which are less intact, in so far as they have retained only a part of the pellet. Since tungsten is known to oxidize fast in steam at the exposure temperatures, which were reached during the experiment, the observed formation of the tungsten/tungsten oxide eutectic should be the main reason for the depicted heater rod degradation. Eutectic melt formation and melt relocation is interpreted to have consumed the rods at the non-protected side (see also following section on SEM/EDX analysis). E.g. rod #18 was directly exposed to an active steam flow channel on its right side, whereas the porosity of the W-rod #10 is due to previous infiltration and later relocation of eutectic melt. [Fig. 62](#) gives examples for very poor fuel rod preservation. Only reacted pellet remnants and tungsten rod residues remain besides accumulated tungsten/tungsten oxide eutectic melt. The latter has protected fully embedded W-rods. [Fig. 63](#) depicts tungsten-rich melt around heater rod #2 in different magnification, showing fine-grained decomposition microstructure. The given features of heater rod degradation are of course only test specific and an artefact, to be accounted in the transcription to accidental reactor core conditions.

The description of this bundle elevation is completed by observations at the bundle periphery. [Fig. 64](#) gives the illustration and interpretation of the peripheral part of an elongated steam flow channel. In combination, respective information is given on a bundle/shroud region, showing crack formation, which occurred during the quench phase, according to non-oxidized crack surfaces. [Fig. 65](#) depicts the S to SE oriented shroud region, for which a bump of melt deserves detailed illustration. According to the examples for a complete series of micrographs across, given to the right of the figure, the melt shows its mixed type and its metallic/ceramic state. The bump is interpreted to result from test insert/cooling jacket interaction after complete penetration of melt through the zirconia insulation package. This dramatic consequence of test insert superheating leads over to the next higher bundle elevation.

Cross section QUE-09-06, bundle elevation 650 mm

The large cross section area, occupied by the test insert after expansion of the reacted shroud into the fibre insulation package around, is only partly filled by the bundle itself in eccentric position, and voluminous porous masses, connected to the shroud ([Fig. 66](#)). Material

losses due to downward relocation have been replaced by corresponding gains from above. The material distribution varies strongly with the elevation, as seen by comparison with the insert to the right of the figure, which indicates some more re-solidified melt within the bundle region at 637 mm elevation. It is quite plausible to interpret, that the magma flow decreased in velocity due to increasing viscous forces in the course of the experiment, until it stopped due to oxidation to the observed ceramic masses. Naturally, this occurred with varying time scale for different steam exposure conditions and magma volumes.

Fig. 67, depicting the magnified bundle region, supplies some assistance for interpretation, which is not repeated here. In addition it is only stressed, that the control rod is completely missing. The porous structure of the melt seems to relate to some minor fractions of control rod components and related formation of gaseous products. Further, the already mentioned formation of low-melting eutectic mixtures should be taken into account with respect to the influence of the destroyed control rod.

The fuel rod simulators are found in quite advanced progress of destruction. Nowhere can cladding be distinguished, and even the pellets have reacted. Consequently, the tungsten heater rods withstood only within an intact melt cover, whereas exposed ones experienced reactive dissolution and continuing diameter loss. More details are shown in Fig. 68 to Fig. 70, a series, in which a part of all fuel rods are grouped and their state is described in the order of increasing degradation.

Cross section QUE-09-08, bundle elevation 700 mm

Qualitatively, the materials distribution is similar to the previous cross section, but more porous melt dominates the picture (Fig. 71). In addition, some lumps of melt, resulting from heater rod degradation, and a melt pool in the bundle center, accentuating the missing of the control rod, are found; both melt types are predominantly metallic, and their melting ranges ought to be high. Another result, better to be seen at the higher magnification of Fig. 72 is the much superior preservation state of most fuel rod simulators, compared to the 650 mm elevation. In this sense, the series Fig. 73 to Fig. 75 of simulator macrographs, are grouped and described in the order of increasing damage, to facilitate comparison to Fig. 68 to 70. Detailed interpretations are given in the figures.

Cross section QUE-09-14, bundle elevation 950 mm

Above a bundle range, which is not examined in detail, and which is characterized as source region for melt relocation, the next considered elevation is depicted in Fig. 76. Brittle shroud scale fragments fell down except one residue in N direction. Whereas the main bundle arrangement is regular, in total four of the simulator rods are found more apart on S and W, so that they cannot be identified. One of the simulator rods (#3) is completely destroyed (only heater rod remains), whereas the others show various states of degradation. The control rod is missing, and the bundle center contains most of the accumulated rubble fragments and melt lumps. All mentioned items are addressed below in more detail.

Rod #6, together with bundle center and adhering melt is illustrated in Fig. 77. Almost the whole rod cladding has disappeared as part of the mostly relocated melt, and the remaining cladding and melt remnants are converted to the ceramic state. The pellet defect is mentioned without deciding between the possible mechanisms, fracture or leaching. The melt at

SW, fine grained, porous and finally ceramic, is identified together with other lumps and fragments of this elevation in the chapter on SEM/EDX results.

Fig. 78 gives details on several degradation mechanisms for the example of rod #21, steam oxidation of exposed cladding, internal cladding melt/pellet interaction, and even some heater rod dissolution trend. The following figure is also focused on the essential interpretation (Fig. 79): Similar observations were made and interpretations are given for rod #9, however, in this case for a position of melt coverage. A documentation of the state of some more fuel rods is given for the first rod ring in Fig. 80 and for the second one in Fig. 81. The same variation range of damage and deduced history is registered for inner and outer bundle positions: Strong oxidation of steam-exposed cladding, related scale bulging and fracture, cladding matrix melting and pellet dissolution, melt release (including the most probable release of control rod interaction melt), partial embedding of rods, conversion of all metallic components and products into ceramic, often porous masses, are observed. According to local and temporal conditions, fragment and melt relocation took place as well.

Cross section QUE-09-16, bottom, bundle elevation 1480 mm

The top side of this cross section slab (1510 mm elevation) showed a rather good condition, due to protection by the alumina plate with heat shield function, installed at 1500 mm bottom level. This is why the inspected side of the slab was the bottom, in contrast to all other reported cross sections. For comparison with the other overviews, Fig. 82 is also depicted as top view (main macrograph mirror inverted, insert macro not inverted). Far above the upper end of the shroud (1300 mm), the missing of the support tube for the control rod arrangement is to be mentioned first. (Since the original boron carbide pellet stack ended at 1008 mm, the stainless steel cladding at 1063 mm, followed by a SS plug, an inconel spring and another plug, there was only the guide tube prolongation, an empty Zry tube at the considered elevation.) Its relocation in form of melt and fragments is plausible for a structure with small heat capacity and for the high temperature, which was reached, according to the partially damaged state of the surrounding rods. Those show in Fig. 82 intact molybdenum electrodes and partially damaged Zry cladding. Closer inspection of rod #19 as example is illustrated in Fig. 83. In contrast to strong Zry melt relocation at other directions, much melt is retained in S direction, according to the micrograph below. A defect of the external scale and a void within the still metallic melt are mentioned. In higher magnification the additional micrographs depict the duplex scale and the intact electrode coating, a plasma sprayed zirconia layer. Figs. 84 and 85 document the state of some other rods, grouped according to less or more damaged rod conditions. The zirconia layer for electrode protection is intact for all of them. The cladding state ranges from considerably oxidized but intact to totally molten or fragmented, respectively. Lateral rearrangement of melt and penetration through defective scale, as well as axial relocation have contributed to fragmentation of bare scale, which will have relocated partially as rubble fragments.

6.5 Lateral Oxide Scale Thickness Distribution and Axial Profile

A flat temperature profile across the bundle was reflected in the measured lateral scale thickness distribution at the 460 mm elevation (Fig. 86). The values around and above ~50 μm are unimportant with respect to the state of the components. Already at 520 mm elevation those are strongly oxidized with a large scale thickness variation (~220 to ~780 μm).

This result indicates local temperature variations and is consistent with the observed melt redistribution (Fig. 87). At the next three elevations, studied otherwise in detail, the respective measurements were not very useful, since no materials remained finally in metallic state. Consequently, measurable scale structures can be either relatively thin after early loss of molten parent metal, or can have grown further in case of enduring melt retention. This means that given data would not be representative figures for the oxidation progress. Therefore, no results are illustrated, and the scale thickness is set to the theoretical value of ~1130 μm , which compares to the total conversion of cladding tube nominal thickness.

At the next higher elevation for which a full measurement set was meaningful (Fig. 88), the obtained values must also be seen in context to full metal conversion. One limit of the data range (~600 to 1400 μm) corresponds to early metal loss by relocation, the other to extended melt oxidation in addition. The obtained statistical average (1083 μm) must be understood in this sense. At the next elevation, far up in the electrode zone (1480 mm) the oxidation is still unusually pronounced in comparison to previous experiments of the QUENCH series (Fig. 89). The given data are influenced by melt relocation at this elevation and the flow pattern of the superheated atmosphere. In comparison, the elevation 1510 mm (Fig. 90) was protected from the flow by presence of the alumina heat shield. Here, only layers up to 10 μm are found. Fig. 91 shows the axial profile for the above reported results.

6.6 SEM/EDX Analysis of Special Components and Products

Procedures

The preparation of the large cross section slabs for SEM/EDX investigation used initially carbon sputter deposition to get the required surface conductivity. Then, a modification of the sputter device allowed sputter coating with gold. In order to exclude an eventual distortion of the carbon signal from the specimen itself, a carbon-coated specimen was re-polished, gold-coated, and the measurements repeated: All larger carbon signals were confirmed. Some ambiguity might arise for traces of carbon content in a carbon-coated specimen, but such results are not considered for the purpose of the report. In addition to the analysis of special bundle interaction products, a tungsten heater rod and an original B_4C pellet (Framatome) were analyzed for comparison.

EDX analysis at cross section QUE-09-02, bundle elevation 520 mm

Figs. 92 and 93 illustrate the SEM/EDX results for the control rod cross section at the given elevation. Only supported by scale of the guide tube, the peripheral zones of the control rod (Fig. 92), which were completely molten by interaction of guide tube (Zry) and CR cladding (stainless steel), remained in place until re-solidification. The element spectra indicate a rather uniform composition distribution, which indicates a “ternary” mixture, involving considerable carbon from pellet dissolution. Fig. 93 gives the analysis, obtained more close to and within the pellet: The decomposed melt contains here much more carbon besides the steel components. The pellet itself is clearly identified, and the quantitative analysis compares well to that of an original pellet.

On this basis, the analysis of melt within the adjacent rod #2 is described: Fig. 94 depicts an overview and the field of integral analysis, for which no spectrum is shown. The spectra, given instead, result from small area analysis at the indicated positions and show larger

compositional differences: Corresponding to the melt decomposition during re-solidification, enrichment of minor components in precipitated phases or residual melt took place, which facilitates the interpretation. Tin enrichment in the metallic part of oxidizing Zry, and finally the formation of a Zr-Sn phase is well known (top spectrum). The spectrum in the middle is typical for Zry/steel interaction, and the lower spectrum indicates a precipitated primary phase of Zr-(C, B) type, which seems to contain some Ta, resulting from thermocouple sheath degradation. Besides those details, the unambiguous identification of control rod components within a fuel rod simulator, which has a closed contour at the given elevation, is remarkable. This fact can be only explained by downward relocation of melt within the rod. At higher elevation "absorber melt" from control rod degradation must have penetrated into the destroyed or perforated cladding of this directly adjacent fuel rod simulator.

This observation is, moreover, not singular and not restricted to neighboring rods. [Fig. 95](#) depicts similar results for fuel rod #8, direct control rod neighbor as well. The small-area analysis results need no further discussion, but it shall be mentioned, that the given element compositions should be considered as examples only. Finally, [Fig. 96](#) illustrates the respectively identified presence of control rod components within fuel rod simulators #5 and #14, the latter one of the outer ring. Its closed scale contour and the spreading of internally relocated melt to opposite directions are accentuated.

EDX analysis at cross section QUE-09-04, bundle elevation 590 mm

The SEM/EDX analysis study was dedicated to typical areas within the bundle itself and allowed to confirm the already given tentative conclusions, deduced from the bundle microstructure investigation. The results can be summarized according to the typical examples, depicted in [Figs. 97 to 99](#).

As previously mentioned, the SW part of the bundle core (see [Fig. 57](#)) is found blocked by dense melt, except penetration of steam flow channels. Since no other elements but zirconium and oxygen (carbon due to sputtering) were detected by EDX analysis ([Fig. 97](#)), the melt pool was formed by fuel rod simulator melting (cladding/pellet interaction), followed by conversion to the completely ceramic state by steam oxidation. It can be assumed that the latter was accelerated by ZrO_2 phase precipitation within the melt according to the pool oxidation mechanism, precipitation phase, described by M. S. Veshchunov [8]. The steam flow channels, which obviously remained open during the melt accumulation phase, continued to support the oxygen transport.

So one can understand those observations as proof for the transformation of a bundle configuration into a melt pool with magma-similar behavior. Provided that the use of ZrO_2 simulator pellets instead of real fuel is no critical point, the behavior mechanisms of a reactor core near the limit between early phase and late phase of core degradation has been experimentally verified for the first time.

The central part of the bundle, partially filled by melt which contains many smaller pores and some larger voids, was analyzed for the suspected degradation products of the completely missing control rod. [Fig. 98](#) gives the clear answer that control rod melt has been diluted during fuel rod simulator attack and dissolution. The porosity of the resulting melt can be related to gas release during oxidative conversion of CR components or products. Complete conversion to the ceramic state took place.

The other studied item, depicted in [Fig. 98](#), is the striking fact of considerable heater rod dissolution. It is not necessary to speculate about excessively high temperatures, necessary to melt tungsten itself. Exposure of tungsten to steam is known to give rise to formation of the tungsten/tungsten oxide eutectic melt. Here, attack of tungsten by melt must be considered in addition to oxidizing conditions to explain a leaching of tungsten rods and the transfer of tungsten into the molten state. The determined spectrum indicates tungsten and the components of stainless steel as main components. Compatibility for molybdenum incorporation (from upper electrode) is indicated as well. Melt decomposition during re-solidification was initiated by precipitation and growth of tungsten-rich primary crystals in residual melt. A more detailed interpretation with respect to the formation of tungsten phases, which is not necessary for the actual purposes, would have required quantitative analysis of especially the light elements carbon, boron and oxygen. Similar results were gained in the inspection of the QUENCH-07 bundle, and are discussed in the post-test examination chapter of reference[17].

[Fig. 99](#) also illustrates the heater rod degradation aspect and confirms the given description fully. Heater rod #2 was completely embedded by relocated product melt and consequently protected from ongoing destruction at the given elevation, whereas other rods, especially steam-exposed ones, continued to degrade heavily.

EDX analysis at cross section QUE-09-14, bundle elevation 950 mm

The central bundle zone with the rods of the first ring, already depicted in [Fig. 77](#), is considered again with respect to the SEM/EDX analysis of the retained rubble fragments and melt lumps ([Fig. 100](#)). The given examples for the measured element spectra illustrate a series of different events: The bottom-left spectrum of a melt lump, denoted by Mo-Zr type is an interaction product between the molybdenum electrodes (main component), control rod arrangement, heater rod(s), and most probably fuel rods as well, according to the detected minor components Zr, Fe, and W. The presence of light elements shall not be further discussed as conclusive, since oxygen was naturally expected, the carbon signal might be somewhat enhanced by the carbon sputter deposition, and the boron signal would require special attention for quantification. In the same sense the top-right spectrum is denoted by Zr-Mo type, since zirconium is the main component and molybdenum one of the minor ones. W and Fe are present in this melt type as well. One of several particles of typical fragment shape is identified in the bottom-right spectrum as piece of the alumina-based ceramic thermal shield plate, installed at 1500 mm lower end elevation.

Further analysis results are presented in [Fig. 101](#) for some examples of more centrally located aggregates, together with the positions, marked in the picture. Aggregate #5, as well as lump #4 can be interpreted as simple zirconium melt. Note, however, that the positions 5-3 (right, bottom) and 5-2 are part of the aggregate #5, but have the different composition of the Mo-Zr type, which was already described in the previous figure. Here, the contribution of the control rod degradation to the formation of this product melt was larger, according to the additionally detected Ni and the higher peaks of the other stainless steel components. The last spectrum of [Fig. 101](#) to be mentioned, Zr-Mo type at right, top, differs from the example, given at same position in [Fig. 100](#), by the higher SS contribution, the much higher Mo content, and the indication of some tungsten and/or tantalum.

In total, apart from the alumina fragments and the zirconium melt, all mixed melts contain elements of high melting point, in case of Mo even as main constituent. This is reflecting the

extreme conditions at high bundle elevations during the steam cooling phase after a period of steam supply limitation. On the other hand, the dissolution of W, Mo and Ta does of course not mean that the respective melting points were reached. Instead, under the oxidative conditions of steam exposure, Ta is known to oxidize with formation of non-protective scale, oxides of Mo and W are also able to evaporate and to form eutectic melts in contact with the parent metal, which have a much lower melting temperature range. Contact to other materials can lead to interaction products with further reduced solidification temperature. In parallel, Zr and the above mentioned metals will form stable phases with eventually available carbon and boron. For the actual purpose the complicated metallurgical interaction behavior of bundle and structural components seems sufficiently documented.

6.7 Hydrogen Absorption by Zircaloy

The hydrogen absorbed in the remaining Zircaloy-4 metal was analyzed by hot extraction in the so-called LAVA facility, which is an inductively heated furnace coupled to a mass spectrometer. Specimens were taken from bundle slabs especially prepared for the destructive posttest examination (see Table 13). Due to the strong degradation of the bundle, hydrogen absorption could only be analyzed for specimens from elevations 435-440 mm, 524-529 mm, and 1512-1517 mm where the bundle was not completely molten and oxidized and the bundle structure was preserved. Samples were heated for 20 minutes to some 1800 K under a well-defined argon flow and the hydrogen released was measured by the mass spectrometer.

Results are shown in Fig. 102. Less than 1 at.% hydrogen in the metal phase was measured for all specimens from elevations 435-440 mm and 1512-1517 mm. Only specimens from elevation 524-529 mm, where stronger oxidation occurred, obtained more significant amounts of hydrogen dissolved by the metal phase, i.e. 1-4 at.%. Nevertheless, these values are lower compared to other QUENCH bundle tests, e.g. QU-02, -06, -07, with maximum hydrogen concentrations of more than 20 at.%.

No integral value of the hydrogen absorbed in the bundle could be given on the basis of the restricted number of single data, and no statement can be made on hydrogen absorption and release during the test by this post-test analyses.

6.8 Summary and Conclusions

The comprehensive metallographic post-test examination of the QUENCH-09 bundle, together with special supporting SEM/EDX analysis, were condensed into the given description, interpretation and illustration. This allows valuable insights into the coupled degradation and meltdown phenomena, to be expected for a fuel rods/control rod configuration under the conditions, simulated in the experiment.

The limited thermal stability of the control rod due to chemical incompatibilities of its components is not only responsible for early CR degradation and CR melt “candling”. The lateral distribution of respective melt can be seen as trigger mechanism for accelerated fuel rod degradation. Consequently, laterally distributed CR melt is further dispersed and diluted during downward relocation within defective fuel rods. Strong oxidation of localized melt pools and complex molten products has supported the downward extension of the hot zone. This effect was more pronounced than observed for any previous QUENCH experiment.

The transition from a bundle configuration to a flow channel / blockage configuration, observed higher within the hot zone, is a unique feature of this test compared to all previous ones, in which no blockage of the bundle or only a short partial one had been formed. Here, the axially extended blockage configuration can be distinguished into the mostly blocked lower part, filled mainly by porous melt, and the more open upper part, the net source of melt relocation. The melt distribution supports the interpretation that flow of mainly metallic melt together with increasing viscous drag forces due to the continuing melt oxidation are responsible for the final distribution of the completely ceramic masses. It is plausible to attribute enclosed melt porosity to gaseous oxidation products of minor melt components from the CR degradation, compared to the observed dense form of pure (Zr,O) type melt.

Unfortunately, the final state does not allow to deduce all essential information on damage progression. According to temperature measurements and gas analysis the response to the quench phase conditions was violent. This compares well with the assumption that residual metallic fractions of the dispersed materials and more recently relocated melt from increasing elevations were oxidized during the phase of high steam supply. However, it is not possible to quantify the importance of the preceding phase of reduced steam supply. In comparison to QUENCH-07 the higher quench water supply rate in QUENCH-09 has to be considered as well.

With respect to the simulation quality, the zirconia pellet behavior is judged to be fairly representative for real fuel, expected to be dissolved according to quite similar mechanisms. The observed axial and lateral distribution of interaction and oxidation products might be less prototypical, taking into account electric heat distribution and heater rod skeleton. The observed tungsten and molybdenum dissolution, clearly a facility specific artefact, requires abstraction from the respective melts at high elevations and from the contribution to the hydrogen evolution signal.

7. Analytical support by the Bundle Code CALUMO

As an absorber rod with B₄C pellets was installed at the center position of the bundle as in the QUENCH-07 test, the same version of the CALUMO code, namely CALUMOQX was used for the pre- and post-test calculations of QUENCH-09. Only the results of the posttest calculations are discussed in this report.

As described in [12], the evolution of the temperatures in the test section is calculated with the help of balance equations obtained from the integral form of the energy conservation law. In the old version of the code there was one balance equation for all the 21 fuel rods of the bundle together with balance equations for the shroud and the coolant. In the new version CALUMOQX of the code we have separate balance equations for the outer ring of 12 heated fuel rods (+ 4 corner rods), for the inner cluster of 8 heated fuel rods, and balance equations for the central rod. In case of QUENCH-07 and QUENCH-09 this is an absorber rod with a Zry guide tube. But there is also the possibility to deal with an unheated fuel rod of normal bundle design.

A model for B_4C oxidation and boric acid formation has also been implemented in CALUMOQX. This para-linear oxidation model is described in more detail in ref. [13] and shall not be repeated here. As the equilibrium oxide film thickness is very small (1-3 μm) under the steam flow conditions of QUENCH-07 and QUENCH-09, a simplified version of the BORCA model is implemented in the code directly starting with the phase of constant oxide film thickness. Thus, the early short phase of growing oxide films is neglected. The same is true of the so-called pore effect, as no indications for this effect have been observed in the CO , CO_2 production rates. One reason for this might be partial filling of the pore channels by the B_4C /steel eutectic. The experimental finding in QUENCH-09 that the reaction of B_4C with steam starts only with the onset of cooldown, was input for the posttest calculations.

The main interest in the calculations with CALUMO is with the oxidation and gas production phenomena (H_2 , CO , and CO_2). A good simulation of the temperature evolutions in the fuel rod simulators and the shroud must, of course, be achieved by the code, otherwise one has no chance to obtain reasonable results. In contrast to the posttest calculations of QUENCH tests done so far, the oxidation correlation of Prater/Courtright [14] has been used for temperatures above 1883 K, whereas for the low temperature region the oxidation correlation of Leistikow [16] was kept. It appears that this choice allows an acceptable simulation of the temperature escalation between about 700 and 1000 mm starting a bit before the steam reduction phase. It is felt, that this temperature escalation is caused by bending of fuel rod simulators in this axial region. But the modelling in CALUMO is not sophisticated enough to describe this effect in a mechanistic manner.

In the cooldown phase there occurred a considerable destruction in the upper part of the test section and considerable relocation of molten material. The CALUMO code has presently no capabilities to cope with such a situation in a proper way. Therefore the calculations for the cooldown phase were done under the premises, that the structure of the test section remains essentially intact. In this way the mechanisms leading to the destruction of the test section can be understood to some extent.

In contrast to all other QUENCH tests done so far, a steam reduction phase was realized in the QUENCH-09 test. As there is no mechanistic model of oxygen diffusion included in CALUMOQX, the effects of oxide scale dissolution can only be described in an approximative way by a reversal of the oxide scale growth law. But a mechanistic solution of the oxygen diffusion equation is implemented in the code version CALUMOQXD. Studies with this version of the code showed that noticeable reductions of oxide scale thickness can only be expected for values below about 120 μm . Thus, the reversal of the growth law was only applied

for oxide scales below this value. This measure avoided the occurrence of a double peak in the axial oxide scale profiles as occurred in the pretest calculations for QUENCH-09.

At the inlet a value of about 0.3 g/s was measured for the steam flow rate during the steam reduction phase. On the other hand the hydrogen measurements by the mass spectrometer suggest a value of 0.45 g/s. Indeed, this value was used in the posttest calculations with CALUMOQX and CALUMOQXD, otherwise the measured hydrogen productions rates could not be reproduced.

Results of code calculations in comparison to the respective data of the test instrumentation are to be found in Figs. 110 to 117. These are the temperature evolutions between 150 and 1350 mm, the axial profiles of oxide scale thickness for the fuel rod simulators and the shroud, and the results on hydrogen production (rates and overall production). It should be noted that the calculation starts at about 420 s into the test with the increase of the electrical power and ends at about 3900 s. Many thermocouples failed in the course of the QUENCH-09 test. These failures are indicated by a capital F in the figures. Also, the great extent of test section destructions in the cooldown phase suggests to take all the thermocouple readings above about 450 mm in this phase with caution, all the more as they are only reliable up to about 2400 K.

The mean temperature in the outer ring of fuel rod simulators "tsurz", that of the inner cluster of 8 fuel rod simulators "tcenz", that of the absorber rod with its guide tube "tcrz", and the mean shroud temperature "tshrz" are plotted in Figs. 110 to 112. They are compared to the available thermocouple readings.

In the overall, the temperature evolution in the heated zone during the heat-up phase prior to steam reduction conditions is simulated in a satisfactory way by the code. As the temperature evolution in this part of the test section is mainly determined by the electrical heating and by the oxidation we can be rather confident that these effects are correctly simulated by the code. There are some problems with the calculated temperature evolutions in the upper part of the test section, as the measured temperatures rise distinctly faster than the calculated ones. The discrepancy is further enlarged during the steam reduction phase. May be that these are effects of thermocouple routing (see Appendix 2).

The steam reduction phase leads to an extension of the hot zone towards lower axial positions in the heated part of the test section. As all the steam has already been consumed in the lower part, the axial profile of electrical heating changes. This effect is also responsible for the decrease of the measured clad temperatures between 850 and 1050 mm after a temperature peak in the first part of the steam starvation phase. This feature is also shown by the calculated temperatures, but not at 1050 mm. The extension of the hot zone calculated by the code is higher by about 100 mm than that measured by the thermocouples. The calculated temperature increase occurs also somewhat earlier. Also, the calculated temperatures rise to much higher values than the measured ones, especially at 450 mm where we find a discrepancy of about 1000 K.

A steam starvation model for Zry oxidation could eventually improve the situation. In the present state of the code only the normal oxidation model is applied with a balance equation on

steam consumption in each axial mesh. As soon as a critical steam flow rate is reached, oxidation is terminated. Results of code calculations for the evolution of steam flow rate during the steam starvation phase are to be found in [Fig. 113](#). But the use of the Prater/Courtright correlation also has considerably contributed to an overestimation of the temperatures.

Up to the onset of the cooldown phase the code yields in the overall a simulation of the experiment, which is, to some extent, satisfying. This is also to be seen in [Fig. 114](#), where measured and calculated hydrogen data are compared.

The CALUMO code operates with an intact coolant channel, bundle and shroud geometry. It is known from PTE that the test section is completely destroyed above about 750 mm. The pressure transducers indicate rod failure at 2600 s and shroud failure at 2623 s, i.e. both failure events occur shortly before the beginning of the steam flow reduction phase. We do not think that these events by themselves invalidate the code calculations for this period.

It is assumed that the severe destruction of the test section occurred only during the cooldown phase. This is indicated by the failure of the inner cooling jacket and the very high hydrogen production rate. Of course, the CALUMO code has no capabilities to simulate the destruction of the test section and its consequences in a mechanistic way. But it is very important to identify the main reasons which led to the severe destructions. In this respect, code calculations are valuable.

The steam flow reduction phase led to dissolution and rearrangement effects of the oxygen distributions in the oxide scales. These effects depend mainly on the temperature, on the scale thickness, and on the duration of steam starvation. Thus, the highest effects are expected in the upper non-heated part of the test section. In [Fig. 115](#) are plotted respective axial distributions of the cladding oxide scale thickness for different times into the steam starvation phase calculated with the code version CALUMOQXD, which has a mechanistic model for oxygen diffusion. Towards the end of this phase the scale thickness above about 1100 mm was very low. This led to a strong escalation of calculated temperatures in this axial region starting with the onset of cooldown. The thermocouple readings gave only faint indications for this effect, but it should be noted that all thermocouples above about 750 mm having still been intact at the onset of the cooldown phase must have failed with the destruction of the test section. The calculated temperatures reach 3000 K and more. Thus, they are above the melting temperature of the Mo electrodes (ca 2850 K). In view of these calculated temperatures the destruction of the test section and the very high hydrogen production rates, as measured by the mass spectrometer are to be expected. From the thermocouple readings alone these severe quench effect would not have been expected. Only at 1350 mm there is a faint indication for a strong temperature increase in the cooldown phase.

The strong temperature escalation as calculated by the code in the upper part of the test section concerns the whole bundle and the shroud. This can also be taken from [Fig. 116](#), where axial distributions of the respective oxide scale thickness values at the beginning of the steam reduction phase and at its end as well as at the end of the calculation are plotted, with "dox" denoting the oxide scales of the inner cluster of 9 heated fuel rods, "doxc" that of the guide tube of the absorber rod, "doxa" that of the outer ring of 12 heated fuel rods and "doxsh" the oxide scale of the shroud.

At the beginning of the steam reduction phase the oxidation ranges between about 700 and 1000 μm with the maximum value at about 900 mm because the oxidation of the inner fuel rod simulators is practically complete at this axial location. During the steam reduction phase the oxidation zone extends downwards to about 400 mm with values of about 500 μm for the fuel rod simulators and the shroud.

During the cool-down phase further oxidation of fuel rod simulators and the shroud takes place, especially in the upper part of the test section. All the inner fuel rod simulators are practically completely oxidized above about 400 mm. The peak in shroud oxidation at 500 mm is probably a consequence of the temperature peak at the end of the steam reduction phase in this axial region. The oxidation of the shroud in the upper part is not yet complete in contrast to the fuel rod simulators.

Despite the severe destruction of the test section some measurements of the oxide scale thickness of fuel rod simulators could be done. The experimental values are compared with the calculated profiles in [Fig. 117](#). The strong oxidation between 400 and 500 mm bundle height calculated by the code is not supported by the experimental data, but the fuel rod simulators are practically completely oxidized above about 560 mm bundle height. This is another confirmation for the fact that the temperature escalation in the lower part of the test bundle occurring during the steam reduction period is overpredicted by the code.

The calculated hydrogen production (rate and accumulated value) matches the curves measured by the mass spectrometer rather well after corrections of the experimental data based on findings of PTE on the remaining B_4C inventory. The peak in the hydrogen production rate due to the temperature escalation starting a bit before the steam reduction phase is relatively well met (height and width), as well as the peak in the cooldown phase, indicating the severe quench effect having occurred in QUENCH-09. There is a time offset of about 30 s in the first peak. But it has to be noted that the code calculates hydrogen production, whereas the mass spectrometer measures the released hydrogen at some distance above the test section and with steam starvation the outlet flow velocity is rather low. The fact that the CALUMO code overpredicts the temperatures during the steam reduction phase in some axial regions has no consequences for the hydrogen production. The fact is that during this period all the steam injected into the system is completely consumed in the oxidation processes. That means that in the upper part of the test section a true steam starvation condition has indeed been reached. This can be inferred from the hydrogen measurements of the mass spectrometer. Of course the assumption of a value of 0.45 g/s for the steam flow rate during the steam reduction phase was essential for this good agreement.

The geometrical effects due to loss of strength and melting of the claddings and shroud are of course very important and can lead to an enhancement of the oxidation rate. As the rise of the hydrogen signal is very steep after the onset of cooldown, we have looked for mechanisms which are fast enough like cracking of claddings and expansion effects in ZrO_2/Zry structures after loss of strength. The temperatures calculated in the inner part of the test section (2500-2800 K) are high enough for this to occur. The solidus temperature of ZrO_2 depends on the oxygen to metal ratio, with values of about 2200 K for ratios below 1.7. Thus, a steam starvation period should also lead to some reduction of strength in the oxide scales.

A mechanism linked to loss of strength is a sort of clad distension, for which we have found in PTE of QUENCH-02, QUENCH-03 [15] and QUENCH-07 [17] direct evidence in the upper part of the test section. Whatever the physical reason for this effect might be, an in-pin gas pressure higher than the pressure in the coolant channel or clad swelling due to oxidation, the steam can then enter the fuel rod simulators leading to inner clad oxidation. This effect could drastically enhance the oxidation rates. We have made sensitivity studies for this effect, assuming a threshold value of 2000 K for the temperature at which ballooning occurs. As the rise of the temperature is very steep, the exact value of this parameter does not seem to be very important.

In [Fig. 114](#) results of code calculations for the hydrogen production are shown. The calculations result in about 200 g of hydrogen produced during the cooldown phase, although with the high oxidation rates the numerical errors in the code might be important leading to some overestimation of the hydrogen production. Also we can not be sure about the amount of steam, which can really enter the fuel rod simulators. Despite all these uncertainties we hold that clad expansion is an important mechanism contributing to the so-called quench effect in the QUENCH-09 test.

A sustained high hydrogen production rate, as was observed by the mass spectrometer but not fully achieved in our sensitivity studies, can be caused by the oxidation of Zr(O) melts, as the oxide scales on these melts do not grow indefinitely but reach a limiting value. This means that we have no parabolic behavior for the oxidation rate with time but rather a linear one. But as big lumps of molten material have a relatively small surface/volume ratio, the effect of melting should be more important in an early phase of oxide scale break-up and melt relocation than in a late stage with melt accumulation.

For the time being we have no information on the role of Mo in the oxidation process. If the measured hydrogen production values are roughly correct, its contribution must have been significant. Liquefied Mo has most probably been mixed into the Zr(O) melts.

According to the mass spectrometer signals gaseous products of B₄C oxidation (CO, CO₂, and CH₄) are only observed during the cooldown phase. The flow channel around the control rod was most probably partially blocked after eutectic steel melting and relocation of melt. Then starts the eutectic interaction of molten steel and ZrO₂, leading eventually to the failure of the guide tube after some time. The PTE revealed failure of the guide tube. The fact that no oxidation reaction products of B₄C are observed by the mass spectrometer must then be linked to the steam reduction condition. It seems that at the axial locations with a free B₄C surface, where, in principle, the reaction with steam is possible, the condition of steam starvation must have been reached.

These experimental findings on B₄C oxidation were taken into account by turning on the respective BORCA model only during the cooldown phase. Recently, also a model for eutectic melt formation between B₄C and stainless steel has been implemented in the code. The respective data correlation was taken from [18]. This eutectic model is only applied up to clad melting. Molten steel is then draining downwards and accumulating at lower axial locations, where the eutectic interaction between steel and B₄C can continue and also that with the

guide tube. But as relocation processes are not yet implemented in the code, this effect cannot be reproduced.

Downwards relocation of molten material from the upper part of the test section was an important mechanism during the cooldown phase. This led to a prolonged heating of the test bundle above about 580 mm axial height and thus might explain the second peak in the CO/CO₂ production rates measured by the mass spectrometer. Of course, this effect cannot yet be simulated by the code and the second peak is therefore not reproduced in the calculation. The same is true for the oxidation of eutectic melt which has been released into the coolant channel. This process could contribute to a CO/CO₂ production.

The mechanisms in the upper part of the test section were decisive for the course of QUENCH-09. The most important ones were the dissolution of the oxide scales during the steam reduction phase leading to a very strong oxidation with the reentry of the steam. Clad distension and cracking further enhance the oxidation rate. The complete breakdown of the bundle structure follows, as very high temperatures have been reached according to the observed Mo electrodes liquefaction.

8. Summary

- The QUENCH-09 test is of special interest in view of the PHEBUS FPT3 experiment which will be dedicated to the fission product chemistry under presence of a control rod of B₄C type.
- QUENCH-09 provides complementary information to that obtained in QUENCH-07 which can serve as reference for comparison.
- Control rod leakage occurred at ~1555 K (compared to ~1585 K for QUENCH-07), reflecting the close similarity of test conduct during initial phases.
- The faint signals of volatile B₄C oxidation products recorded until the cooling phase (contrasting to much stronger ones for QUENCH-07) indicate much later or less exposure of control rod interaction products to the atmosphere. This identified “variability of behavior” in comparison of both bundles cannot be distinctly explained. Possible reasons as assumed differences in leak size, leak clogging, or internal melt distribution cannot be proved by inspection of the final bundle state. The phase of reduced steam supply may have played a major role as well but cannot explain the difference between both tests observed already before that phase.
- Complementary to the previous point it is plausible to expect more violent absorber melt oxidation and interaction with the surrounding bundle after the delayed release at a meanwhile higher temperature level. In the same sense it is concluded that the phase of reduced steam supply has triggered temperature escalation and bundle degradation dur-

ing the following test phase. The importance of both contributions cannot be quantified on basis of test data and bundle analysis.

- Observed facts are the downward extension of the severely damaged zone to ~560 mm elevation (compared to ~750 mm for QUENCH-07), considerable lateral distribution of porous melt from control rod origin, the axial distribution of such melt in the bundle, within several split and funnel shaped fuel rods (identified by SEM/EDX analysis down to 520 mm), and within the control rod itself.
- A blockage at ~590 mm level, consisting of some dense fuel rod melt, more melt of mixed composition and porous form, as well as rod residues, all converted to the ceramic state, allows to distinguish the finally active flow channels. The bundle sections above contain oxidized melt in more open distribution.
- Observations of tungsten heater rod and molybdenum electrode degradation via melt formation are related to the steam exposure of those metals at rather high temperatures but below their melting points. Abstraction from those interfering but facility-specific phenomena is necessary.
- The mass spectrometer data are consistent with the post-test bundle analysis. 60 g hydrogen were produced during all phases before quench initiation, giving a very similar integral figure for the degree of pre-oxidation to QU-07 (62 g). During the quench phase about 400 g hydrogen were released which is the highest amount recorded up to now in a QUENCH experiment. The gaseous products of the boron carbide oxidation, namely 33 g CO, 22 g CO₂ and less than 1 g CH₄, were predominantly released during the quench phase.
- The successful conduct of QUENCH-09 has extended the range of studied conditions towards the late phase of core meltdown, as far as possible with the QUENCH equipment. Accordingly, open questions deserve further attention.

References

- [1] J.M. Broughton, P. Kuan, and D.A. Petti, "A Scenario of the Three Mile Island Unit 2 Accident," *Nuclear Technology*, 87, 34, 1989.
- [2] P. Hofmann, S. Hagen, V. Noack, G. Schanz, L. Sepold, "Chemical-Physical Behavior of Light Water Reactor Core Components Tested under Severe Reactor Accident Conditions in the CORA Facility," *Nuclear Technology*, vol. 118, 1997, p. 200.
- [3] S. Hagen, P. Hofmann, V. Noack, L. Sepold, G. Schanz, G. Schumacher, "Comparison of the Quench Experiments CORA-12, CORA-13, CORA-17," FZKA 5679, Forschungszentrum Karlsruhe, 1996.
- [4] S.M. Modro and M.L. Carboneau, "The LP-FP-2 Severe Fuel Damage Scenario; Discussion of the Relative Influence of the Transient and Reflood Phase in Affecting the Final Condition of the Bundle," OECD/LOFT Final Event, ISBN 92-64-03339-4, 1991, p. 388.
- [5] L. Sepold, A. Miassoedov, G. Schanz, U. Stegmaier, M. Steinbrück, J. Stuckert, C. Homann, "Hydrogen Generation in Reflooding Experiments with LWR-type Rod Bundles (QUENCH Program)," *Journal Nuclear Technology*, Vol. 147, Aug. 2004, pp. 202-214.
- [6] P. Hofmann, V. Noack, M.S. Veshchunov, A.V. Berdyshev, A.V. L.V. Matweev, A.V. Palagin, V.E. Shestak: „Physico-Chemical Behavior of Zircaloy Fuel Rod Cladding Tubes During LWR Severe Accident Reflood," FZKA 5846, Forschungszentrum Karlsruhe, 1997.
- [7] P. Hofmann, A. Miassoedov, L. Steinbock, M. Steinbrück, M. Veshchunov et al.: "Quench Behavior of Zircaloy Fuel Rod Cladding Tubes. Small-Scale Experiments and Modeling of the Quench Phenomena," FZKA 6208, Forschungszentrum Karlsruhe, 1999
- [8] M. S. Veshchunov, J. Stuckert, A. V. Berdyshev, "Modelling of Zr-O and U-Zr-O Melts Oxidation and New Crucible Tests," FZKA 6792, Forschungszentrum Karlsruhe, 2002
- [9] M. Steinbrück, A. Meier, U. Stegmaier, L. Steinbock, "Experiments on the Oxidation of Boron Carbide at High Temperatures", FZKA 6979, Forschungszentrum Karlsruhe, 2004.
- [10] M. Steinbrück, A. Meier, E. Nold, U. Stegmaier, "Degradation and Oxidation of B₄C Control Rod Segments at High Temperatures,FZKA 6980, Forschungszentrum Karlsruhe, 2004.
- [11] Ch. Homann, W. Hering, "Analytical Support for B₄C Control Rod Test QUENCH-09," FZKA 6853, 2003.

- [12] H. Steiner, M. Heck, "The Code CALUMO a Tool for the Analysis of Temperature Transients in QUENCH Tests," FZKA 6501, 2000.
- [13] H. Steiner, "Modelling of boron carbide oxidation and boric acid formation," Proceedings Jahrestagung Kerntechnik 2003, pp. 129-36, 2003.
- [14] J.T. Prater, E.L. Courtright, "Zircaloy Oxidation at 1300 to 2400 °C," NUREG/CR-4889, 1987.
- [15] P. Hofmann, C. Homann, W. Leiling, A. Miassoedov, D. Piel, G. Schanz, L. Schmidt, L. Sepold, M. Steinbrück, "Experimental and Computational Results of the Experiments QUENCH-02 and QUENCH-03," FZKA 6295, Forschungszentrum Karlsruhe, 2000.
- [16] S. Leistikow et al., „Kinetik und Morphologie der isothermen Dampfoxidation von Zircaloy-4 bei 700 bis 1300 °C“, KFK 2587, Forschungszentrum Karlsruhe, 1978.
- [17] M. Steinbrück, C. Homann, A. Miassoedov, G. Schanz, L. Sepold, U. Stegmaier, H. Steiner, J. Stuckert, "Results of the B₄C Control Rod Test QUENCH-07," FZKA 6746, Forschungszentrum Karlsruhe, 2004.
- [18] P. Hofmann et al., "Results of Separate-Effects Tests; Influence of cladding oxidation on chemical interactions with other bundle components," Contribution to the International CORA Workshop 1990.
- [19] A. de Bremaeker, "Experimental study of the interaction of boron carbide and oxidation products with materials under FPT3 representative conditions", PHEBUS FP Information Meeting, Bergen (NL), Mar. 31, 2004.
- [20] C. Homann, private communication.

Acknowledgments

The experimental and analytical work described in this report was co-financed by the European Commission under the Euratom Fifth Framework Programme on Nuclear Fission Safety 1998-2002.

At the Karlsruhe Research Center the broad support needed for preparation, execution, and evaluation of the experiment is gratefully acknowledged. In particular, the authors would like to thank Messrs. S. Horn and L. Anselment for assembling the fuel rod simulators, Mr. J. Moch for assembling and instrumenting the test bundle, Mr. S. Horn for the preparation of the hydrogen measurement with the "Caldos" analyzer and the various support. Furthermore, the authors would like to express their gratitude to Dr. C. Homann for extensive pretest calculations, Mr. D. Piel for the test data acquisition, Dr. W. Krauss for the hydrogen measurement with the "Prisma" mass spectrometer, to Mrs. J. Laier and Mrs. I. Werner for processing the test data, and to Mrs. M. Heck for processing the results of the metallographic examination.

Table 1: QUENCH Test Matrix

Test	Quench medium	Flooding rate ¹⁾	Heat-up rate	Pre-oxidation	Max. ZrO ₂ layer thickness ²⁾	Temp. at onset of flooding ³⁾	Remarks, objectives
QUENCH-01 Febr. 26, 1998	Water	1.6 cm/s from the bottom	0.5 K/s	+	~500 µm	~1900 K	COBE Project, reference for pre-oxidation tests.
QUENCH-02 July 7, 1998	Water	1.6 cm/s from the bottom	0.4 K/s	-	completely oxidized	> 2400 K	COBE Project, reference for tests without pre-oxidation.
QUENCH-03 Jan. 20, 1999	Water	1.4 cm/s from the bottom	0.4 K/s	-	completely oxidized	> 2400 K	Delayed quenching.
QUENCH-04 June 30, 1999	Steam	~50 g/s from the bottom	0.4 K/s	-	~270 µm	~2300 K	Reference for steam injection tests.
QUENCH-05 Mar. 29, 2000	Steam	~50 g/s from the bottom	0.3 K/s	+	~400 µm	~2300 K	As QUENCH-04, but with pre-oxidation.
QUENCH-06 Dec. 13, 2000	Water	1.4 cm/s from the bottom	0.3 K/s	+	~660 µm	~2300 K	As QUENCH-04, but water injection, OECD-ISP 45
QUENCH-07 July 25, 2001	Steam	~15 g/s from the bottom	0.4 K/s	+	completely oxidized	> 2300 K	COLOSS Project, reference test with B ₄ C absorber.
QUENCH-08 July 24, 2003	Steam	~15 g/s from the bottom	0.4 K/s	+	completely oxidized	> 2300 K	Reference test without B ₄ C absorber.
QUENCH-09 July 3, 2002	Steam	~50 g/s from the bottom	0.4 K/s	+	completely oxidized	~2500 K	COLOSS Project, as QUENCH-07, but with steam starvation.

¹⁾ Flooding rate for water: rise of the water level at the -250 mm bundle elevation (single-phase flow).

²⁾ Measured posttest, at the bundle elevation of maximum temperature.

³⁾ Maximum measured or estimated bundle temperature.

Revised: April, 2004

Table 2: Design characteristics of the QUENCH-09 test bundle

Bundle type		PWR, 21 rods
Pitch		14.3 mm
Number of rods heated/ unheated		20/ 1
Cladding	heated rod	Zircaloy-4, \varnothing 10.75 / 9.3 mm L = 2278 mm (EL -593 to 1685)
Cladding	control (central) rod	SS, \varnothing 10.24 / 7.72 mm L = 1083 mm (EL -20 to 1063)
Pellet	heated rod (annular) control rod (full)	ZrO ₂ , \varnothing 9.15/ 6.15 mm, L=11 mm B ₄ C, \varnothing 7.48 mm, L=14 mm
Internal rod pressure	heated rod control rod	0.22 MPa abs. Ar5%Kr 0.12 MPa abs. He
Central rod guide tube		Zircaloy-4, \varnothing 12.1 / 11.3 mm L = 1187 mm (EL -42 to 1145) Holes: 4 x \varnothing 4 mm at EL -34 and +1179 mm
Overall rod length	heated rod (levels) control rod (levels)	2480 mm (EL -690 to 1790) 2842 mm (EL -827 to 2015, incl. extension piece)
Heater material		Tungsten (W)
Heater diameter		6 mm
Pellet stack length	heated rod control rod	EL 0 to 1024 mm EL 0 to 1008 mm
Grid spacer (5)	material length location of lower edge	Zircaloy-4 (Zry), Inconel 718 (Inc) Zry 42 mm, Inc 38 mm Inc: -200 mm; Zry: 50, 550, 1050, 1410 mm
Shroud	material wall thickness outside diameter length (extension)	Zircaloy-4 2.38 mm 84.76 mm 1600 mm (EL -300 to 1300)
Shroud insulation	material insulation thickness extension	ZrO ₂ fiber ~ 37 mm EL -300 to 1000 mm
Molybdenum-copper electrodes:		
length of upper electrodes		766 mm (576 Mo, 190 mm Cu)
length of lower electrodes		690 mm (300 Mo, 390 mm Cu)
diameter of electrodes:	- prior to coating	8.6 mm
	- after coating with ZrO ₂	9.0 mm
Cooling jacket	material inner tube outer tube	1.4541 stainless steel \varnothing 158.3 / 168.3 mm \varnothing 181.7 / 193.7 mm

Table 3: List of instrumentation for the QUENCH-09 Test

Channel	Designation	Instrument, location	Output in
0	TFS 2/12T	TC (W/Re) fuel rod simulator 2 (type 2), 850 mm, 315°, top penetration	K
1	TFS 2/11	TC (W/Re) fuel rod simulator 8 (type 2), 750 mm, 135°	K
2	TFS 2/13	TC (W/Re) fuel rod simulator 2 (type 2), 950 mm, 225°	K
3	TFS 2/15	TC (W/Re) fuel rod simulator 4 (type 2), 1150 mm, 315°	K
4	TFS 2/17	TC (W/Re) fuel rod simulator 6 (type 2), 1350 mm, 45°, fluid temperature	K
5	TSH 15/180	TC (W/Re) shroud outer surface, 1150 mm, 206°	K
6	TFS 3/10	TC (W/Re) fuel rod simulator 7 (type 3), 650 mm, 135°	K
8	TFS 3/13	TC (W/Re) fuel rod simulator 3 (type 3), 950 mm, 315°	K
9	TFS 3/14	TC (W/Re) fuel rod simulator 5 (type 3), 1050 mm, 45°	K
10	TFS 4/11	TC (W/Re) fuel rod simulator 14 (type 4), 750 mm, 45°	K
11	TFS 4/13	TC (W/Re) fuel rod simulator 20 (type 4), 950 mm, 135°	K
12	TFS 5/10	TC (W/Re) fuel rod simulator 12 (type 5), 650 mm, 225°	K
13	TFS 5/11	TC (W/Re) fuel rod simulator 13 (type 5), 750 mm, 45°	K
14	TFS 5/12	TC (W/Re) fuel rod simulator 15 (type 5), 850 mm, 315°	K
15	TFS 5/13	TC (W/Re) fuel rod simulator 16 (type 5), 950 mm, 135°	K
16	TFS 5/14	TC (W/Re) fuel rod simulator 18 (type 5), 1050 mm, 45°	K
17	TSH 16/180 I	TC (W/Re) shroud outer surface, 1250 mm, 206°; TC sheath is led between shroud insulation and inner cooling jacket	K
18	TSH 13/90	TC (W/Re) shroud outer surface, 950 mm, 116°	K
19	TSH 14/90	TC (W/Re) shroud outer surface, 1050 mm, 116°	K
20	TSH 11/0	TC (W/Re) shroud outer surface, 750 mm, 26°	K
21	TSH 12/0	TC (W/Re) shroud outer surface, 850 mm, 26°	K
22	TFS 2/5	TC (NiCr/Ni) fuel rod simulator 2 (type 2), 150 mm, 225°	K
23	TFS 2/7	TC (NiCr/Ni) fuel rod simulator 6 (type 2), 350 mm, 45°	K
24	F 902	Flow rate off-gas, upstream Caldos	Nm ³ /h
25	FM 401	Bundle argon gas mass flow rate	g/s
32	TIT A/13	TC (W/Re) corner rod A, center, 950 mm	K
34	TFS 2/12 B	TC (W/Re) fuel rod simulator 2 (type 2), 850 mm, 315°, bottom penetration	K
35	TSH 9/90	TC (NiCr/Ni) shroud outer surface, 550 mm, 116°	K
36	TSH 9/270	TC (NiCr/Ni) shroud outer surface, 550 mm, 296°	K
37	TFS 3/16	TC (W/Re) fuel rod simulator 7 (type 3), 1250 mm, 135°	K
38	TFS 5/9	TC (NiCr/Ni) fuel rod simulator 10 (type 5), 550 mm, 315°	K
39	TFS 2/9	TC (NiCr/Ni) fuel rod simulator 8 (type 2), 550 mm, 135°	K
40	TIT D/12	TC (W/Re) corner rod D, center, 850 mm	K
42	TFS 5/8	TC (NiCr/Ni) fuel rod simulator 21 (type 5), 450 mm, 135°	K
43	TFS 3/8	TC (NiCr/Ni) fuel rod simulator 5 (type 3), 450 mm, 45°	K
46	TIT C/9	TC (NiCr/Ni) corner rod C, center, 550 mm	K
47	TFS 5/15	TC (W/Re) fuel rod simulator 19 (type 5), 1150 mm, 225°	K
48	TFS 5/16	TC (W/Re) fuel rod simulator 21 (type 5), 1250 mm, 135°	K
49	TFS 5/17	TC (W/Re) fuel rod simulator 10 (type 5), 1350 mm, 315°	K
52	TSH 13/270	TC (W/Re) shroud outer surface, 950 mm, 296°	K

Channel	Designation	Instrument, location	Output in
53	TSH 14/270	TC (W/Re) shroud outer surface, 1050 mm, 270°	K
54	TSH 11/180	TC (W/Re) shroud outer surface, 750 mm, 206°	K
55	TSH 12/180	TC (W/Re) shroud outer surface, 850 mm, 206°	K
61	T 206	Temperature pertinent to steam flow instrument F 206	K
62	P 206	Pressure pertinent to steam flow instrument F 206	bar
63	F 206	Flow rate steam 1 g/s	g/s
64	T 402b	Temperature of the tube surface after gas heater	K
66	TSH 15/0 I	TC (W/Re) shroud outer surface, 1150 mm, 26°; TC sheath is led between shroud insulation and inner cooling jacket	K
67	TSH 16/0	TC (W/Re) shroud outer surface, 1250 mm, 26°	K
68	T 512	Gas temperature at bundle outlet	K
72	TFS 2/1	TC (NiCr/Ni) fuel rod simulator 4 (type 2), -250 mm, 315°, fluid temperature	K
73	TFS 2/2	TC (NiCr/Ni) fuel rod simulator 6 (type 2), -150 mm, 45°	K
74	TFS 2/3	TC (NiCr/Ni) fuel rod simulator 8 (type 2), -50 mm, 135°	K
75	TCRI 11	TC (NiCr/Ni) B ₄ C control rod, embedded in SS cladding, 750 mm	K
76	TFS 2/6	TC (NiCr/Ni) fuel rod simulator 4 (type 2), 250 mm, 315°, fluid temperature	K
77	TCRI 12	TC (NiCr/Ni) B ₄ C control rod, embedded in SS cladding, 850 mm	K
78	TFS 5/4/0	TC (NiCr/Ni) fuel rod simulator 15 (type 5), 50 mm, 315°, fluid temperature	K
79	TFS 5/4/180	TC (NiCr/Ni) fuel rod simulator 21 (type 5), 50 mm, 135°	K
80	TFS 5/5	TC (NiCr/Ni) fuel rod simulator 16 (type 5), 150 mm, 135°	K
81	TFS 5/6	TC (NiCr/Ni) fuel rod simulator 18 (type 5), 250 mm, 45°	K
82	TFS 5/7	TC (NiCr/Ni) fuel rod simulator 19 (type 5), 350 mm, 225°	K
83	TSH 4/270	TC (NiCr/Ni) shroud outer surface, 50 mm, 296°	K
84	TSH 3/180	TC (NiCr/Ni) shroud outer surface, -50 mm, 206°	K
85	TSH 4/180	TC (NiCr/Ni) shroud outer surface, 50 mm, 206°	K
86	TSH 7/180	TC (NiCr/Ni) shroud outer surface, 350 mm, 206°	K
87	TSH 4/90	TC (NiCr/Ni) shroud outer surface, 50 mm, 116°	K
88	TSH 1/0	TC (NiCr/Ni) shroud outer surface, -250 mm, 26°	K
89	TSH 4/0	TC (NiCr/Ni) shroud outer surface, 50 mm, 26°	K
90	TSH 7/0	TC (NiCr/Ni) shroud outer surface, 350 mm, 26°	K
91	TCI 9/270	TC (NiCr/Ni) cooling jacket inner tube wall, 550 mm, 270°	K
92	TCI 10/270	TC (NiCr/Ni) cooling jacket inner tube wall, 650 mm, 270°	K
93	TCI 11/270	TC (NiCr/Ni) cooling jacket inner tube wall, 750 mm, 270°	K
94	TCI 13/270	TC (NiCr/Ni) cooling jacket inner tube wall, 950 mm, 270°	K
95	TCRI 13	TC (NiCr/Ni) B ₄ C control rod, embedded in SS cladding, 950 mm	K
96	TCI 1/180	TC (NiCr/Ni) cooling jacket inner tube wall, -250 mm, 180°	K
97	TCI 4/180	TC (NiCr/Ni) cooling jacket inner tube wall, 50 mm, 180°	K
98	TCI 7/180	TC (NiCr/Ni) cooling jacket inner tube wall, 350 mm, 180°	K
99	TCI 11/180	TC (NiCr/Ni) cooling jacket inner tube wall, 750 mm, 180°	K
100	TCI 12/180	TC (NiCr/Ni) cooling jacket inner tube wall, 850 mm, 180°	K
101	TCI 13/180	TC (NiCr/Ni) cooling jacket inner tube wall, 950 mm, 180°	K
102	TCI 15/180	TC (NiCr/Ni) cooling jacket inner tube wall, 1150 mm, 180°	K
104	TCI 9/90	TC (NiCr/Ni) cooling jacket inner tube wall, 550 mm, 90°	K

Chan- nel	Designation	Instrument, location	Output in
105	TCI 10/90	TC (NiCr/Ni) cooling jacket inner tube wall, 650 mm, 90°	K
106	TCI 11/90	TC (NiCr/Ni) cooling jacket inner tube wall, 750 mm, 90°	K
107	TCI 13/90	TC (NiCr/Ni) cooling jacket inner tube wall, 950 mm, 90°	K
109	TCI 1/0	TC (NiCr/Ni) cooling jacket inner tube wall, -250 mm, 0°	K
110	TCI 4/0	TC (NiCr/Ni) cooling jacket inner tube wall, 50 mm, 0°	K
111	TCI 7/0	TC (NiCr/Ni) cooling jacket inner tube wall, 350 mm, 0°	K
112	TCI 11/0	TC (NiCr/Ni) cooling jacket inner tube wall, 750 mm, 0°	K
113	TCI 12/0	TC (NiCr/Ni) cooling jacket inner tube wall, 850 mm, 0°	K
114	TCI 13/0	TC (NiCr/Ni) cooling jacket inner tube wall, 950 mm, 0°	K
115	TCI 15/0	TC (NiCr/Ni) cooling jacket inner tube wall, 1150 mm, 0°	K
117	TCO 9/270	TC (NiCr/Ni) cooling jacket outer tube surface, 550 mm, 270°	K
118	TCO 4/180	TC (NiCr/Ni) cooling jacket outer tube surface, 50 mm, 180°	K
120	TCO 1/0	TC (NiCr/Ni) cooling jacket outer tube surface, -250 mm, 0°	K
121	TCO 7/0	TC (NiCr/Ni) cooling jacket outer tube surface, 350 mm, 0°	K
122	TCO 13/0	TC (NiCr/Ni) cooling jacket outer tube surface, 950 mm, 0°	K
123	T 601	Temperature pertinent to off-gas flow instrument F 601	K
128	T 104	Temperature quench water	K
129	T 201	Temperature steam generator heating pipe	K
130	T 204	Temperature pertinent to steam flow instrument F 204	K
131	T 205	Temperature pertinent to steam flow instrument F 205	K
132	T 301A	Temperature behind superheater	K
133	T 302	Temperature superheater heating pipe	K
134	T 303	Temperature pertinent to total flow instrument F 303	K
135	T 401	Temperature pertinent to gas bundle argon flow instrument F 401	K
136	T 403	Temperature at inlet argon cooling gas	K
137	T 404	Temperature at outlet argon cooling gas	K
138	T 501	Temperature at containment	K
139	T 502	Temperature at containment	K
140	T 503	Temperature at containment	K
141	T 504	Temperature at containment	K
142	T 505	Temperature at containment	K
143	T 506	Temperature at containment	K
144	T 507	Temperature at containment	K
145	T 508	Temperature at containment	K
146	T 509	Temperature bundle head outside (wall)	K
147	T 510	Temperature at containment	K
148	T 511	Gas temperature at bundle inlet	K
149	T 901	Temperature pertinent to off-gas flow instrument F 901	K
152	P 201	Pressure steam generator	bar
153	P 204	Pressure pertinent to steam flow instrument F 204	bar
154	P 205	Pressure pertinent to steam flow instrument F 205	bar
155	P 303	Pressure pertinent to total flow instrument F 303	bar
156	P 401	Pressure pertinent to bundle argon flow instrument F 401	bar
157	P 511	Pressure at bundle inlet	bar
158	P 512	Pressure at bundle outlet	bar

Chan- nel	Designation	Instrument, location	Output in
159	P 601	Pressure pertinent to off-gas flow instrument F 601	bar
160	P 901	Pressure pertinent to off-gas flow instrument F 901	bar
161	L 201	Liquid level steam generator	mm
162	L 501	Liquid level quench water	mm
163	L 701	Liquid level condensation vessel	mm
164	Q 901	H ₂ concentration, off-gas (Caldos analyzer)	% H ₂
165	P 411	Pressure Ar-Kr supply	bar
166	P 403	Pressure Ar cooling of cooling jacket	bar
167	P 406	Pressure of annulus shroud/inner cooling jacket	bar
168	F 104	Flow rate quench water	l/h
169	F 204	Flow rate steam 50 g/s	g/s
170	F 205	Flow rate steam 10 g/s	g/s
171	F 303	Flow rate at bundle inlet (steam+argon), orifice	mbar
172	F 401	Bundle argon gas flow rate	Nm ³ /h
173	F 403	Flow rate argon cooling gas	Nm ³ /h
174	F 601	Flow rate off-gas (orifice)	mbar
175	F 901	Flow rate off-gas, upstream Caldos	Nm ³ /h
176	E 201	Electric current steam generator	A
177	E 301	Electric current superheater	A
178	E 501	Electric current inner ring of fuel rod simulators	A
179	E 502	Electric current outer ring of fuel rod simulators	A
180	E 503	Electric voltage inner ring of fuel rod simulators	V
181	E 504	Electric voltage outer ring of fuel rod simulators	V
250	E 505	Electric power inner ring of fuel rod simulators	W
251	E 506	Electric power outer ring of fuel rod simulators	W

Note: Tips of thermocouples TFS 2/1, TFS 5/4/0, TFS 2/6, and TFS 2/17 are fixed at the rod cladding and bent into flow channel to measure the fluid temperature.

Table 4: QUENCH-09; Failure of thermocouples

Thermocouple	Elevation [mm]	Time at failure [s]	Failure temperature [K]
TCO 7/0	350	Pretest failure	
TFS 2/9	550	3122	1742
TFS 5/9	550	3141	1772
TIT C/9	550	3127	1770
TSH 9/90	550	3134	1772
TSH 9/270	550	3142	1768
TFS 3/10	650	3414	2191
TFS 2/11	750	2896	2473
TFS 4/11	750	2969	2469
TFS 5/11	750	3317	2344
TCRI 11	750	2954	1773
TSH 11/0	750	3399	2153
TFS 2/12 T	850	3341	2116
TFS 5/12	850	3345	2177
TCRI 12	850	2618	1721
TSH 12/0	850	3316	2030
TFS 2/13	950	3341	1271
TFS 3/13	950	3230	2086
TFS 4/13	950	3337	2323
TFS 5/13	950	3325	2356
TCRI 13	950	2871	1772
TSH 13/270	950	3333	2429
TFS 3/14	1050	3333	2407
TFS 5/14	1050	3338	2335
TFS 2/15	1150	3341	2362
TFS 5/15	1150	3344	2270

Thermocouple	Elevation [mm]	Time at failure [s]	Failure temperature [K]
TSH 15/0 I	1150	3324	2338
TCI 15/0	1150	Pre-test failure	
TCI 15/180	1150	Pre-test failure	
TFS 3/16	1250	3338	2073
TFS 5/16	1250	3344	1519
TSH 16/180 I	1250	3333	1616
TFS 2/17 (fluid)	1350	3345	1040
TFS 5/17	1350	3362	2440
T 512 (fluid)	1350	3345	1634

Table 5: QUENCH-09; Sequence of events

Time [s]	Event
0	Start of data recording, test bundle at ~873 K, steam flow of 3.4 g/s, argon flow of 3 g/s
465	Start of heatup from ~873 K.
1950	~13 kW electric power reached
2280	Absorber rod failure at ~1555 K, based on TCRI 13 and He detection at the mass spectrometer
2581	Temp. of ~1773 K reached (TFS 2/13); beginning of temp. excursions at the 950, 1050, and 1150 mm levels
2593-2666	Intermediate CO release measured by MS
2600	First rod failure, based on P 411 and Kr detection
2602	End of electric power plateau at ~13 kW
2605-3156	Electric power at ~8 kW, then stepwise increase to ~15 kW
2623	Shroud failure, based on P 406
2636	Steam flow reduced to 0.4 g/s (F 206)
3316	Cooling initiation
3340	Start of electric power reduction from ~15 to ~4 kW, within 16 s
3344	Failure of inner tube of cooling jacket (based on P403 and F403)
3358	Cooling steam flow at ~50 g/s (F 204)
3427	Electric power shut off
4491	Cooling steam turned off
4551	End of data recording

0 s = 09:33:04 h on July 03, 2002

Table 6: QUENCH-09; Excursion temperatures

Elevation [mm]	Thermocouple	Time at excursion [s]	Excursion temperature [K]
550	TFS 2/9	3101	1500
550	TFS 5/9	3087	1413
550	TIT C/9	3040	1335
550	TSH 9/90	3058	1337
550	TSH 9/270	3044	1332
650	TFS 3/10	2895	1466
650	TFS 5/10	2895	1433
750	TFS 2/11	2580	1642
750	TFS 4/11	2585	1563
750	TFS 5/11	2585	1527
750	TSH 11/0	2809	1562
750	TSH 11/180	2804	1597
850	TFS 2/12 B	2698	1787
850	TFS 2/12 T	2582	1747
850	TFS 5/12	2609	1639
850	TIT D/12	2694	1714
850	TSH 12/0	2707	1711
850	TSH 12/180	2707	1711
950	TFS 2/13	2582	1807
950	TFS 3/13	2602	1693
950	TFS 4/13	2615	1721
950	TFS 5/13	2603	1748

Elevation [mm]	Thermocouple	Time at excursion [s]	Excursion temperature [K]
950	TIT A/13	2599	1821
950	TSH 13/90	2623	1745
950	TSH 13/270	2619	1796
1050	TFS 3/14	2584	1524
1050	TFS 5/14	2599	1686
1050	TSH 14/90	2607	1426
1050	TSH 14/270	2594	1524
1150	TFS 2/15	2595	1646
1150	TFS 5/15	2607	1462
1150	TSH 15/0 I	2608	1229
1150	TSH 15/180	2612	1377
1250	TSH 16/0	2559	1284
1350	TFS 5/17	3316 *)	905

*) After cooling initiation

Table 7: QUENCH-09; Maximum measured test rod temperature of each elevation

Elevation [mm]	Thermocouple	Time [s]	Maximum temperature [K]
- 250	TFS 2/1 (coolant)	2197	650
- 150	TFS 2/2	2112	719
- 50	TFS 2/3	2151	767
50	-	-	-
50	TFS 5/4/180	3315	864
150	TFS 2/5	3316 *	1026
250	TFS 2/6	3316 *	1141
350	TFS 2/7	3316 *	1282
450	TFS 3/8	3316 *	1711
550	**	-	-
650	TFS 3/10	3175	2335
750	TFS 2/11	2896 ***	2473
850	TFS 5/12	2623	2100
950	TFS 4/13	2629	2283
1050	TFS 5/14	2624	2232
1150	TFS 2/15	2634	2025
1250	**	-	-
1350	**	-	-

*) Exactly at cooling initiation.

***) The maximum temperature cannot be determined; it is somewhere during the temperature excursion which is followed by TC failure.

***) This value is the last data considered reliable, before TC failure.

Table 8: QUENCH-09; Maximum measured shroud temperature of each elevation

Elevation [mm]	Thermocouple	Time [s]	Maximum temperature [K]
- 250	TSH 1/0	2485	581
- 50	TSH 3/180	3311	686
50	TSH 4/90	3316 *	805
350	TSH 7/0	3316 *	1207
550	**	-	-
750	TSH 11/180	3316 *	2076
850	TSH 12/0	3279	2108
950	TSH 13/90	3232	2265
1050	TSH 14/270	3317 *	2204
1150	TSH 15/180	2726	2072
1250	TSH 16/0	3333	2211

*) Exactly at cooling initiation.

**) The maximum temperature is somewhere during the temperature excursion which is followed by TC failure.

Table 9: QUENCH-09; Onset of cooling based on cladding TCs (TFS and TCR), central rod centerline TC (TCRC 13), corner rod TCs (TIT), and shroud TCs (TSH)

Thermocouple	Elevation [mm]	Onset of cooling		Mean value per elevation	
		Time [s]	Temp. [K]	Time [s]	Temp. [K]
TFS 2/1	- 250	3317	580		
TFS 2/2	- 150	3316	679		
TFS 2/3	- 50	3315	763		
TFS 5/4/0	50	3315	793	3315	829
TFS 5/4/180	50	3315	864		
TFS 2/5	150	3316	1004	3316	1015
TFS 5/5	150	3316	1026		
TFS 2/6	250	3315	1141	3316	1142
TFS 5/6	250	3316	1142		
TFS 2/7	350	3316	1282	3316	1269
TFS 5/7	350	3316	1256		
TFS 3/8	450	3316	1711	3316	1682
TFS 5/8	450	3316	1653		
TFS 5/10	650	3316	2159	3317	2195
TFS 3/10	650	3317	2231		
TFS 5/11	750	3316	2389		
TFS 2/12 B	850	3317	2135	3317	2170
TFS 5/12	850	3316	2005		
TFS 4/13	950	3318	2128	3324	2191
TFS 3/13	950	3330	2253		
TFS 3/14	1050	3318	1796	3323	2004
TFS 5/14	1050	3327	2212		

Thermocouple	Elevation [mm]	Onset of cooling		Mean value per elevation	
		Time [s]	Temp. [K]	Time [s]	Temp. [K]
TFS 2/15	1150	3321	1867	3326	1874
TFS 5/15	1150	3330	1881		
TFS 5/16	1250	3343	2398		
TFS 2/17	1350	3341	2378	3343	2181
TFS 5/17	1350	3345	1984		
TIT D/12	800	3317	2156		
TIT A/13	950	3318	2200		
TSH 1/0	- 250	3317	535		
TSH 3/180	- 50	3316	686		
TSH 4/0	50	3316	789	3316	791
TSH 4/90	50	3316	805		
TSH 4/180	50	3316	788		
TSH 4/270	50	3316	783		
TSH 7/0	350	3316	1208	3316	1208
TSH 7/180	350	3316	1207		
TSH 11/180	750	3317	2077		
TSH 12/0	850	3316	2034		
TSH 13/270	950	3316	2179	3317	2145
TSH 13/90	950	3318	2111		
TSH 14/90	1050	3317	2190	3317	2197
TSH 14/270	1050	3317	2204		
TSH 15/0	1150	3322	1325	3320	1691
TSH 15/180	1150	3317	2057		
TSH 16/0	1250	3318	2206		

Table 10: QUENCH-07 and -09; Comparison of hydrogen data and results on the B₄C oxidation products

	QUENCH-07;	QUENCH-09;
Maximum measured H ₂ rate	2.3 g/s*)	5.6 g/s
Total H ₂	182 g	460 g
Contribution of B ₄ C oxidation to total H ₂	2.4 %	2.2 %
Total CO	8.6 g	33 g
Total CO ₂	11.6 g	22 g
Percentage of B ₄ C oxidized	20 %	50 %
CH ₄ produced	negligible	negligible

*) Measured value is too high for an steam injection of 15 g/s (Should not exceed 1.7 g/s).

Table 11: QUENCH-09; Chemical analysis of condensate samples from MS off-gas pipe

Probe No.	Middle point of fluid accumulation interval s	Duration of fluid accumulation s	Fluid g	B $\mu\text{g}/(\text{g fluid})$	B μg
1	-120	1200	107.434	0.053	5.7
2	780	600	58.028	0.036	2.1
3	1380	600	62.357	0.096	6.0
4	1980	600	64.086	0.287	18.4
5	2430	300	32.081	0.335	10.7
6	2670	180	7.564	7.64	57.5
7	2850	180	3.106	7.94	24.7
8	3030	180	2.028	5.49	11.2
9	3210	180	1.558	4.03	6.27
10	3570	540	15.34	59.2	906

Table 12: QUENCH-09; Chemical analysis of the debris taken posttest from bundle elevation 1300 – 1400 mm

Element	Concentration, wt%	Accuracy, wt%	Analysis method	Probable source
O	24.65	± 2.90		
B	0.063	± 0.003	ICP-OES	
Al	6.7	± 2.01	RFA	Al ₂ O ₃ thermal shield
Bi	0.07	± 0.021	RFA	
Cr	0.9	± 0.27	RFA	control rod cladding
Fe	1.4	± 0.42	RFA	control rod cladding
Hf	0.2	± 0.06	RFA	TC
Mn	0.08	± 0.024	RFA	
Mo	7.6	± 2.28	RFA	electrodes
Na	1.7	± 0.51	RFA	
Ni	0.2	± 0.06	RFA	control rod cladding
Si	0.2	± 0.06	RFA	
Sn	0.3	± 0.09	RFA	Zry-4
Ta	1.6	± 0.48	RFA	TC
W	1.7	± 0.51	RFA	heaters
Y	0.2	± 0.06	RFA	ZrO ₂ pellets stabilizer
Zr	52.7	± 15.81	RFA	

Oxygen was determined three times quantitatively both in the rough and the fine fractions. For the boron measurement the samples were mixed with soda, dissolved in acid and the solution was measured in comparison with adapted standards by means of ICP-method. The other elements were determined with RFA-method. The concentration was calculated from the X-ray peak intensities with a relative reliability of ± 30 %.

Table 13: QUENCH-09; Cross sections for the metallographic examination

Sample	Sample length (mm)	Axial position		Remarks
		bottom (mm)	top (mm)	
Cut	4	-104	-100	Cut 1 made with large machine
QUE-09-a	156	-100	56	
Cut	4	56	60	
QUE-09-1	13	60	73	Reference, 73 mm polished
Cut	4	73	77	
QUE-09-b	103	77	180	
Cut	4	180	184	Cut 2 made with large machine
QUE-09-c	247	184	431	
Cut	4	431	435	
QUE-09-17	5	435	440	Sample for H ₂ absorption
Cut	4	440	444	Cut 3 made with large machine
QUE-09-18	16	444	460	460 mm polished
Cut	2	460	462	
QUE-09-d	41	462	503	
Cut	4	503	507	
QUE-09-2	13	507	520	520 mm polished
Cut	4	520	524	
QUE-09-3	5	524	529	Sample for H ₂ absorption
Cut	4	529	533	
QUE-09-e	40	533	573	
Cut	4	573	577	
QUE-09-4	13	577	590	590 mm polished
Cut	4	590	594	
QUE-09-f	39	594	633	
Cut	4	633	637	
QUE-09-6	13	637	650	TC elevation 10, 650 mm polished
Cut	4	650	654	
QUE-09-g	29	654	683	
Cut	4	683	687	
QUE-09-8	13	687	700	700 mm polished
Cut	4	700	704	

Sample	Sample length (mm)	Axial position		Remarks
		bottom (mm)	top (mm)	
QUE-09-9	5	704	709	Sample for H ₂ absorption
Cut	4	709	713	Cut 4 made with large machine
QUE-09-h-12	137	713	850	Longitudinal cut, 0 – 180° orientation
Cut	4	850	854	
QUE-09-j	79	854	933	
Cut	4	933	937	
QUE-09-14	13	937	950	TC elevation 13, 950 mm polished
Cut	4	950	954	
QUE-09-15	5	954	959	Sample for H ₂ absorption
Cut	4	959	963	Cut 5 made with large machine
QUE-09-k		963		Remnant
...				
Cut	2	1478	1480	Electrode zone, bundle diameter <140 mm
QUE-09-16	30	1480	1510	Transition oxidized-unoxidized, bottom and top polished
Cut	2	1510	1512	
QUE-09-19	5	1512	1517	Sample for H ₂ absorption

Note: a) In regions where the diameter of the epoxied bundle is >140 mm the cutting thickness is assumed to be 4 mm instead of the regular width of 2 mm due to additional handling.

b) The axial top positions are meant as final levels, i.e. after grinding.

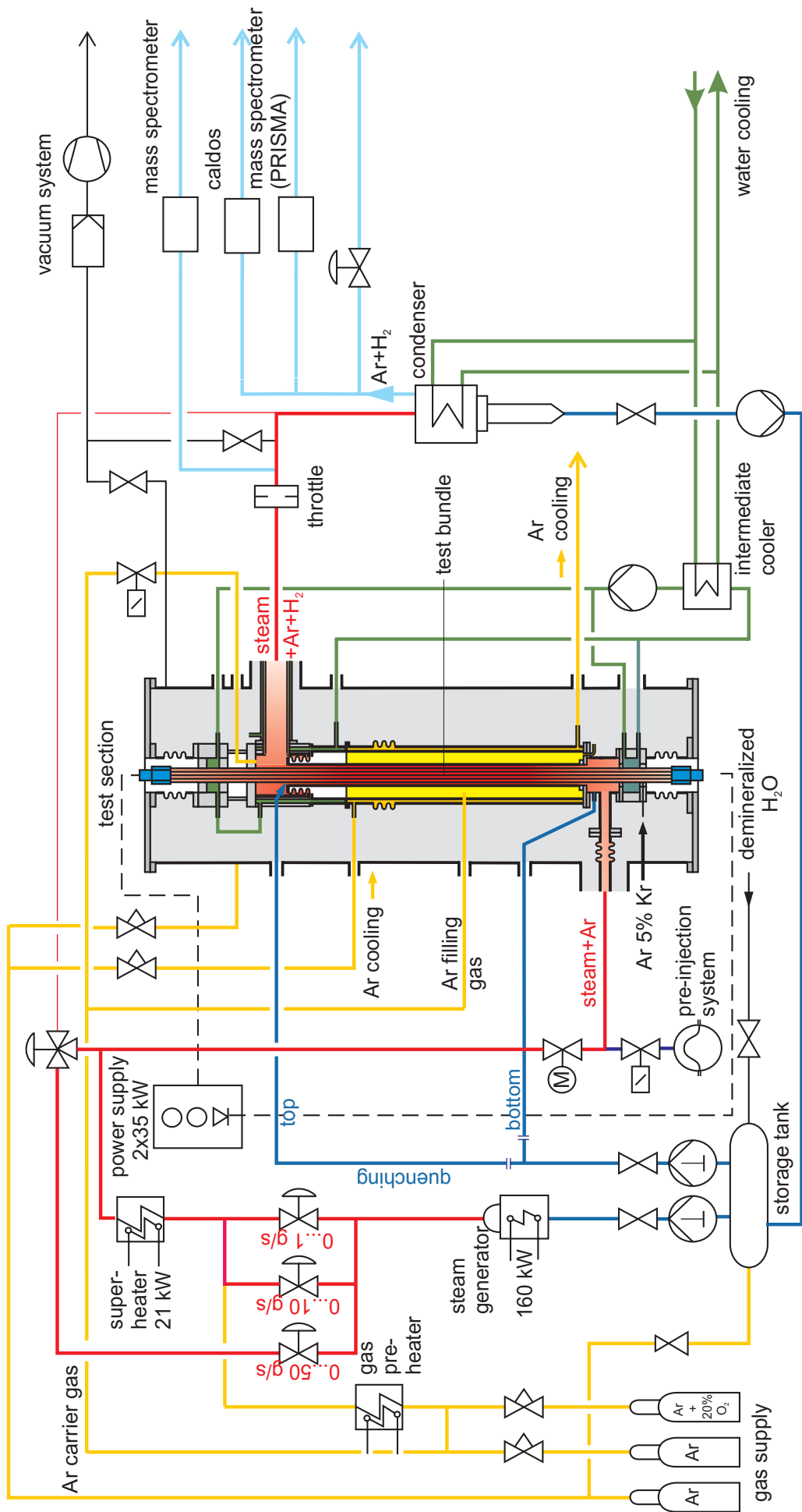


Fig.1-QUE09-Flow diagram.cdr
12.08.02 - IMF

Fig. 1: Flow diagram of the QUENCH test facility

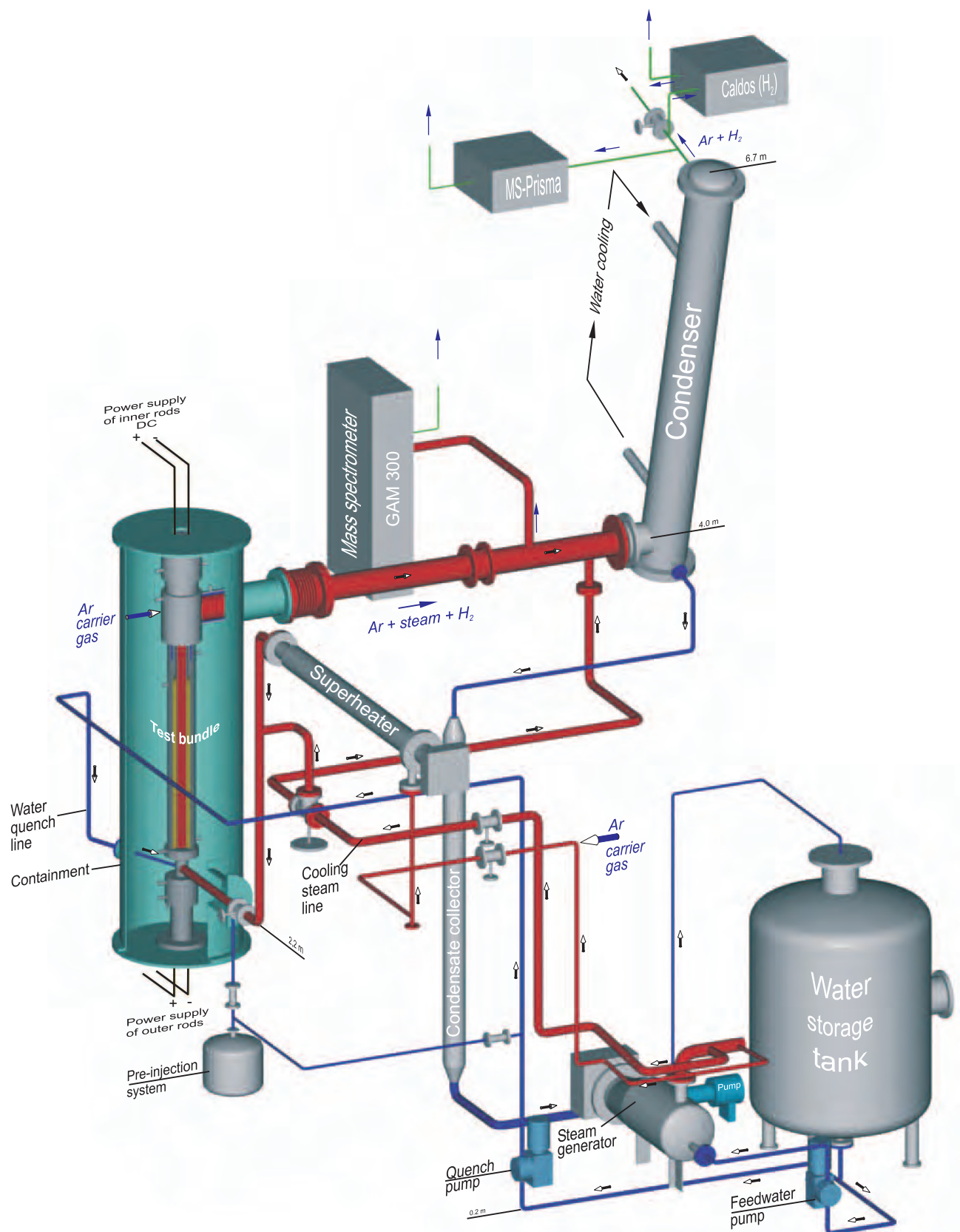


Fig.2-QUE09-Gesamtanlage.cdr
07.04.03 - IMF

Fig. 2: QUENCH Facility - Main components

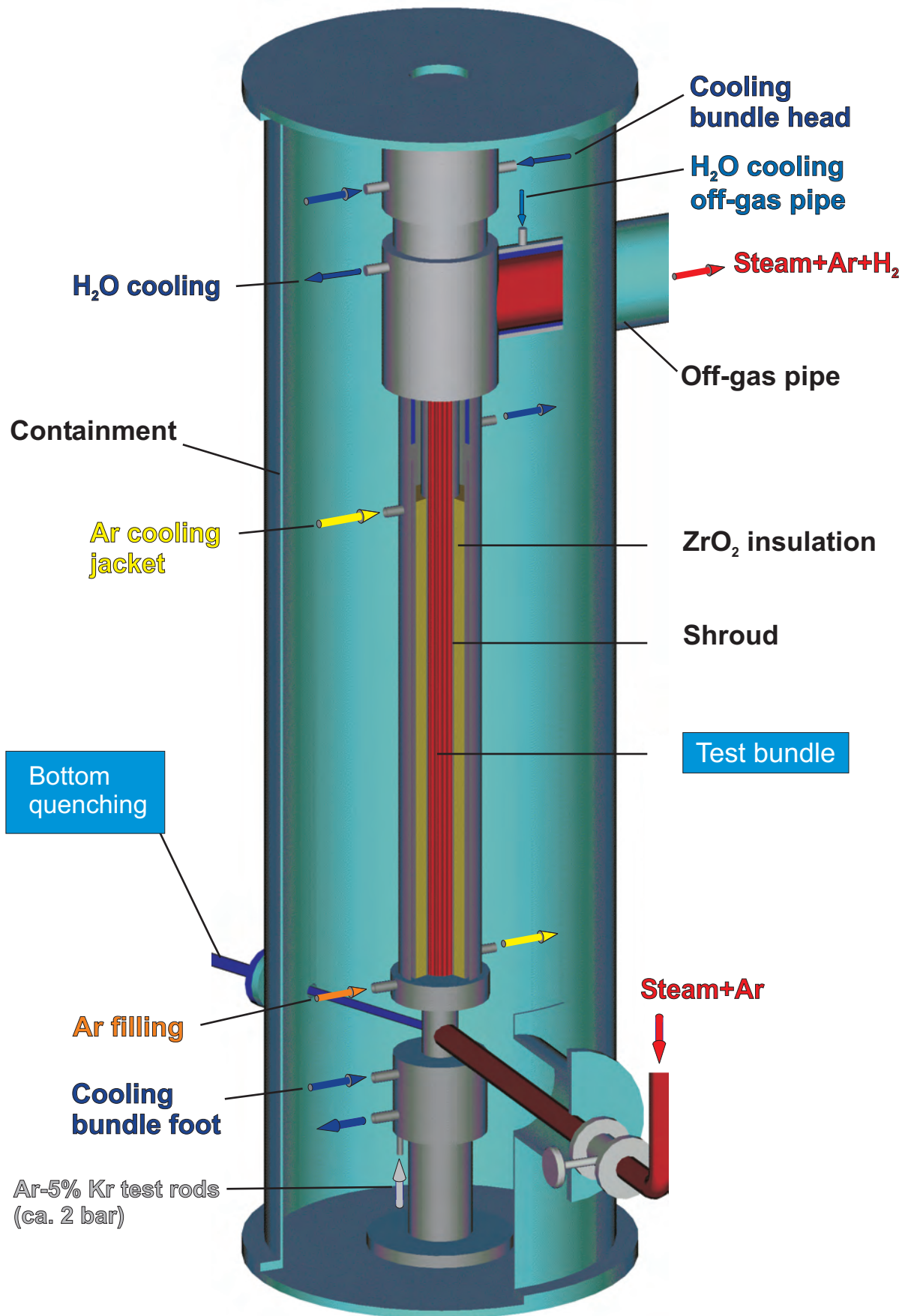


Fig. 3: QUENCH Facility; Containment and test section

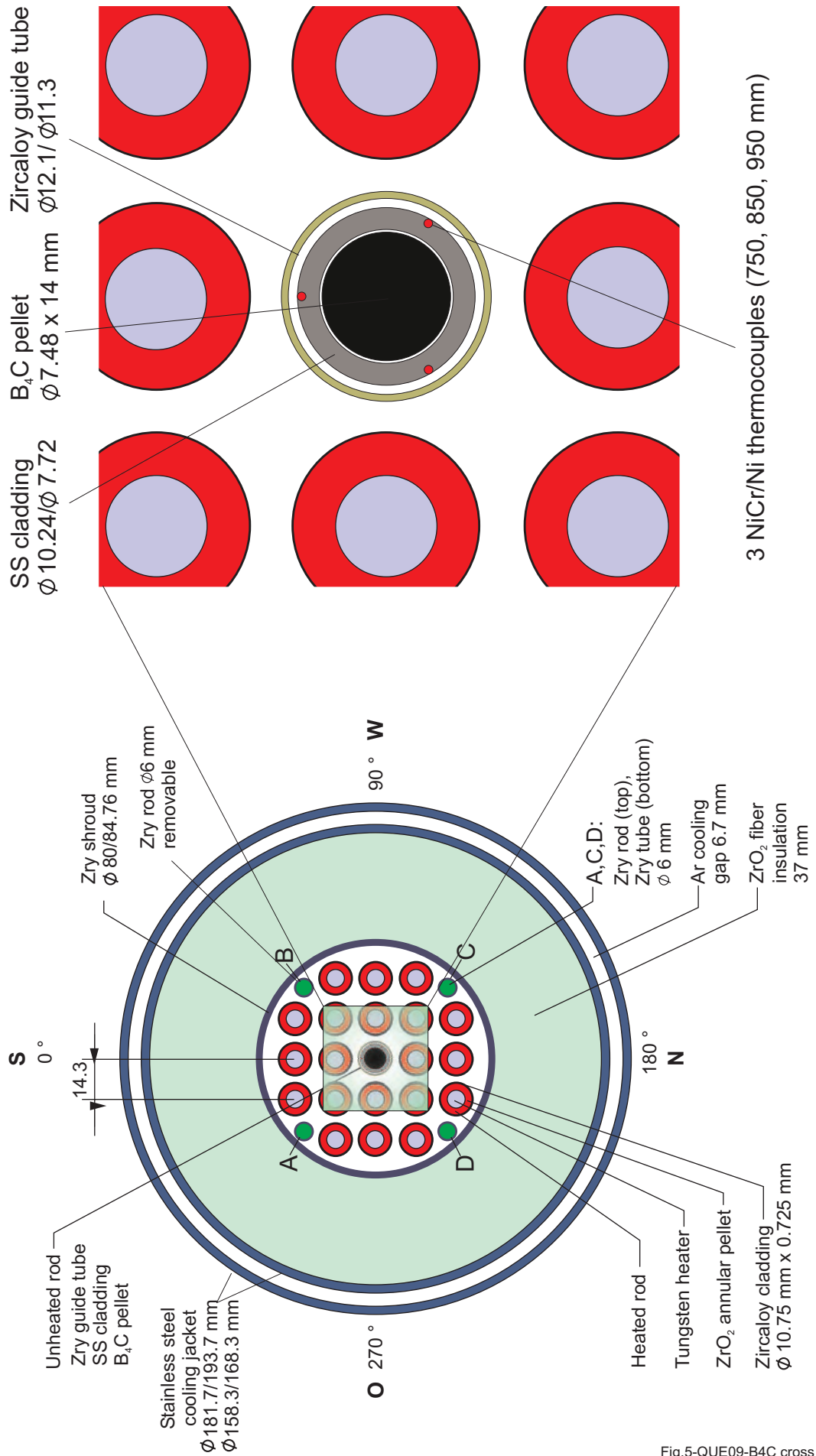


Fig.5-QUE09-B4C cross section.cdr
08.08.02 - IMF

Fig. 5: QUENCH-09; Fuel rod simulator bundle (cross section)

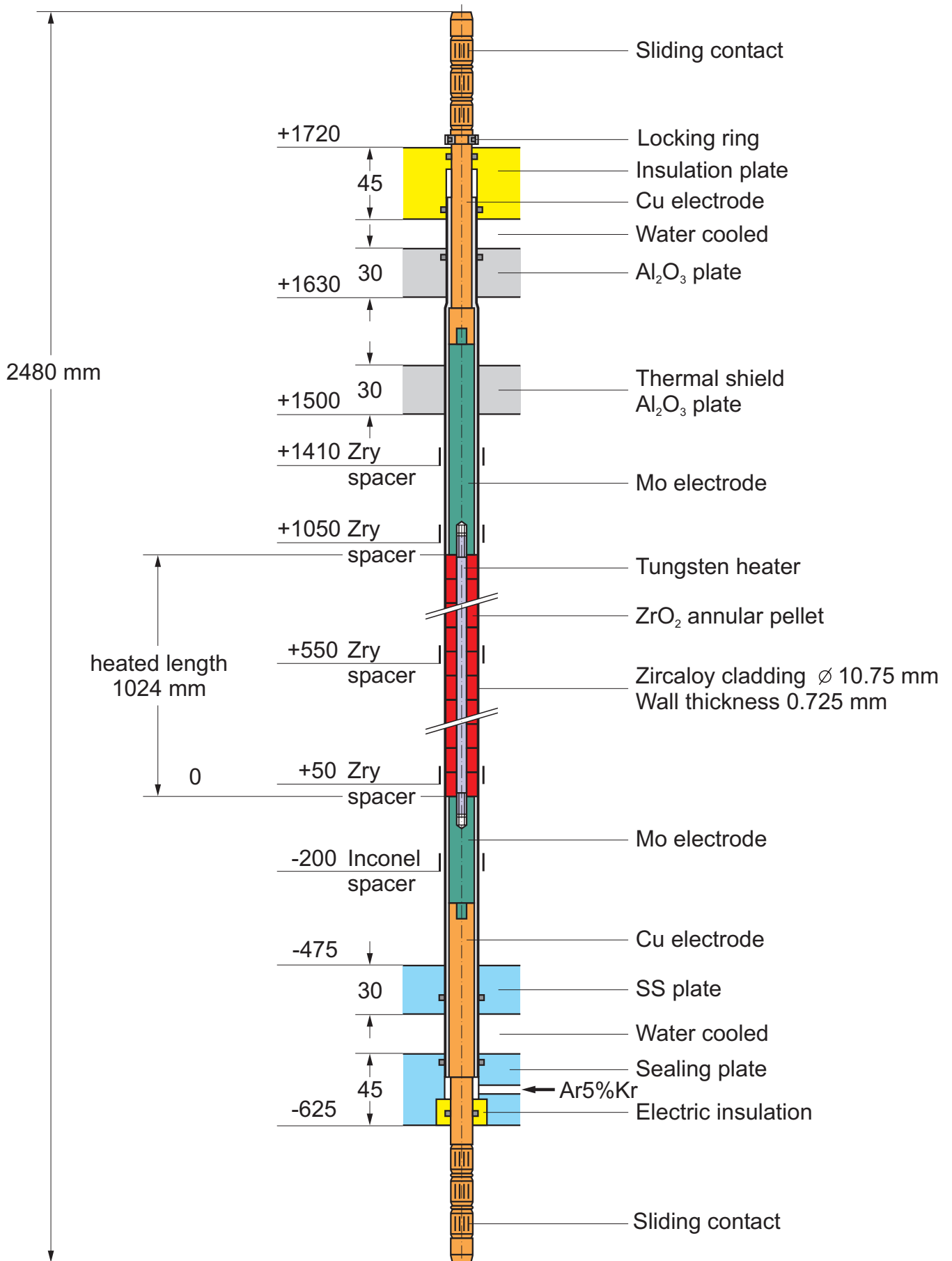


Fig.6-QUE09-Heated fuel rod sim.cdr
27.03.03 - IMF

Fig. 6: Heated fuel rod simulator

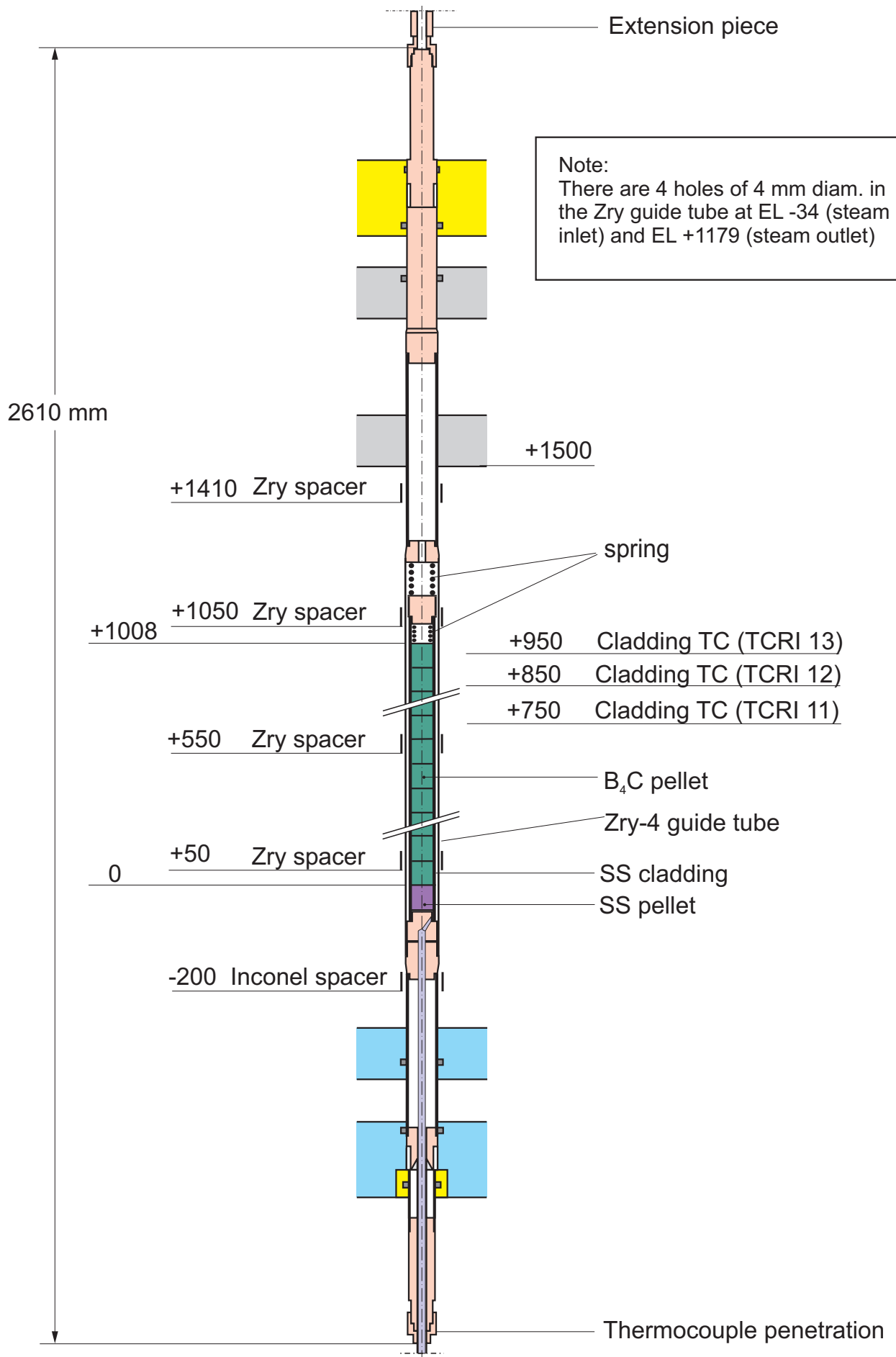


Fig.7-QUE09-Control rod simulator (unheated).cdr
27.03.03 - IMF

Fig. 7: Control rod simulator (unheated)

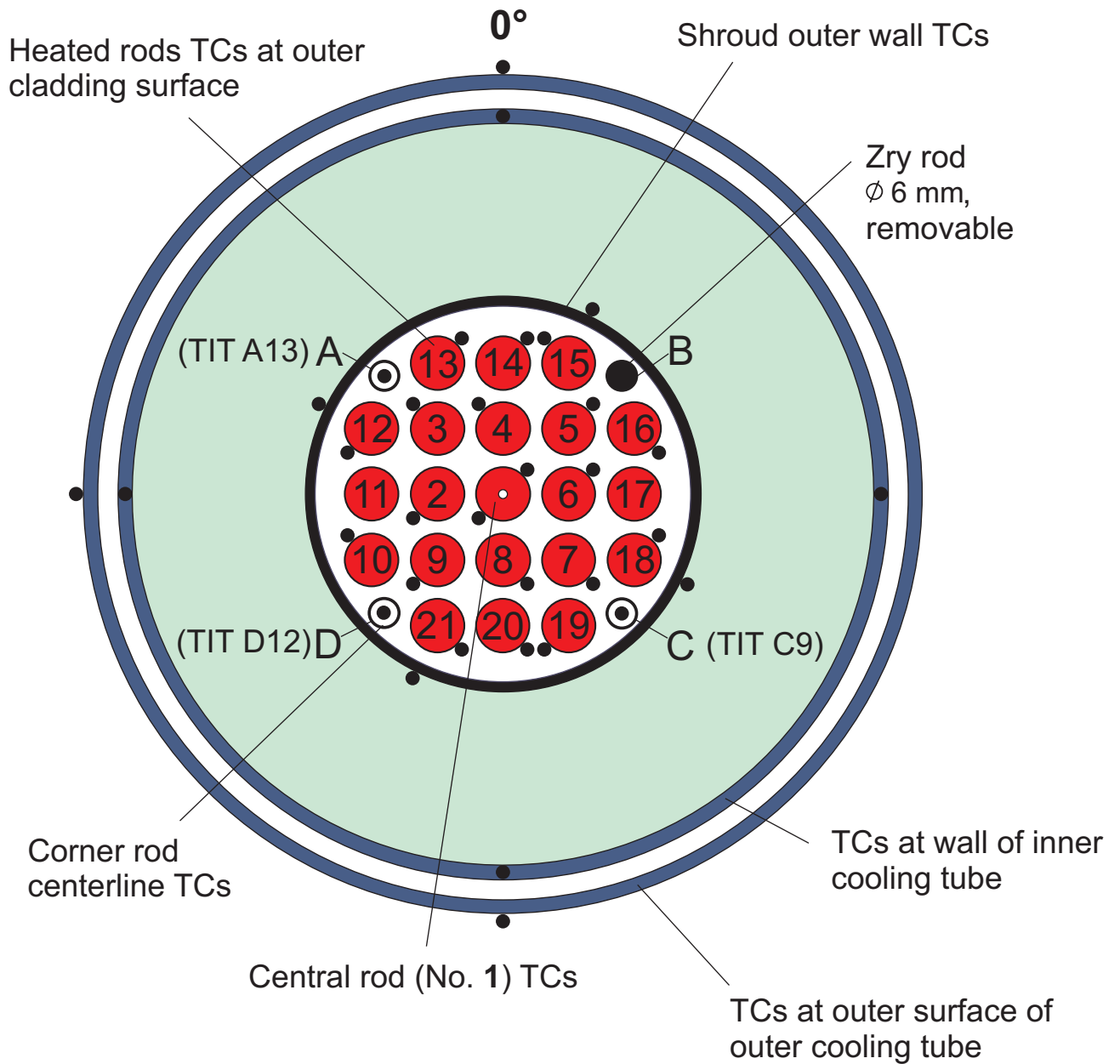


Fig.8-QUE09 TC instr.cdr
31.08.04 - IMF

Fig. 8: QUENCH-09; Test bundle instrumentation (azimuthal orientation) and rod designation (top view)

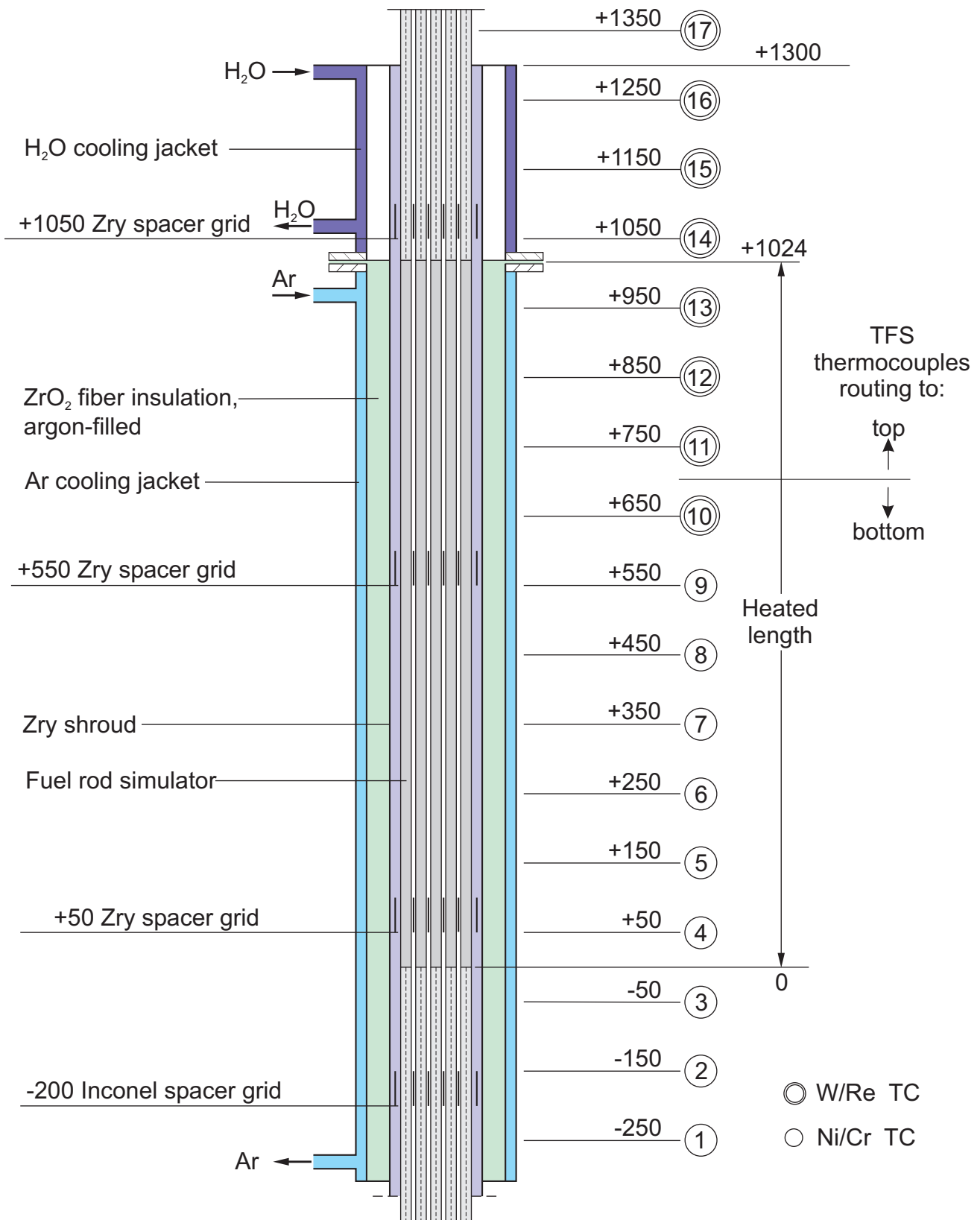
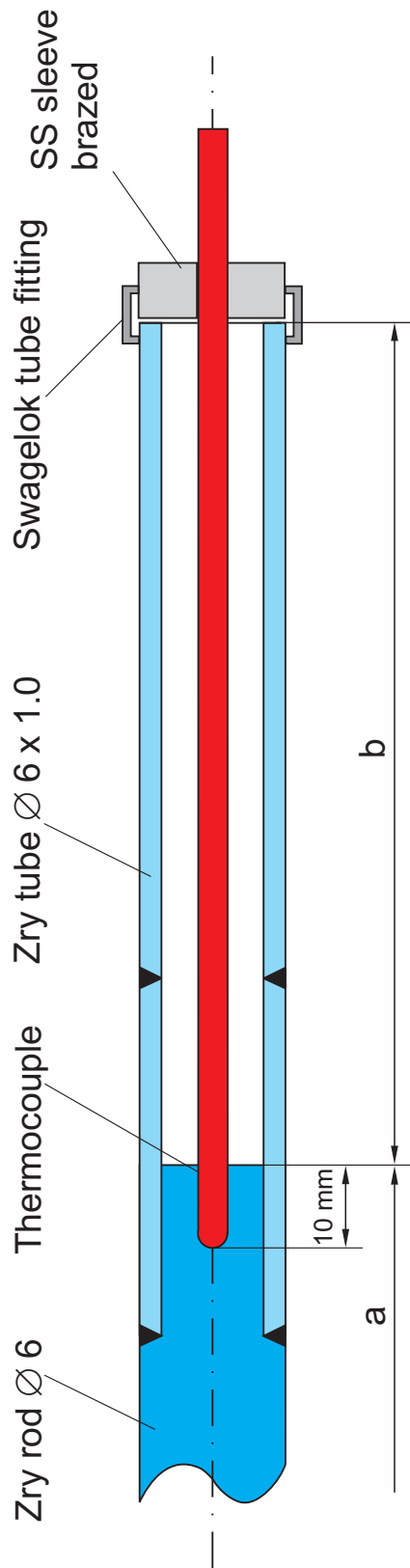


Fig.9-QUE09-TC elevations.cdr
15.04.03 - IMF

Fig. 9: Axial temperature measurement locations in the QUENCH test section.

(TIT A13, TIT D12, TIT C9)



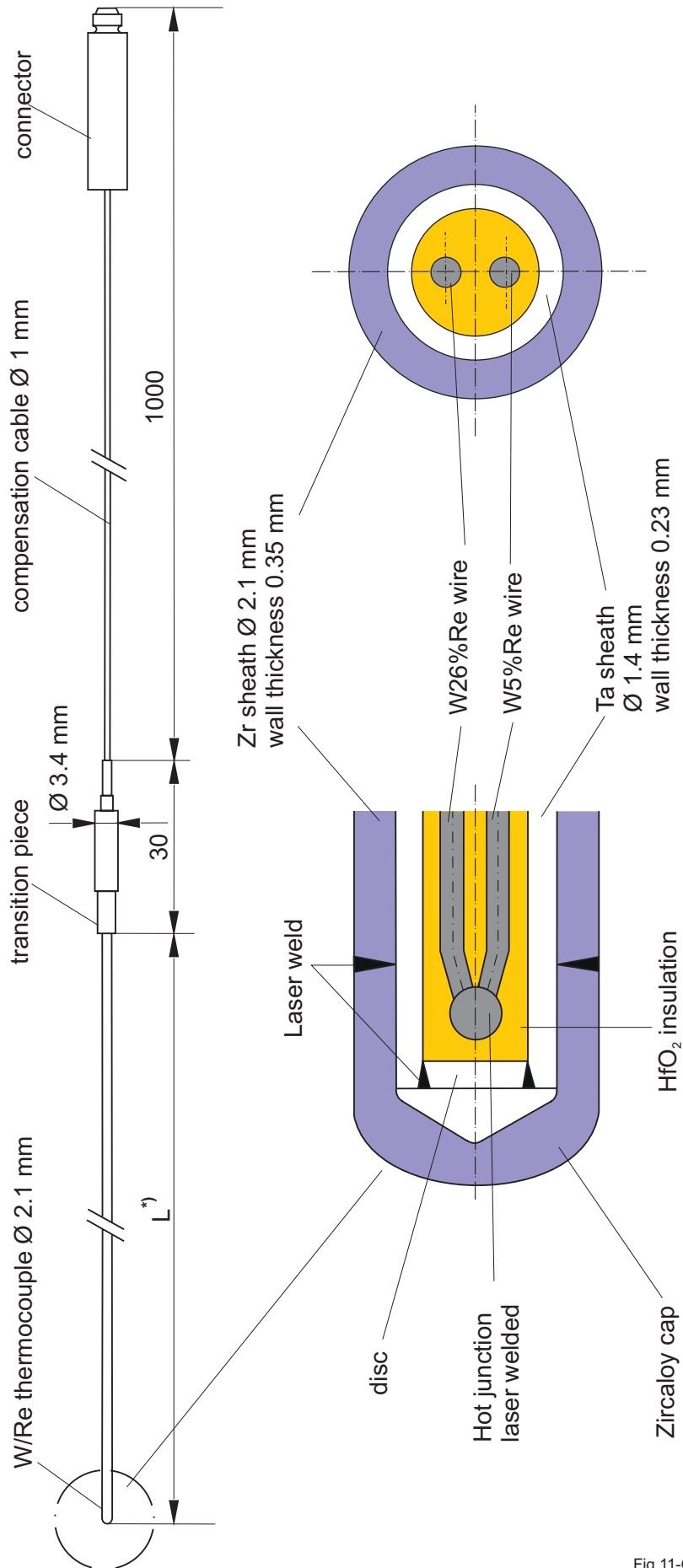
Rod A: TIT A13 (950 mm), W/Re, Ø 2.1 mm, a = 360 mm, b = 2080 mm

Rod D: TIT D12 (850 mm), W/Re, Ø 2.1 mm, a = 460 mm, b = 1980 mm

Rod C: TIT C 9 (550 mm), NiCr/Ni, Ø 1 mm, a = 760 mm, b = 1680 mm

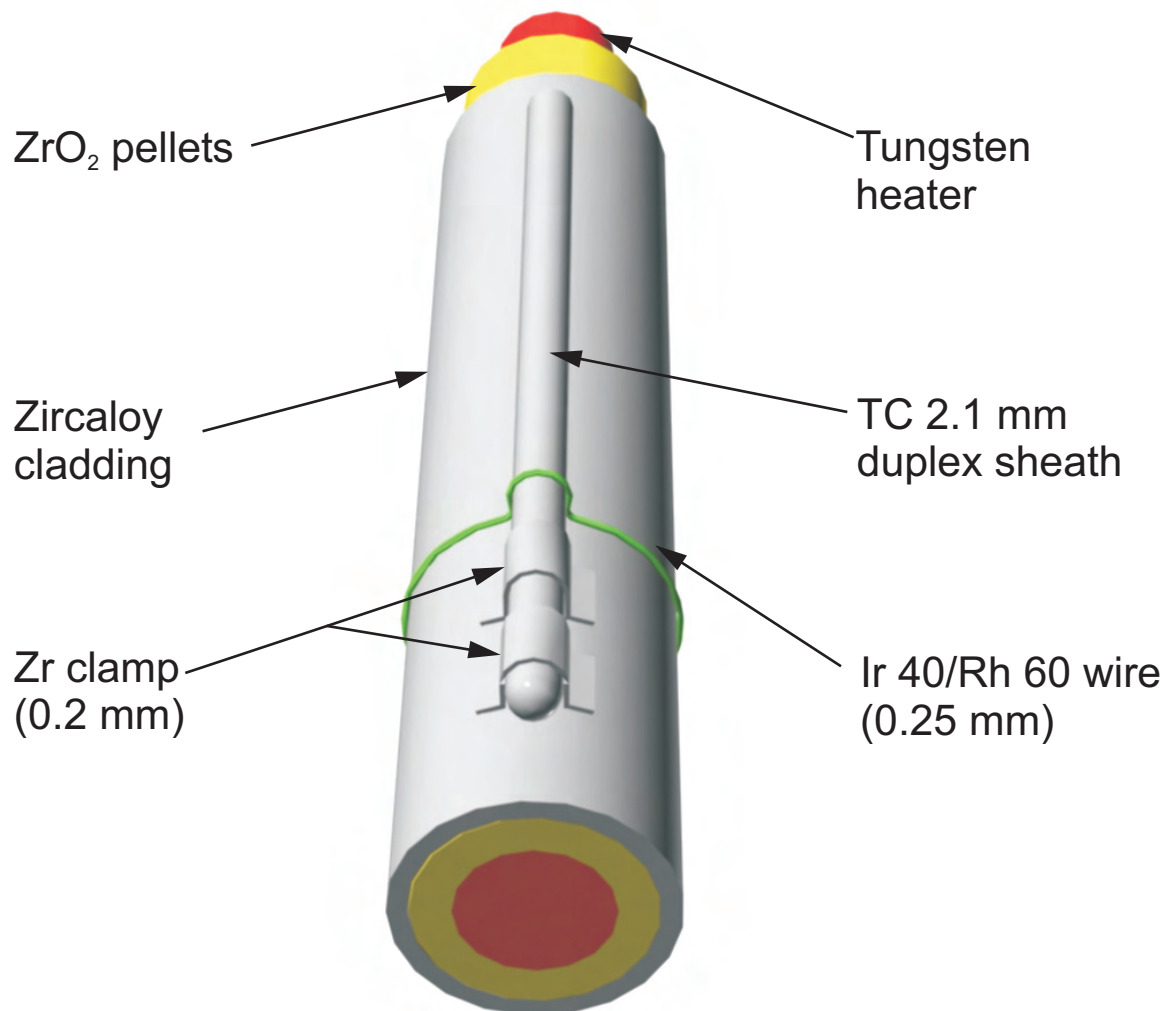
(Rod B: Zry-4 rod, Ø 6 mm, removable)

Fig. 10: QUENCH-09; Arrangement of the thermocouples inside the corner rods



*) L : high-temperature section length dependent on the TC position in the test bundle 500 mm - 1700 mm

Fig. 11: QUENCH; High-temperature thermocouple



Tests with pre-oxidation: Zr clamp + wire

Tests without pre-oxidation: Zr clamp

Fig. 12: TC fastening concept for the QUENCH test rod

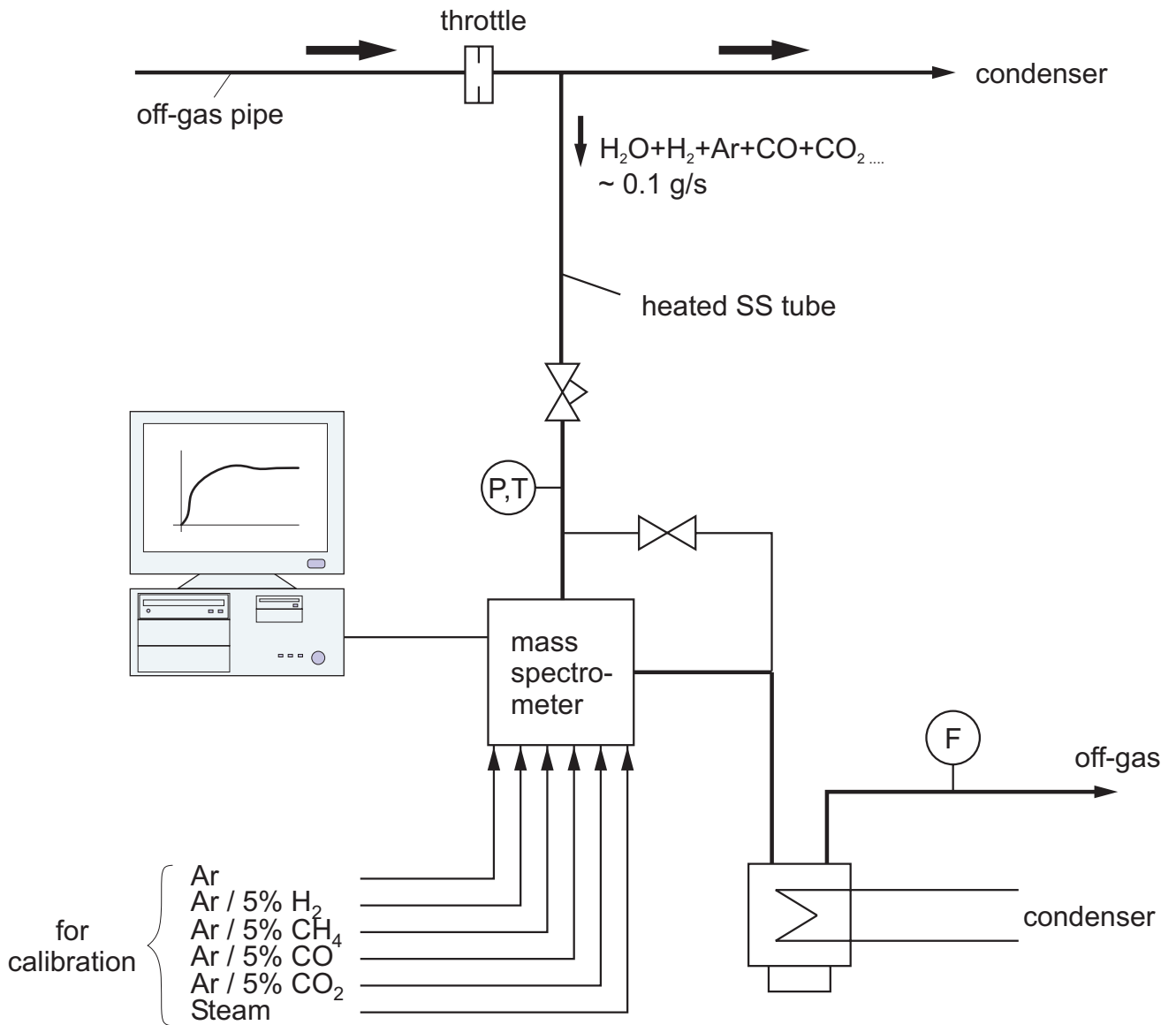


Fig.13-QUE09-MS Quench facility.cdr
12.08.02 - IMF

Fig. 13: QUENCH Facility; H₂ measurement with the GAM 300 mass spectrometer

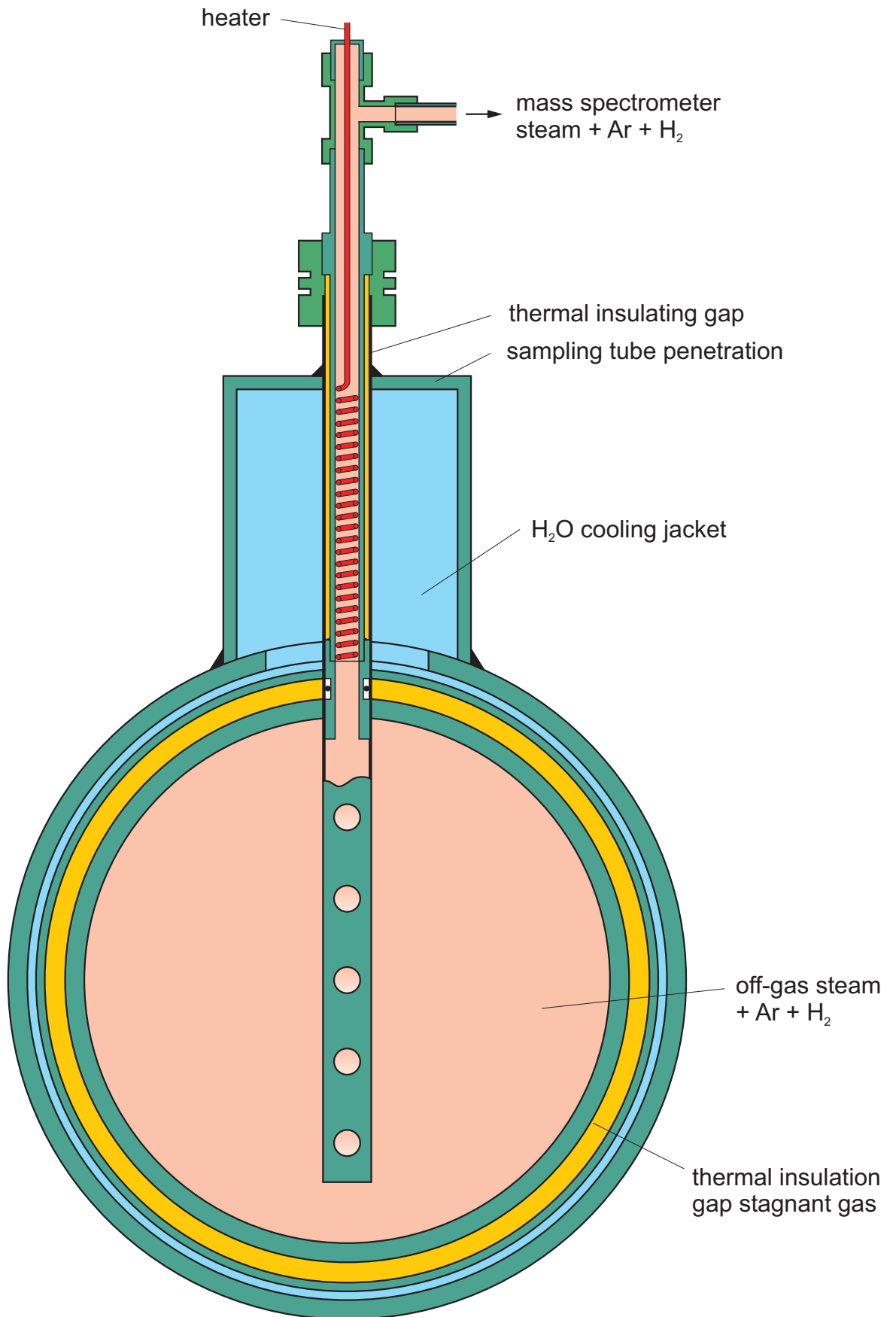


Fig 14-QUE09-MS sampling position new.cdr
12.08.02 - IMF

Fig.14: QUENCH; Mass spectrometer sampling position at the off-gas pipe

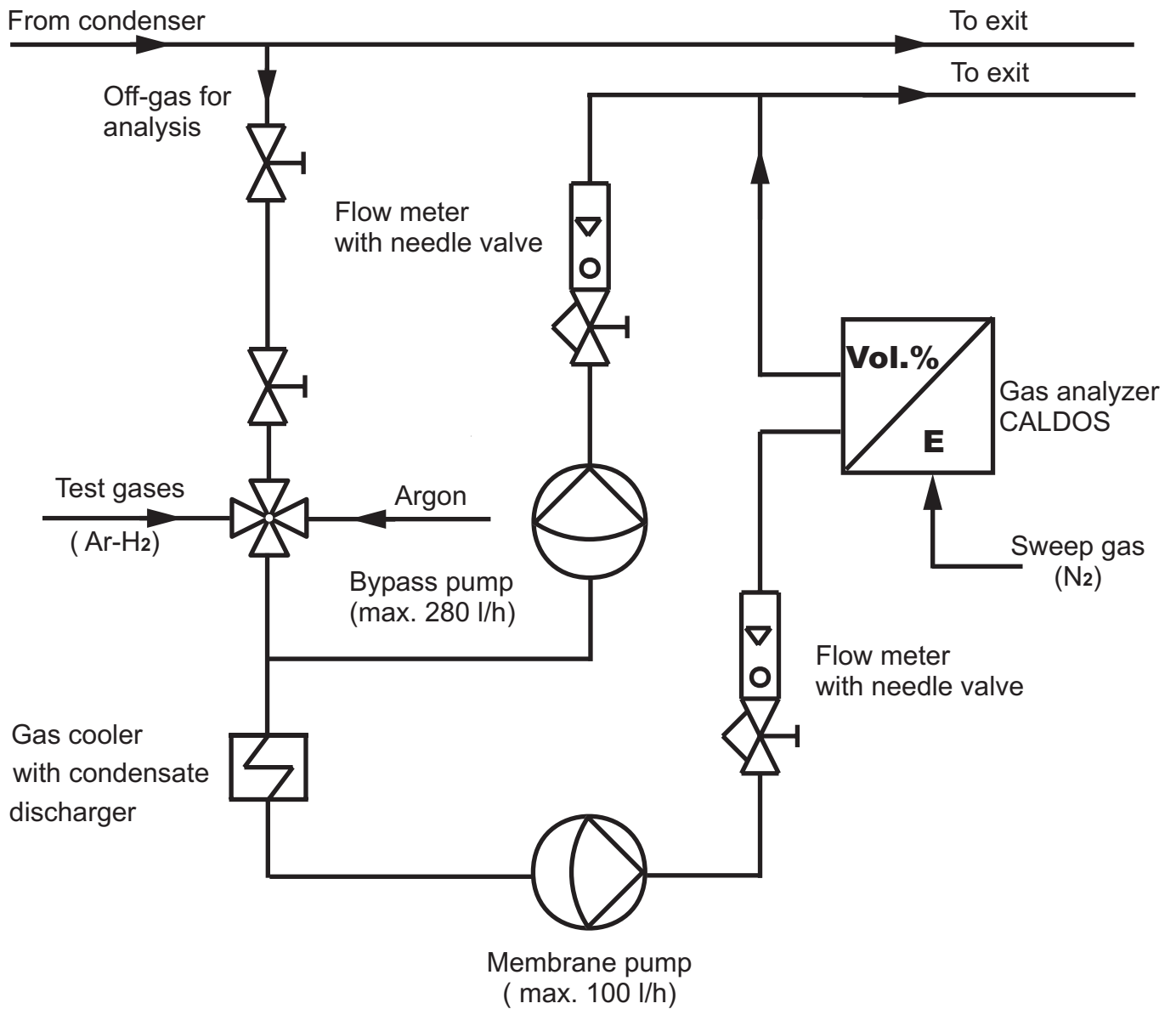


Fig 15-QUE09-Caldos Schema (ab QUE04).cdr
12.08.02 - IMF

Fig.15: QUENCH; Hydrogen measurement with the CALDOS analyzer

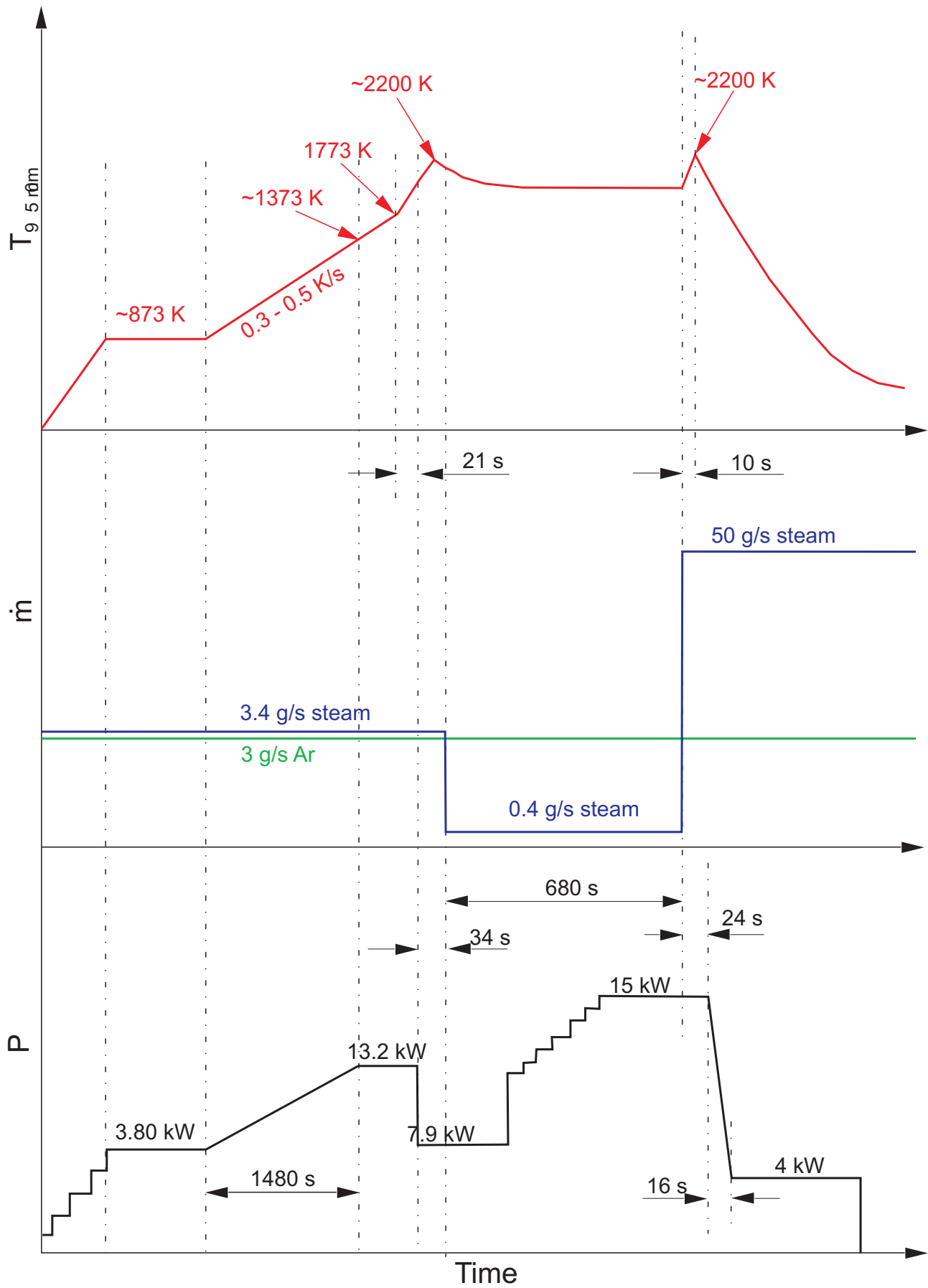


Fig.16-QUE09-as performed.cdr
06.10.04 - IMF

Fig. 16: QUENCH-09; Test as performed

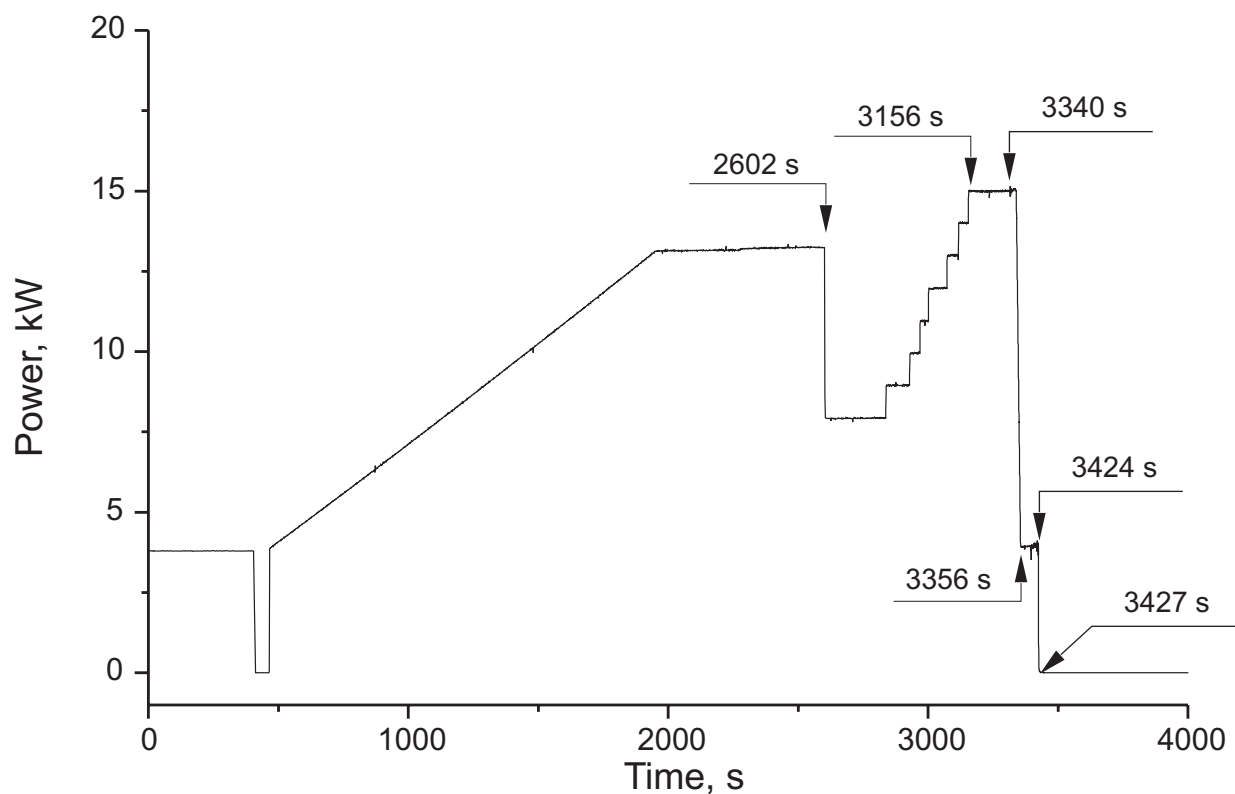
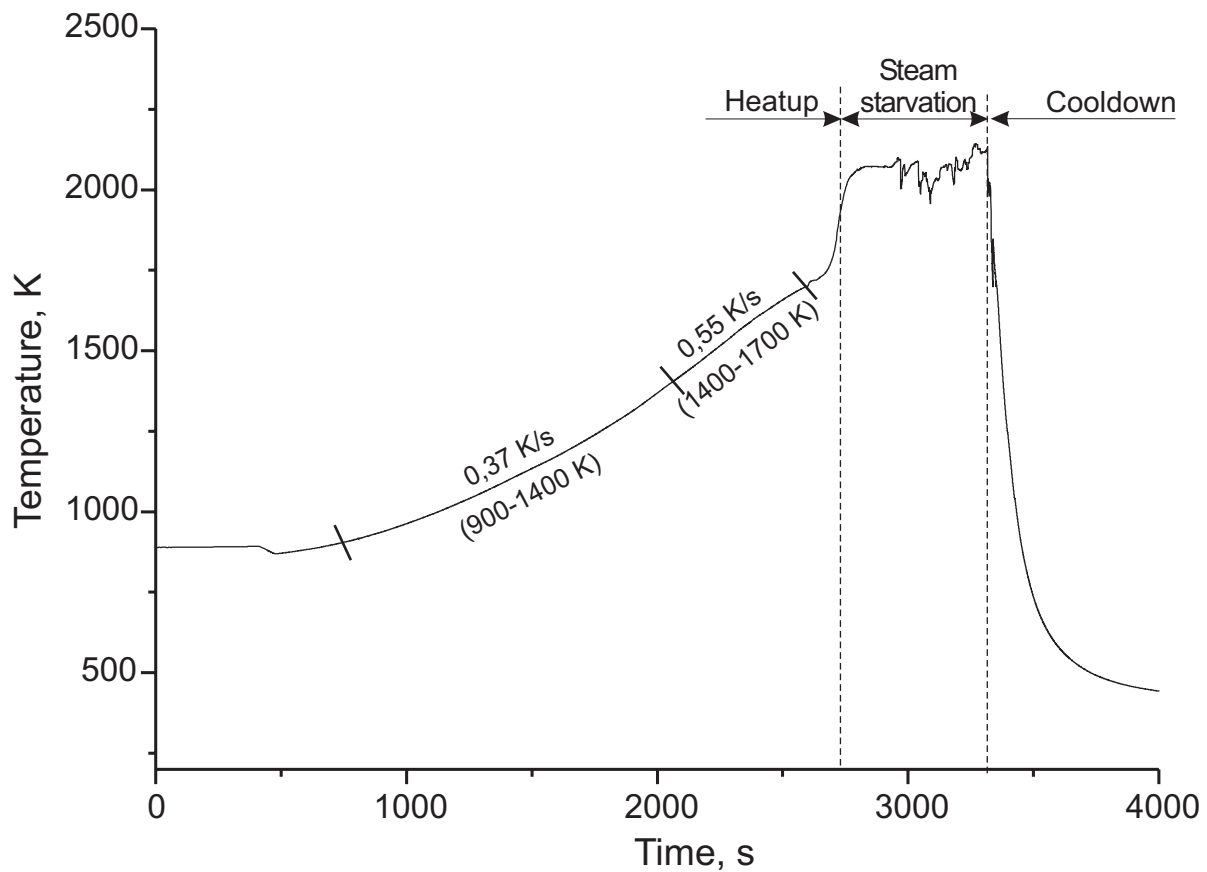


Fig.17-QUE09-Leistung.cdr
25.10.04 - IMF

Fig. 17: QUENCH-09; Test phases illustrated with help of the temperature measured by the thermocouple TFS 2/12 B together with the heatup rate, top, and total electric power vs. time, bottom.

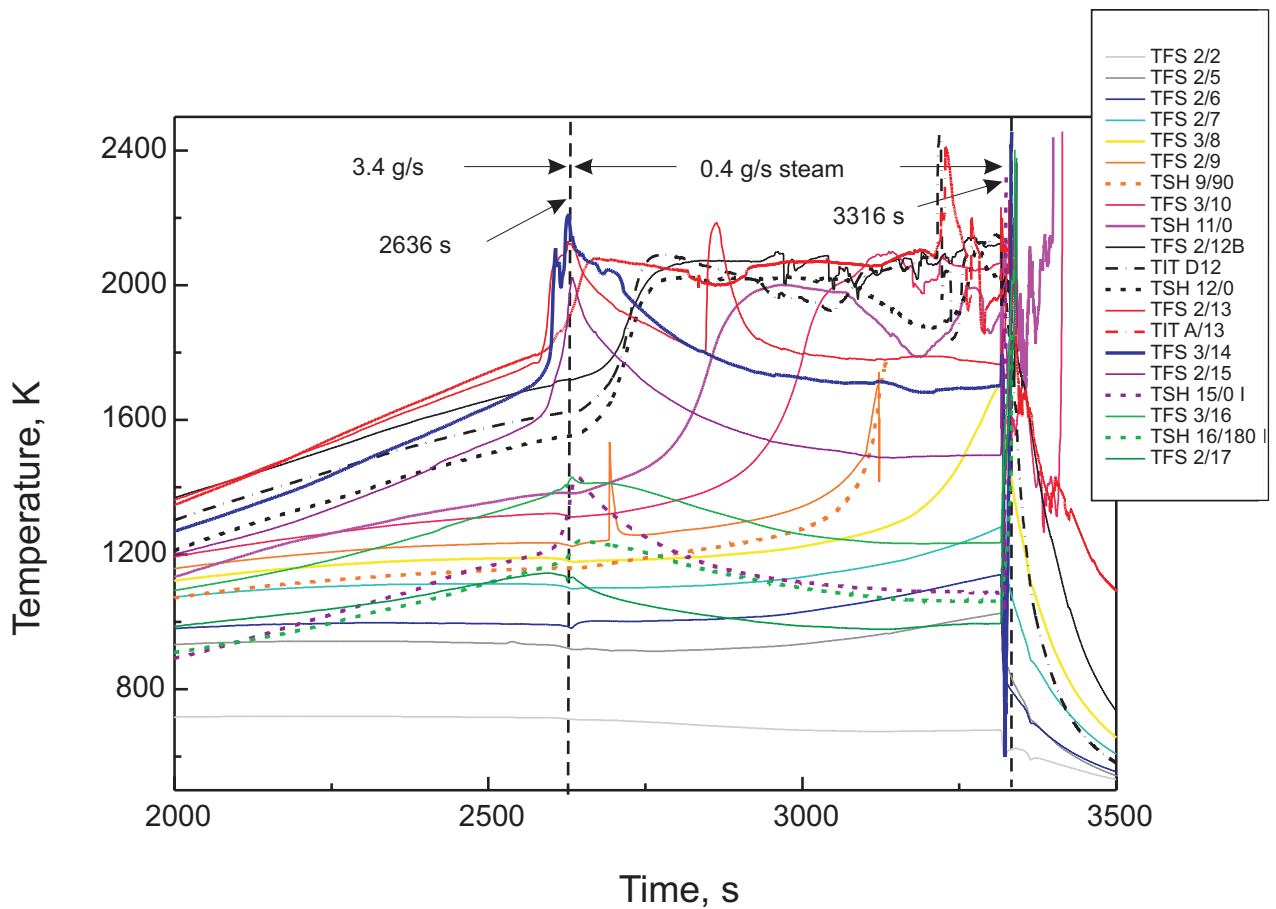
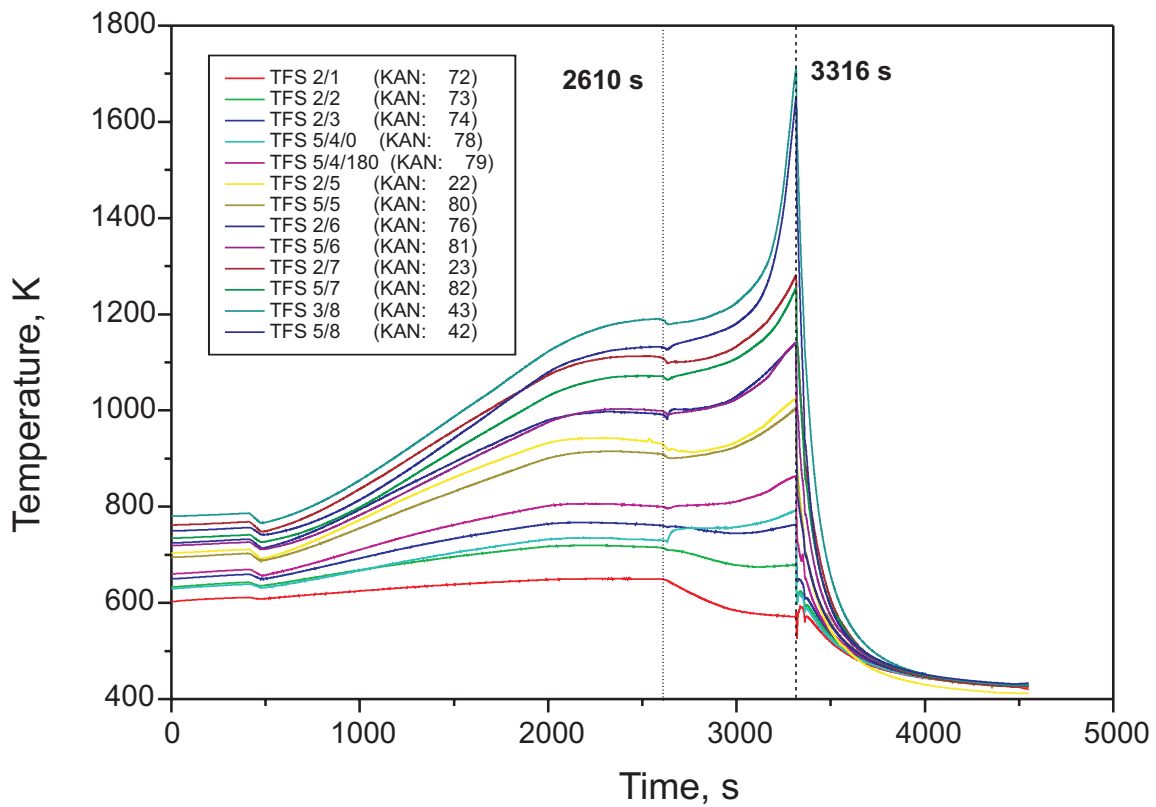


Fig.18-QUE09-Temp-Zeit-all.cdr
25.10.04 - IMF

Fig. 18: QUENCH-09; Temperature histories of rod cladding thermocouples (TFS) at the lower elevations for the entire test time, top, and of the various thermocouples between 2000 and 3500 s, bottom.

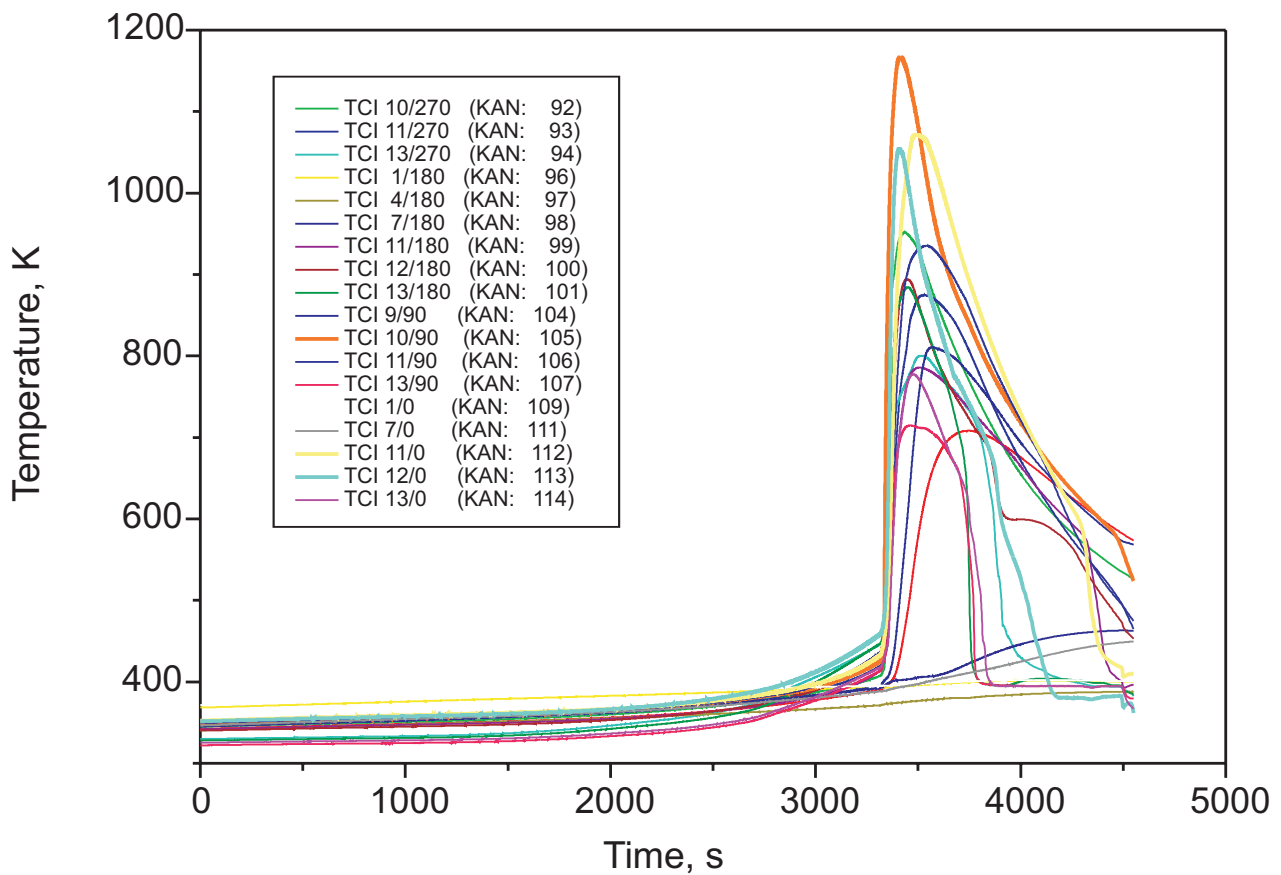
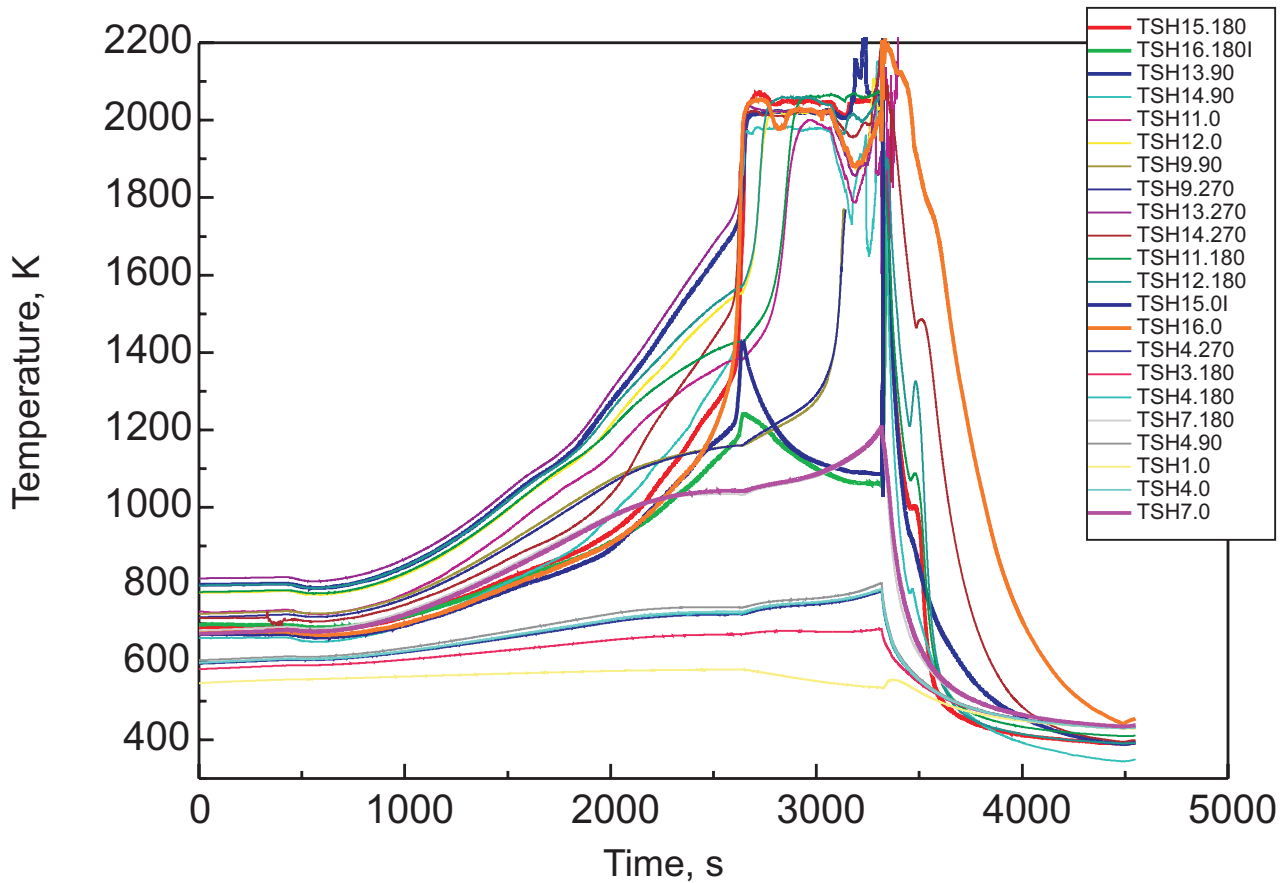


Fig.19-QUE09-Temp-Zeit-TSHall.cdr
25.02.03 - IMF

Fig. 19: QUENCH-09; Overview of shroud temperature (TSH) histories, top, and the histories of the TCI (inner cooling jacket) temperatures, bottom

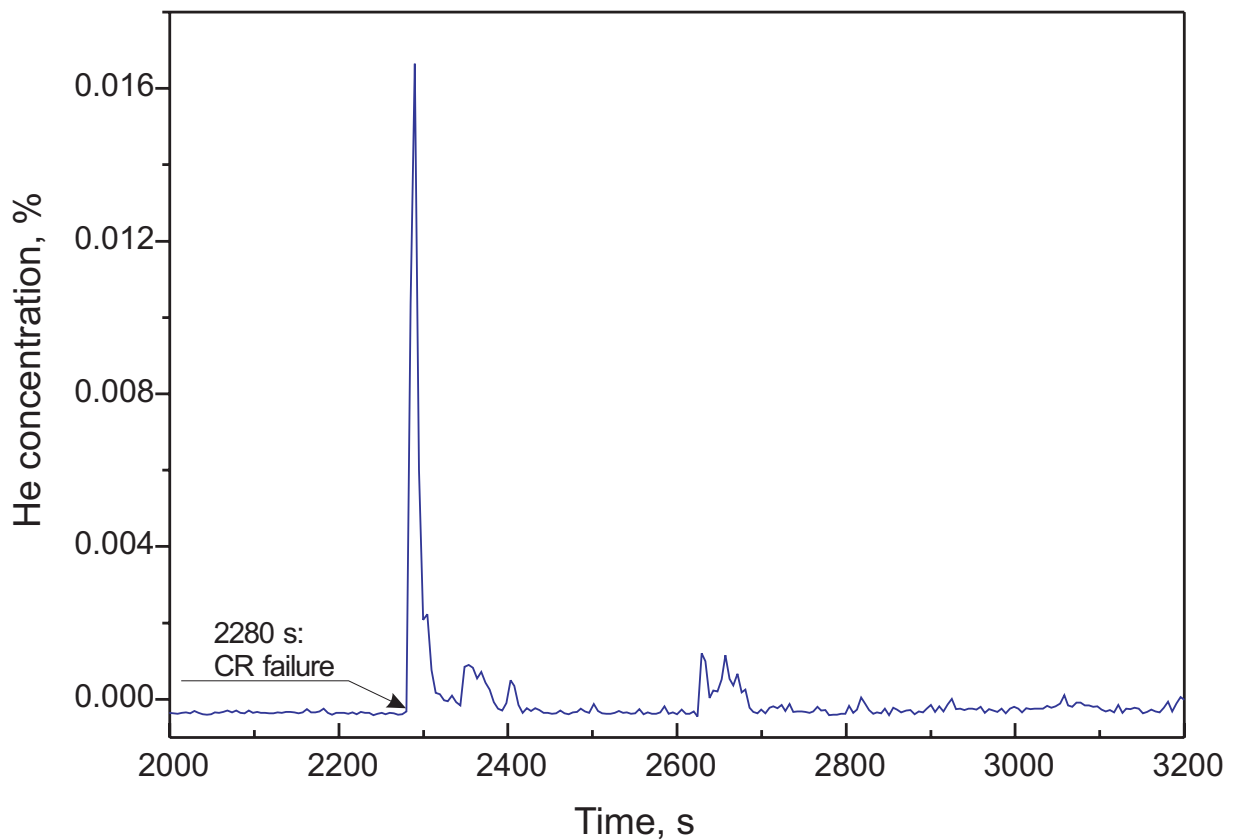
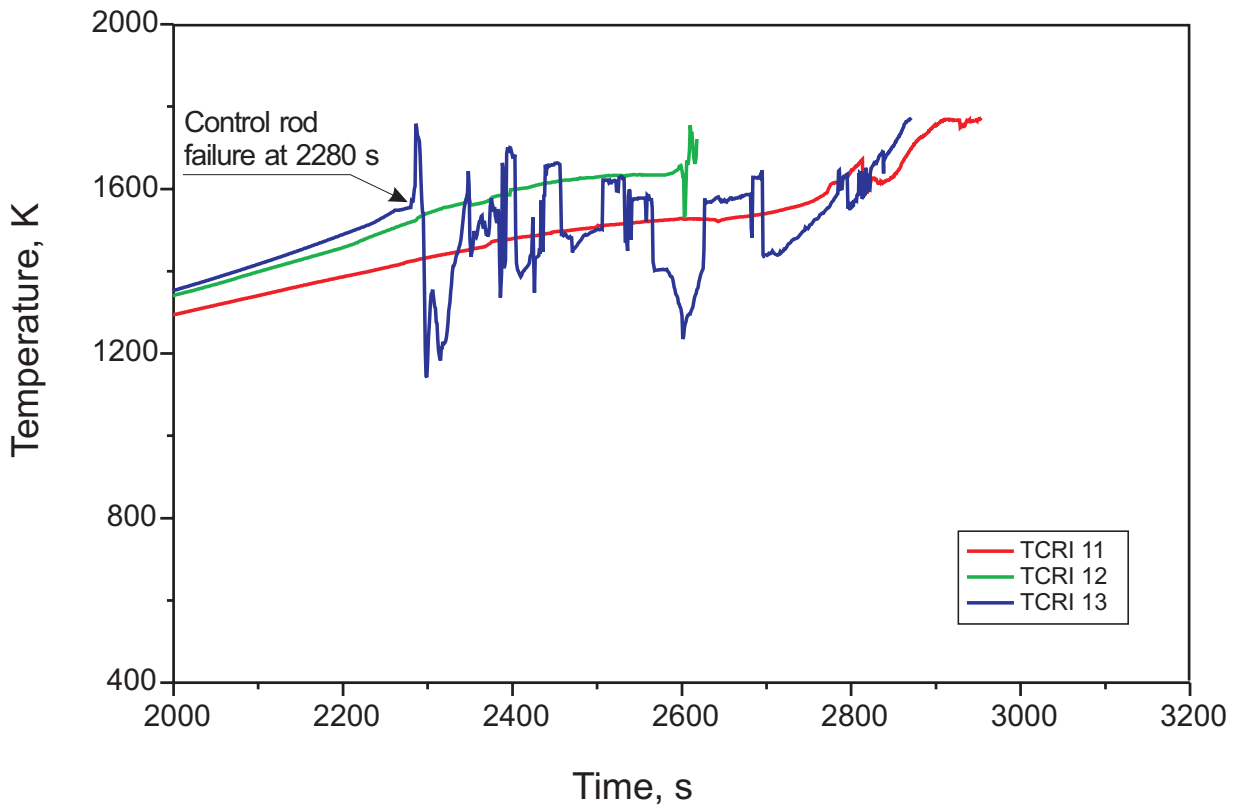


Fig.20-QUE09-Temp-Zeit-alle TCRI.cdr
11.10.04 - IMF

Fig. 20: QUENCH-09; Absorber rod cladding temperatures at 750, 850, and 950 mm elevation, top, and helium concentration, bottom, to demonstrate initiation of control rod failure

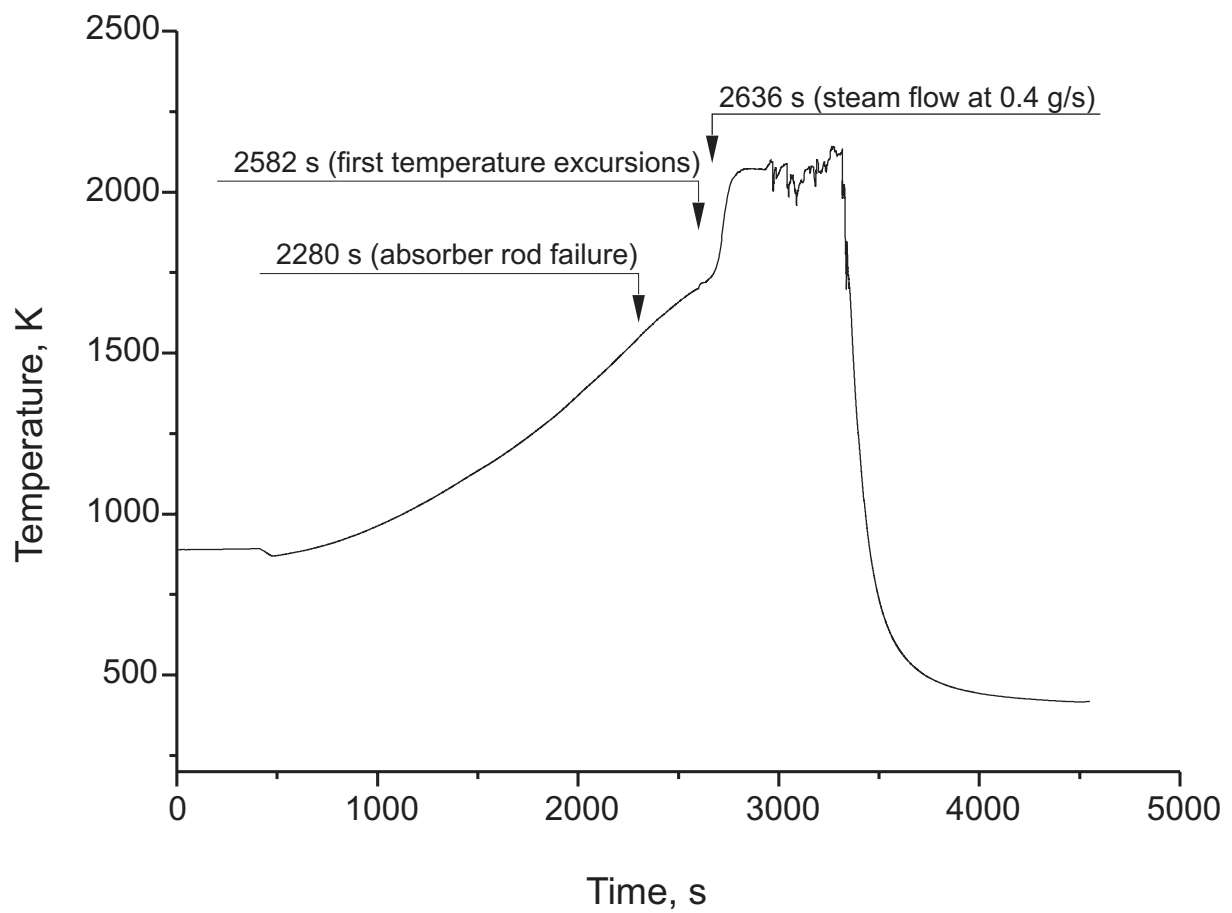


Fig.21-QUE09-Temp-Zeit-TFS2-12B.cdr
25.02.03 - IMF

Fig. 21: QUENCH-09; Selected times for the axial temperature profiles (illustrated with help of thermocouple TFS 2/12 B)

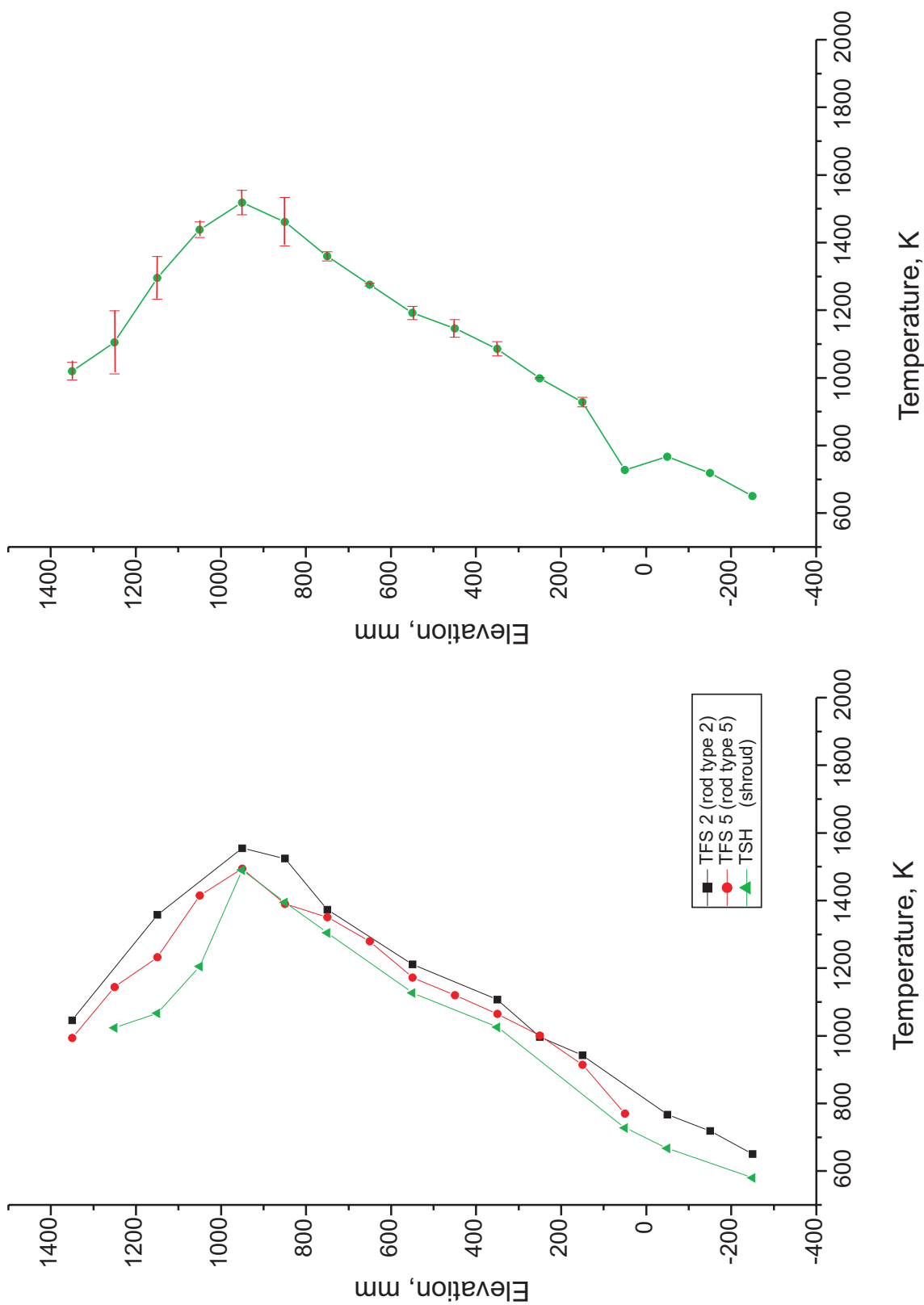


Fig. 22-QUE09-Axial-Temp-Profil+2280s.cdr
02.11.04 - IMF

Fig. 22: QUENCH-09; Axial temperature profile TFS 2, TFS 5, TSH, left, and axial temperature profile of all TFS, right, at 2280 s (absorber rod failure)

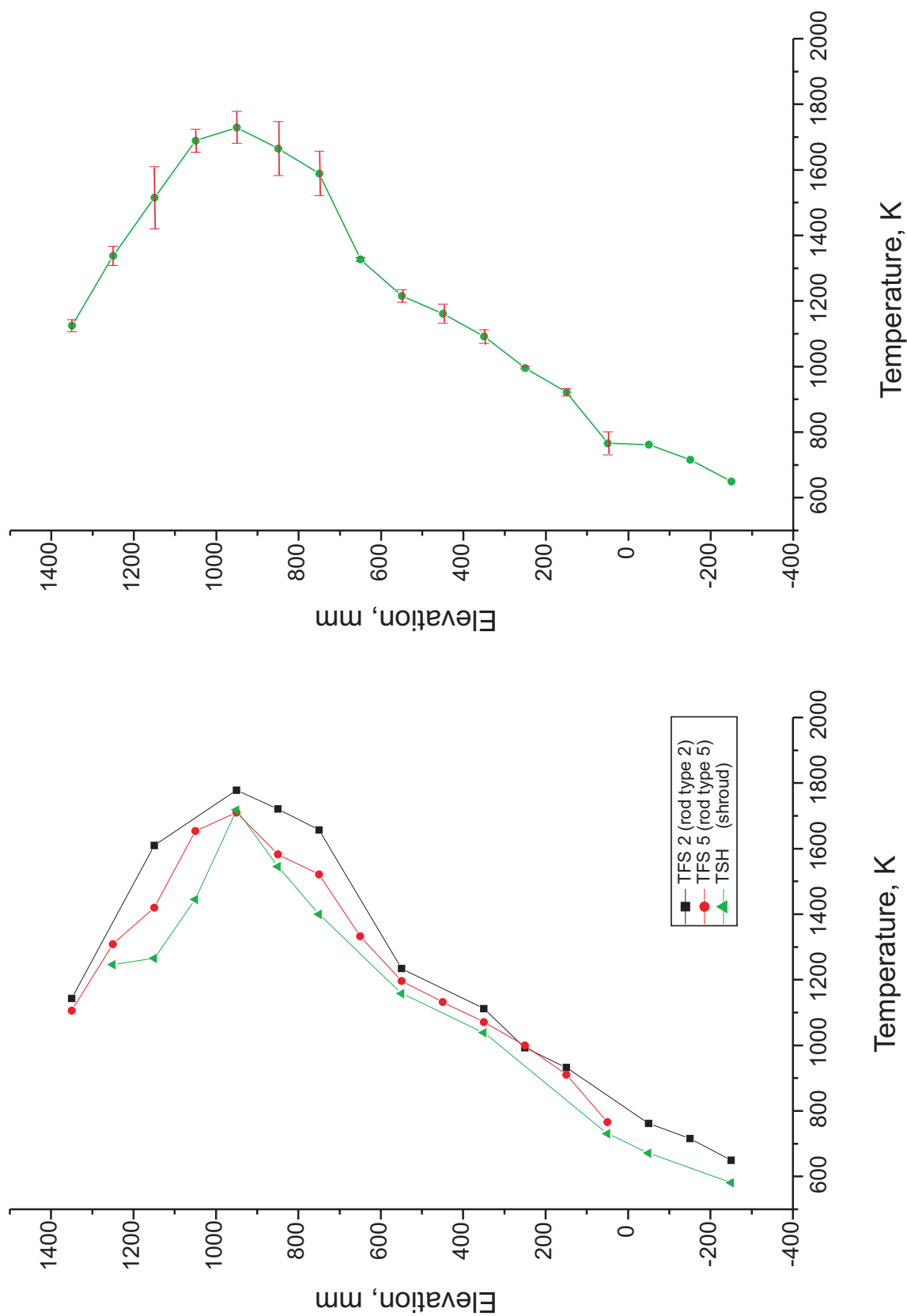


Fig.23-QUE09-Axial-Temp-Profil-2582s.cdr
02.11.04 - IMF

Fig. 23: QUENCH-09; Axial temperature profile TFS 2, TFS 5, TSH, left, and axial temperature profile of all TFS, right, at 2582 s (beginning of temperature excursions)

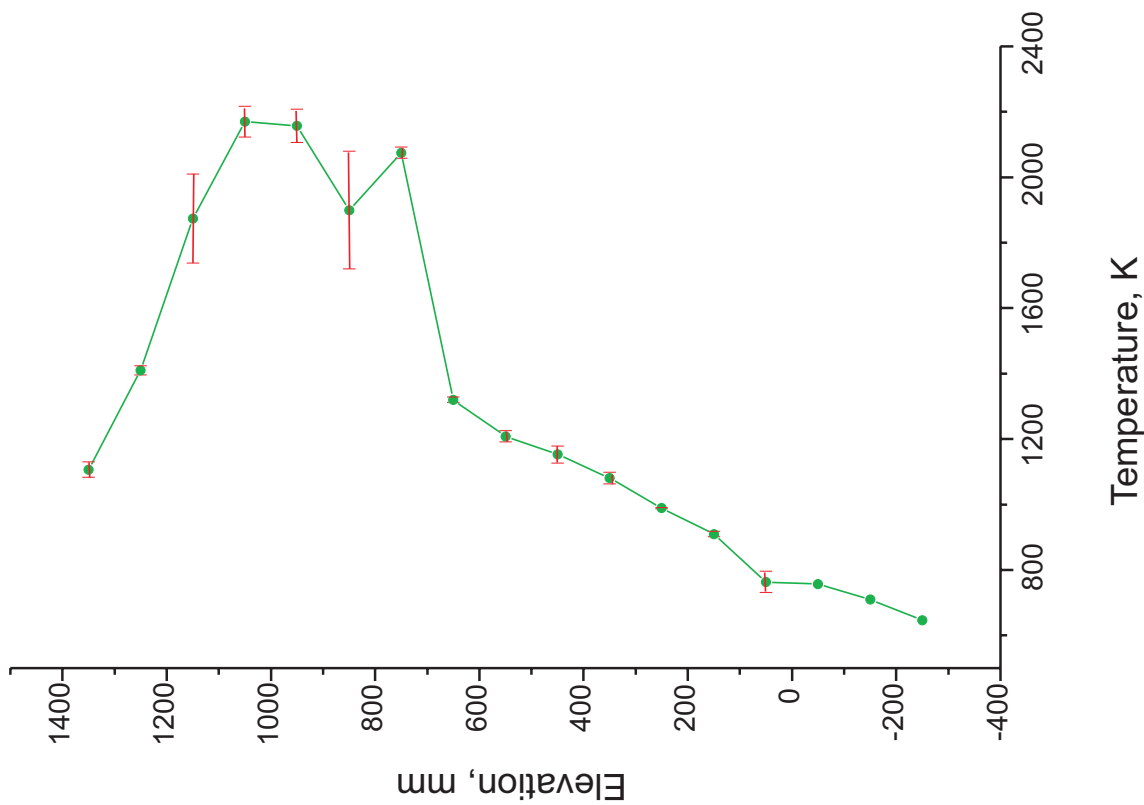


Fig.24-QUE09-Axial-Temp-Profil-2636s.cdr
02.11.04 - IMF

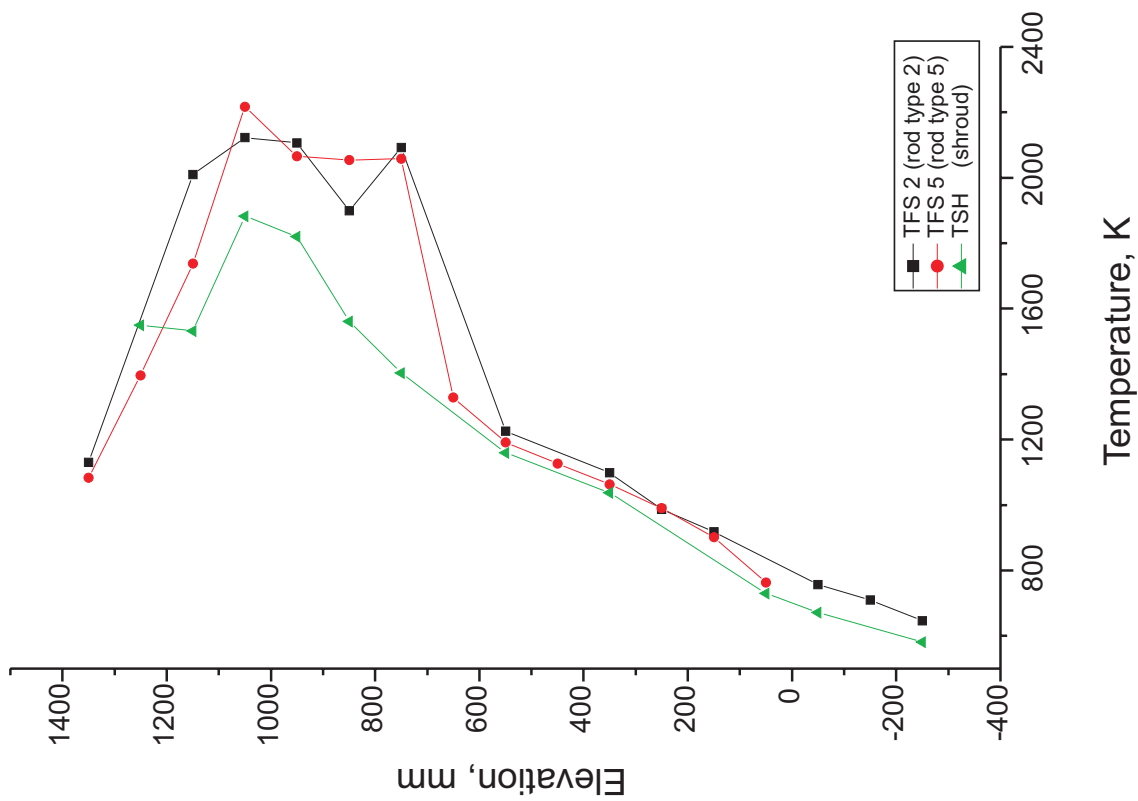


Fig. 24: QUENCH-09; Axial temperature profile TFS 2, TFS 5, TSH, left, and axial temperature profile of all TFS, right, at 2636 s (beginning of steam flow reduction)

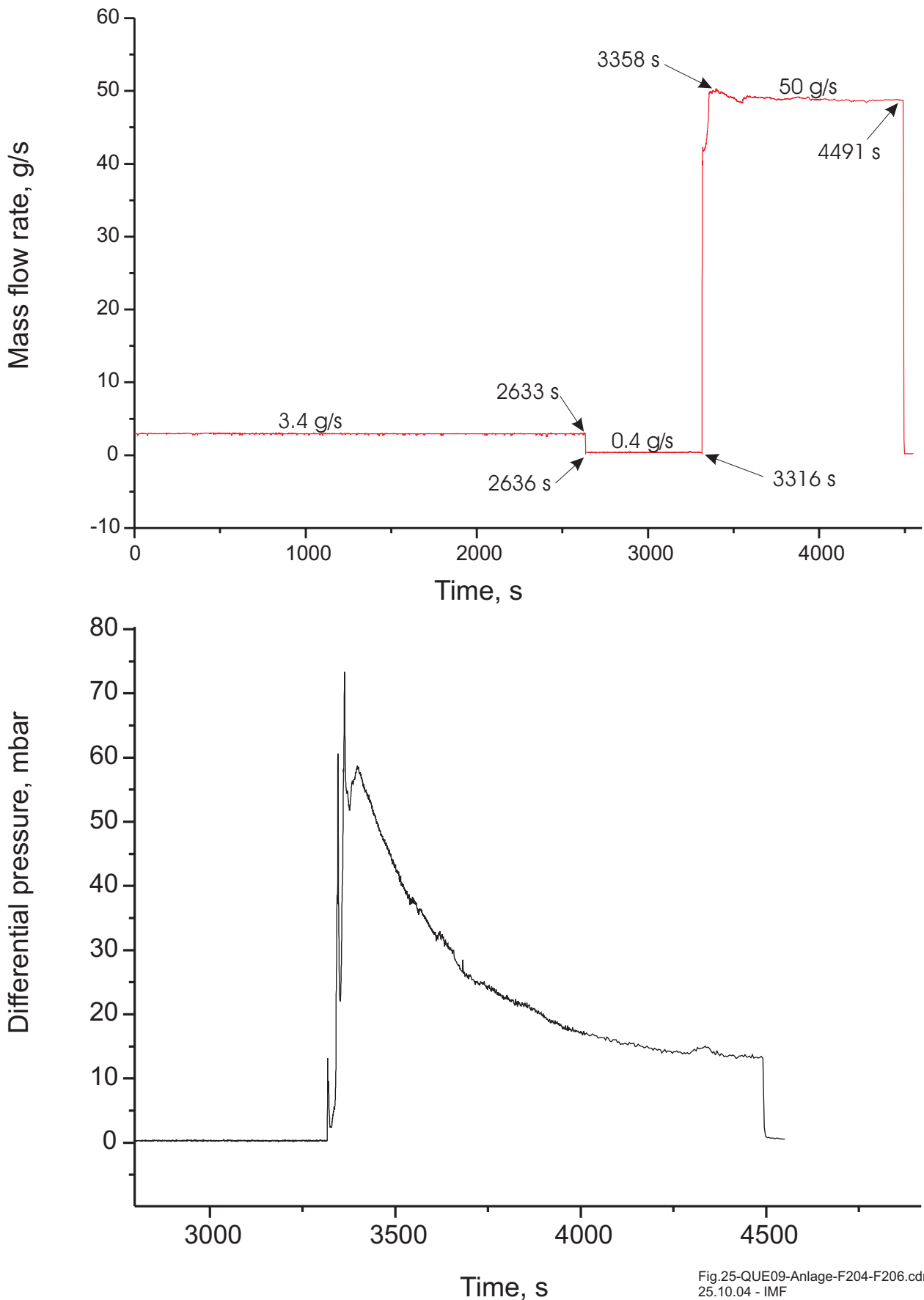


Fig.25-QUE09-Anlage-F204-F206.cdr
25.10.04 - IMF

Fig. 25: QUENCH-09; Steam flow rate based on flow meters F 205 and F 206 (before cooldown) and F 204 (cooldown), top, and qualitative flow rate of the offgas pipe (F 601) during the cooling phase, bottom.

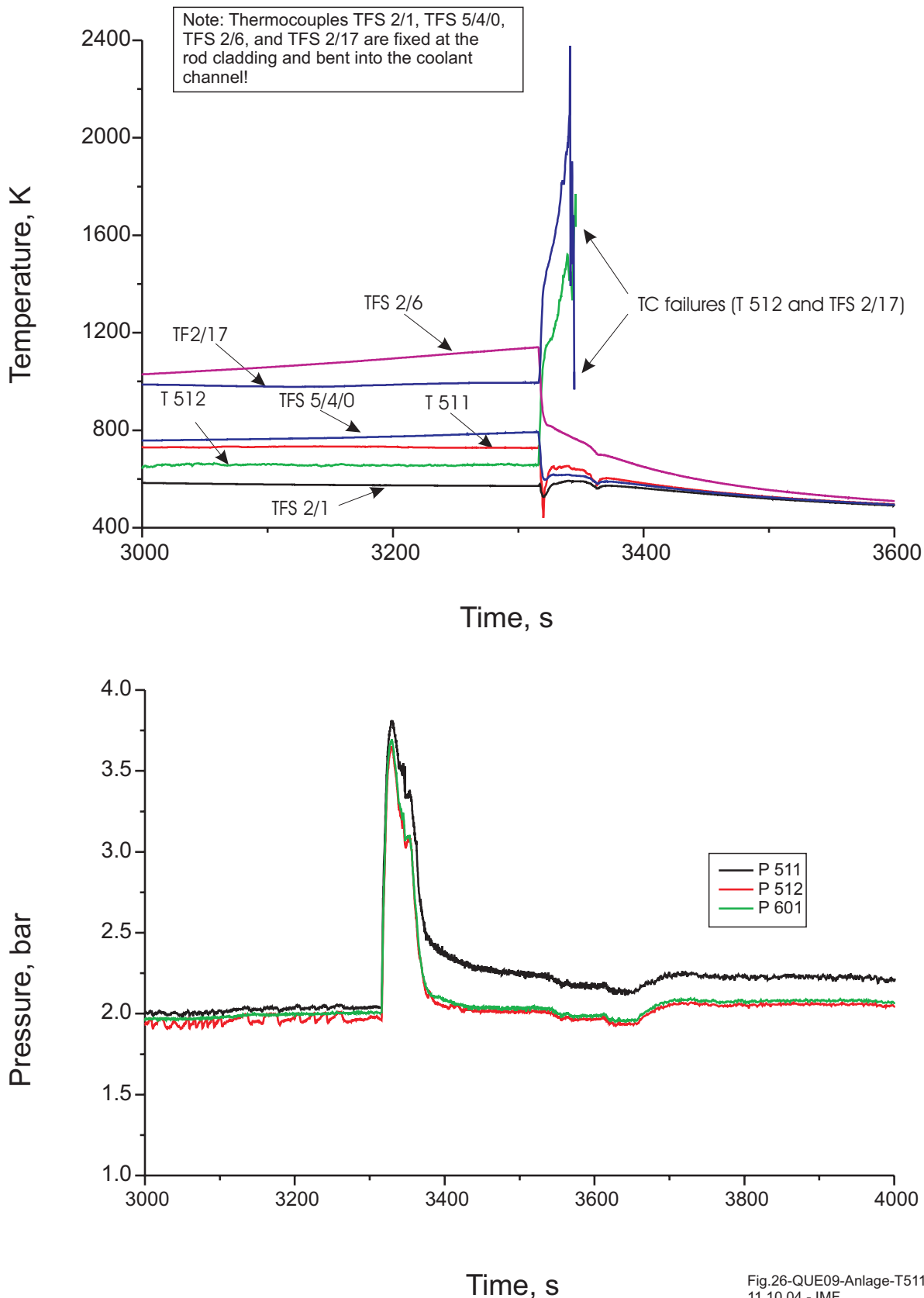


Fig.26-QUE09-Anlage-T511-P511.cdr
11.10.04 - IMF

Fig. 26: QUENCH-09; Coolant temperatures T 511 (bundle inlet), TFS 2/1 (-250 mm), TFS 5/4/0 (-50 mm), TFS 2/6 (250 mm), TFS 2/17 (1350 mm), and T 512 (bundle outlet, ~1350 mm), top, and system pressure at test section inlet (P 511), at outlet (P 512), and in the off-gas pipe (P 601) before and during the cooldown phase, bottom.

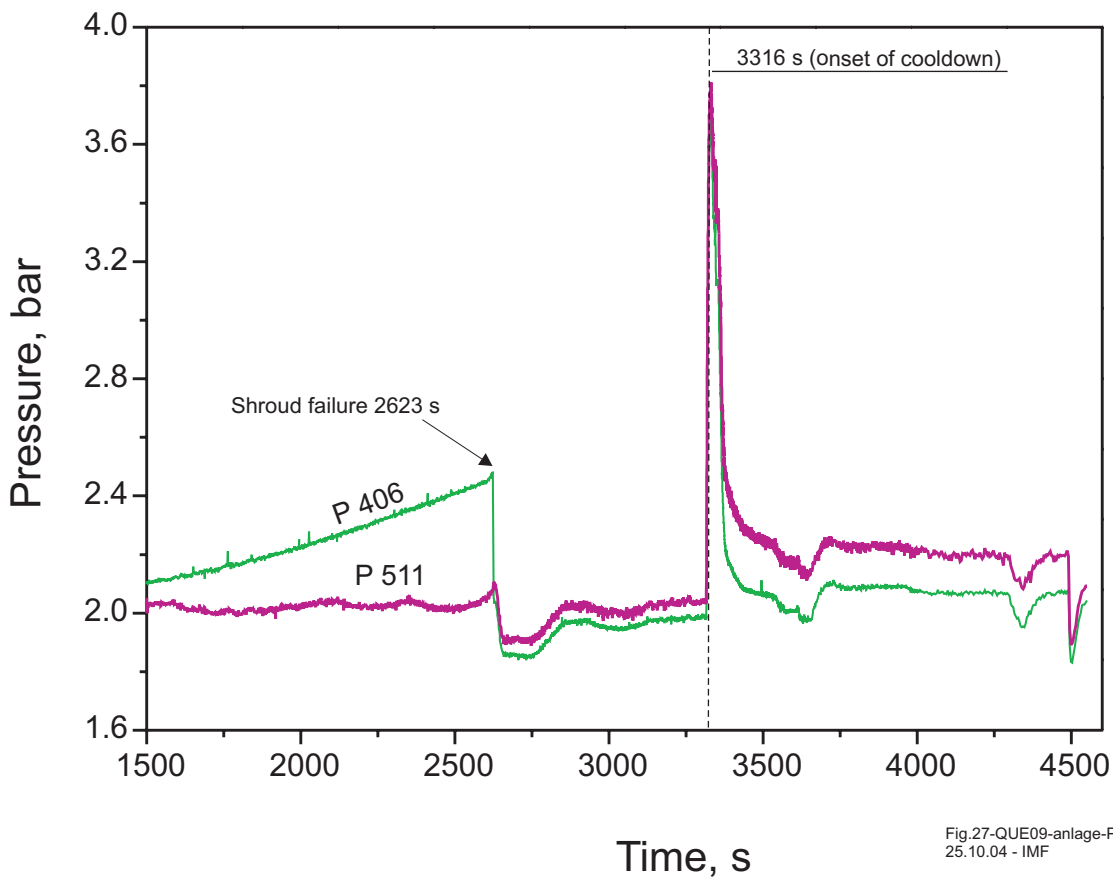
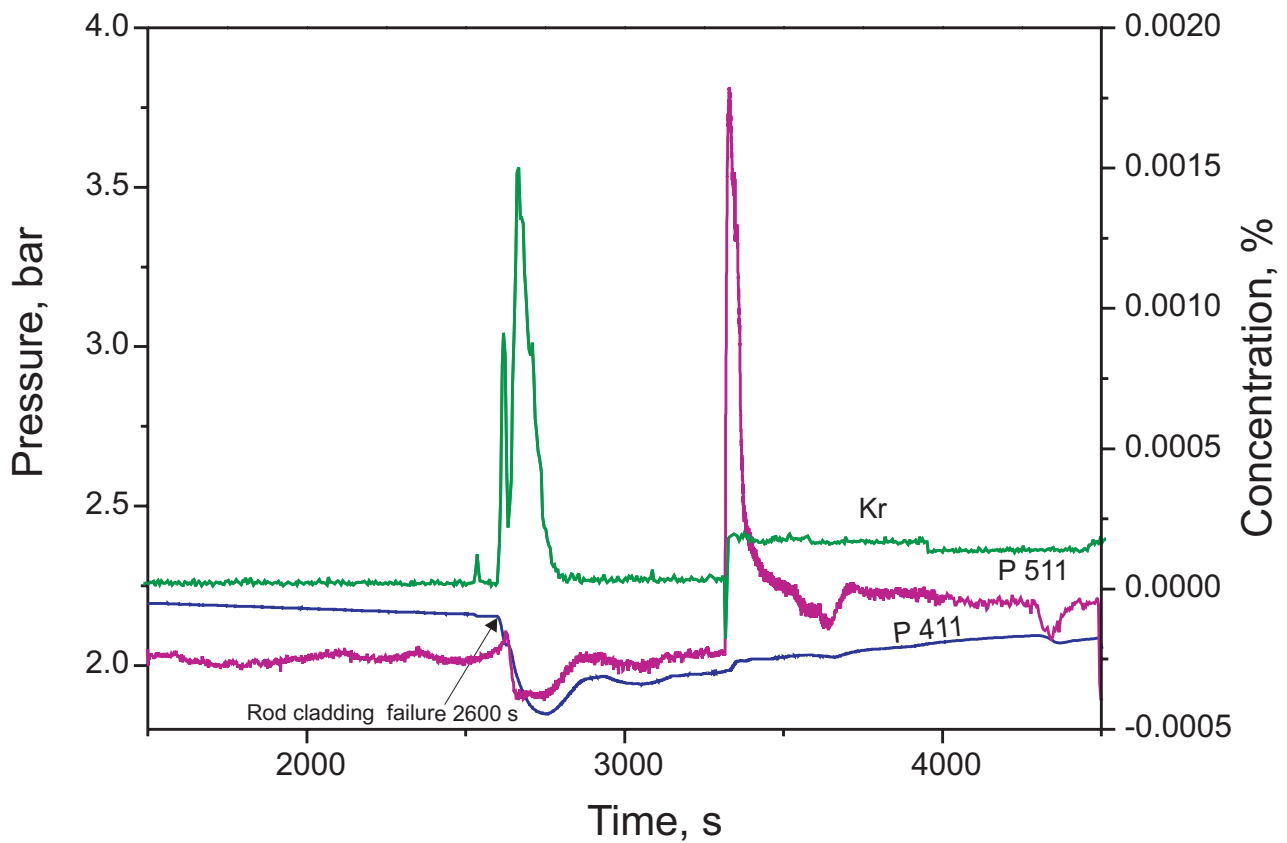


Fig.27-QUE09-anlage-P411-P406.cdr
25.10.04 - IMF

Fig. 27: QUENCH-09; Rod internal pressure (P 411) together with the pressure at the test section inlet (P 511), and the krypton concentration to demonstrate rod cladding failure, top, and shroud insulation pressure (P 406) together with the pressure at the test section inlet (P 511) to demonstrate shroud failure, bottom

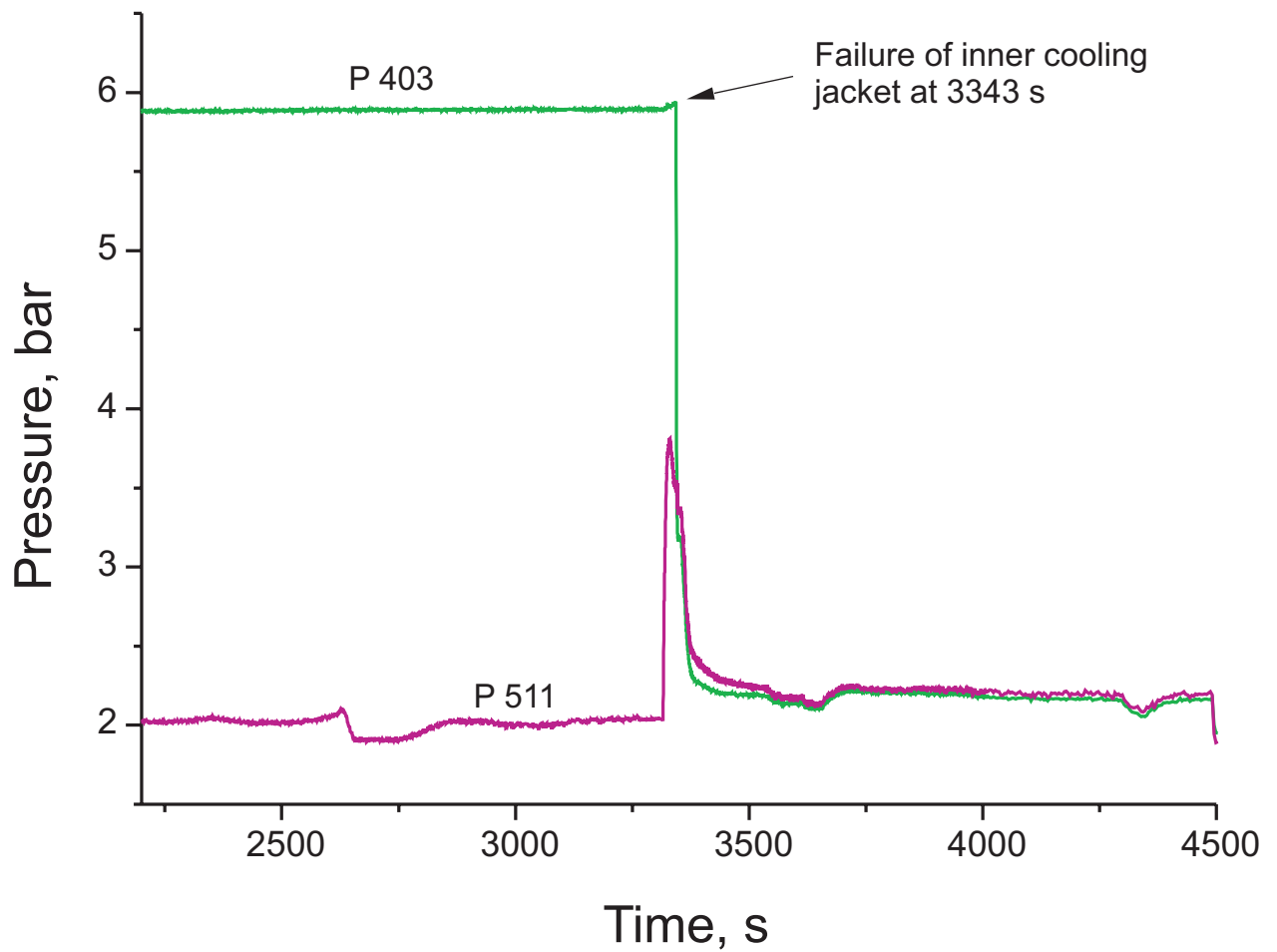


Fig.28-QUE09-anlage-P403.cdr
25.02.03 - IMF

Fig. 28: QUENCH-09; Argon coolant pressure of the cooling jacket (P 403) together with the pressure at the test section inlet (P 511) indicating failure of the inner cooling jacket

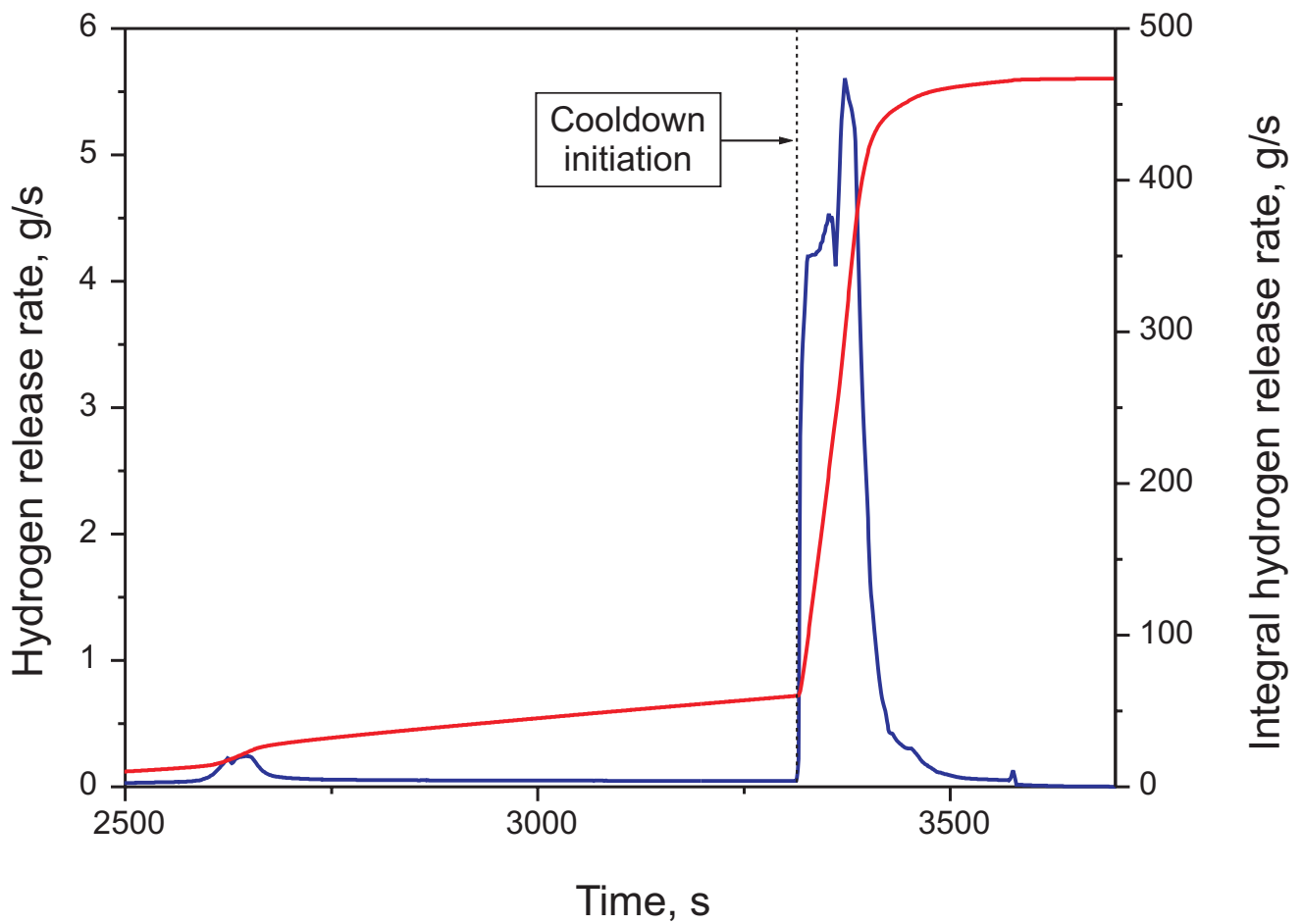


Fig.29-QUE09-anlage-Graph31+35.cdr
25.02.03 - IMF

Fig. 29: QUENCH-09; Hydrogen release rate together with the total H_2 measured by MS GAM 300

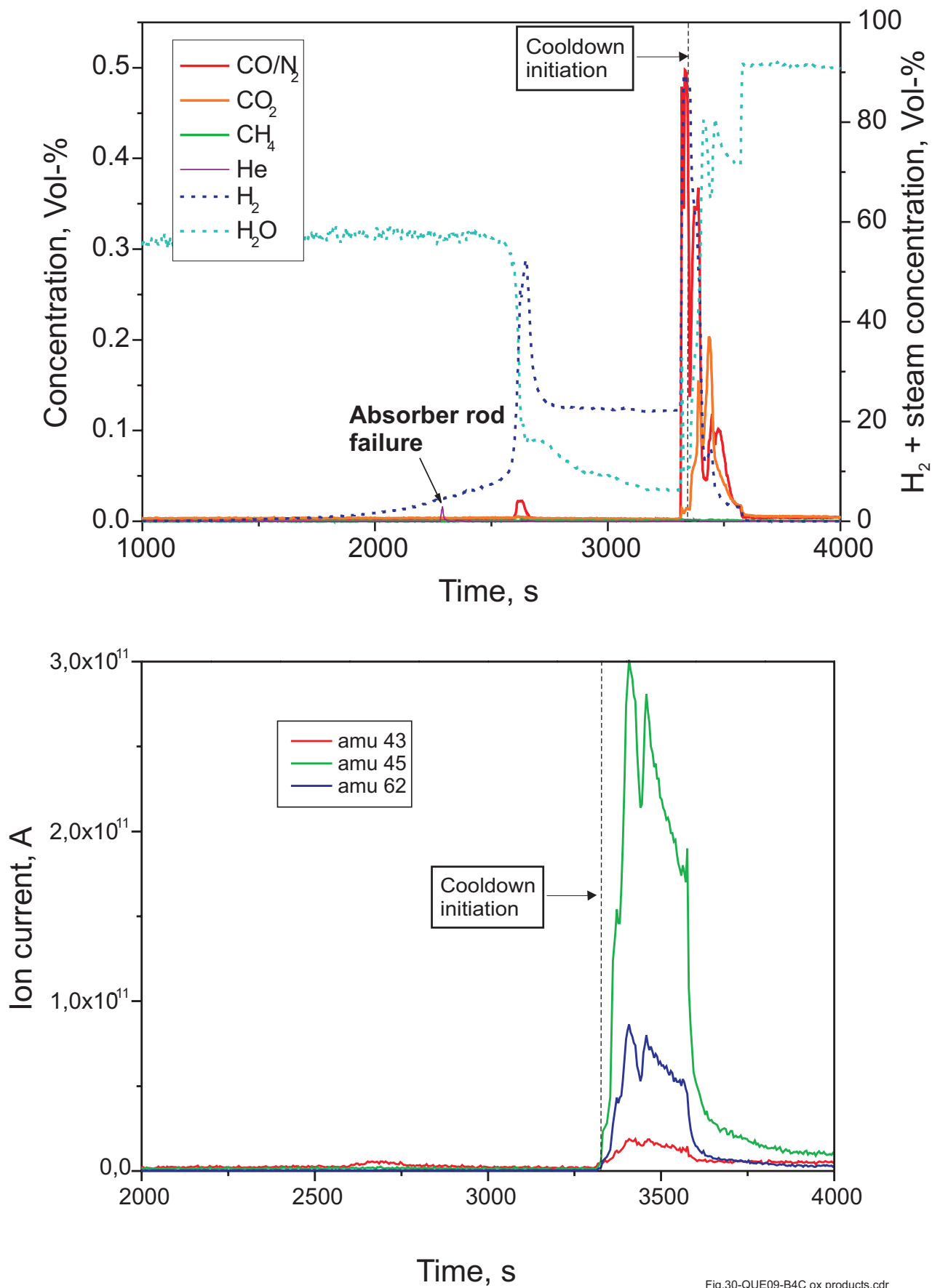


Fig.30-QUE09-B4C ox products.cdr
11.10.04 - IMF

Fig. 30: QUENCH-09; Boron carbide oxidation products CH₄, CO₂, and CO, top, and boric acids vs. time, bottom.

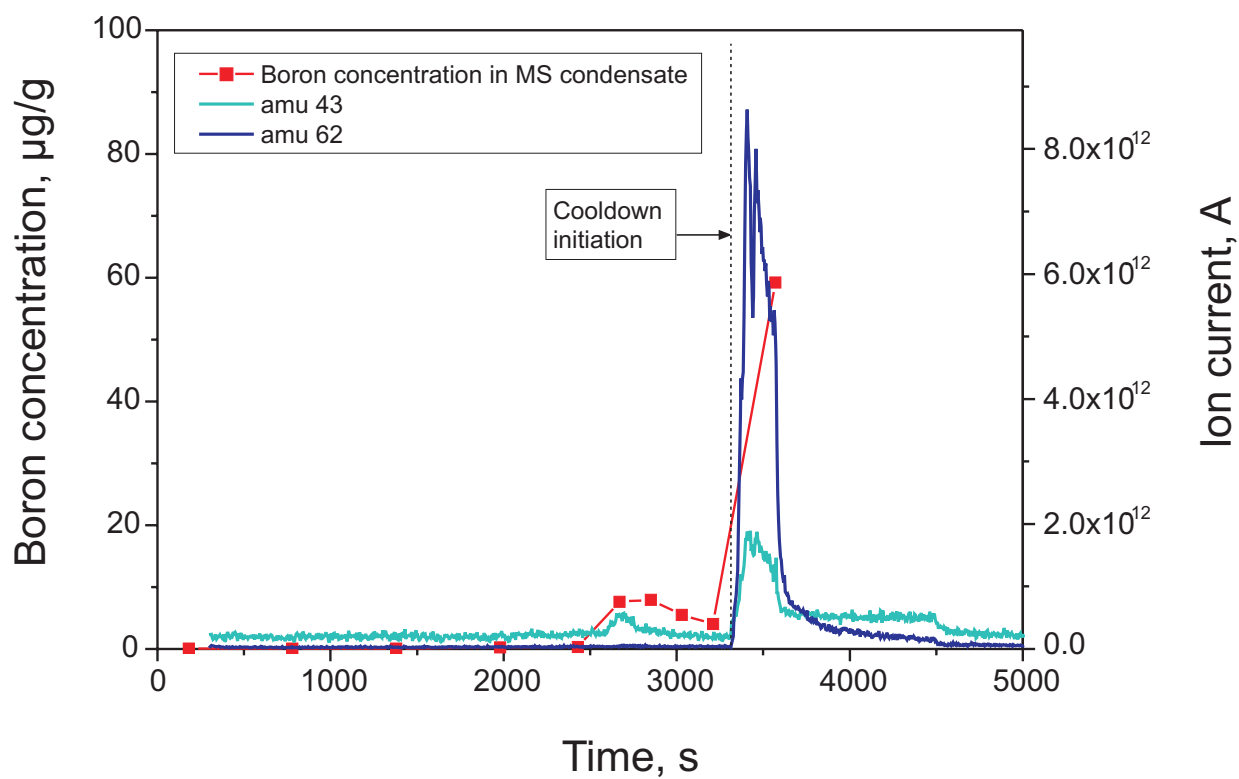


Fig.31-QUE09-Graph36.cdr
11.10.04 - IMF

Fig. 31: QUENCH-09; Boron concentration in the MS off-gas condensate together with the mass spectrometer signals at atomic masses 43 and 62.

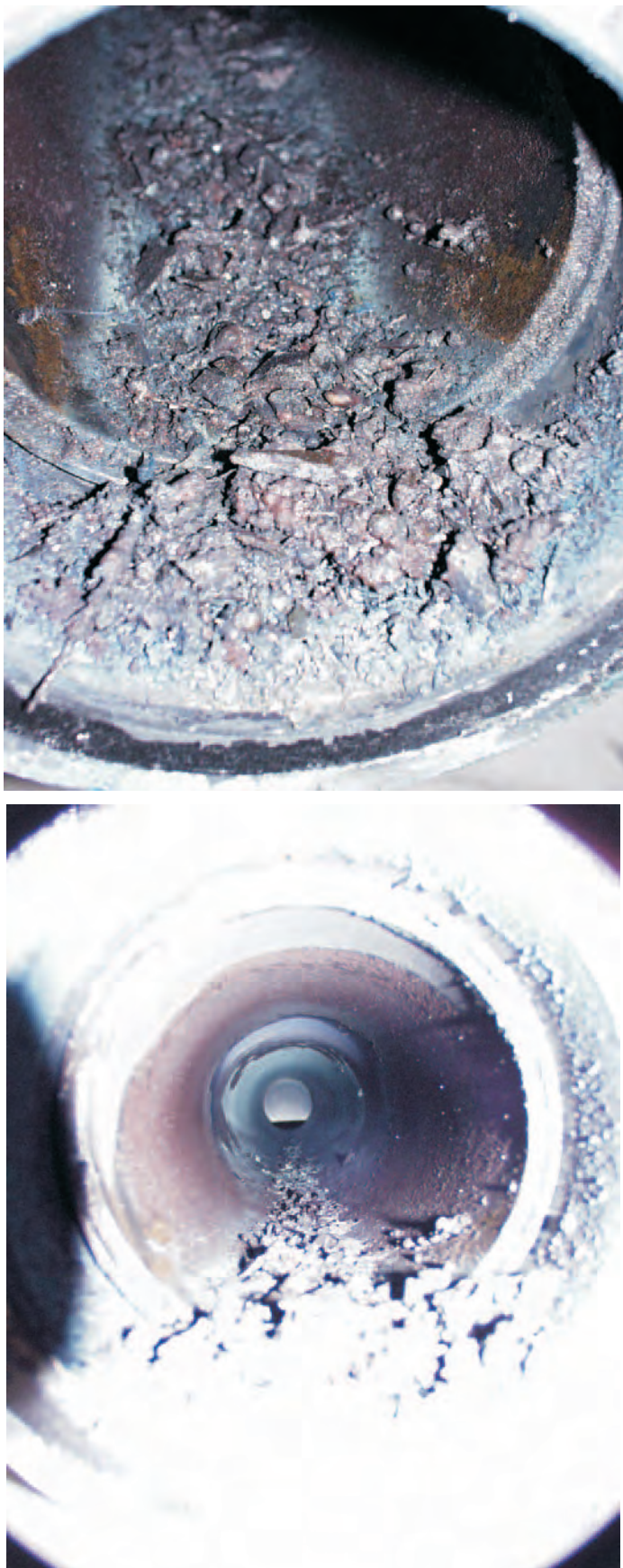


Fig.32-QUE09-Posttest off-gas pipe.cdr
26.02.03 - IMF

Fig. 32: QUENCH-09; Posttest view into the off-gas pipe demonstrating debris transported from the upper bundle region

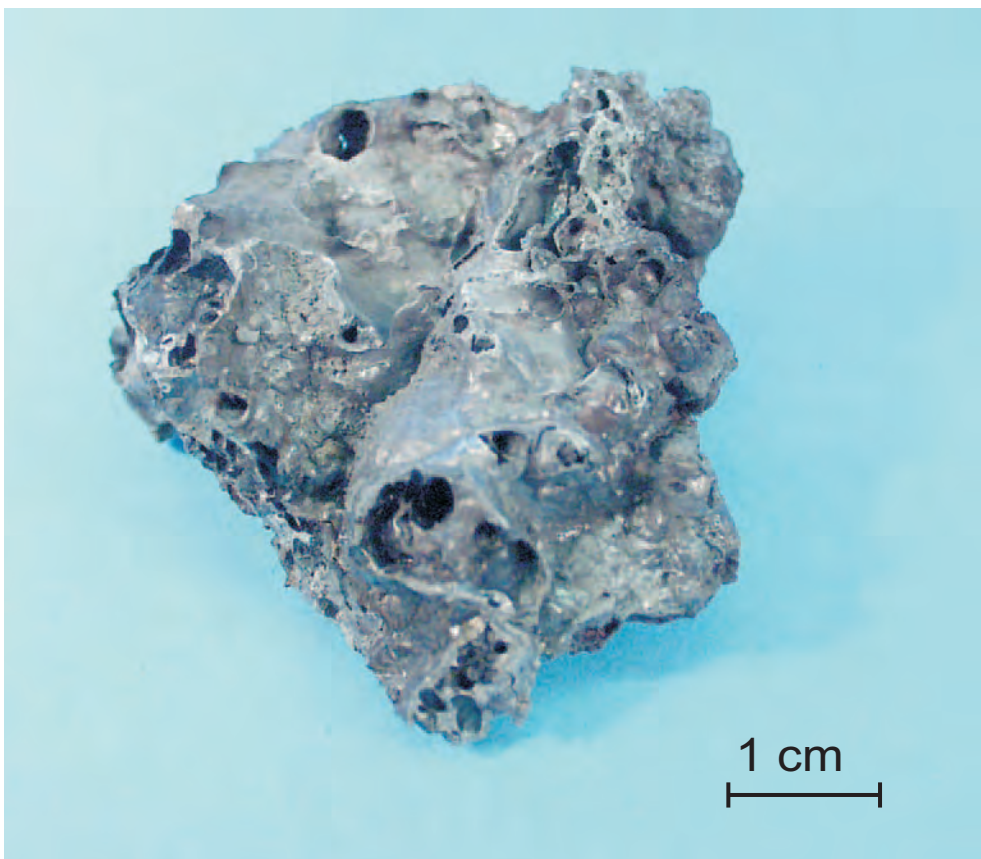
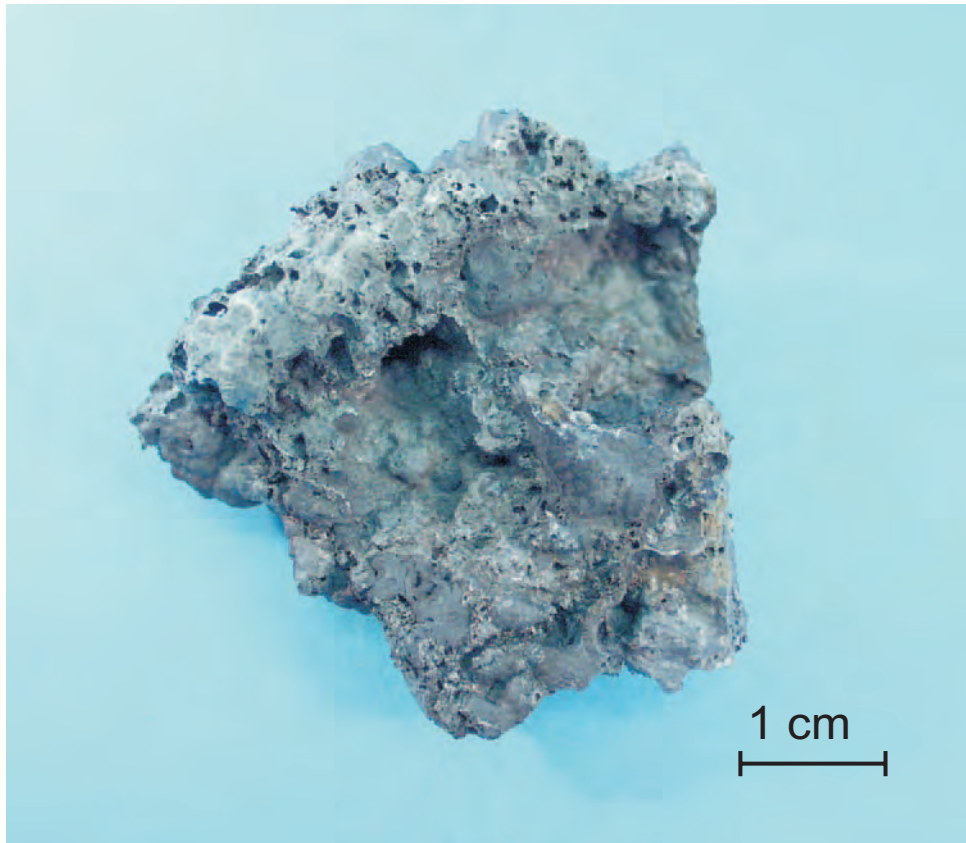


Fig.33-QUE09-Posttest debris.cdr
28.04.03 - IMF

Fig. 33: QUENCH-09; Debris taken posttest from bundle elevation 1300-1400 mm. Two views of the heaviest sample with a weight of approx. 55 g.



Fig.34-QUE09-Posttest 0 and 270 degrees.cdr
25.02.03 - IMF

Fig. 34: QUENCH-09; Posttest appearance of bundle and shroud from around 500 mm upward, 0° (left) and 270° (right) orientation



Fig.35-QUE09-Posttest 90 degrees.cdr
25.02.03 - IMF

Fig. 35: QUENCH-09; Posttest appearance of bundle and shroud from about 500 mm upward, 90° orientation



Fig.36-QUE09-Posttest 180 degrees.cdr
07.10.04 - IMF

Fig. 36: QUENCH-09; Posttest appearance of bundle and shroud at 180° orientation from about 500 mm upward, left, and of the topmost zone, right

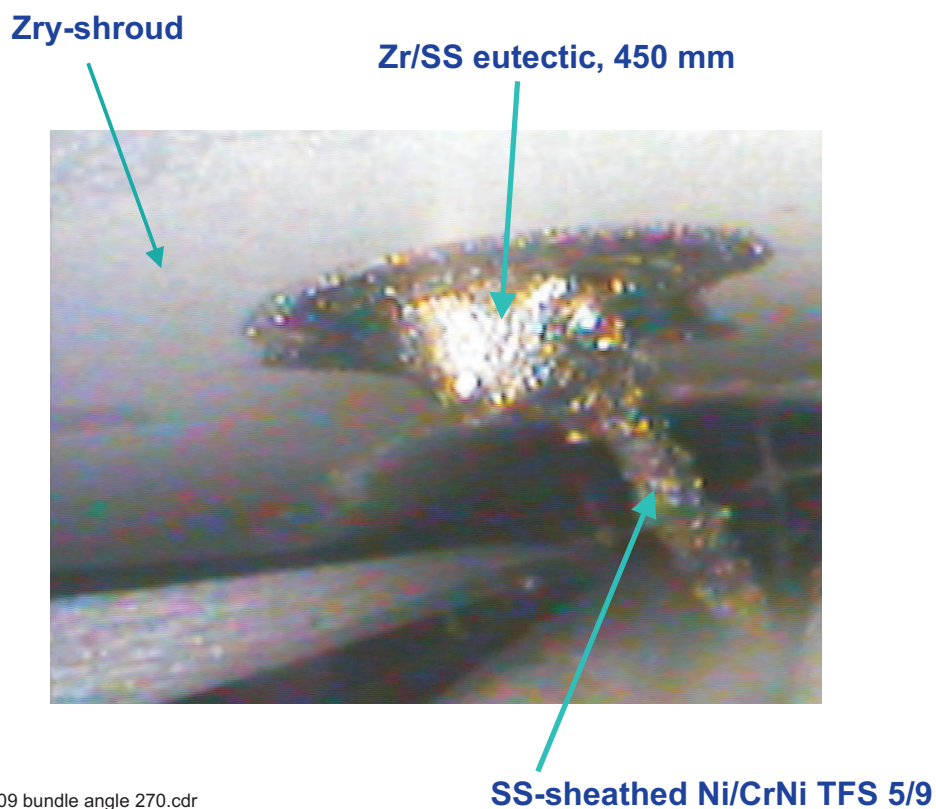
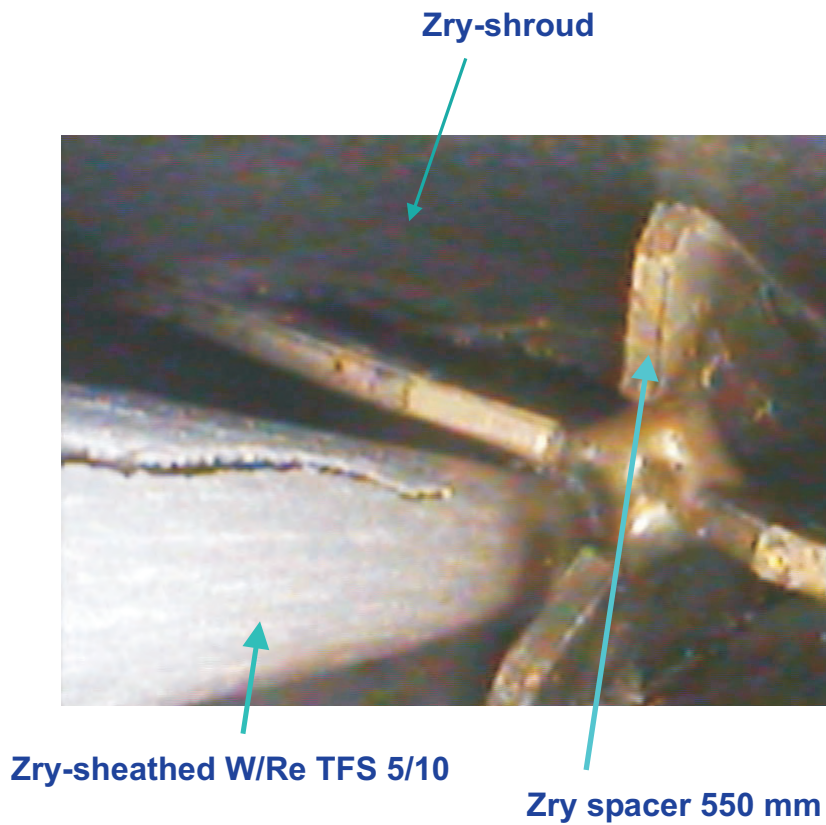


Fig.37-QUE09 bundle angle 270.cdr
07.10.04 - IMF

Fig. 37: QUENCH-09; Posttest photographs from inside the test bundle at axial levels of approx. 450 mm (bottom) and 550 mm (top).

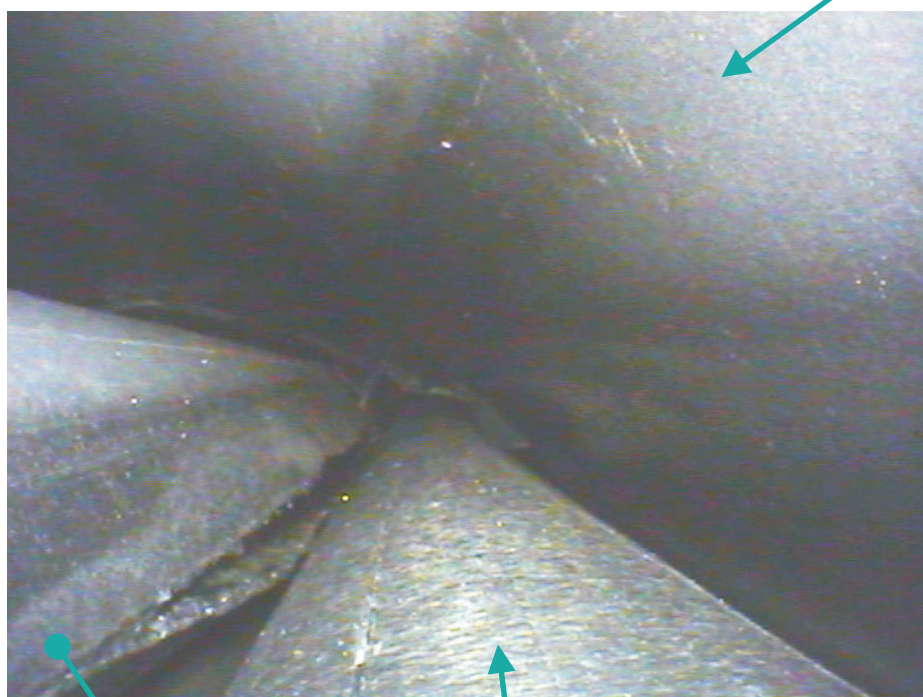
shroud



rod 17

rod 16, 500 mm

shroud



rod 17, 490 mm

rod 16

Fig.38-QUE09 bundle angle 90-1.cdr
23.03.03 - IMF

Fig. 38: QUENCH-09; Posttest photographs from inside the test bundle demonstrating rod cladding rupture at approx. 490 mm (bottom) and 500 mm (top)

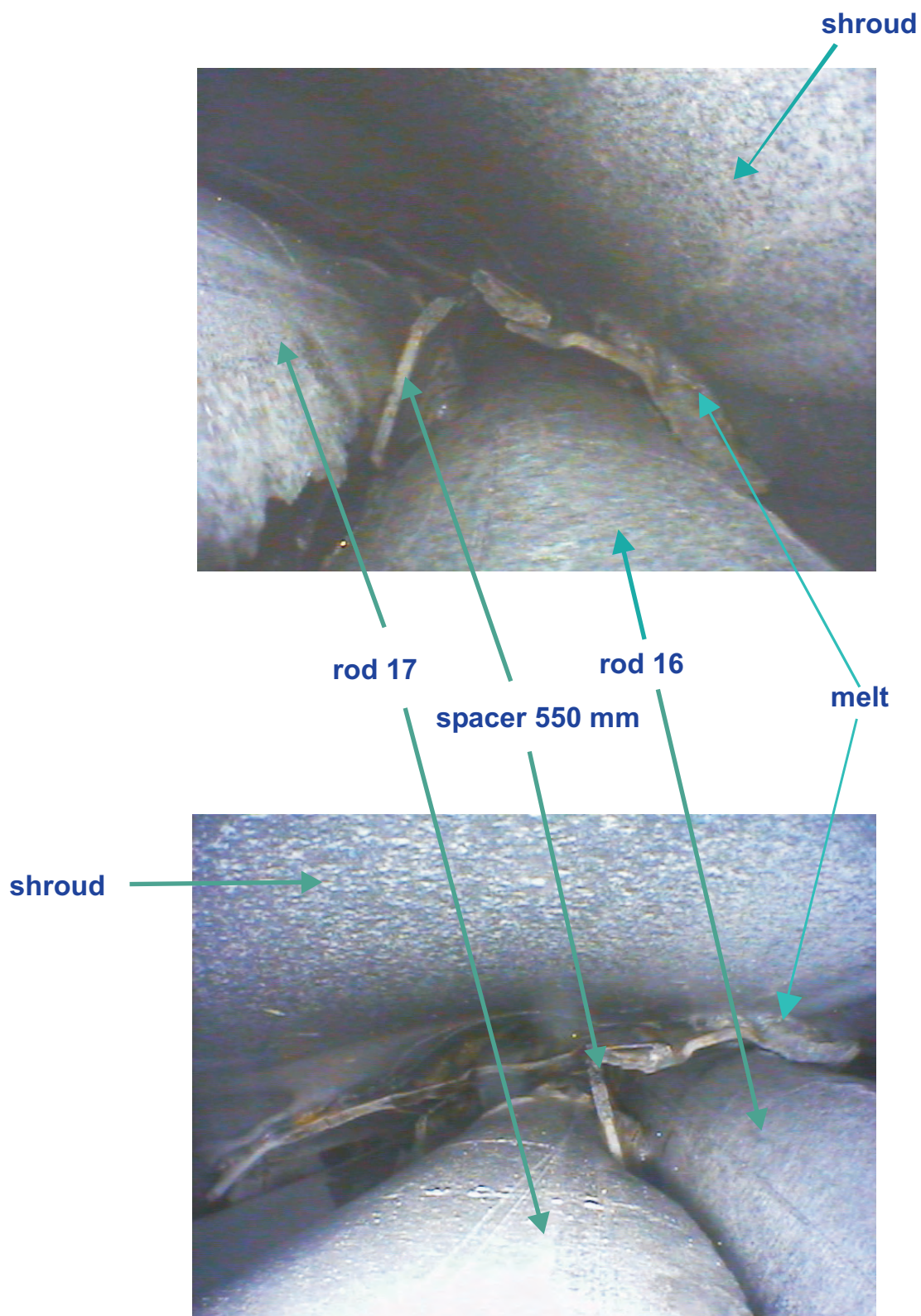
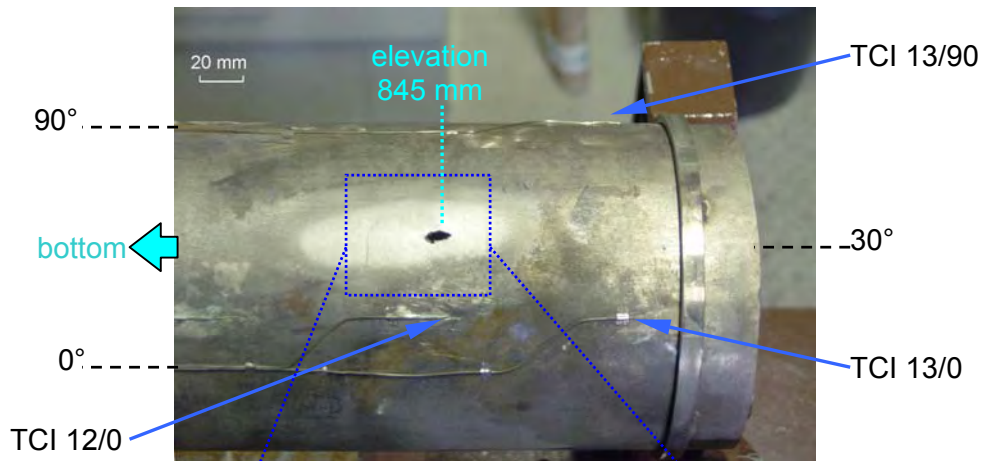
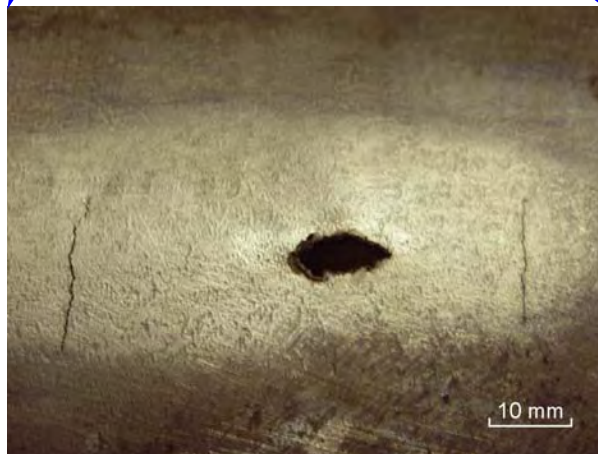


Fig.39-QUE09 bundle angle 90-2.cdr
07.10.04 - IMF

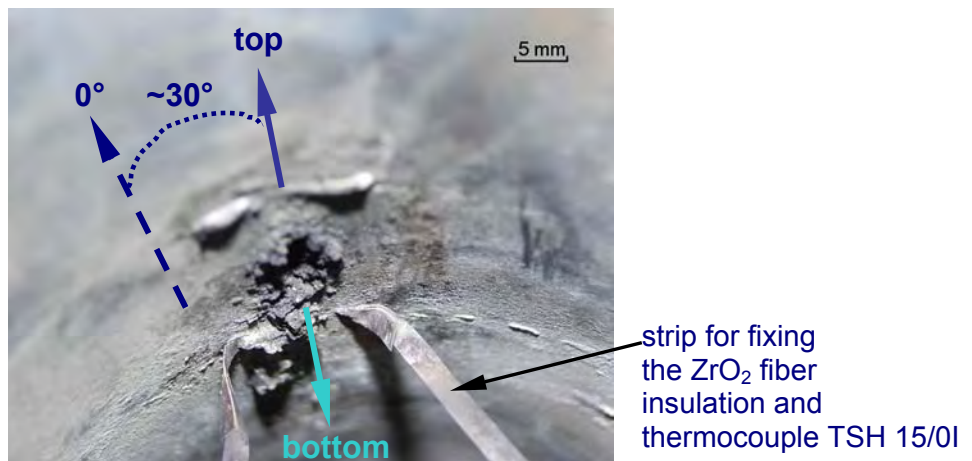
Fig. 39: QUENCH-09; Posttest photographs from inside the test bundle at 540 mm elevation.



View of the inner cooling jacket (top part)



Failure of the inner cooling jacket due to interaction of Zr with SS (~940 °C);
 area of the hole: 39.6 mm²



Look into the inside of the inner cooling jacket

Fig 40-QUE09 cooling jacket.doc
 30.09.04 - IMF

Fig. 40: QUENCH-09; Photographs of the failure location of the inner cooling jacket.

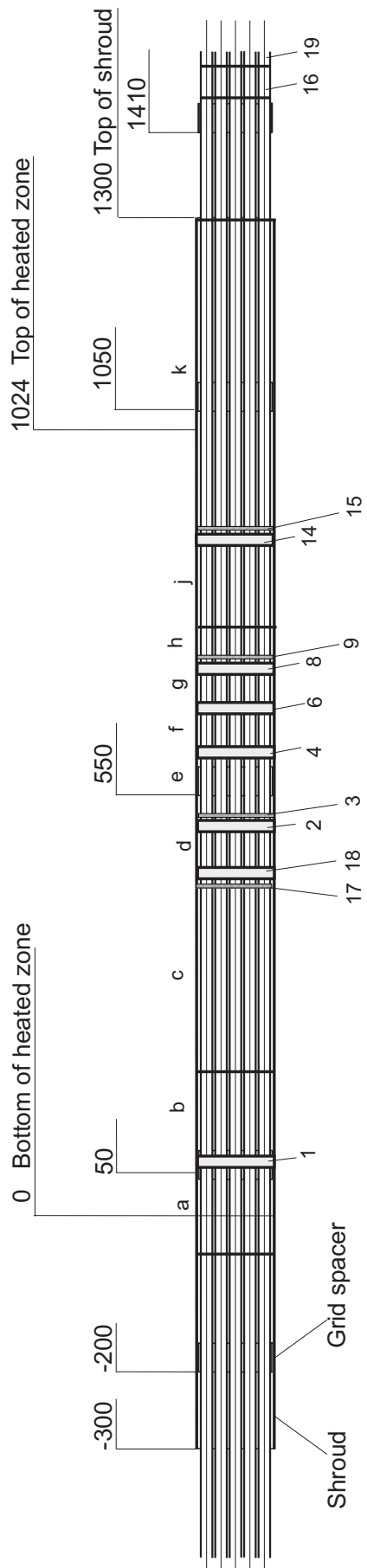


Fig 41-QUE09 Schnittplan.cdr
21.05.03 - IMF

Fig. 41: QUENCH-09; Sectioning of the test bundle

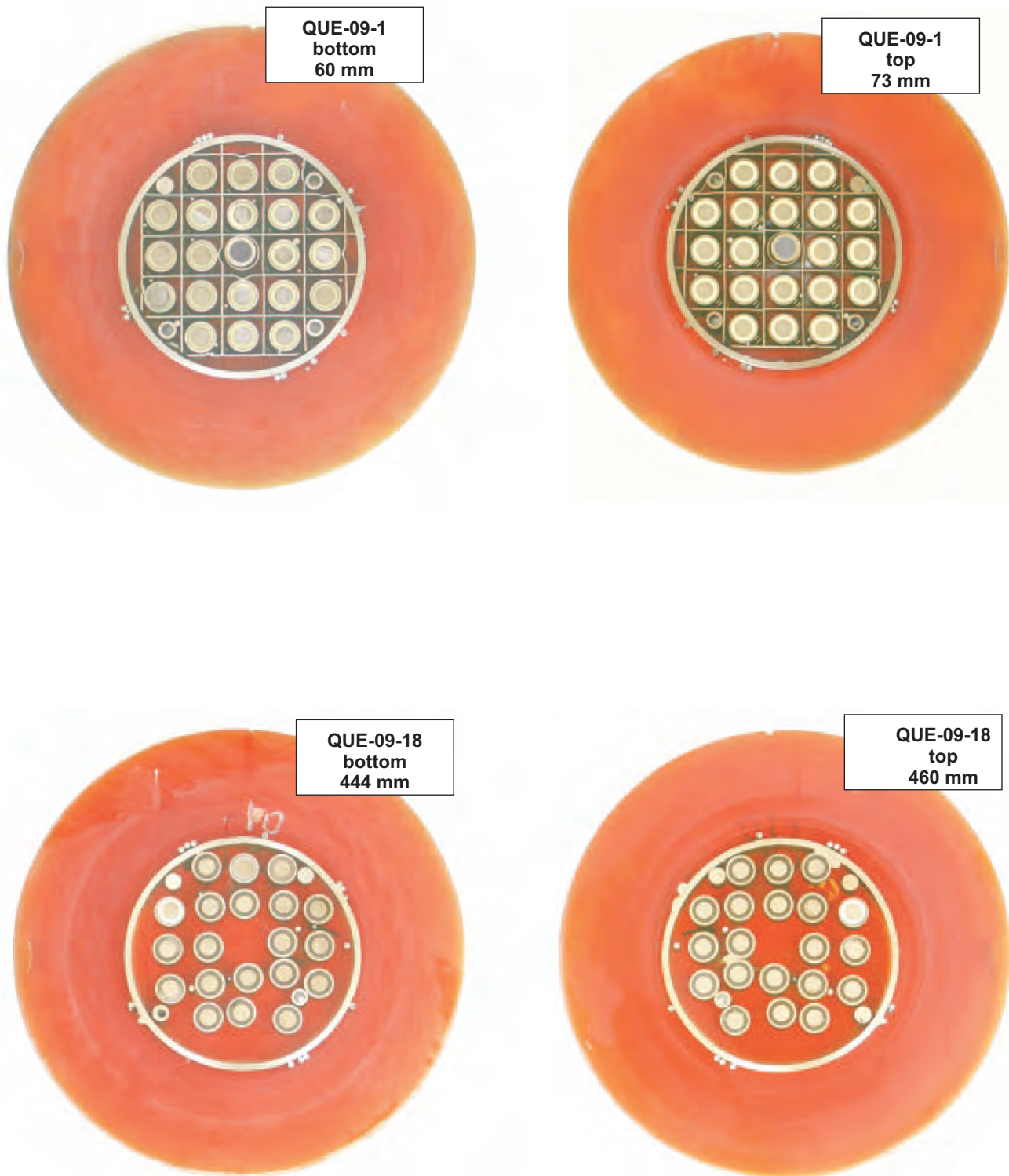


Fig 42-QUE09 Cross section1+18.cdr
30.10.03 - IMF

Fig. 42: QUENCH-09; Cross sections at 60 mm, 73 mm, 444 mm, and 460 mm

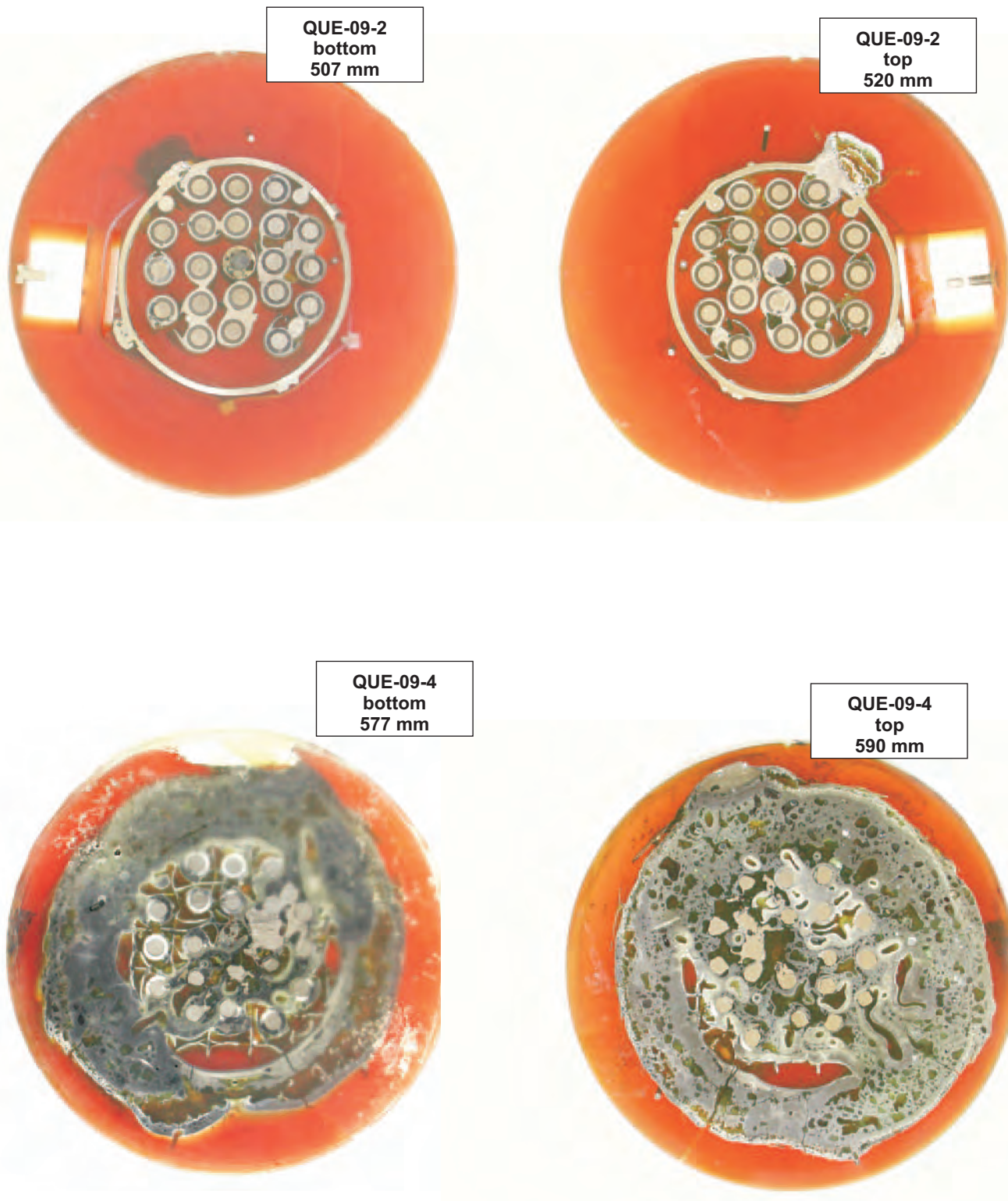


Fig 43-QUE09 Cross section2+4.cdr
27.10.03 - IMF

Fig. 43: QUENCH-09; Cross sections at 507 mm, 520 mm, 577 mm, and 590 mm



Fig 44-QUE09 Cross section6+8.cdr
27.10.03 - IMF

Fig. 44: QUENCH-09; Cross sections at 637 mm, 650 mm, 687 mm, and 700 mm

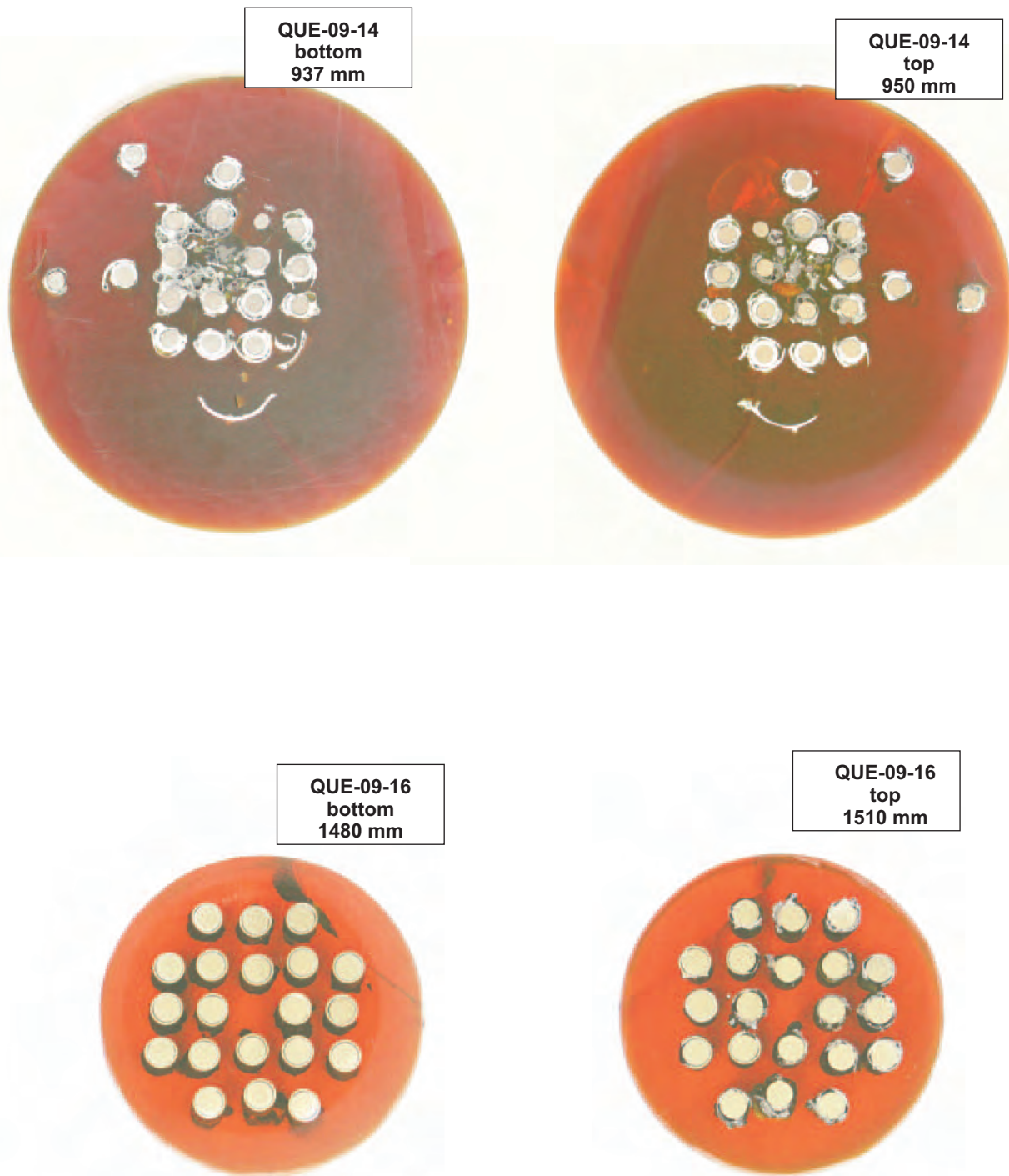


Fig 45-QUE09 Cross section14+16.cdr
27.10.03 - IMF

Fig. 45: QUENCH-09; Cross sections at 937 mm, 950 mm, 1480 mm, and 1510 mm

Bottom of cross section slab, 60 mm elevation, inverted to top view

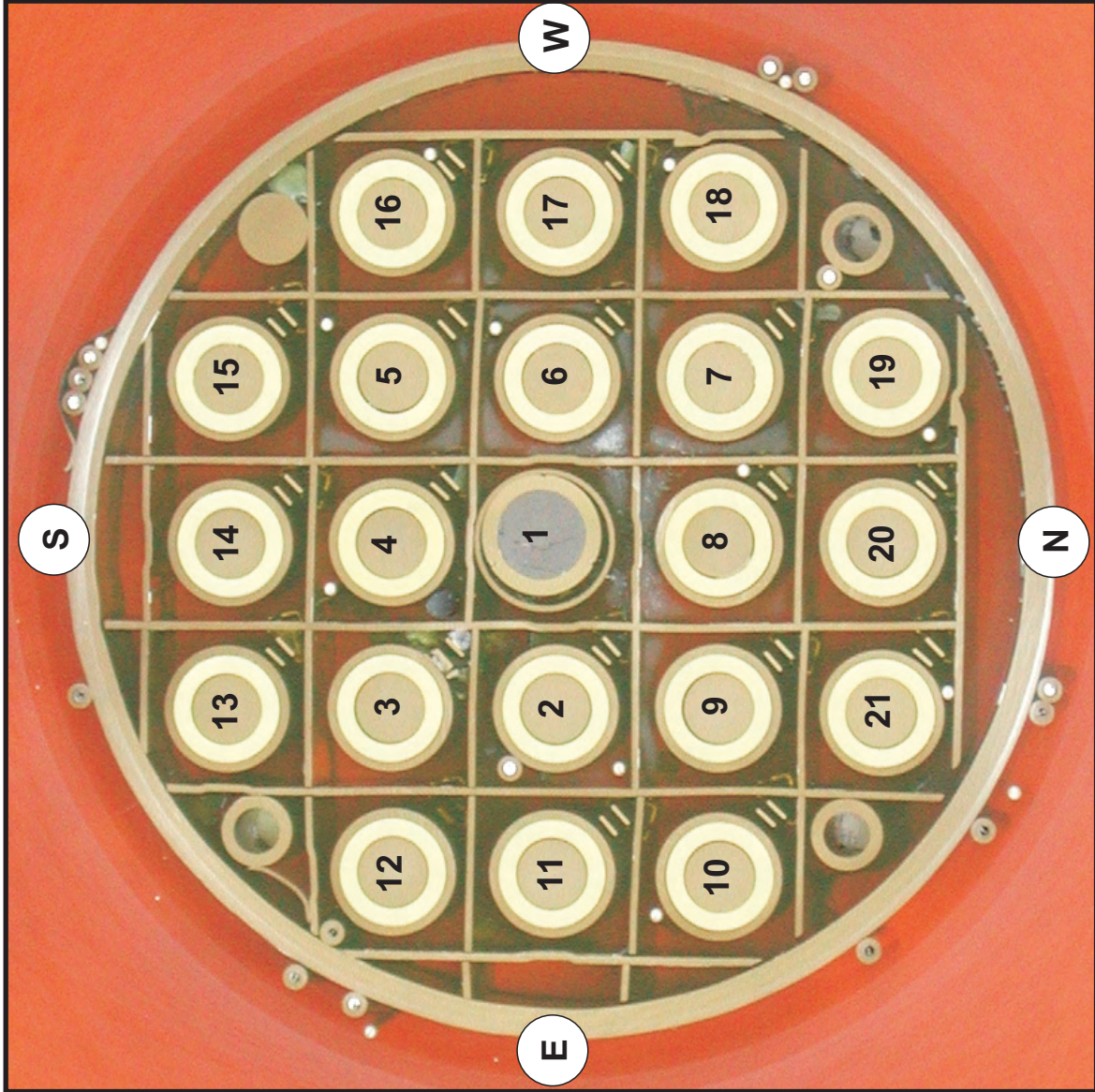
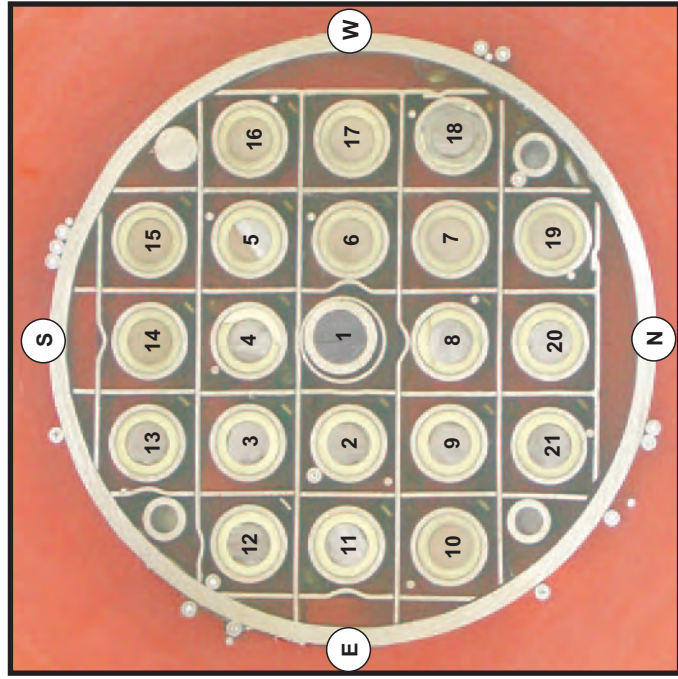


Fig. 46: QUENCH-09; Cross section at 73 mm bundle elevation (QUE-09-1); overview from top

Bottom of cross section slab, 444 mm elevation, inverted to top view

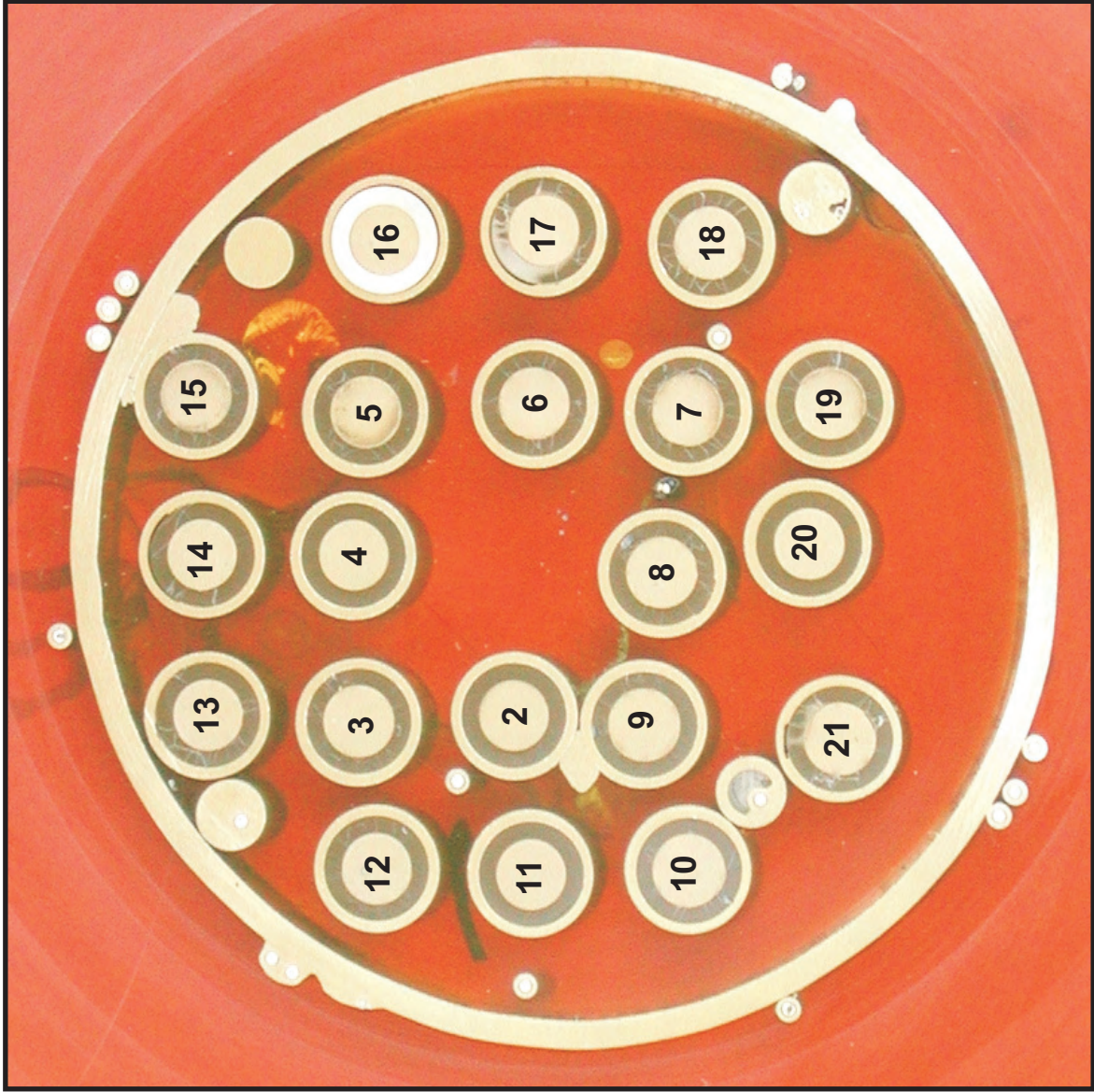
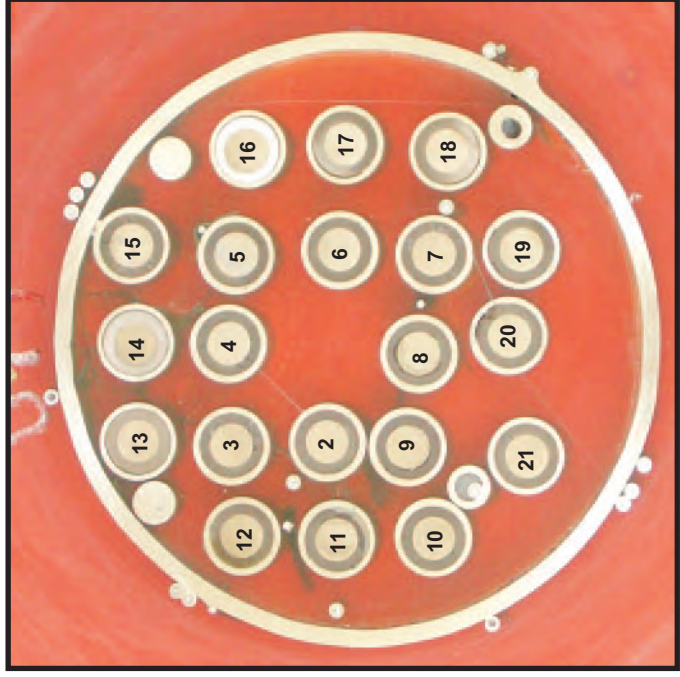
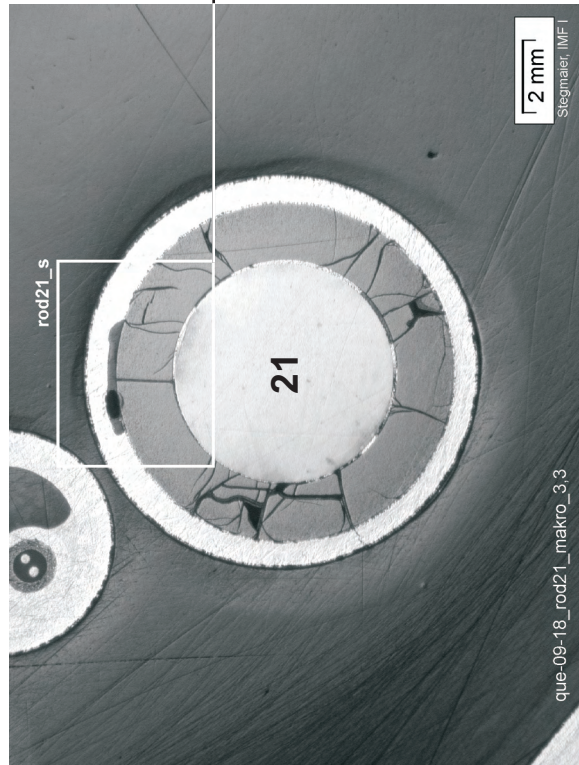
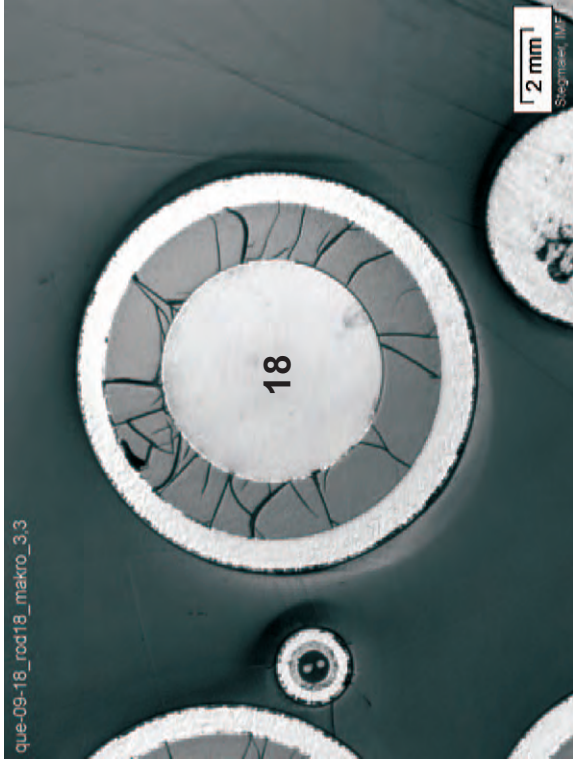


Fig. 47: QUENCH-09; Cross section at 460 mm bundle elevation (QUE-09-18); overview from top



Filling of corner rod tubes at SE (left) and NW (right) by relocated melt



Partial filling of NE corner rod

Void formation within the adjacent rod #21

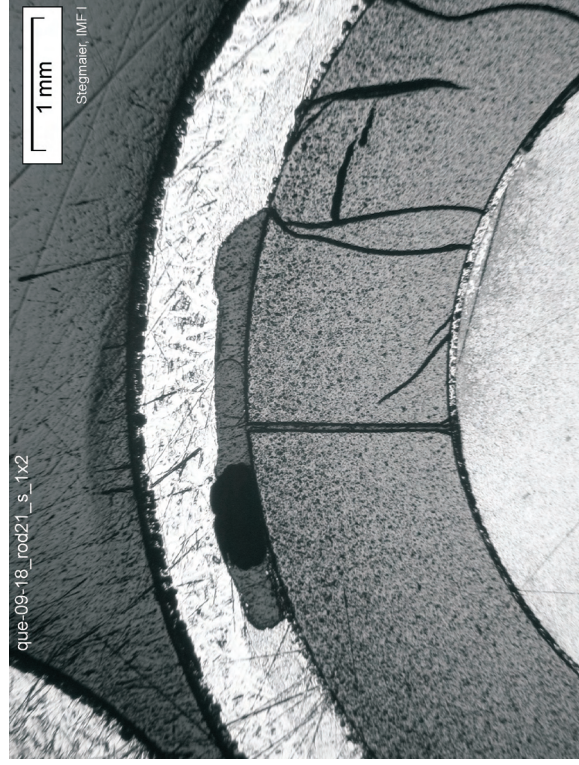
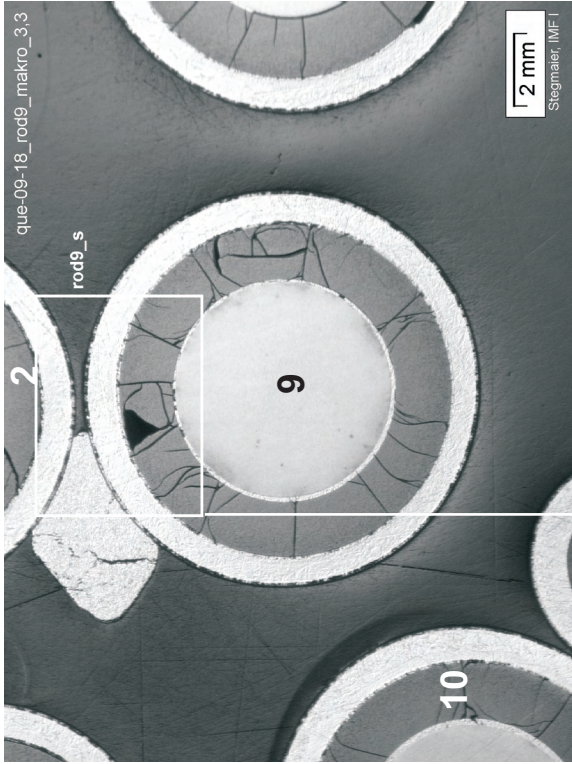
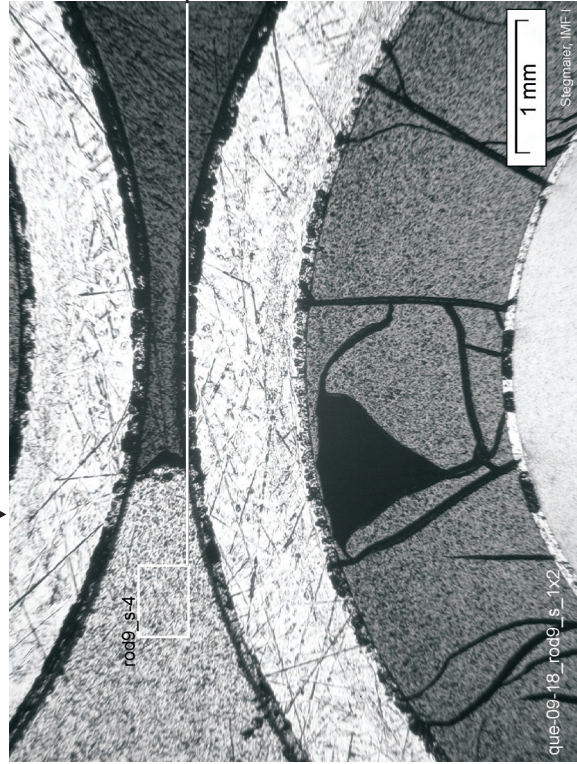


Fig. 48: QUENCH-09; Cross section at 460 mm bundle elevation (QUE-09-18); melt relocation at bundle corners



Melt between rods #2 and #9 (left) and between rod #15 and shroud (right)



Details of rod #9 with adjacent rod #2 and melt lump

Microstructure of melt



Fig. 49: QUENCH-09; Cross section at 460 mm bundle elevation (QUE-09-18); small melt lumps

Bottom of cross section slab, 507 mm elevation, inverted to top view

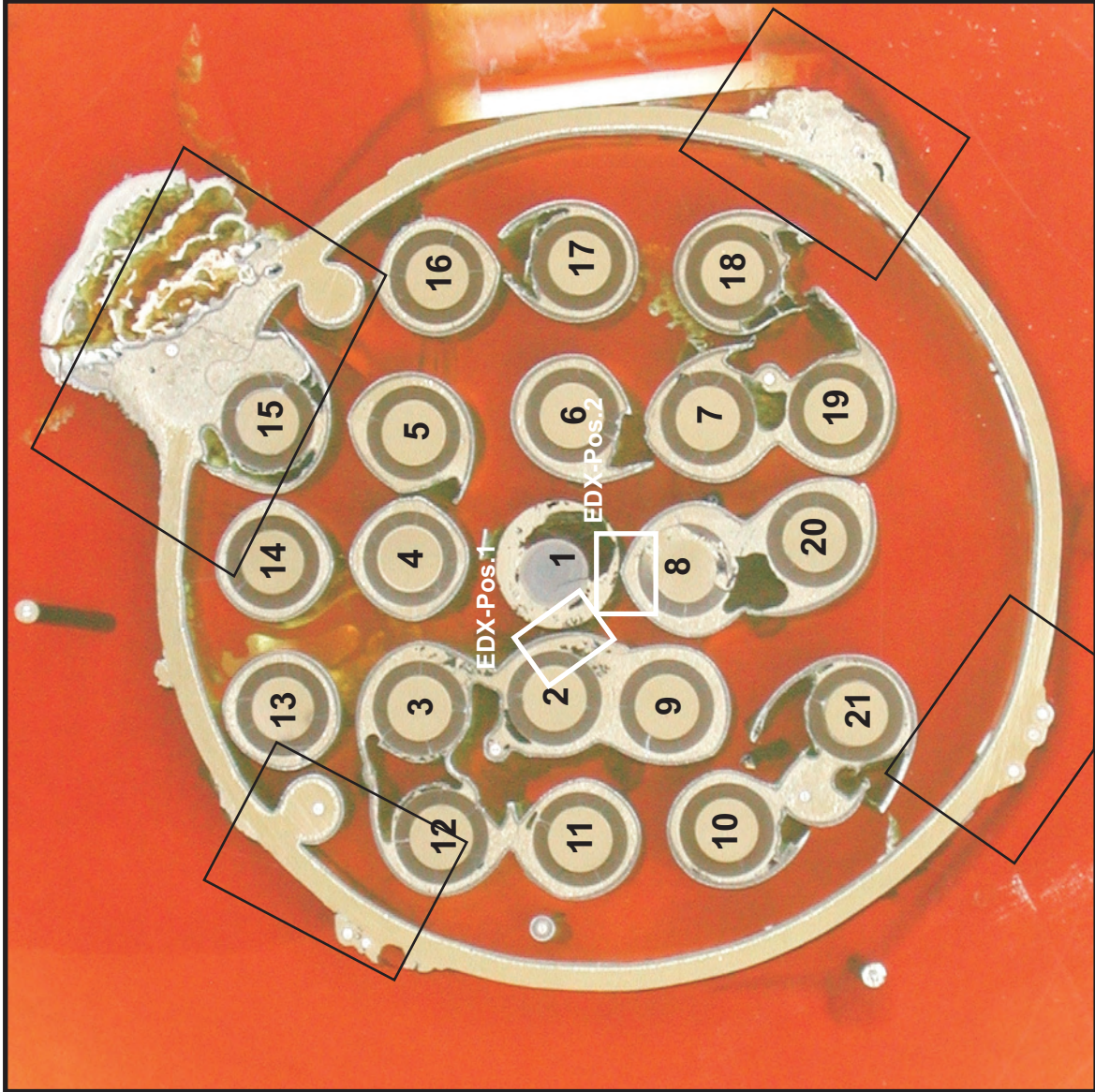
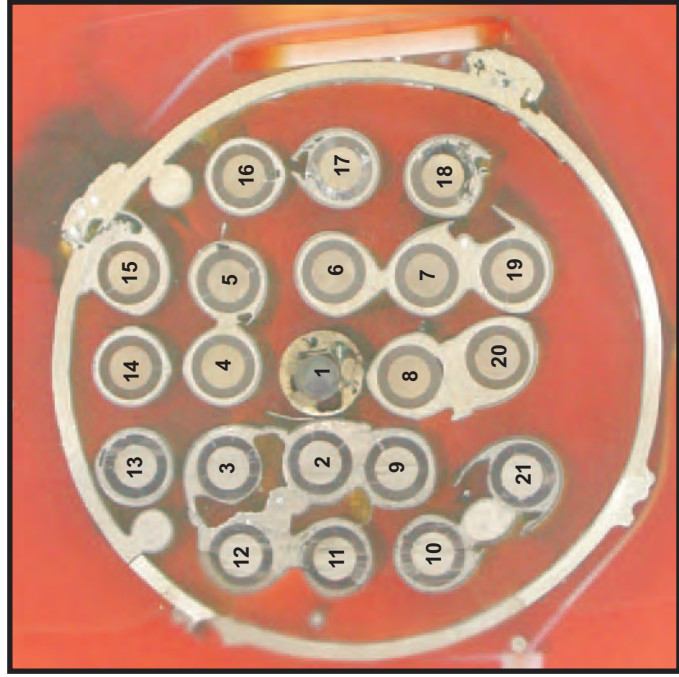
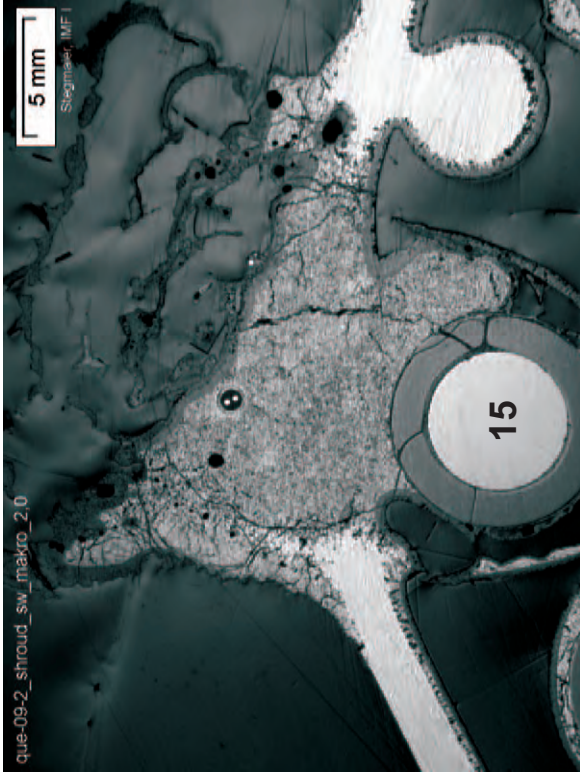


Fig. 50: QUENCH-09; Cross section at 520 mm bundle elevation (QUE-09-2); overview from top



SE

SW



NE

NW

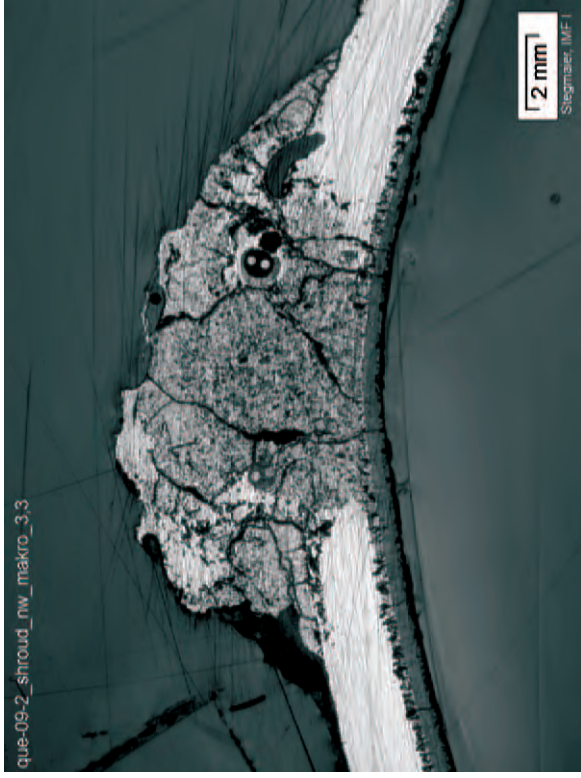


Fig. 51: QUENCH-09; Cross section at 520 mm elevation (QUE-09-2); melt accumulation (left) and shroud melting (right) related to external shroud thermocouples

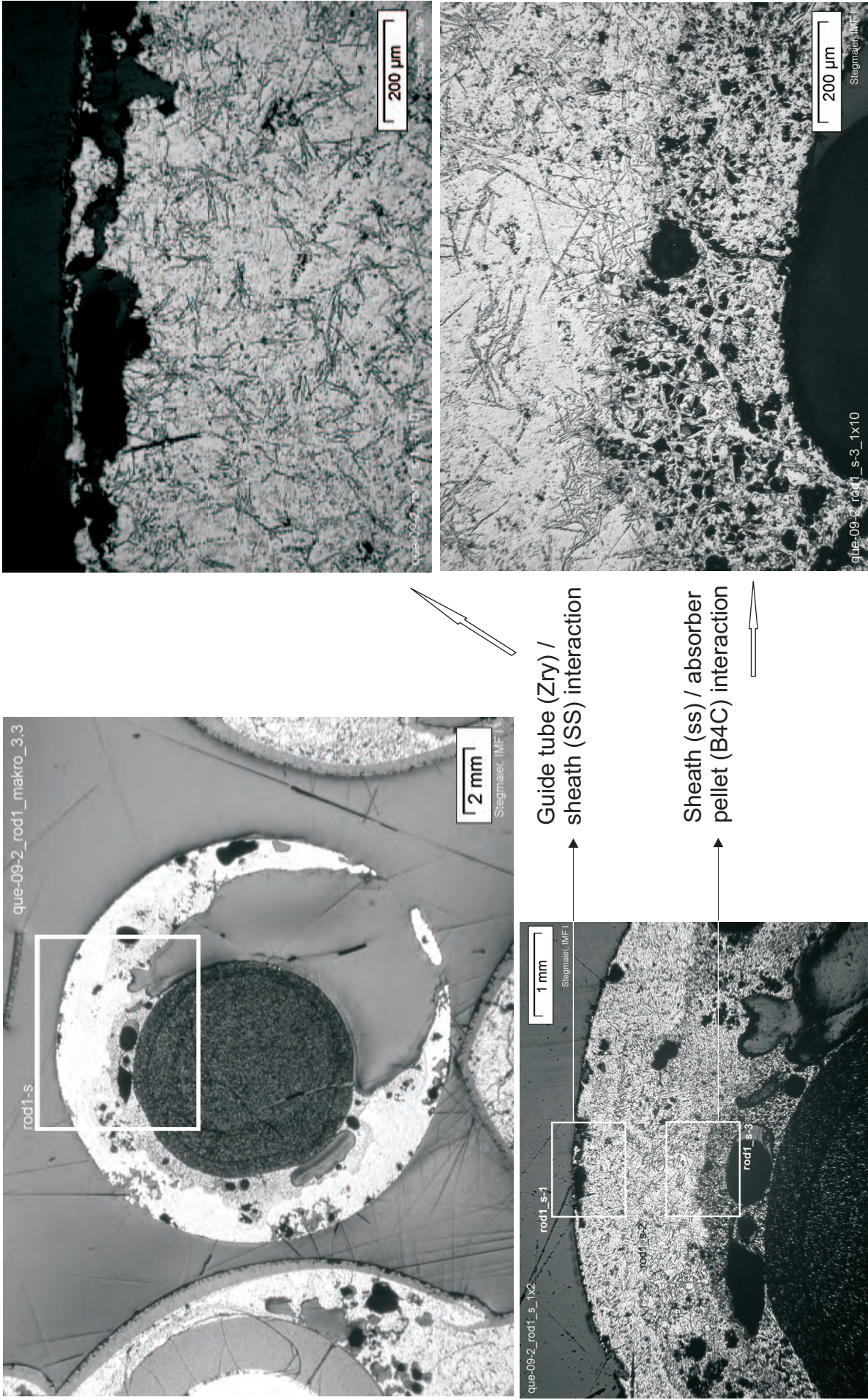
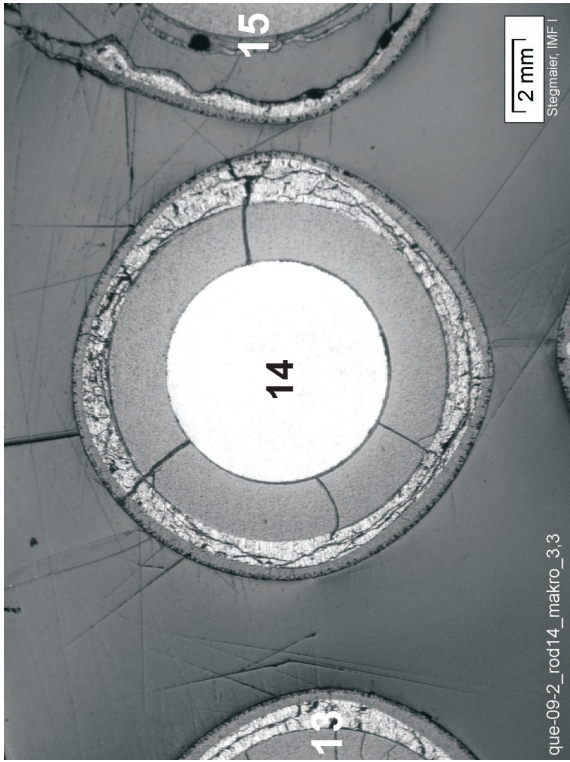
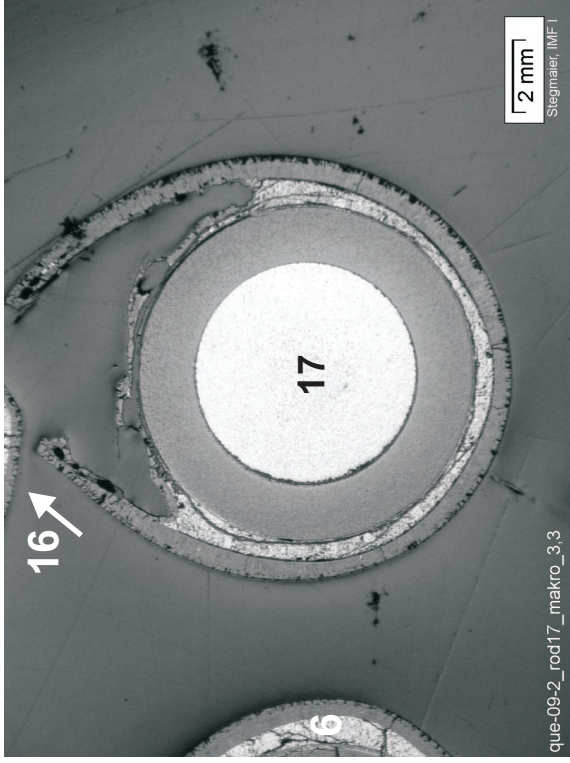


Fig. 52: QUENCH-09; Cross section at 520 mm elevation (QUE-09-2); interaction and melting of control rod components



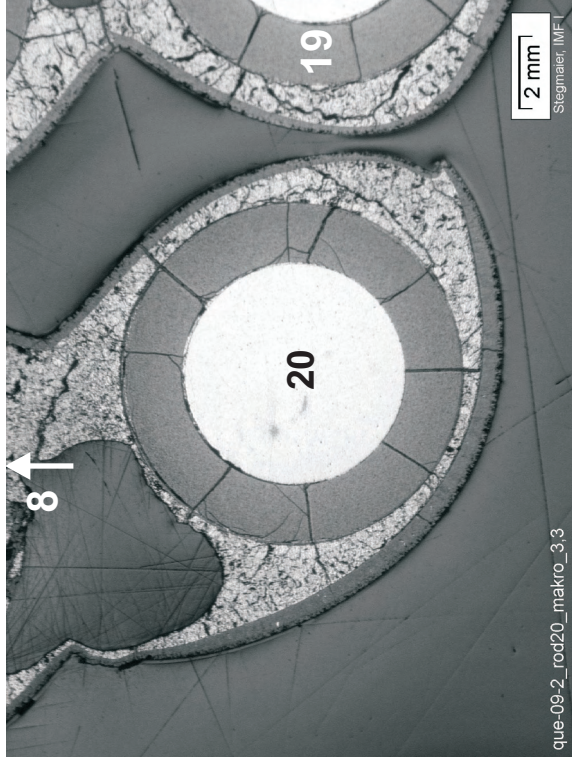
Rod #14, closed scale,
no internal steam
oxidation



Rod #17, split scale,
internal steam oxidation



Rod #3 (connected
to #12 by melt bridge
residues), showing
oxidation of void
surface (failed melt
pool scale)



Rod #20 (connected
to #8 by melt bridge
residues), showing no
oxidation of internal
void surface (intact
melt pool scale)

Fig. 53: QUENCH-09; Cross section at 520 mm elevation (QUE-09-2); examples for rods in various degradation states

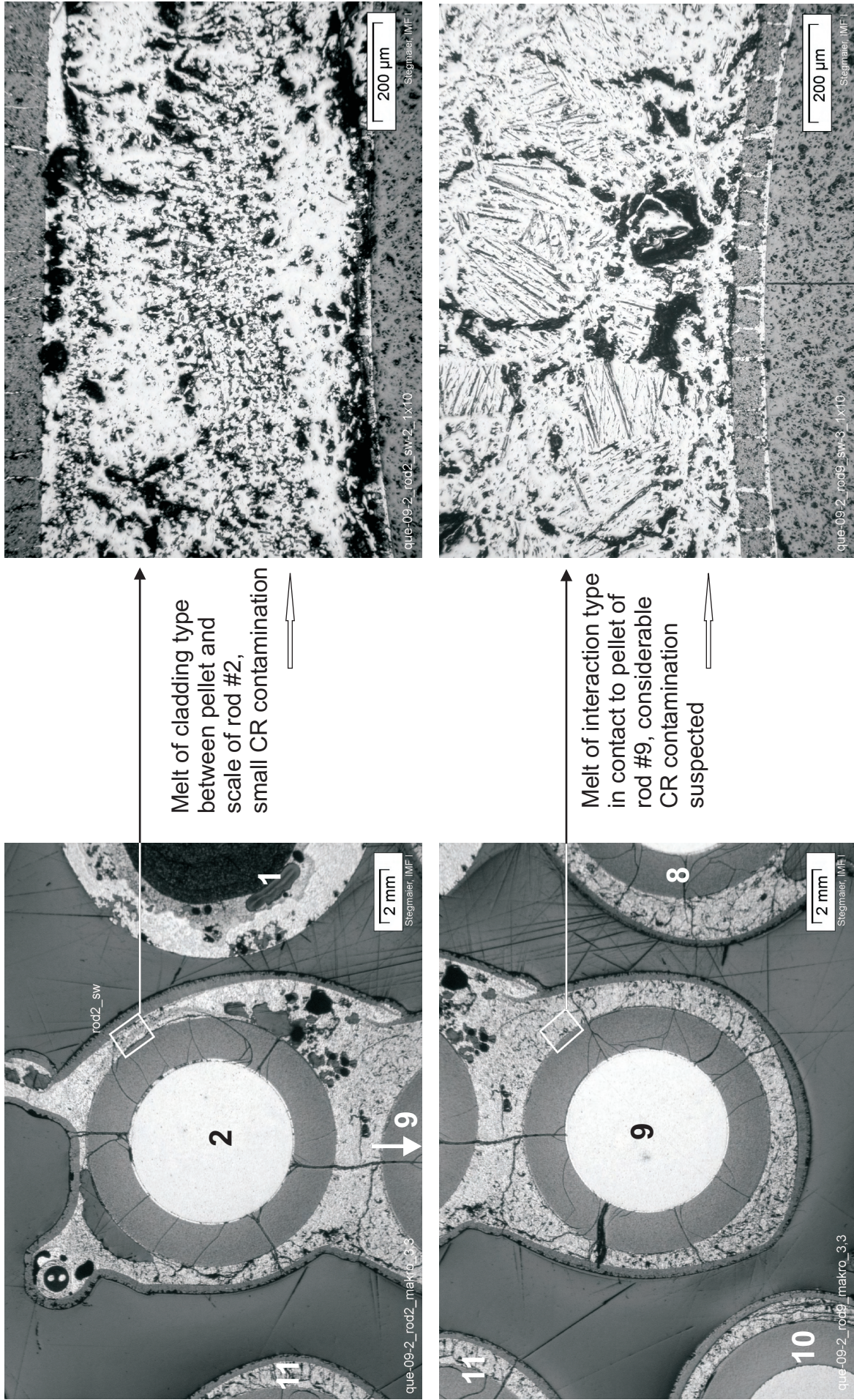


Fig. 54: QUENCH-09; Cross section at 520 mm elevation (QUE-09-2); common melt pool of rods #2 (top) and #9 (bottom), indicating control rod components transfer via melt relocation from above

Bottom of cross section slab, 577 mm elevation, inverted to top view

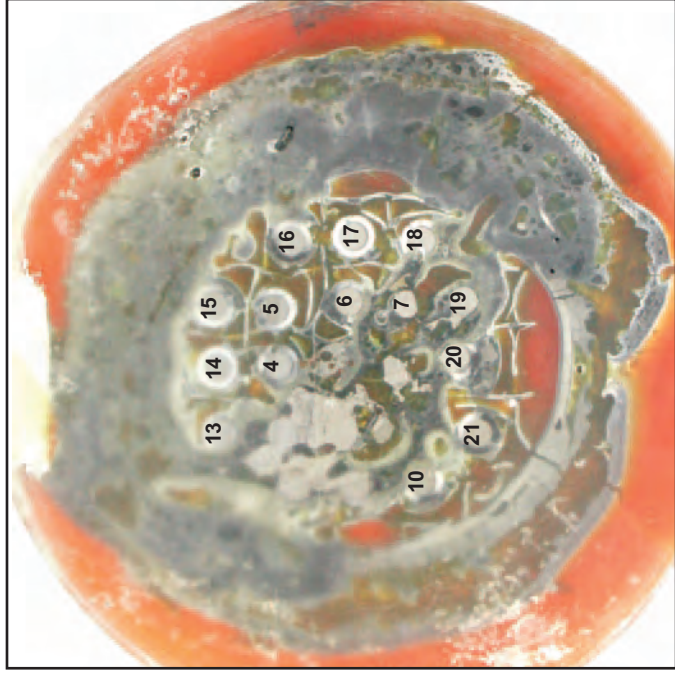


Fig. 56: QUENCH-09; Cross section at 590 mm bundle elevation (QUE-09-4); overview from top



Fig. 57: QUENCH-09; Cross section at 590 mm bundle elevation (QUE-09-4); central part, top view; EDX-analysis positions are indicated



Rod #15 indicates
heater rod degradation




Rods #14 and #16
show pellet with
columnar grains due to
recrystallization



Rod #5 includes
isolated cladding
fragment

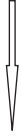
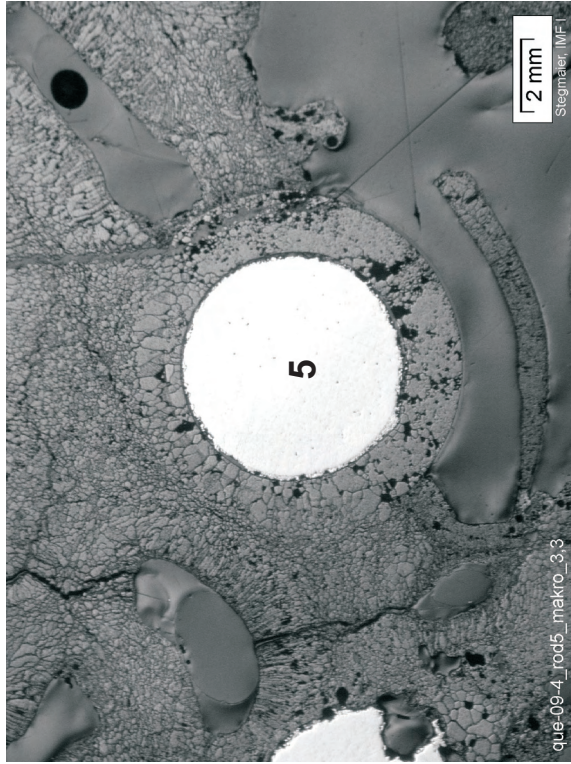
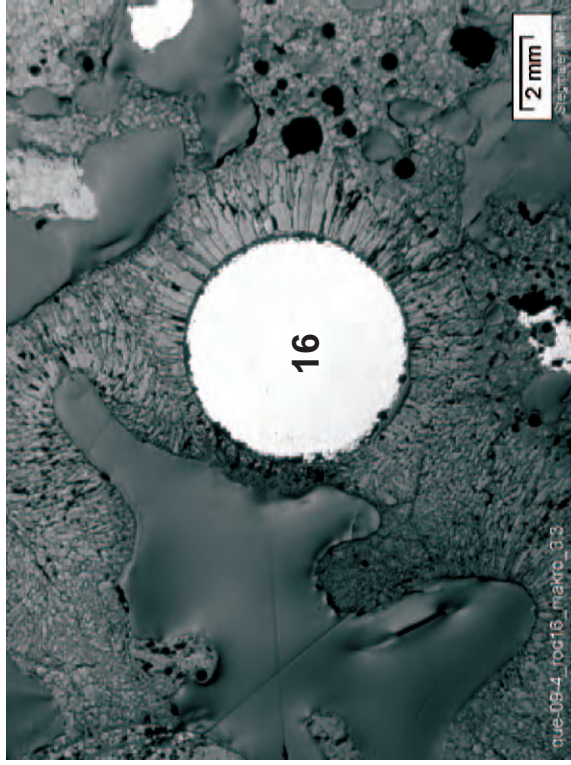
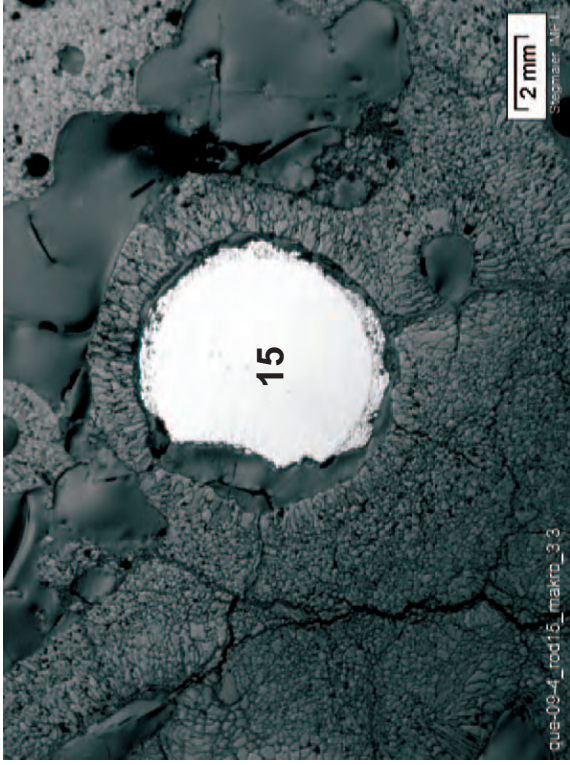



Fig. 58: QUENCH-09; Cross section at 590 mm elevation (QUE-09-4); examples for fuel rod simulators in relatively fair preservation; all at the SW part of the bundle, and in contact with blockage by dense melt

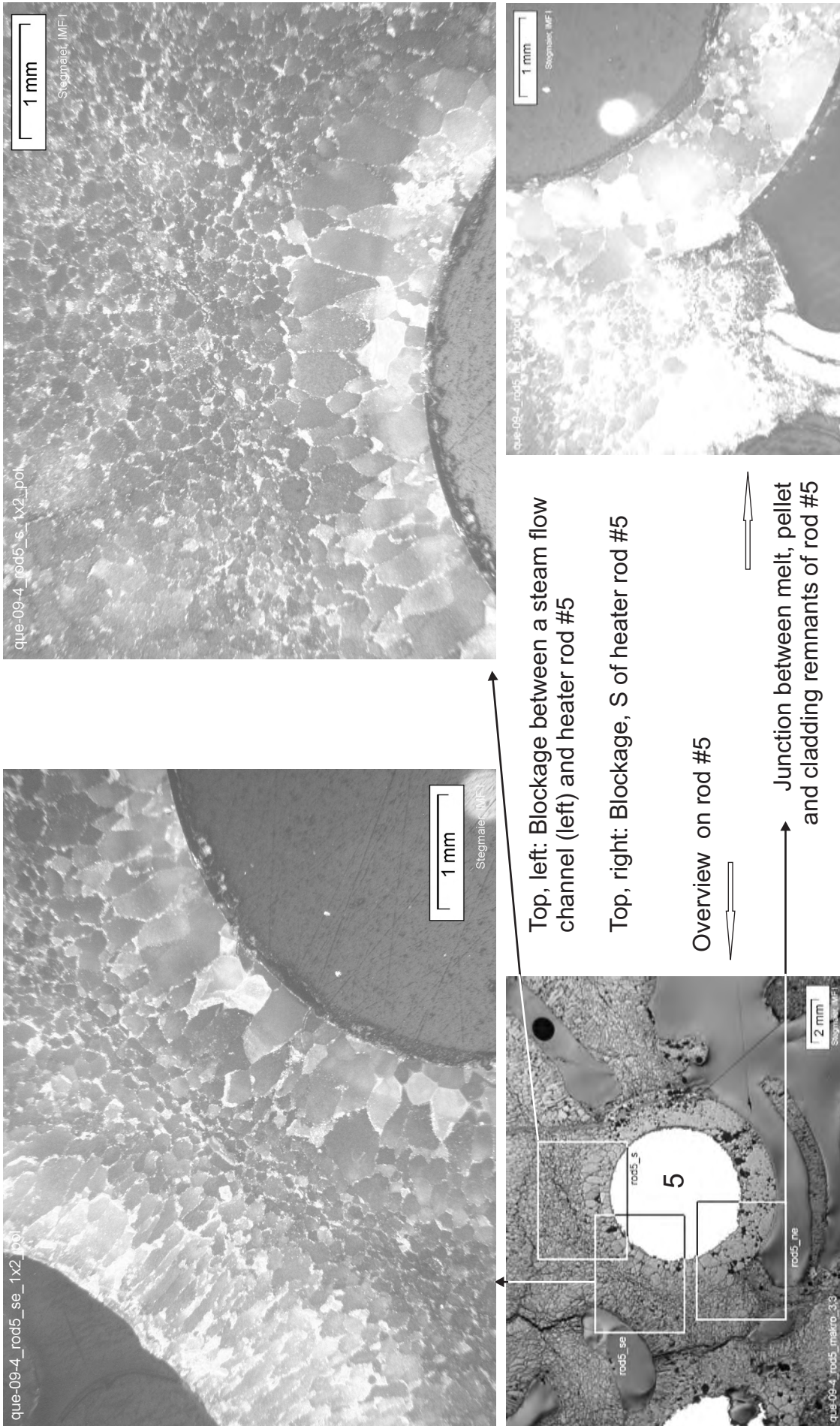
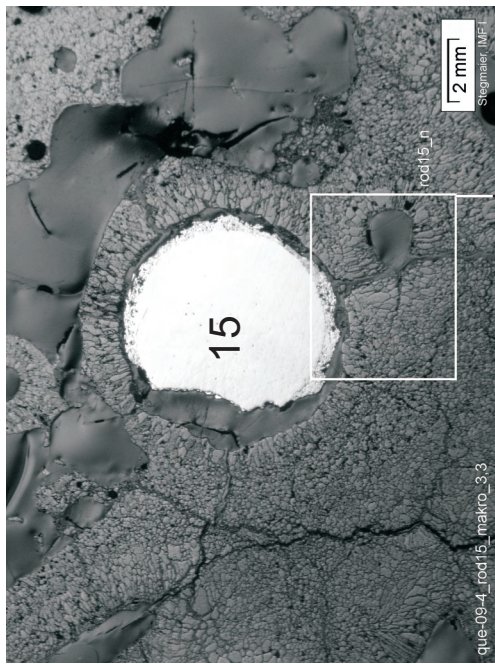
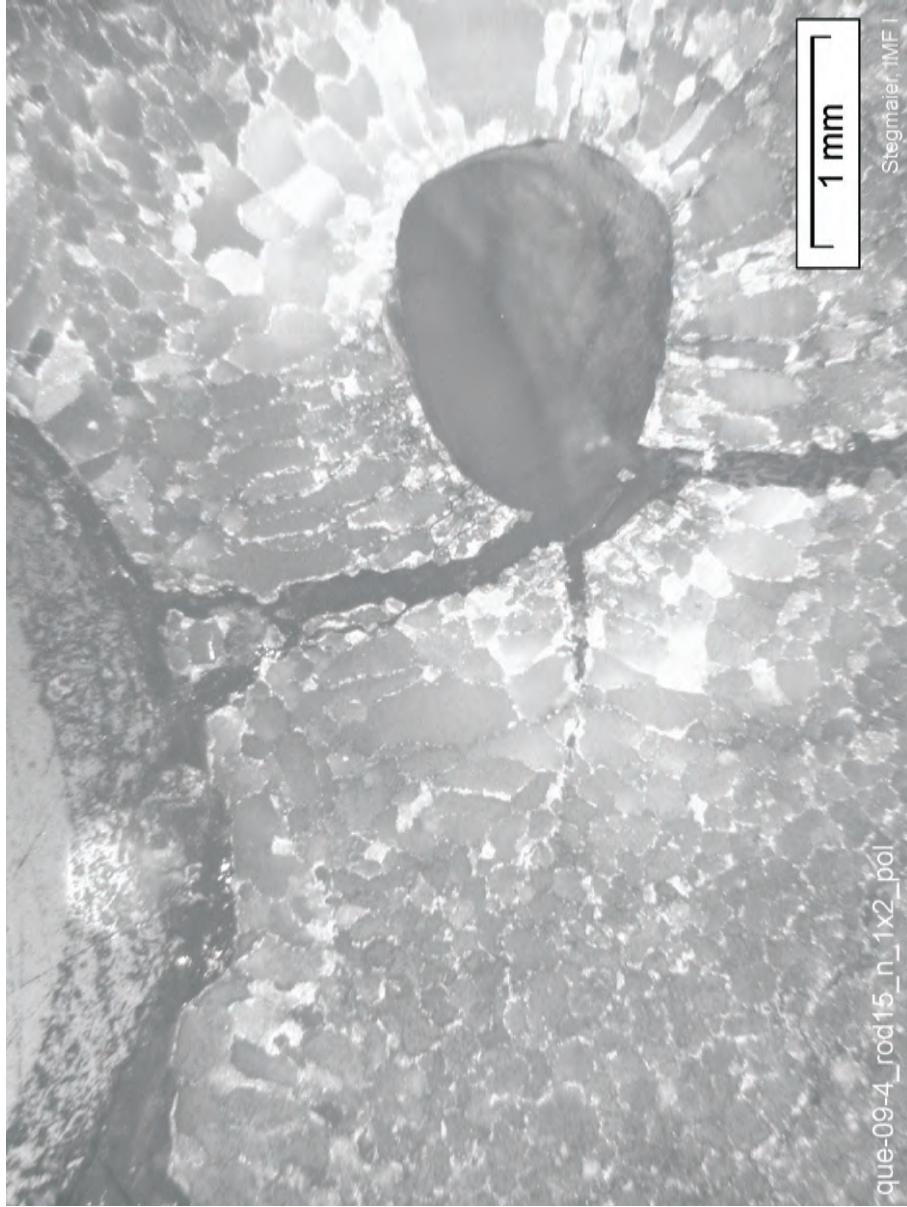
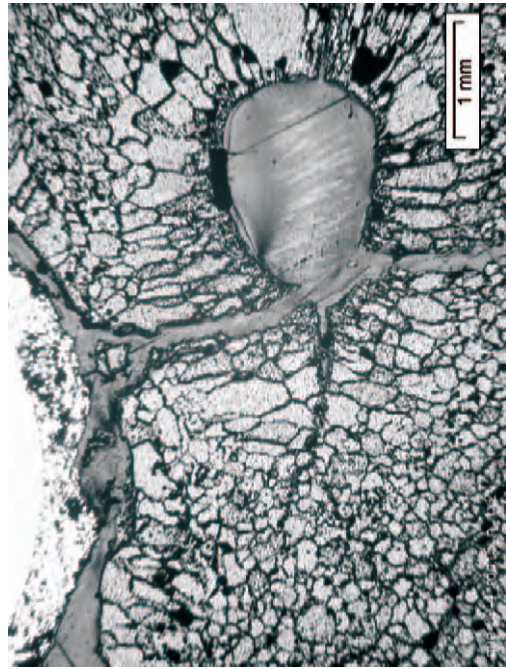


Fig. 59: QUENCH-09; Cross section at 590 mm elevation (QUE-09-4). Blockage, adjacent to rod #5, shows (in polarized light) dense character and equiaxed grains. Pellet indicated by growth of columnar scale identified by growth of columnar scale



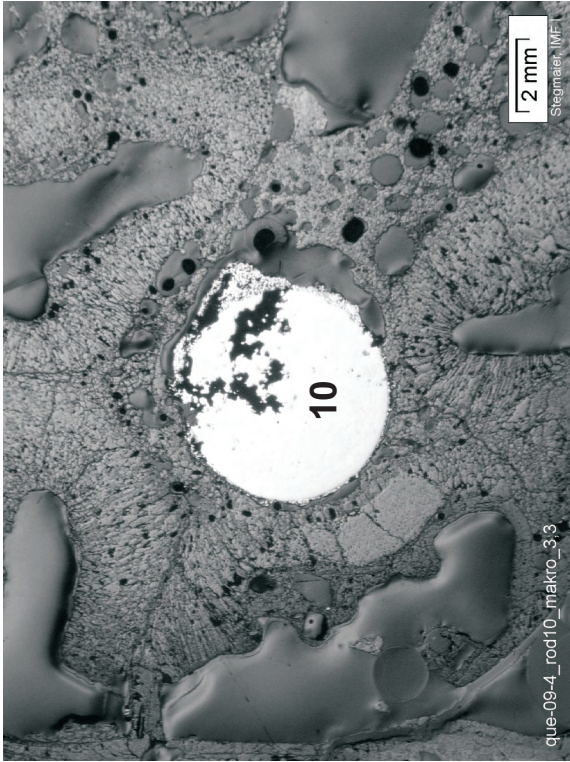
Overview on rod #15

Void-related crack formation



Same detail as bottom, left, here in polarized light instead of bright field. A pore or steam flow channel on the pellet was formed by cladding melt accumulation. Melt oxidation, re-solidification and crack formation occurred; crack growth directions across the pellet, along its contour and into the blockage support the given interpretation

Fig. 60: QUENCH-09; Cross section at 590 mm elevation (QUE-09-4); some information on the history of the blockage at the SW part of the bundle: embedding of rods, in-situ oxidation, re-solidification



All rods with partially remaining pellet, by which heater rod degradation is delayed

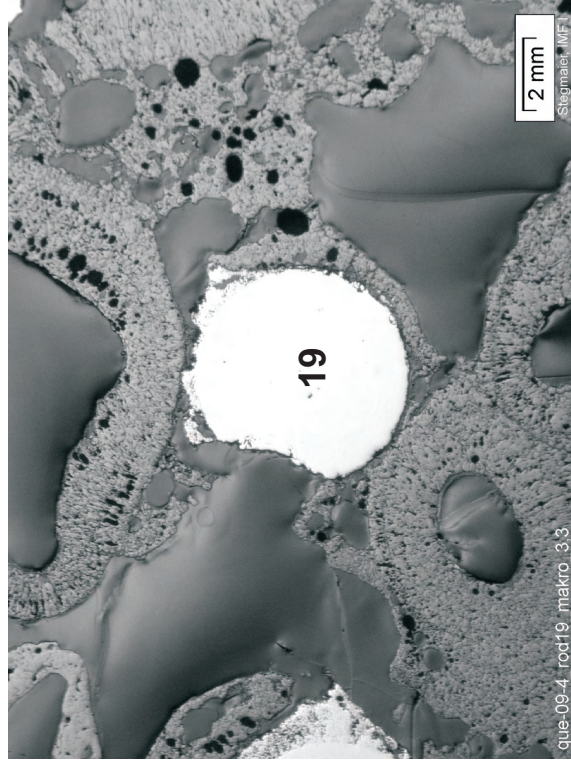
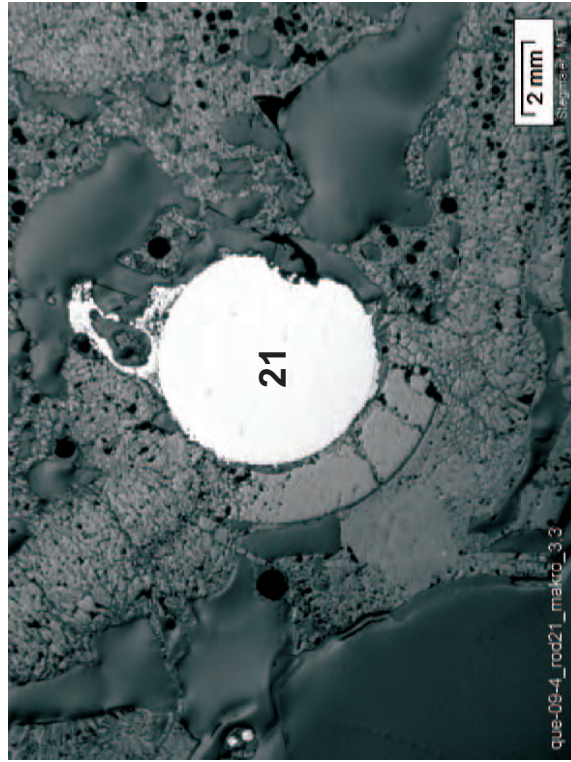
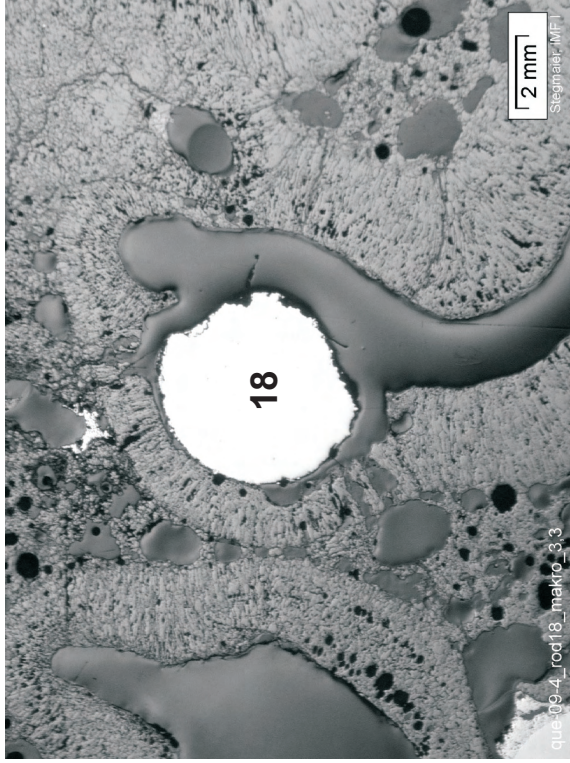
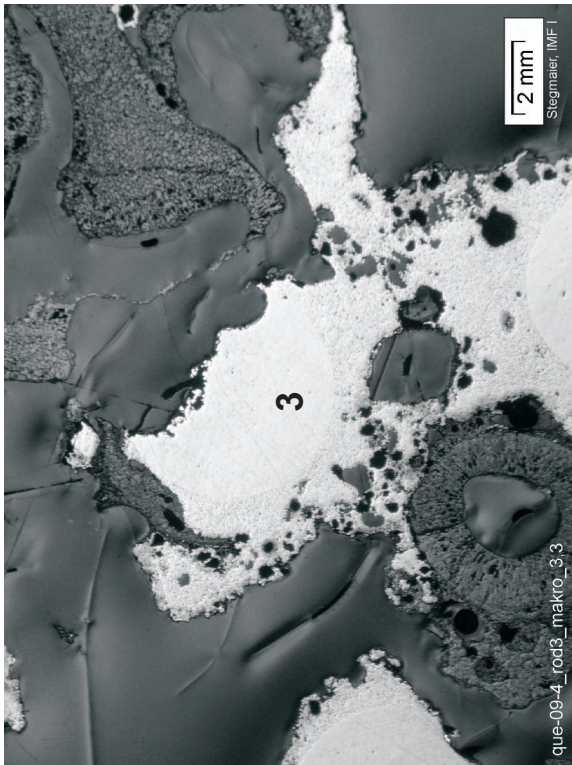


Fig. 61: QUENCH-09; Cross section at 590 mm elevation (QUE-09-4); examples for fuel rod simulators in partial preservation; locally remaining pellet, elsewhere heater rod destruction



All fuel rod simulators are found in advanced degradation, and show either no pellet remnants or only displaced ones

Tungsten heater rod degradation is related to melt formation and relocation; however, embedding in melt exerts some protection

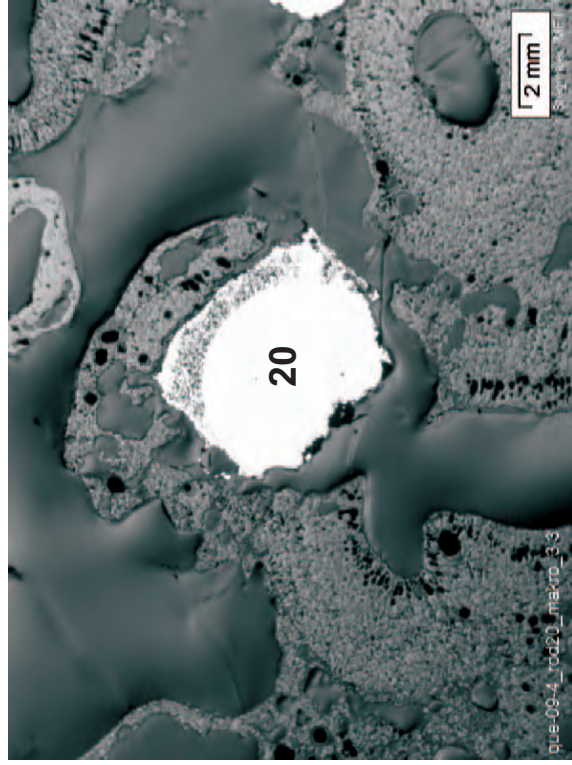
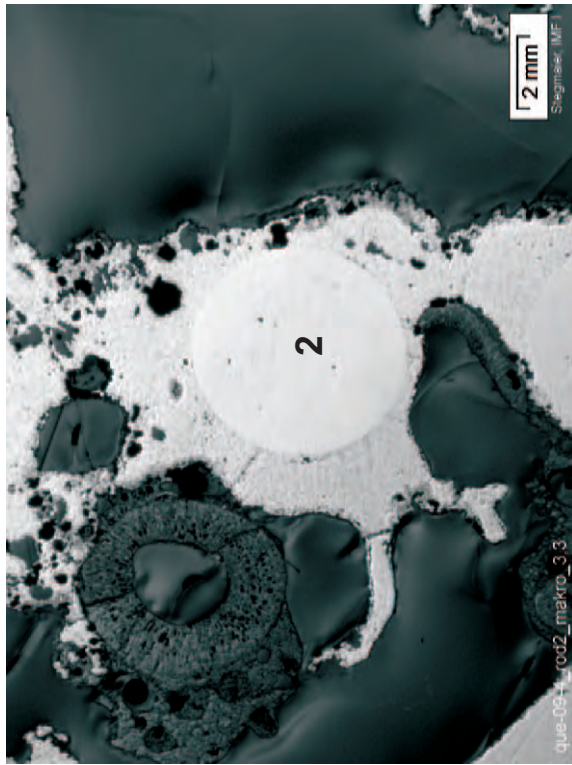
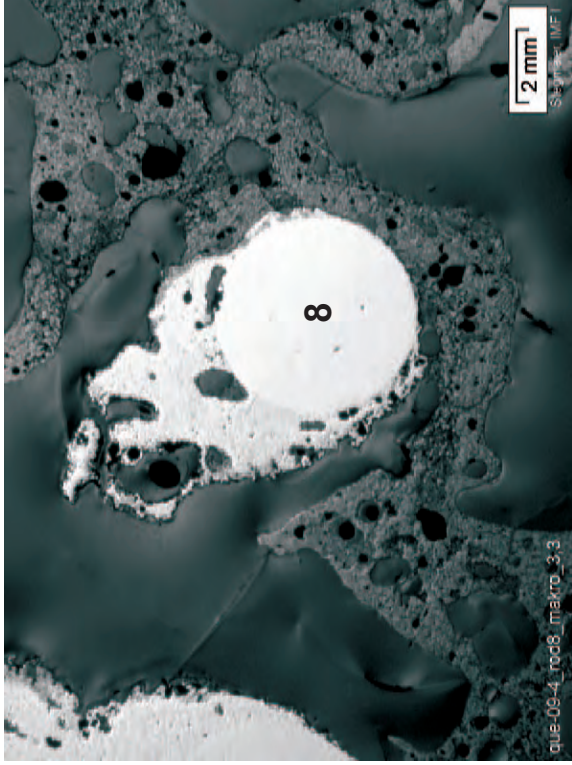


Fig. 62: QUENCH-09; Cross section at 590 mm elevation (QUE-09-4); examples for strongly damaged fuel rod simulators, and tungsten heater rod degradation via melt formation

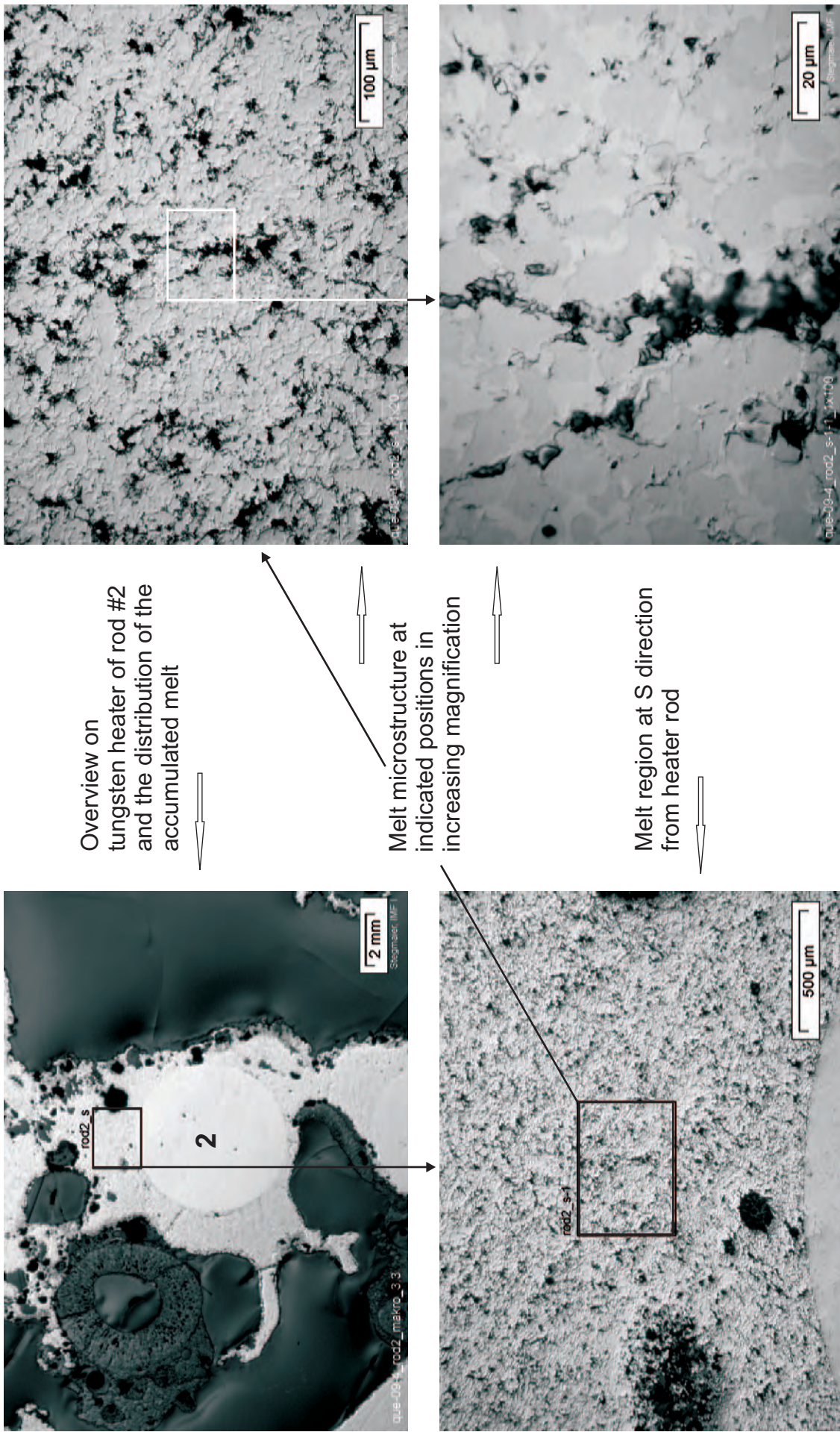
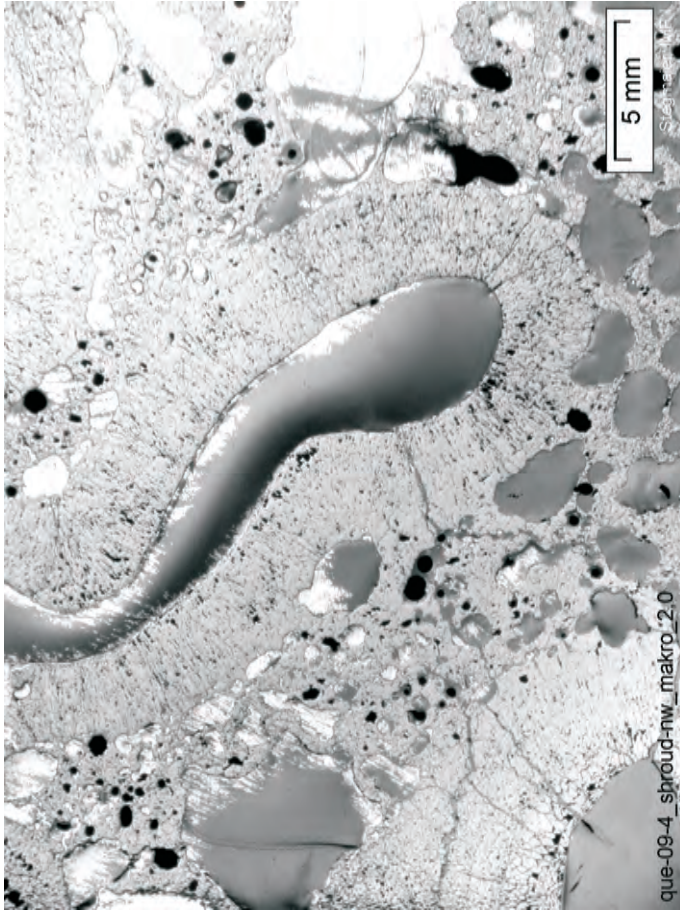
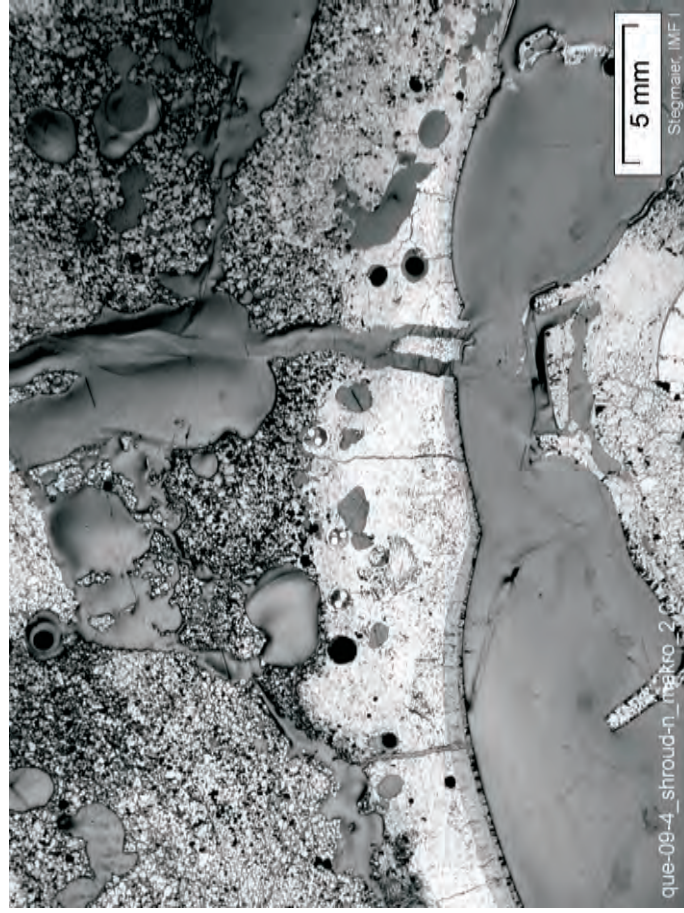
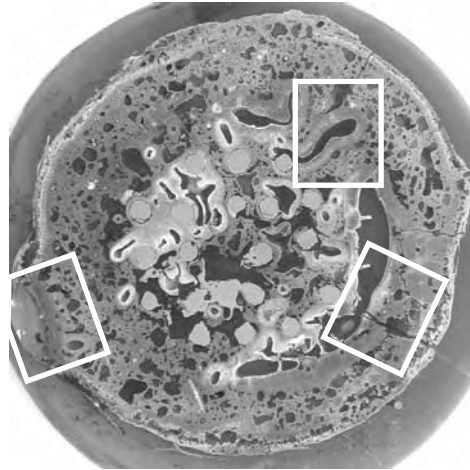


Fig. 63: QUENCH-09; Cross section at 590 mm elevation (QUE-09-4); microstructure of melt, accumulated around tungsten heater of fuel rod simulator #2, resulting from heater rod degradation at the relocation sources (see other figures for analysis)

Overview on the N/NE region between bundle (bottom, viewer's position) and shroud (top). The thin structures, connected with the bundle, are spacer grid remnants. Three shroud TCs are embedded by the still metallic shroud wall melt. External side of the shroud in contact with accumulated melt (porous, mainly ceramic). Crack through shroud wall formed in quench phase

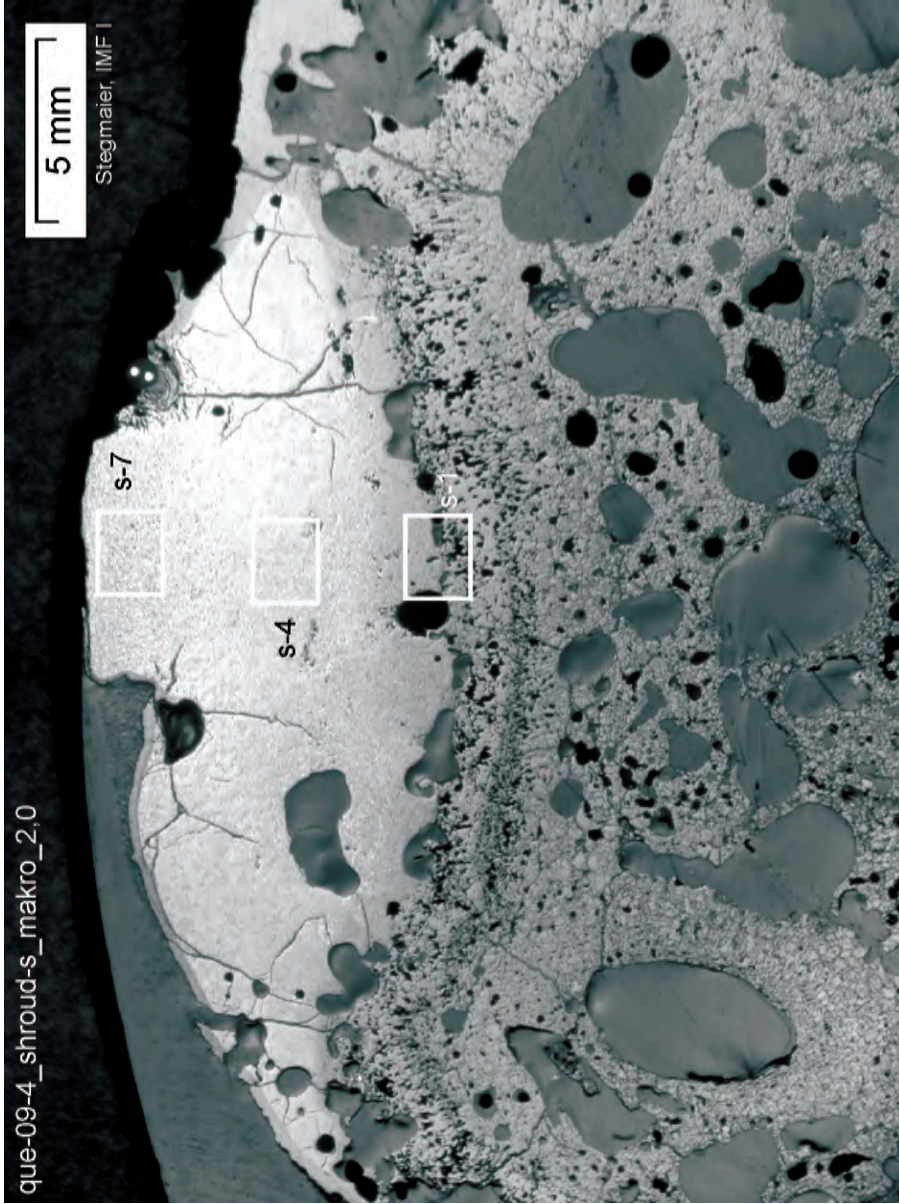


Part of a steam flow channel, ranging from rod #18 to the shroud at NW (this part shown). Massive barrier of scale, directly around, is easily distinguished from the adjacent melt, which is oxidized as well



Overview from top

Fig. 64: QUENCH-09; Cross section at 590 mm elevation (QUE-09-4); a steam flow channel at the bundle periphery and the shroud at a position of crack formation during quenching



Shroud at S/SE direction, converted to porous melt in ceramic final state. Contact to the cooling jacket after complete consumptive penetration of the ZrO2 fibre insulation pack gave rise to interaction melt of mostly metallic form. The microstructure profile of the interaction product melt is depicted in the series of highly magnified micrographs, given to the right.

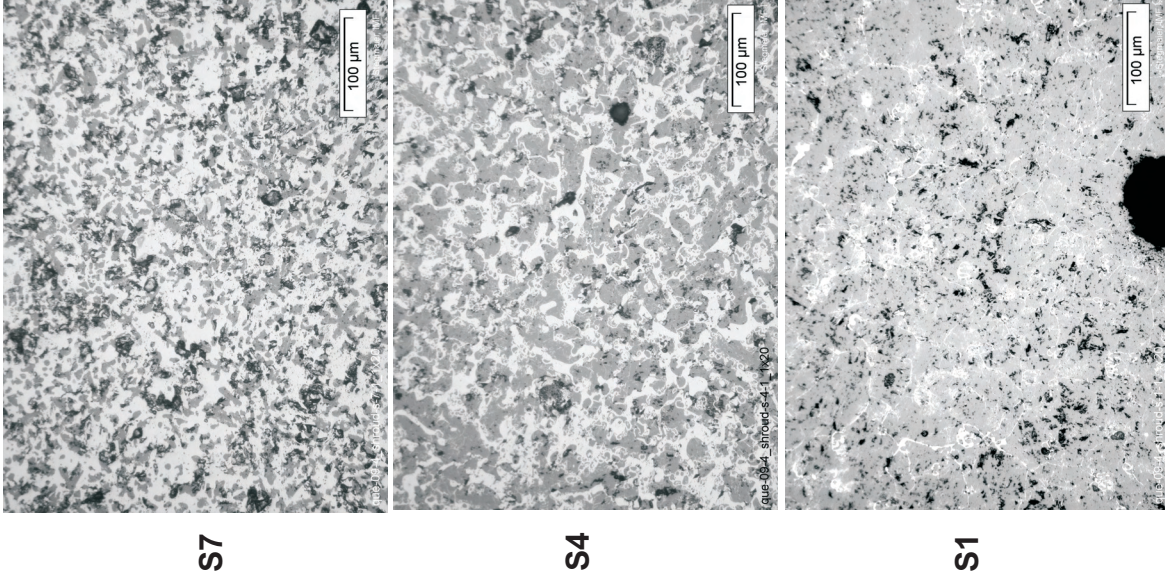


Fig. 65: QUENCH-09; Cross section at 590 mm elevation (QUE-09-4); metallic melt at S to SE position of the shroud, resulting from stainless steel cooling jacket attack

Bottom of cross section slab, 637 mm elevation, inverted to top view

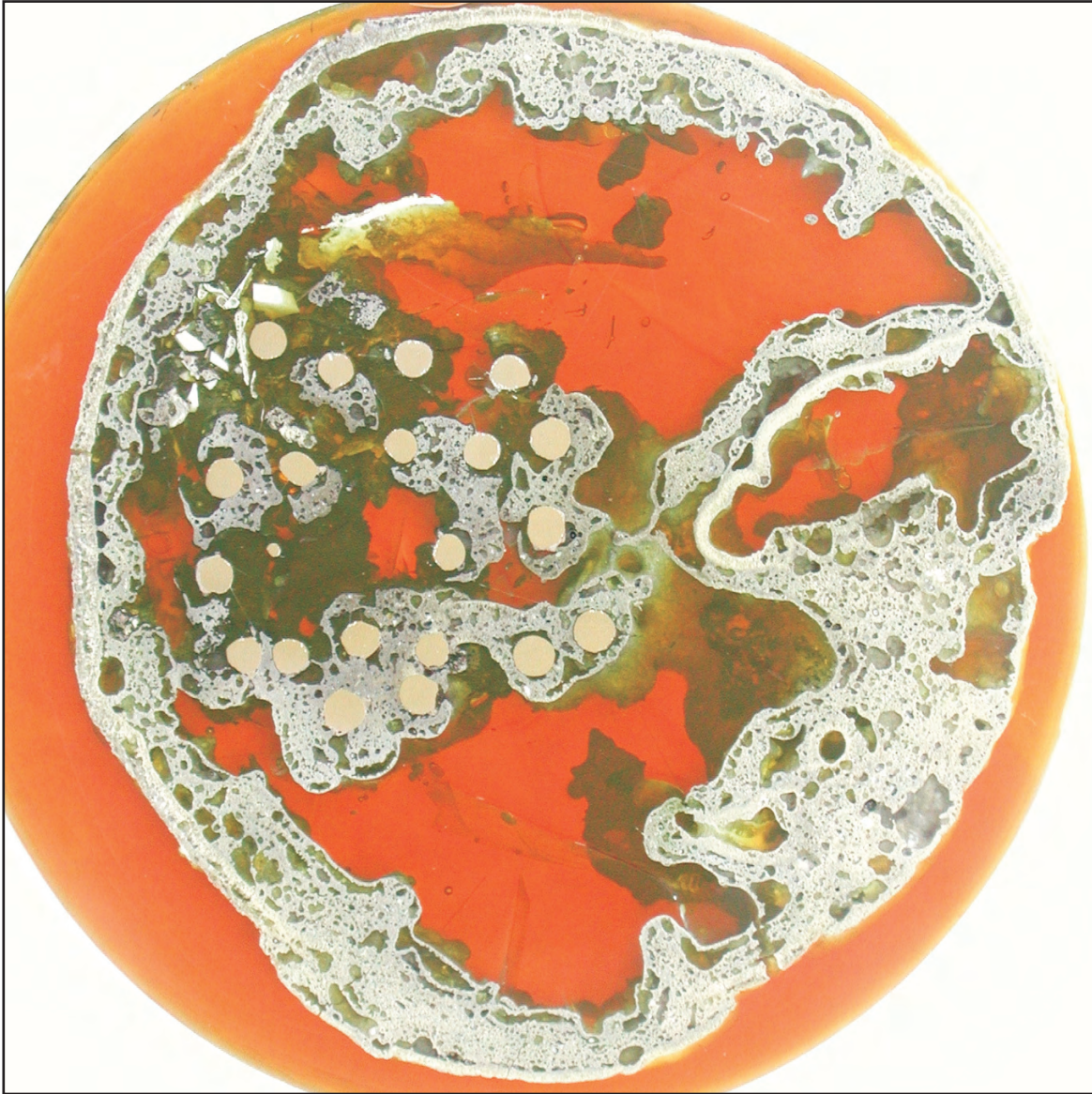


Fig. 66: QUENCH-09; Cross section at 650 mm bundle elevation (QUE-09-6); overview from top

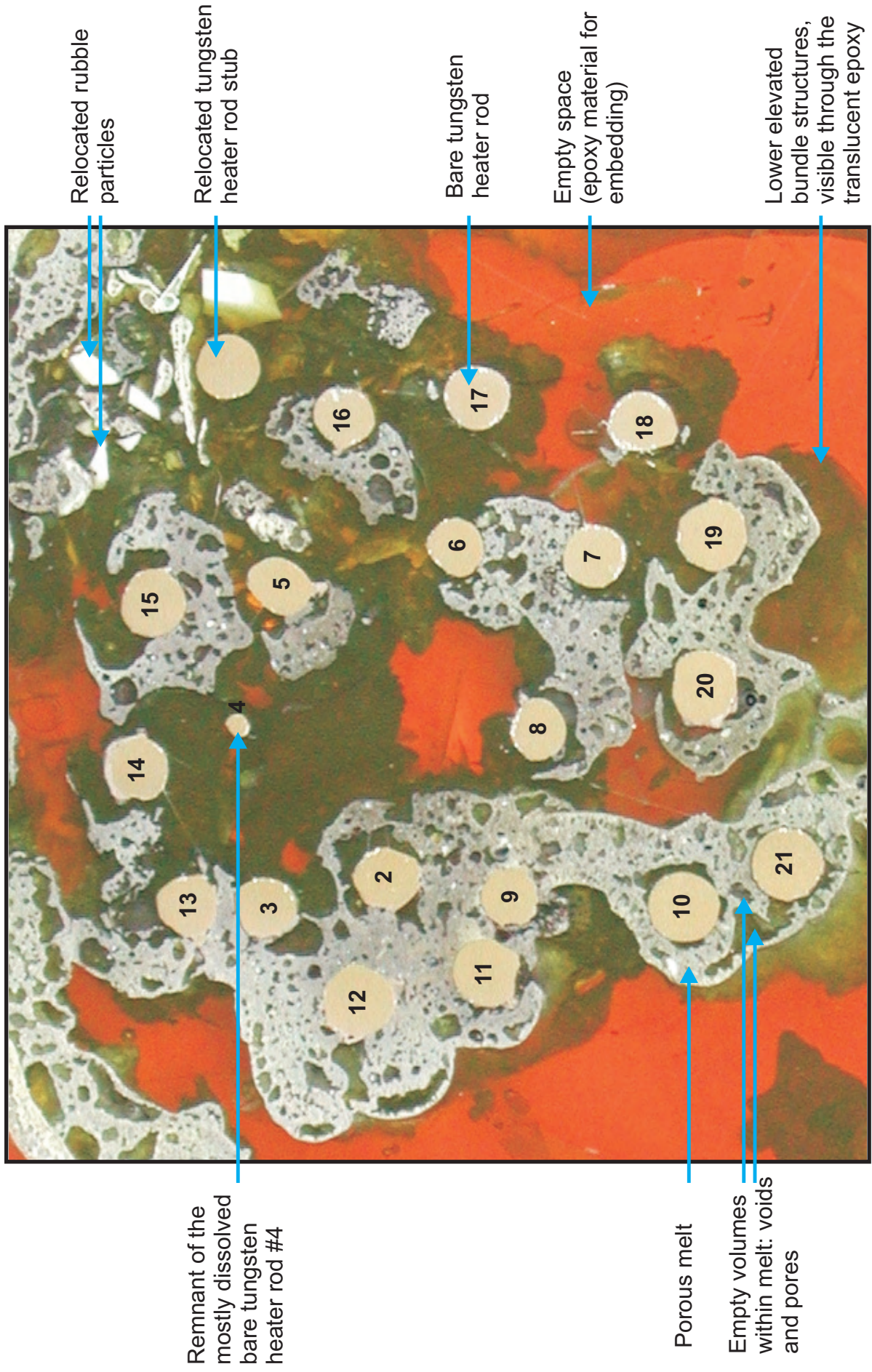
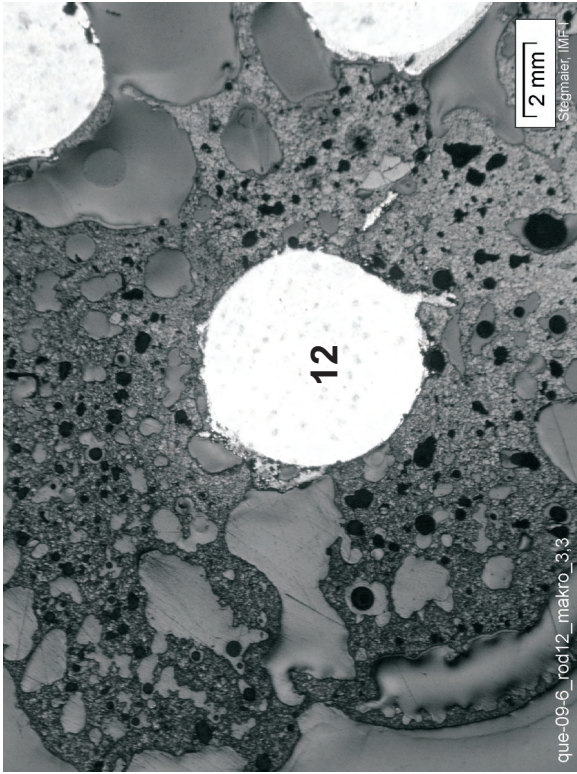


Fig. 67: QUENCH-09; Cross section at 650 mm bundle elevation (QUE-09-6); central part, top view



All the depicted fuel rod simulators are seriously damaged at the given elevation. Cladding and pellet have interacted under melt formation. This melt has at least protected the tungsten heater rods from more serious degradation

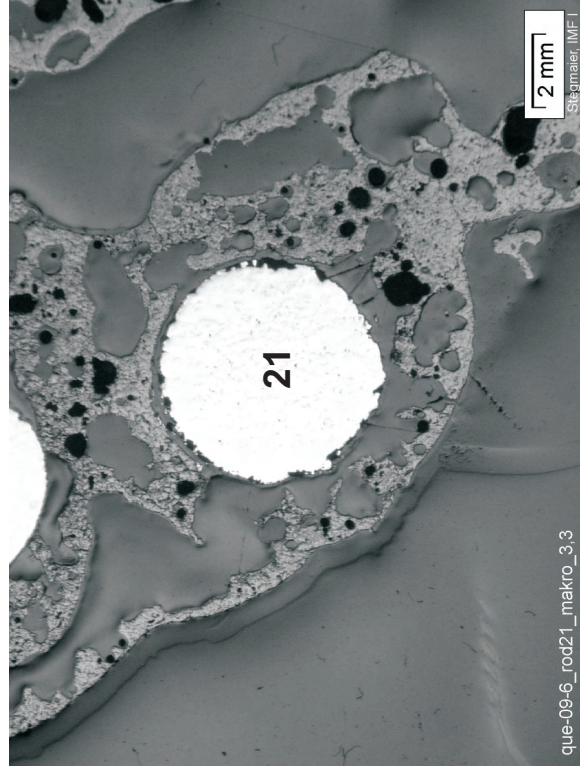
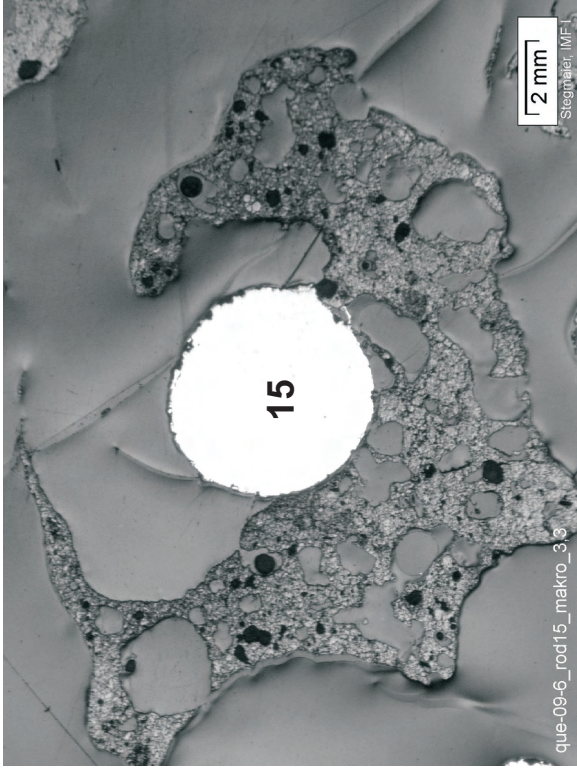
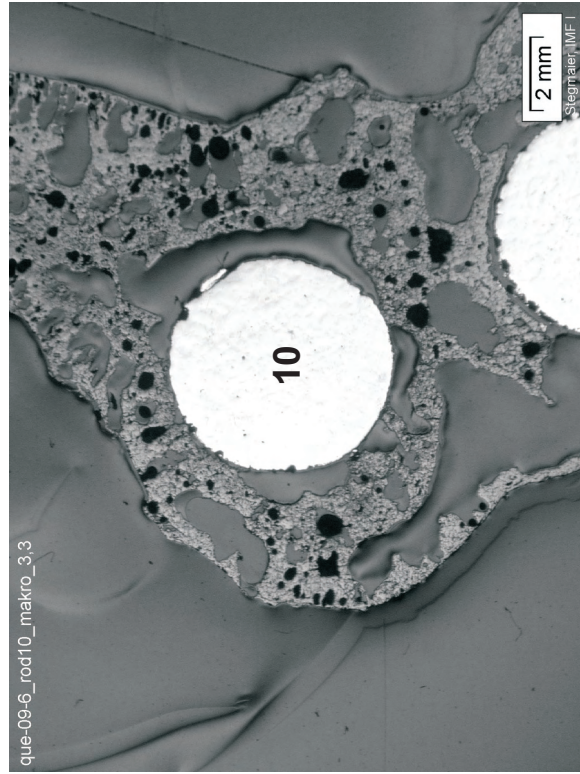
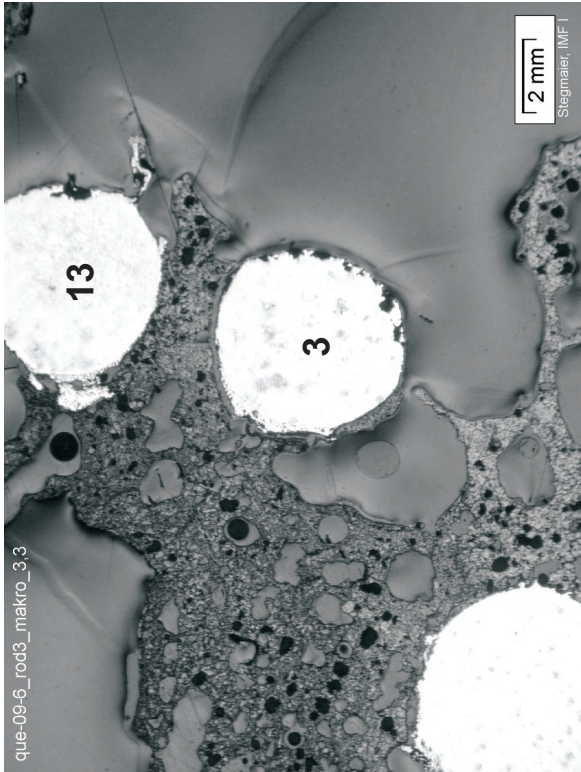


Fig. 68: QUENCH-09; Cross section at 650 mm elevation (QUE-09-6); examples for fuel rod simulators in fair preservation, relative to the advanced bundle destruction



All simulator rods without cladding and pellet remnants, only some porous interaction product melt remains.

Heater rods are attacked at parts of their contour, or have lost in diameter by dissolution

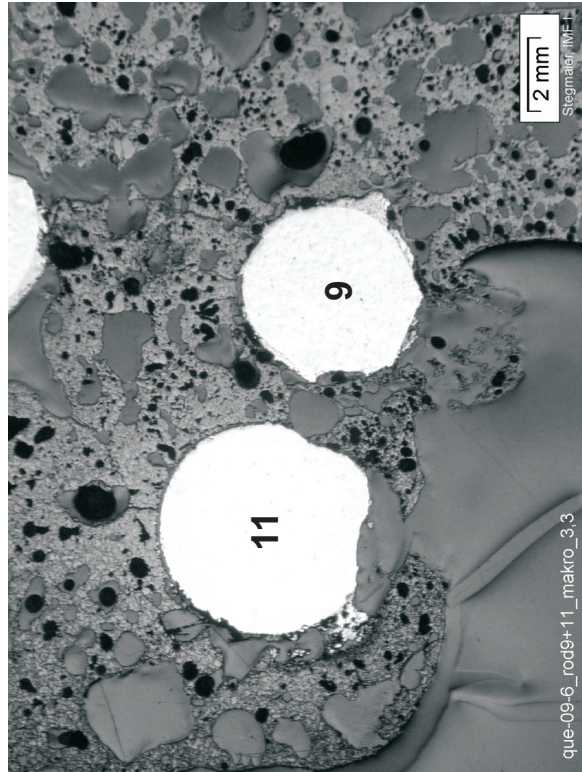
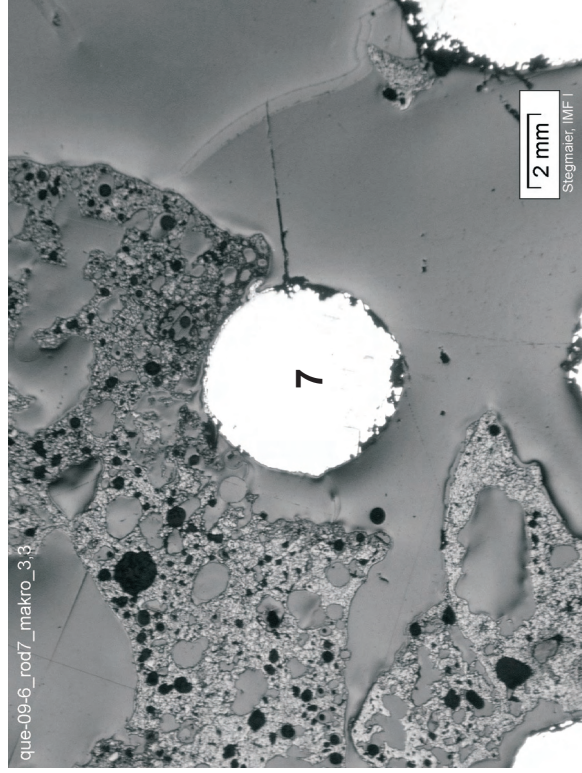
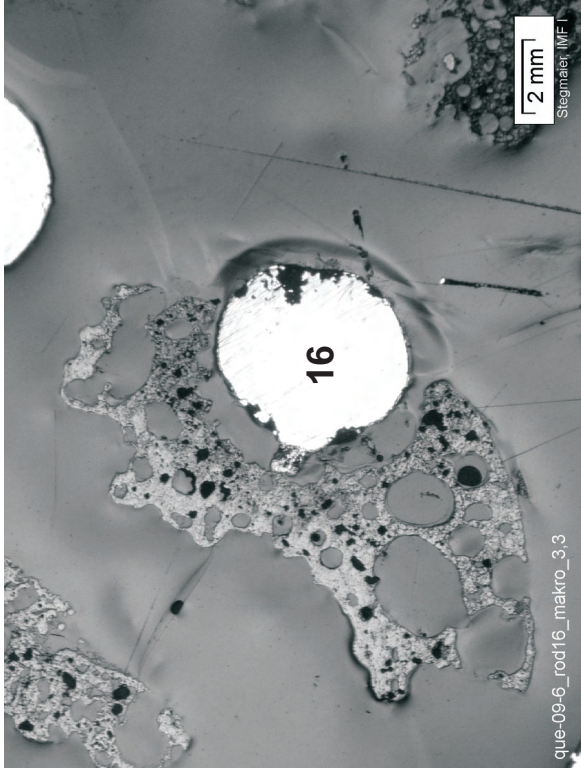
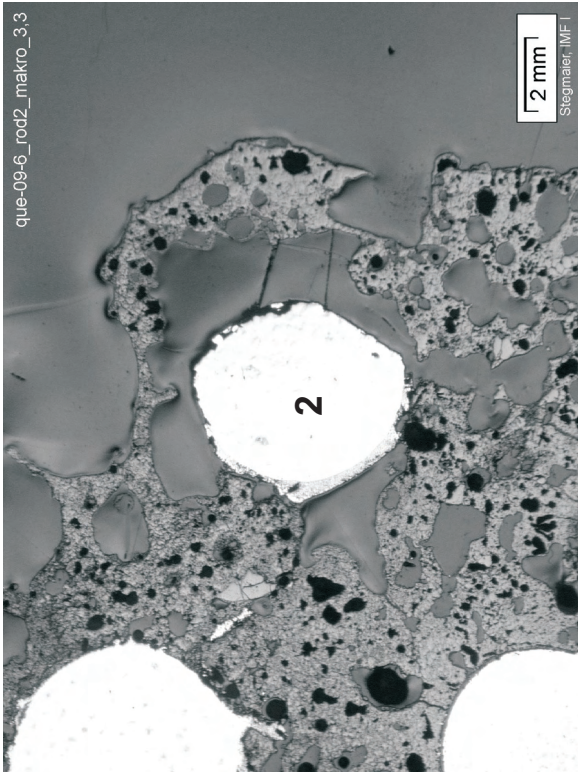


Fig. 69: QUENCH-09; Cross section at 650 mm elevation (QUE-09-6); examples for fuel rod simulators in the advanced degradation, characteristic for the elevation





All fuel rod simulators so destroyed, that the tungsten heater rod underwent dissolution due to exposure to the test atmosphere. Examples for even stronger degradation (e.g. rod #4) not depicted

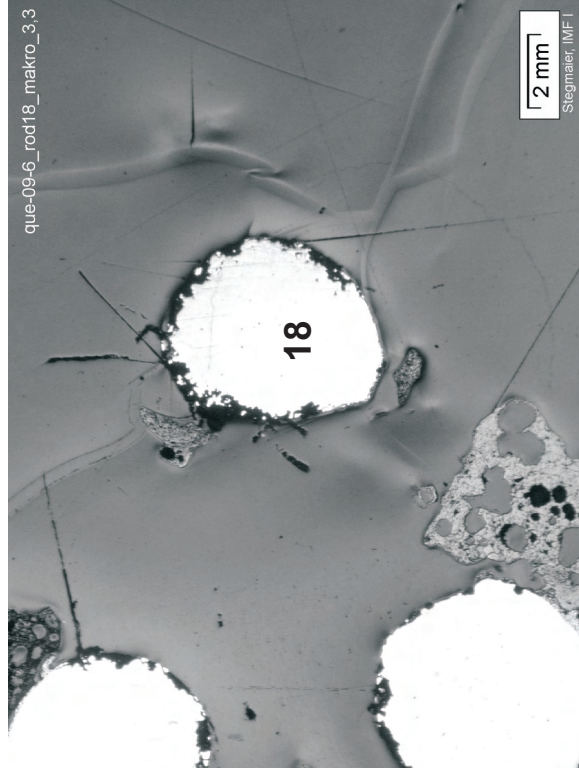
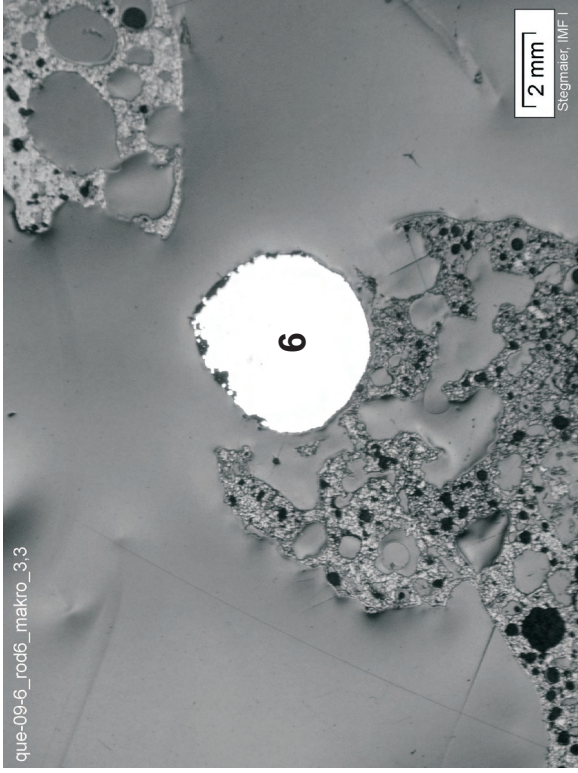


Fig. 70: QUENCH-09; Cross section at 650 mm elevation (QUE-09-6); examples for fuel rod simulators in bad condition

Bottom of cross section slab, 687 mm elevation, inverted to top view

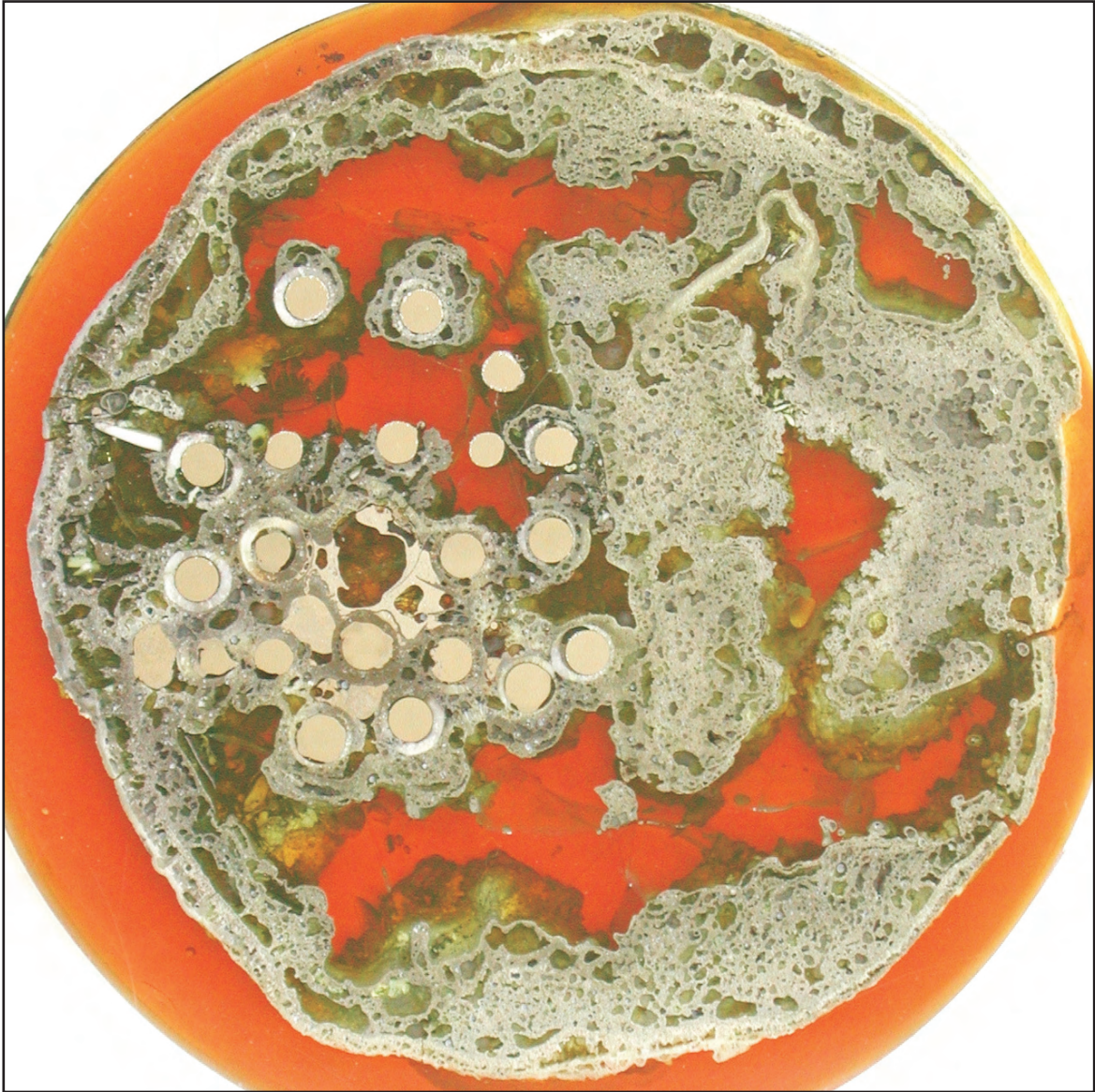


Fig. 71: QUENCH-09; Cross section at 700 mm bundle elevation (QUE-09-8); overview from top

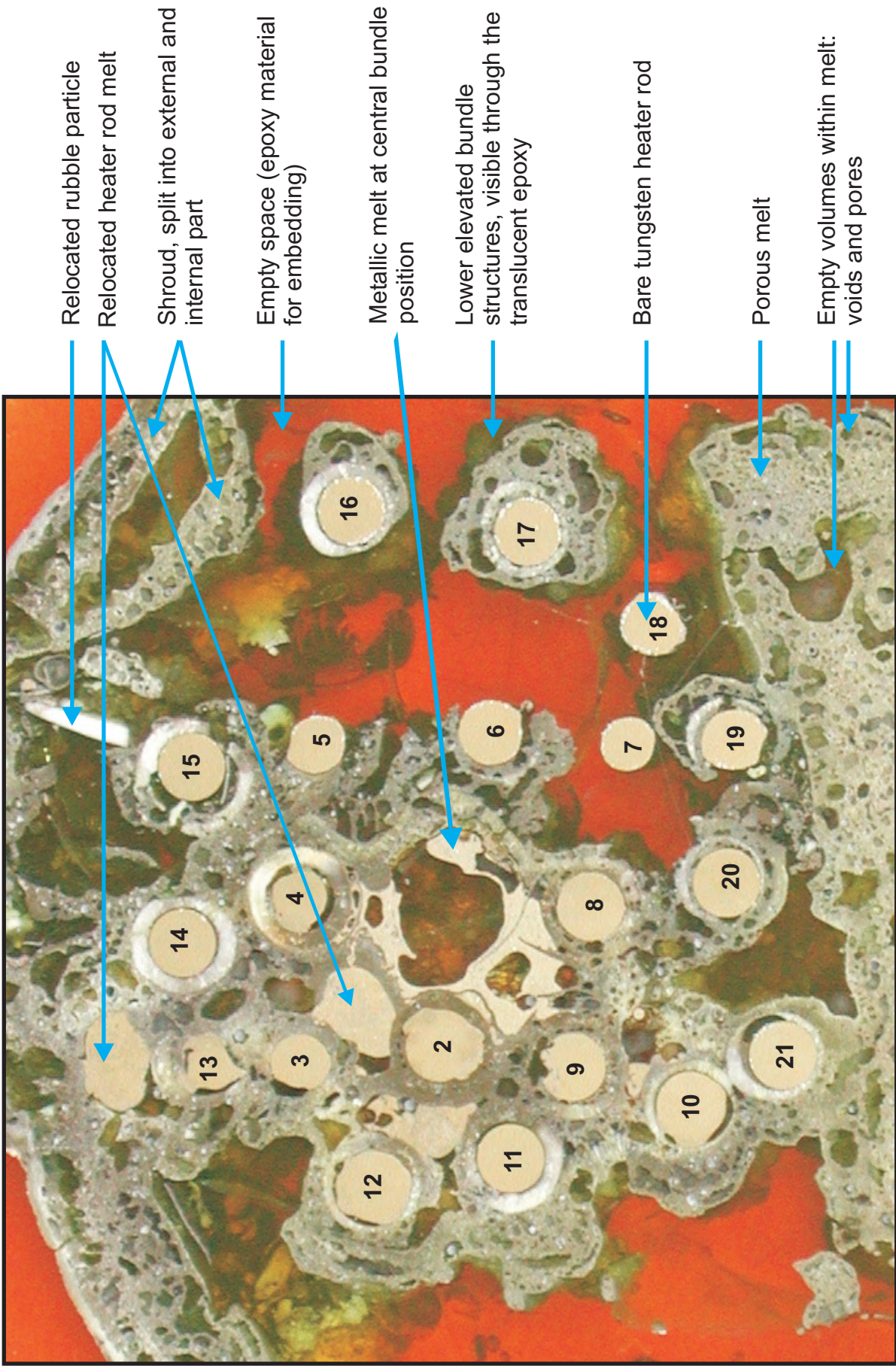
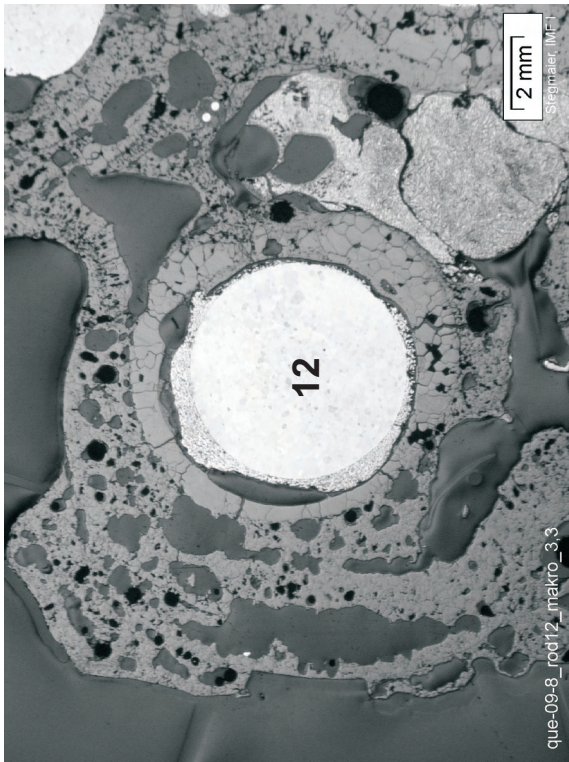


Fig. 72: QUENCH-09; Cross section at 700 mm bundle elevation (QUE-09-8); central part, top view



All the depicted fuel rod simulators are less seriously damaged at the given elevation, compared to QUE-09-6, elevation 650 mm. No cladding, except some scale of rod #8, embedded in metallic melt, remains. Some pellets, however, survived without much damage. Pellet and melt have protected most of the tungsten heater rods from exposure to the test atmosphere.

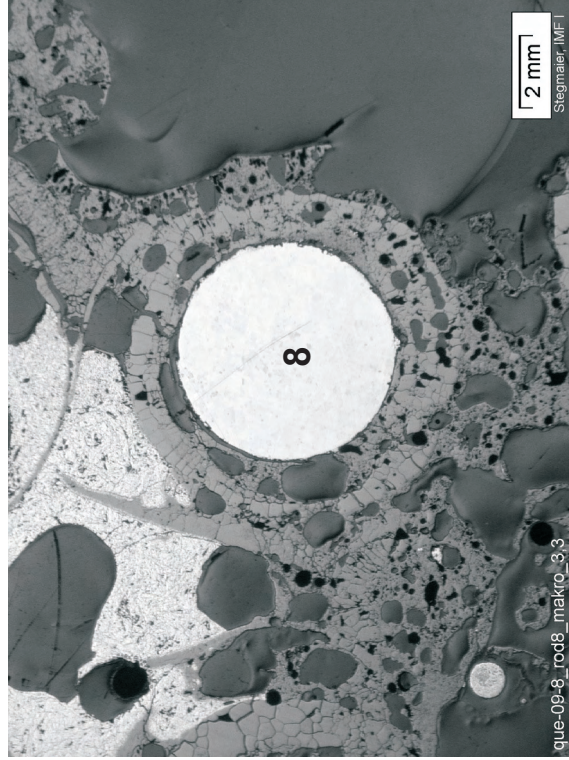
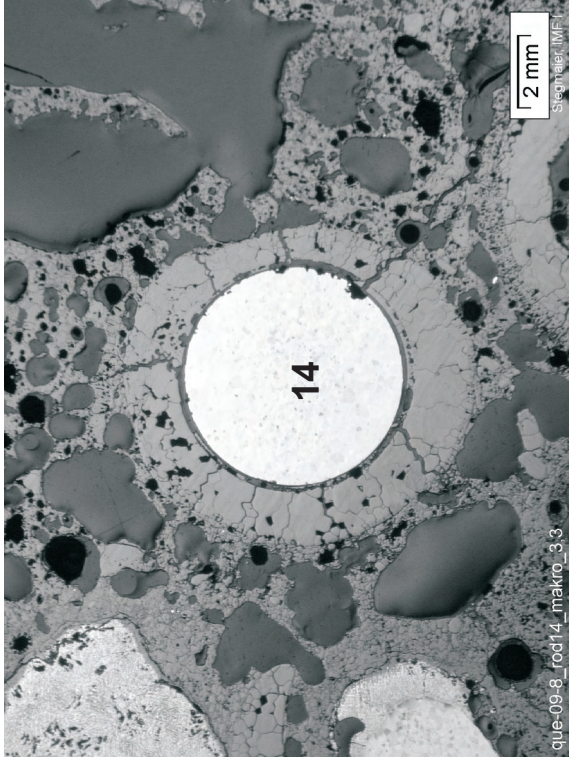
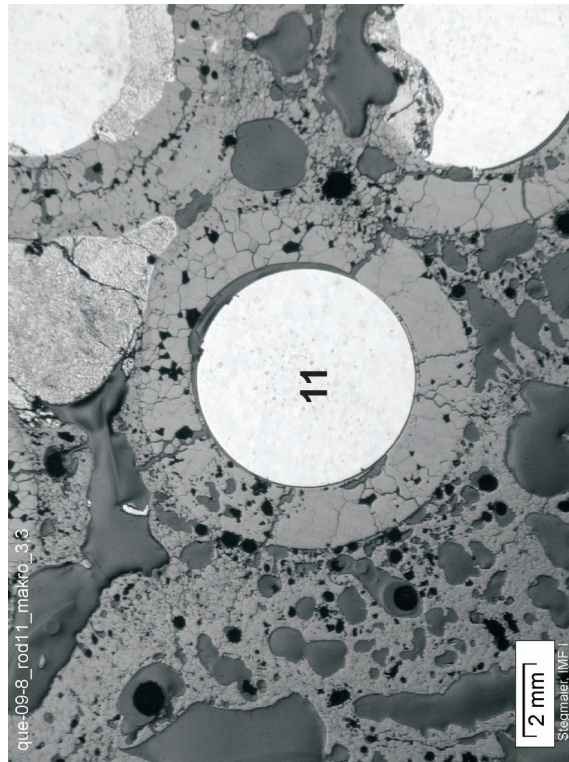
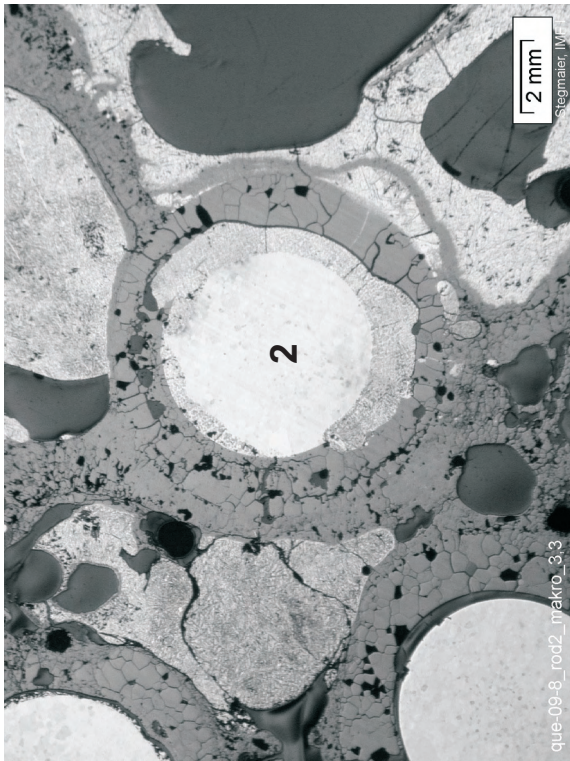


Fig. 73: QUENCH-09; Cross section at 700 mm elevation (QUE-09-8); examples for fuel rod simulators in better condition, compared to the elevation QUE-09-6 (650 mm)



All simulator rods are without cladding remnants (except scale of rod #2, embedded in the metallic melt, which has accumulated at central bundle position). Pellets are partially retained. Heater rod #2 is surrounded by metallic melt (most probably tungsten-rich melt).

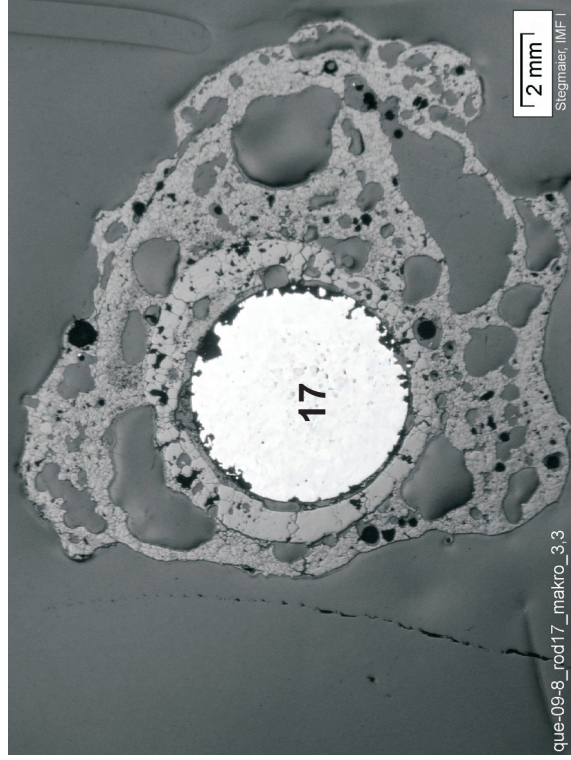
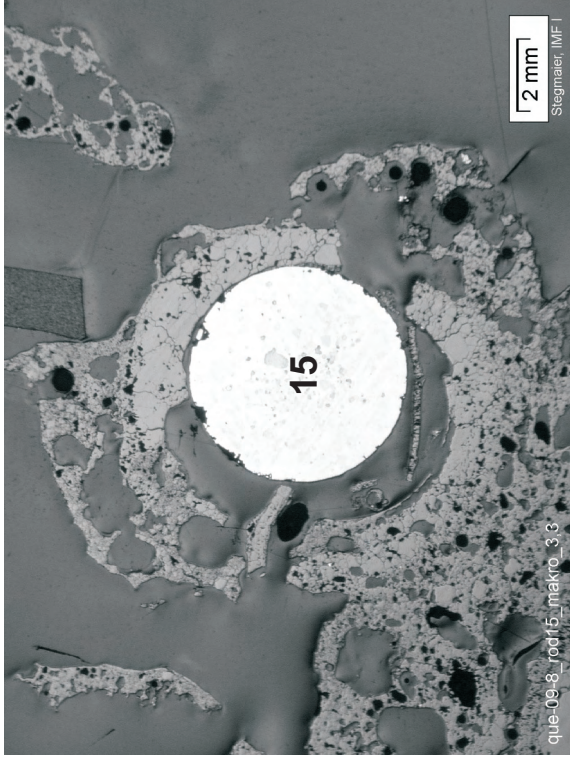
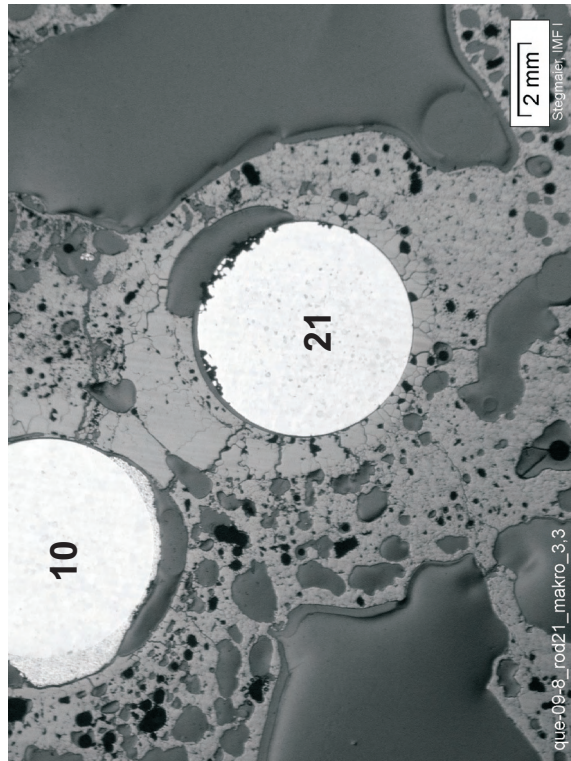


Fig. 74: QUENCH-09; Cross section at 700 mm elevation (QUE-09-8); examples for fuel rod simulators in the characteristic degradation state of the elevation



Rod #13 (see also lump of W-rich melt above)



All fuel rod simulators destroyed in so far, as the tungsten heater rods have been exposed to the test atmosphere. Rod #13 (top, left) is the strongest degraded rod of the bundle at the given elevation

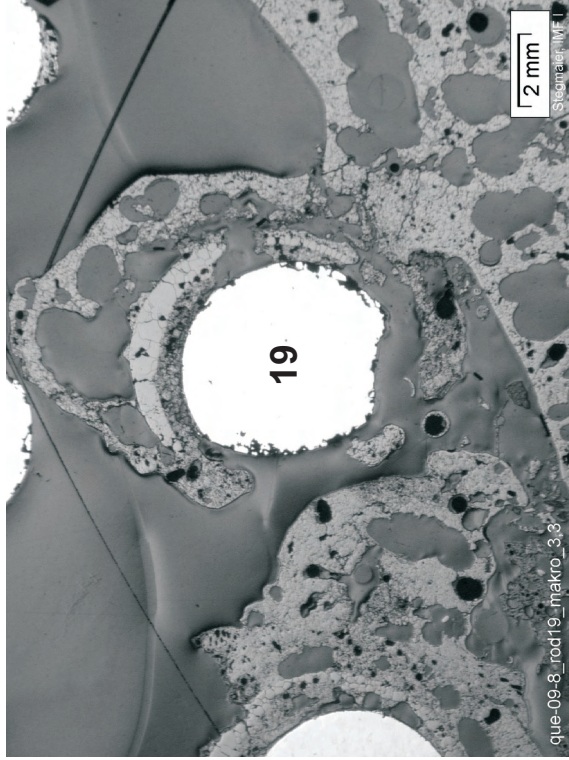
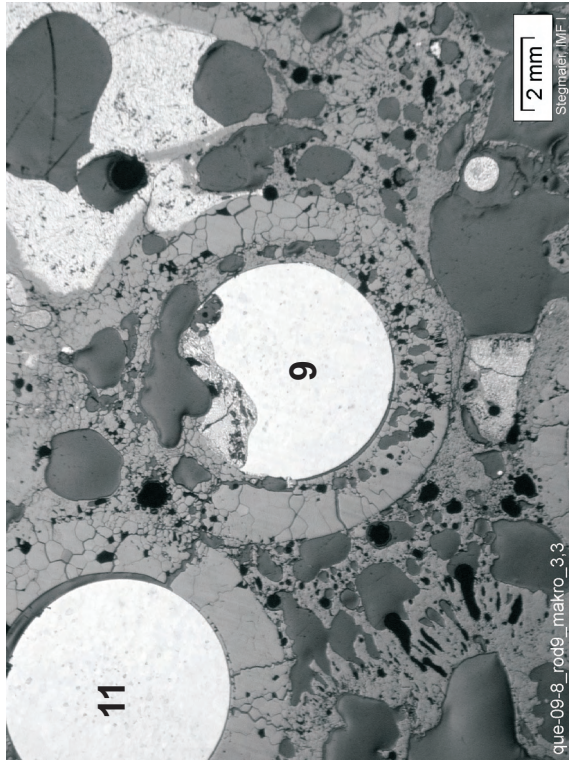
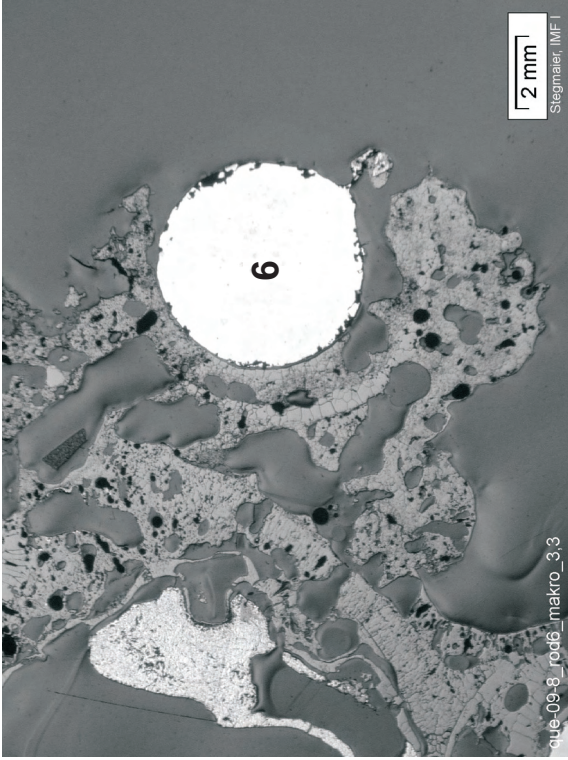


Fig. 75: QUENCH-09; Cross section at 700 mm elevation (QUE-09-8); examples for fuel rod simulators in relatively bad condition

Bottom of cross section slab, 937 mm elevation, inverted to top view

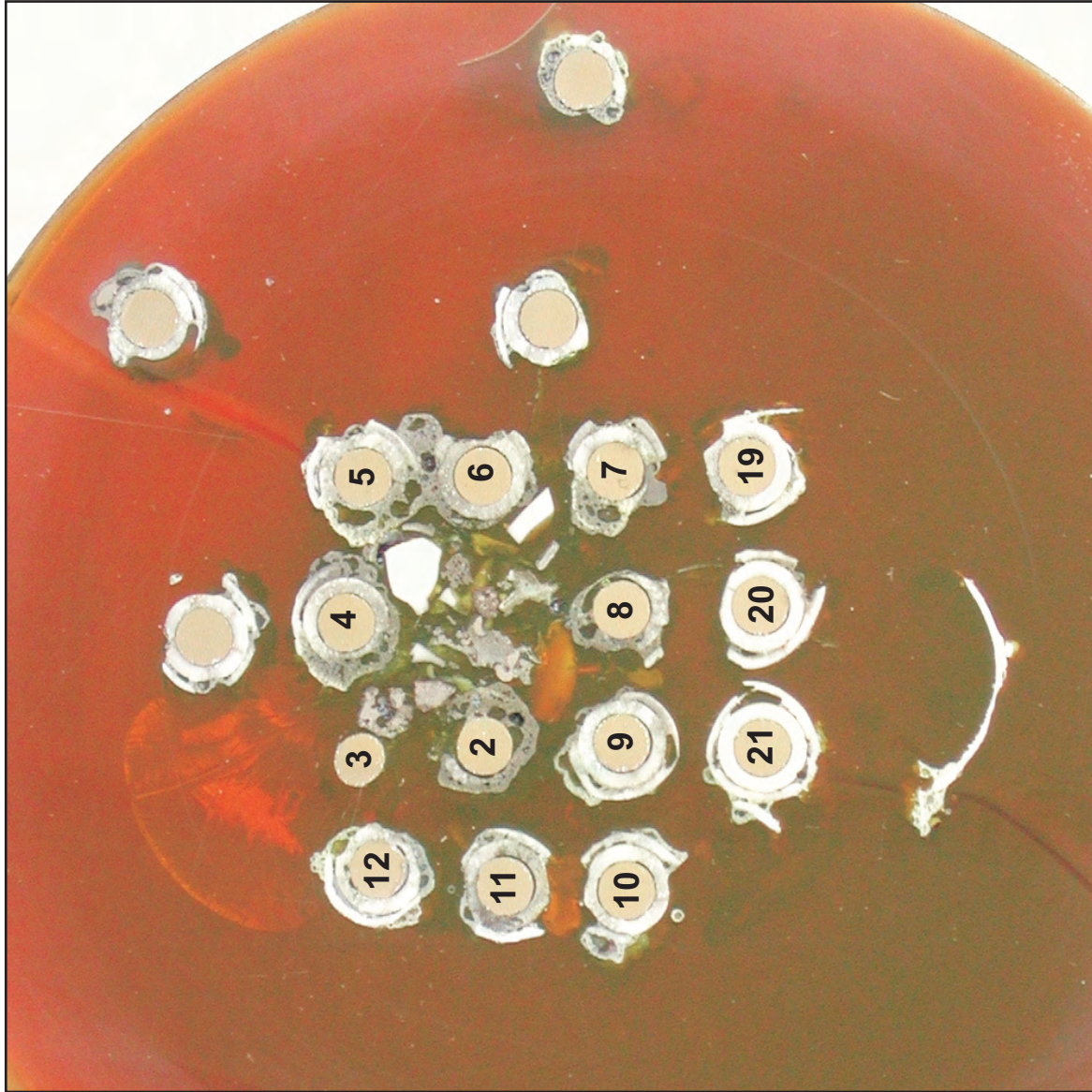
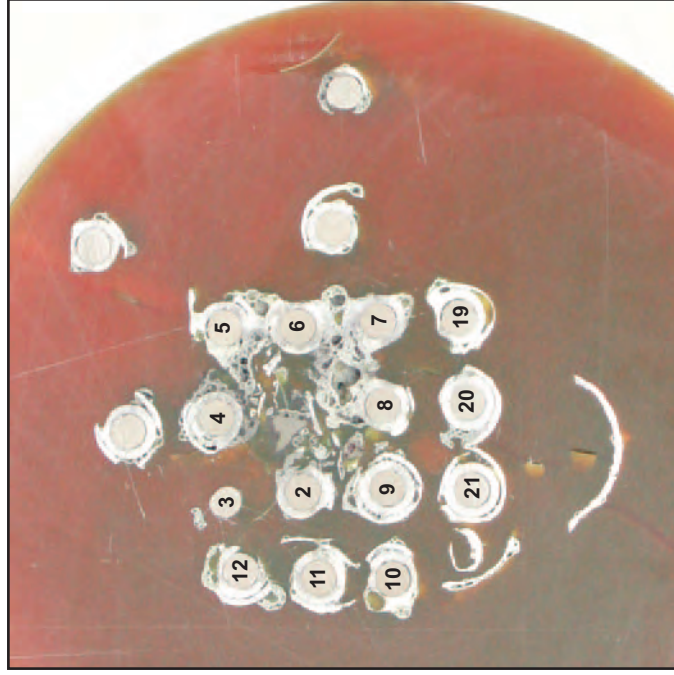
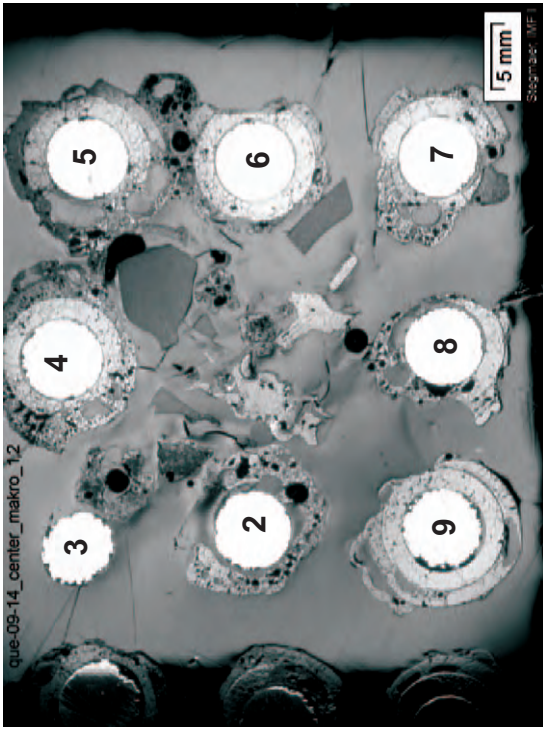
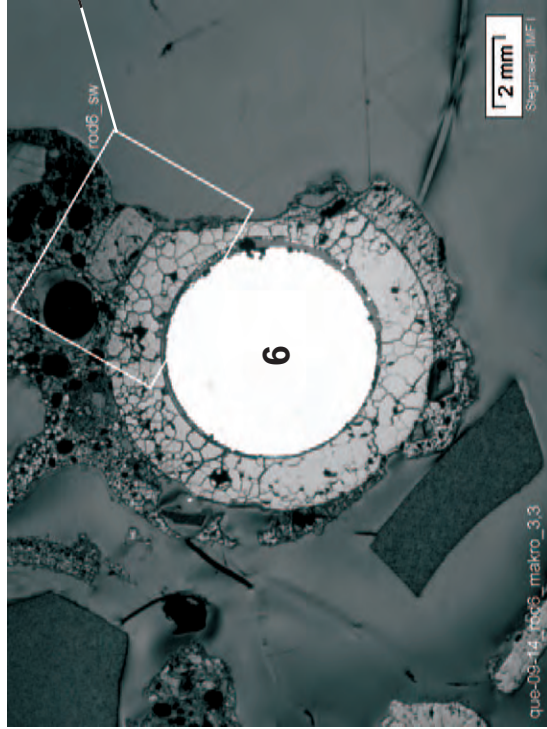
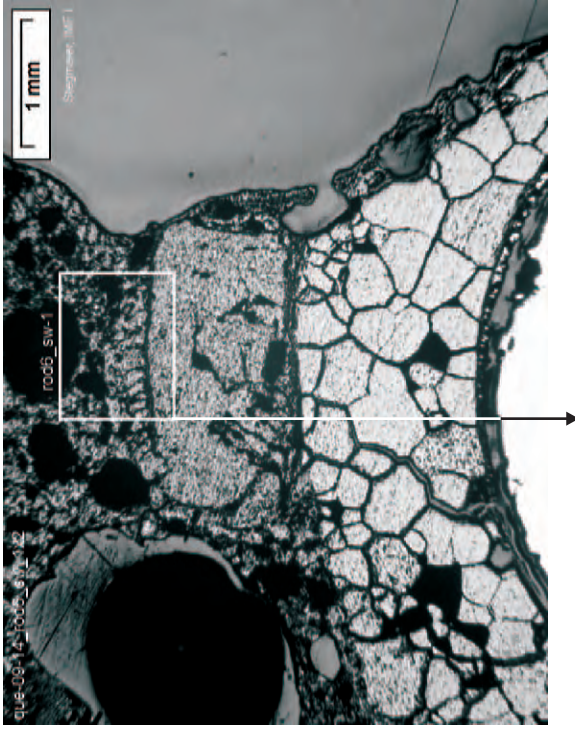


Fig. 76: QUENCH-09; Cross section at 950 mm bundle elevation (QUE-09-14); overview from top



Bundle centre, showing rubble fragments and the fuel rod simulators of the first ring

Details in SW direction from rod #6; tungsten heater, pellet, porous melt on enclosed cladding scale remnant



Macrograph of simulator rod #6

Melt, enclosing scale remnant within the above depicted range, in higher magnification

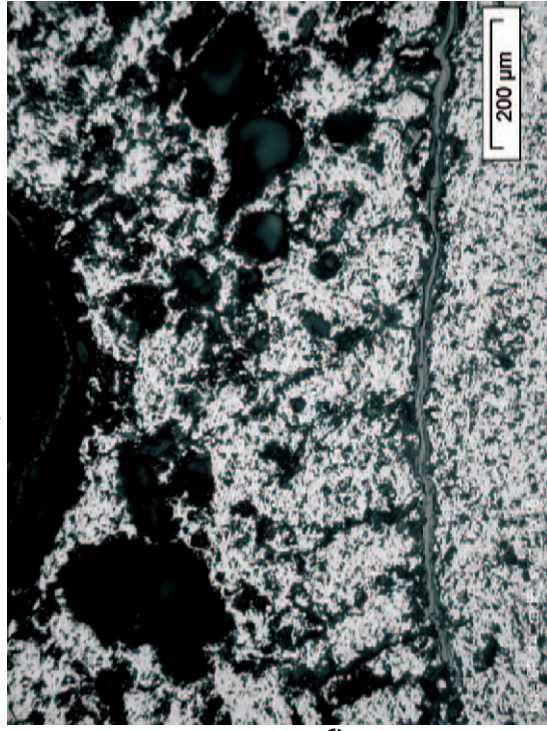
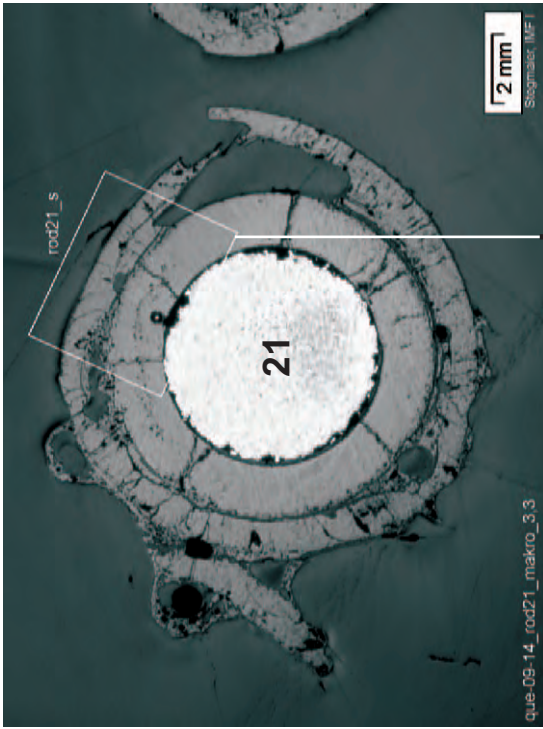
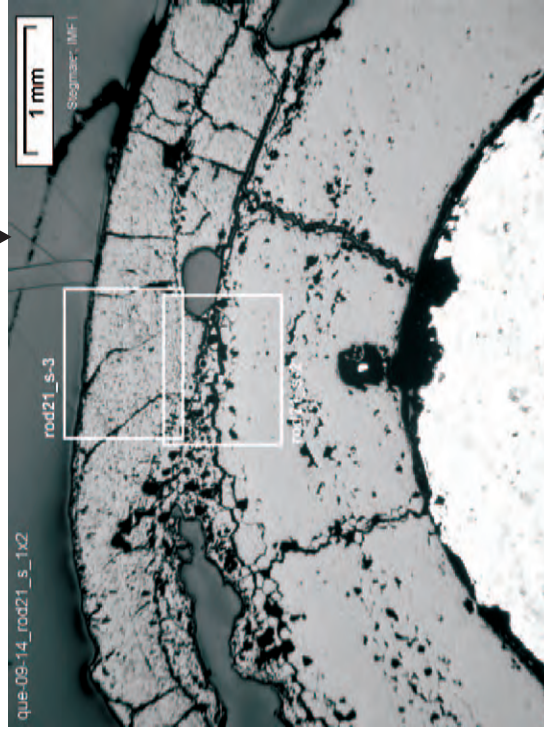


Fig. 77: QUENCH-09; Cross section at 950 mm elevation (QUE-09-14); bundle centre in closer view, state of fuel rod simulator #6, and details of melt in connection



Macrograph of fuel rod simulator #21

External part of the cladding, converted to compact, coarse-grained scale



State of cladding and pellet in SW direction



Internal part of the cladding and contact zone to the pellet, showing previous pellet interaction with molten metallic cladding, and intergranular crack path through ceramic product

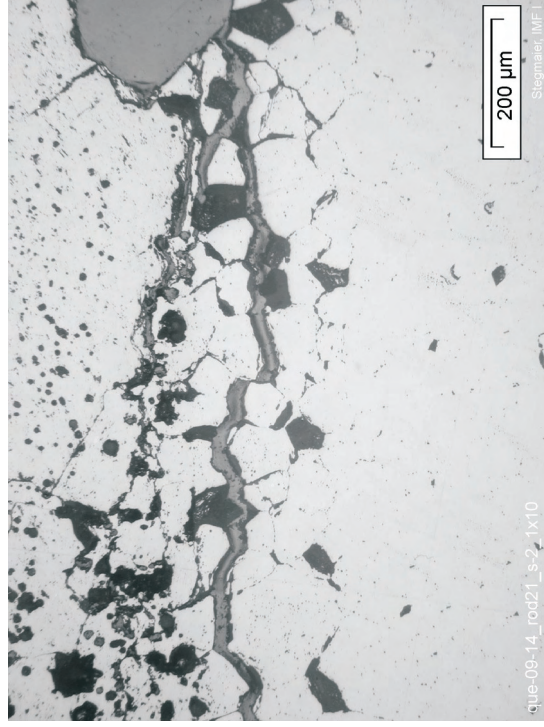
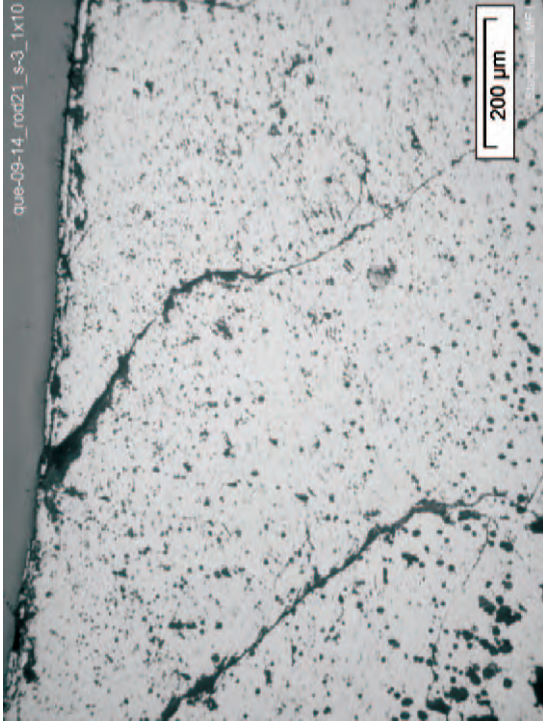


Fig. 78: QUENCH-09; Cross section at 950 mm elevation (QUE-09-14); fuel rod simulator #21 in SW direction, showing previous interaction of the cladding with the pellet and complete conversion to zirconia during free steam exposure

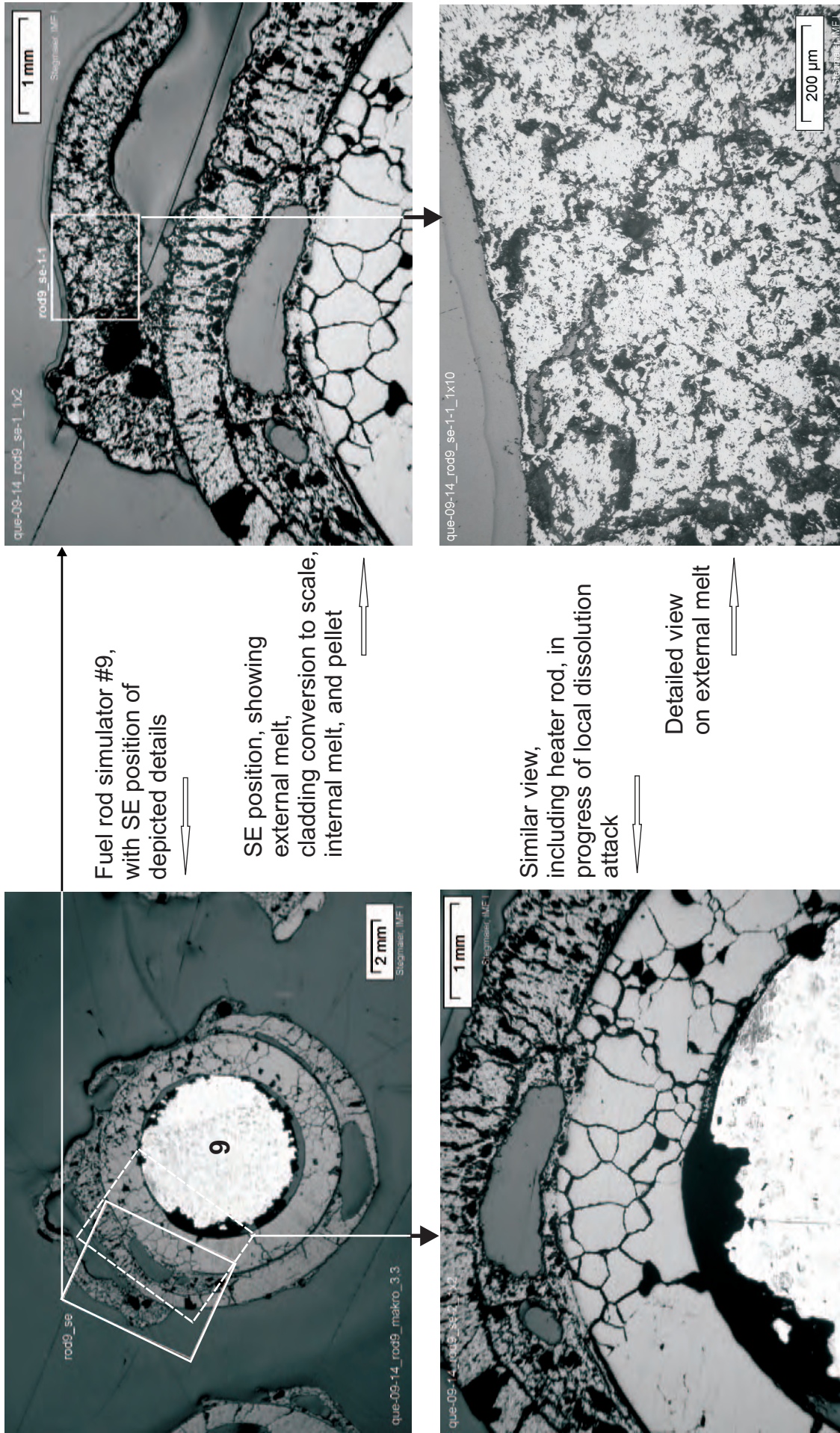
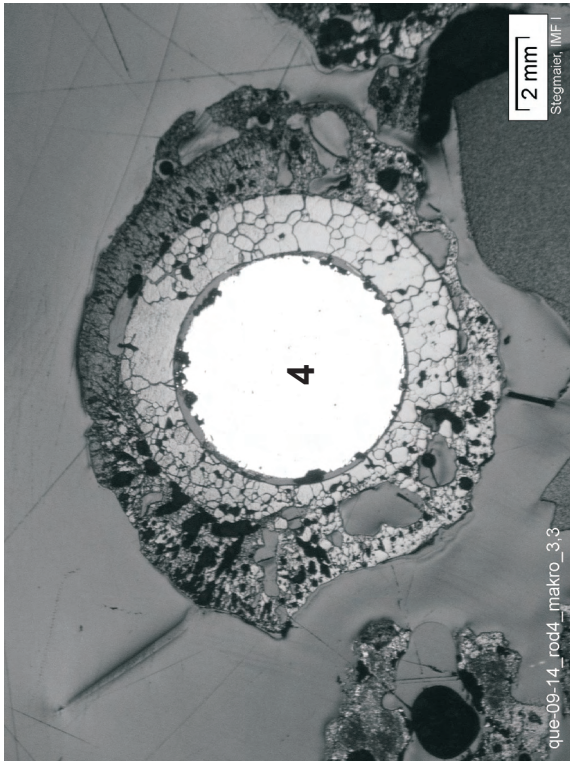


Fig. 79: QUENCH-09; Cross section at 950 mm elevation (QUE-09-14); fuel rod simulator #9 in SE direction, showing earlier internal cladding melting, adhering external melt, and considerable heater rod dissolution



The depicted simulator rods show essentially intact heater, mostly to partly remaining pellet, some residual converted cladding, and some external melt after complete oxidation

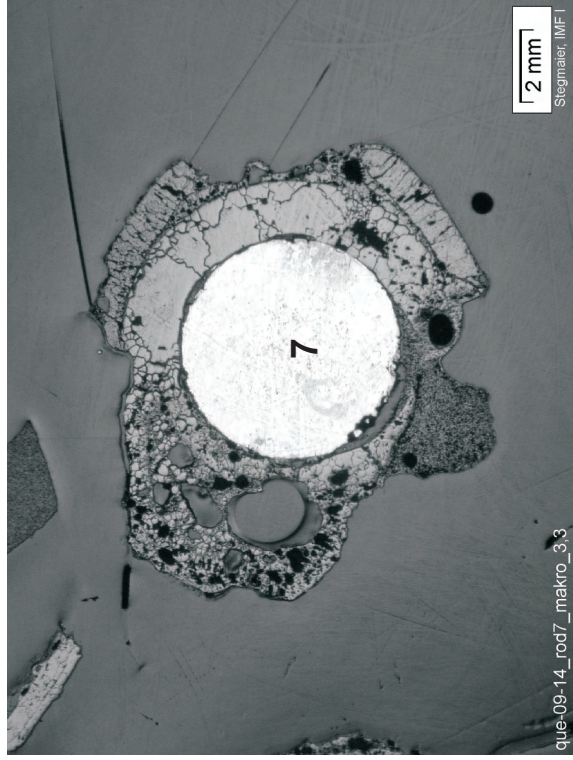
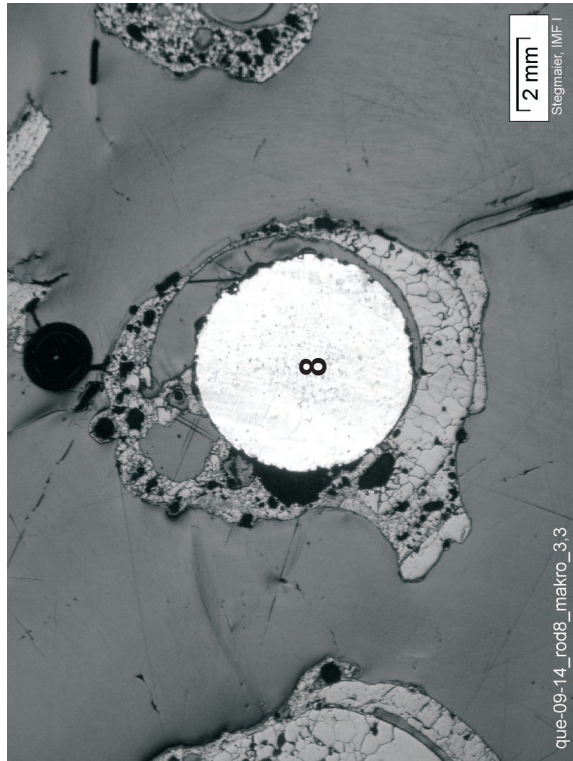
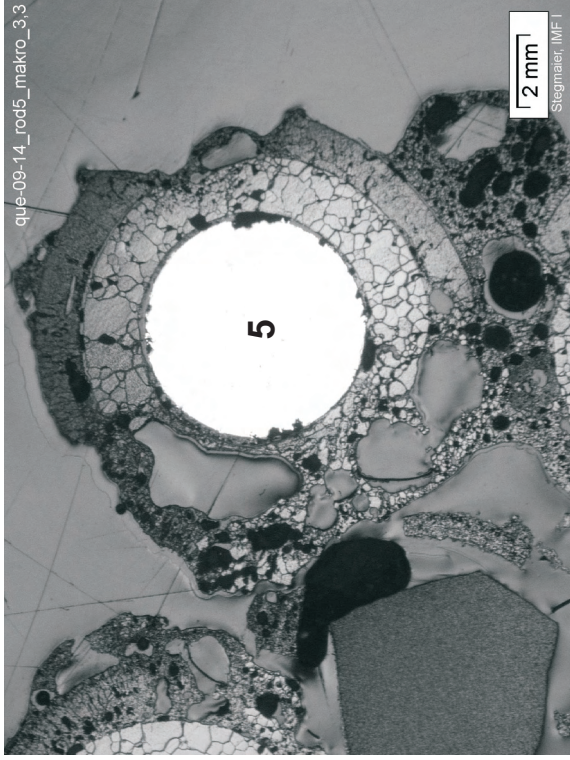
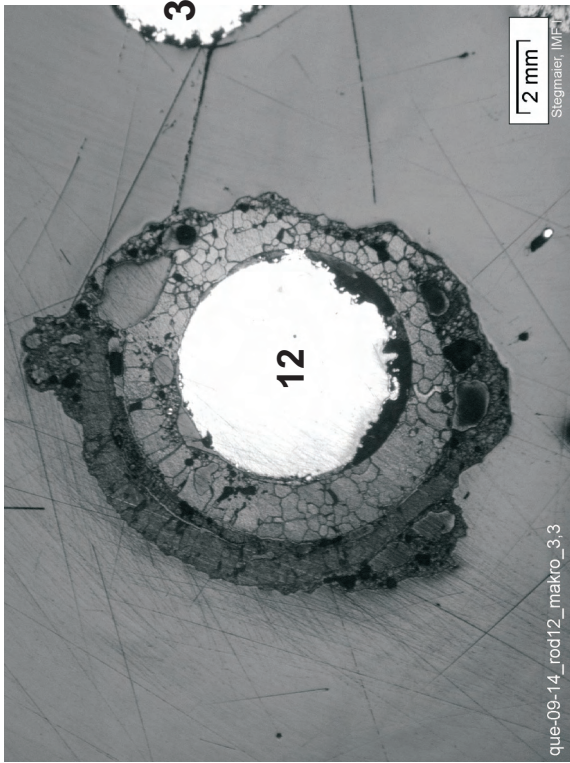


Fig. 80: QUENCH-09; Cross section at 950 mm elevation (QUE-09-14); examples for fuel rod simulators of the inner ring



Rod #12 and part of the bare heater of rod #3



Rod at S orientation (probably rod #13 or #14)



The depicted simulators show varying heater rod attack, completely remaining pellet circumference despite local dissolution, some residual oxidized cladding (only rods #10 and #19, bottom), and some converted external melt

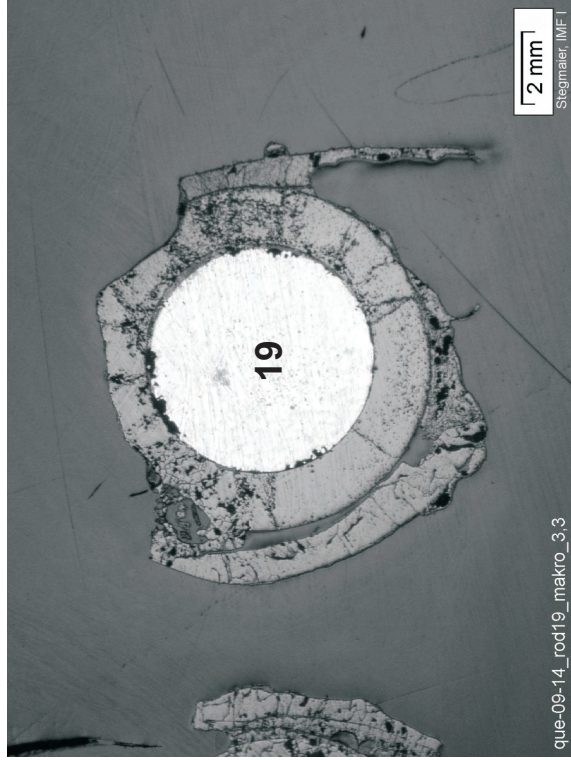
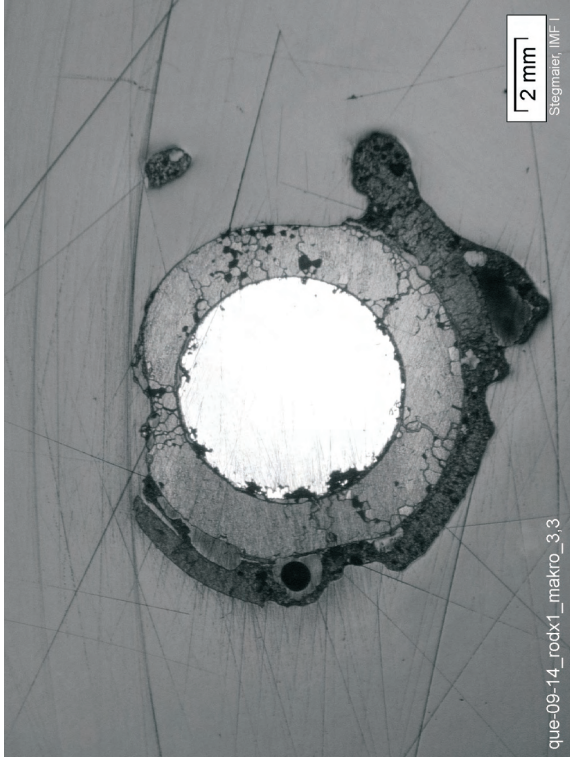


Fig. 81: QUENCH-09; Cross section at 950 mm elevation (QUE-09-14); examples for fuel rod simulators of the outer ring

Bottom of cross section slab, 1480 mm elevation, inverted to top view

Top of cross section slab, 1510 mm elevation, not inverted

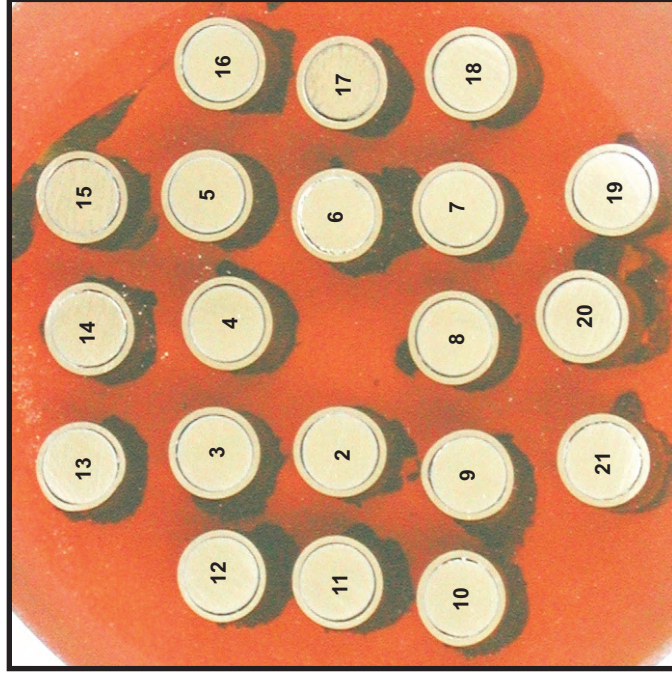
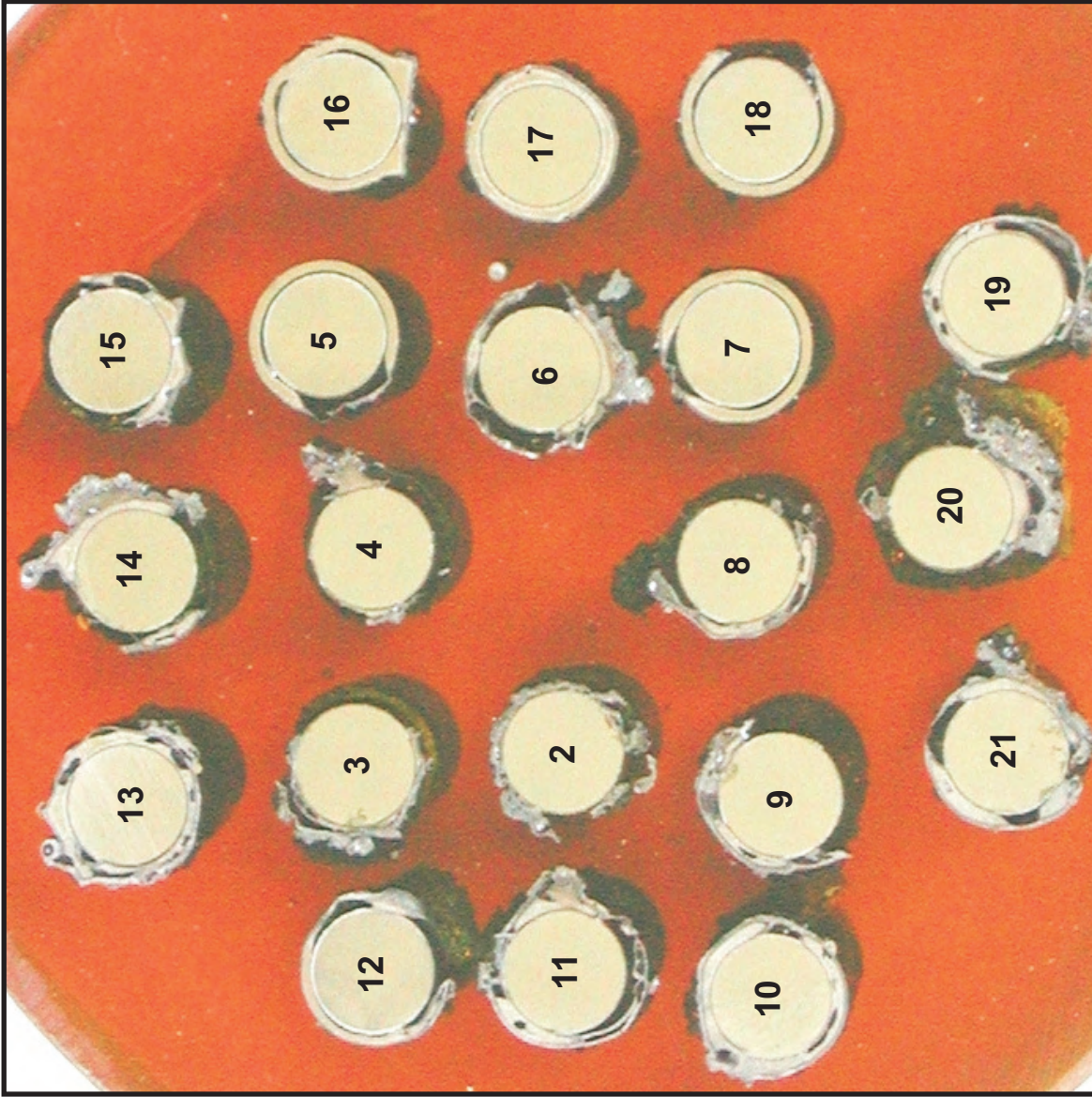
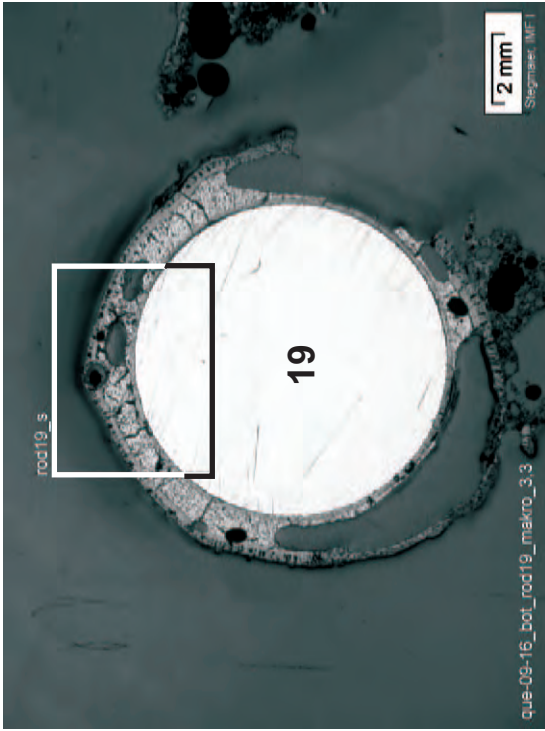
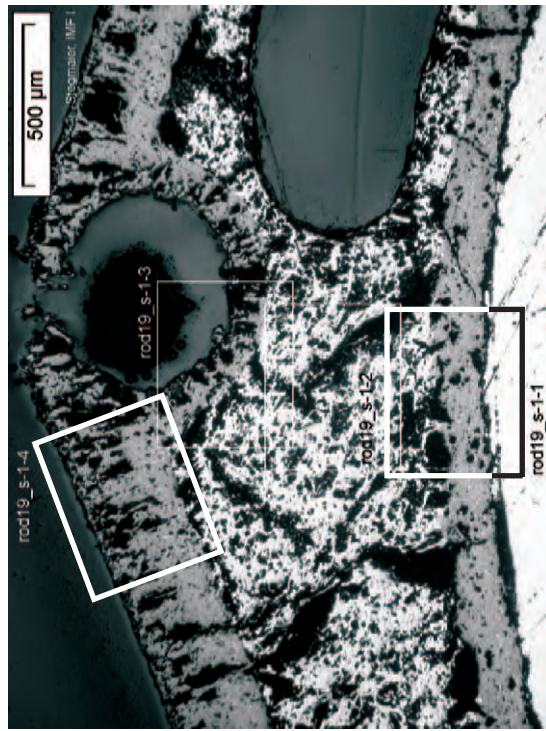
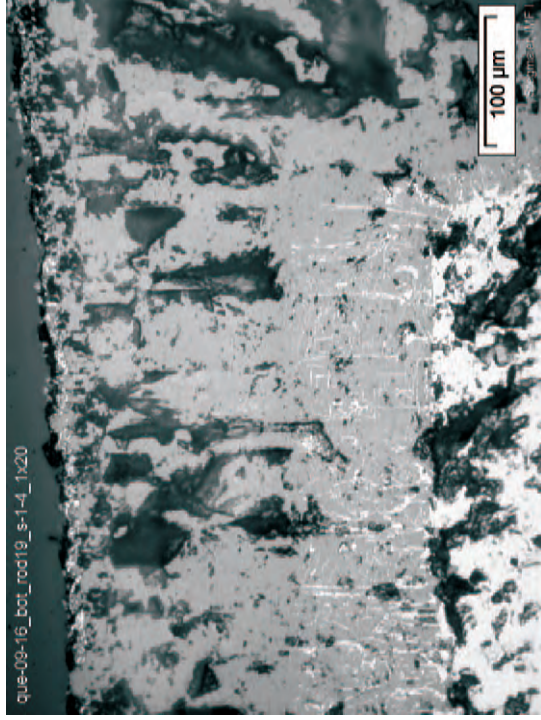


Fig.82: QUENCH-09; Cross section at 1480 mm bundle elevation (QUE-09-16, bottom); overview from top



Overview on rod #19 with position of micrograph series

Cladding scale with duplex (tetragonal/cubic) microstructure



Cladding, showing the external scale with a local defect, and a void in the once molten metallic cladding matrix; melt formation indicates peak temperature above 2030K

Once molten metallic cladding matrix, intact plasma-coating layer of zirconia, and molybdenum electrode

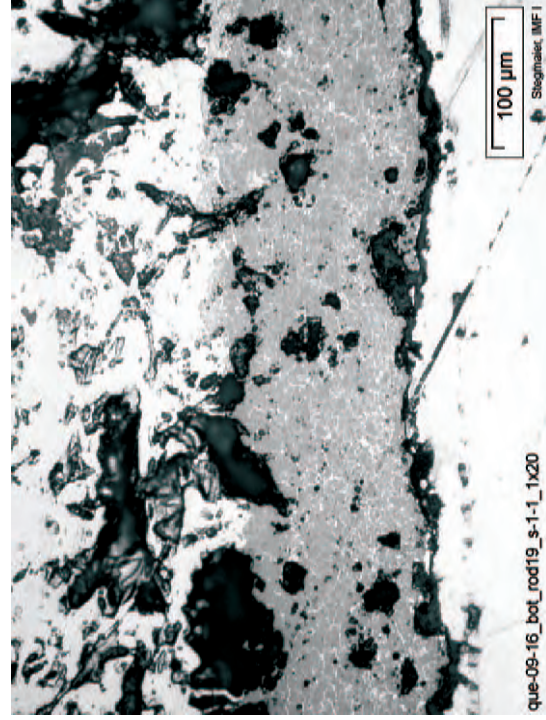
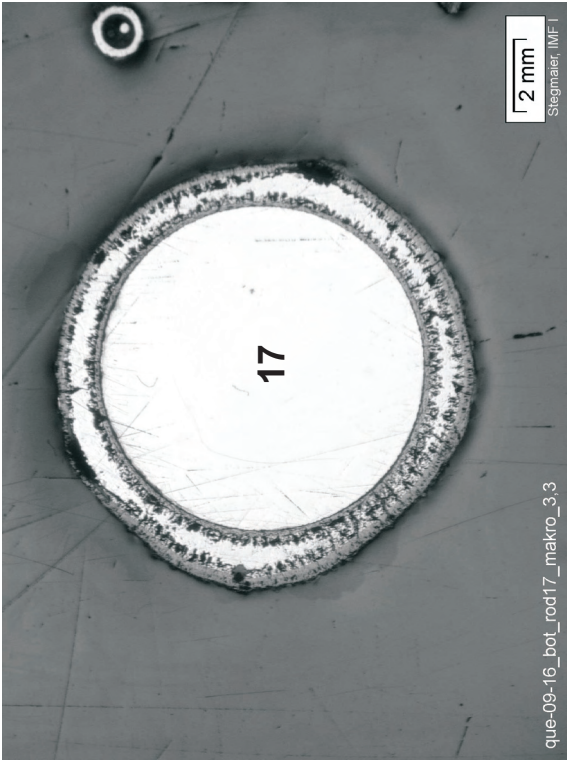
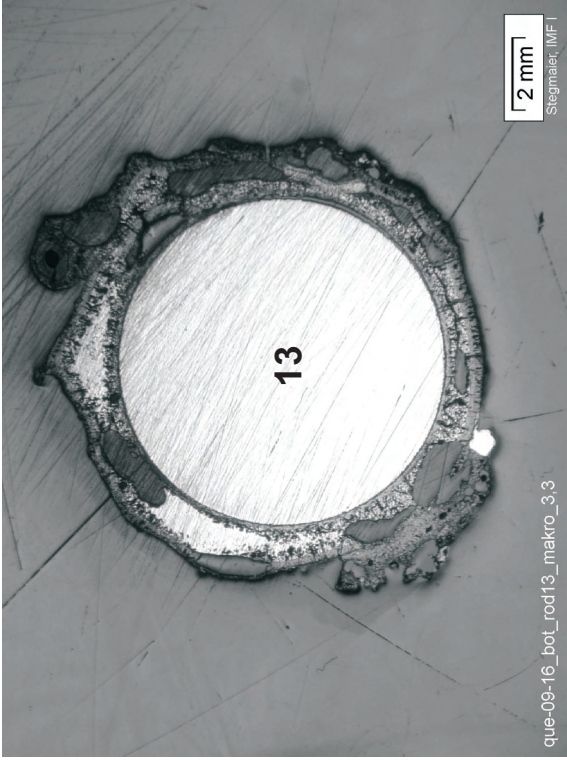


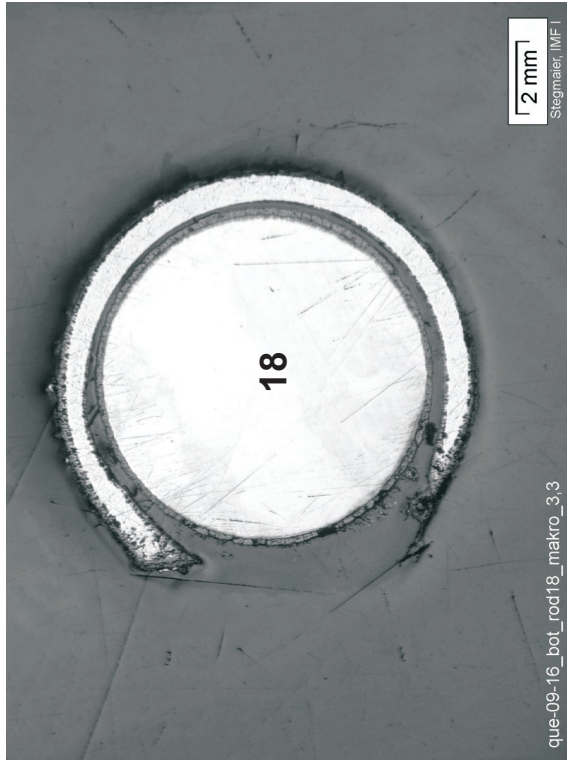
Fig. 83: QUENCH-09; Cross section at 1480 mm elevation (QUE-09-16, bottom); oxidation state of fuel rod simulator #19, consisting of molybdenum electrode rod, plasma-coated by zirconia layer, and the Zry cladding



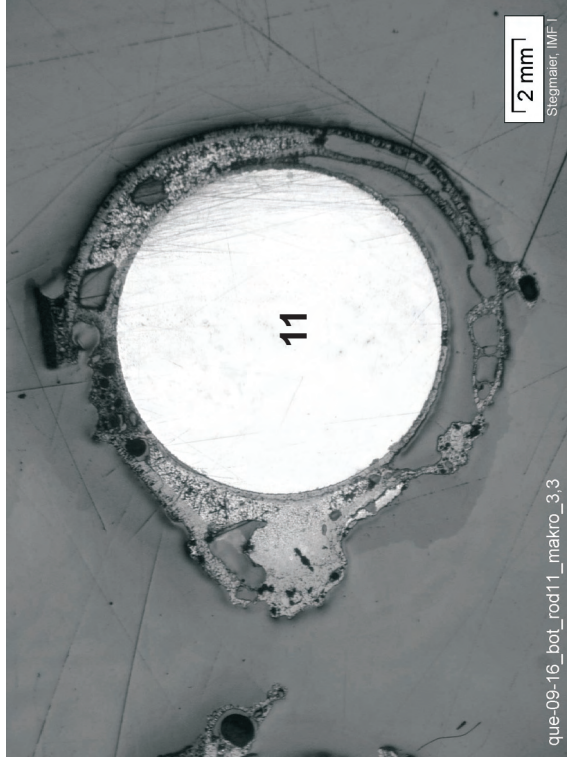
Rod #17, with totally remaining oxidized cladding



Rod #13 with remaining heavily oxidized cladding some cladding melt relocation, and some external melt

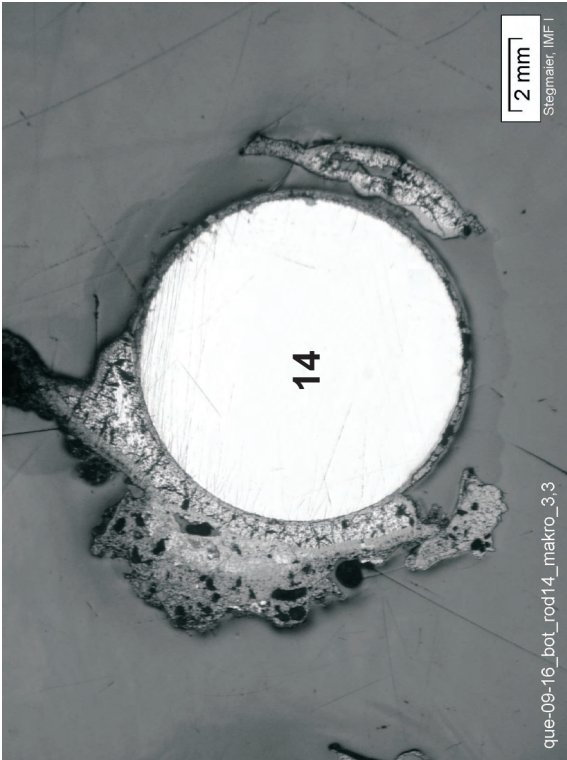


Rod #18, showing cladding breach, open due to melt loss



Rod #11, showing melt relocation and empty scale structures

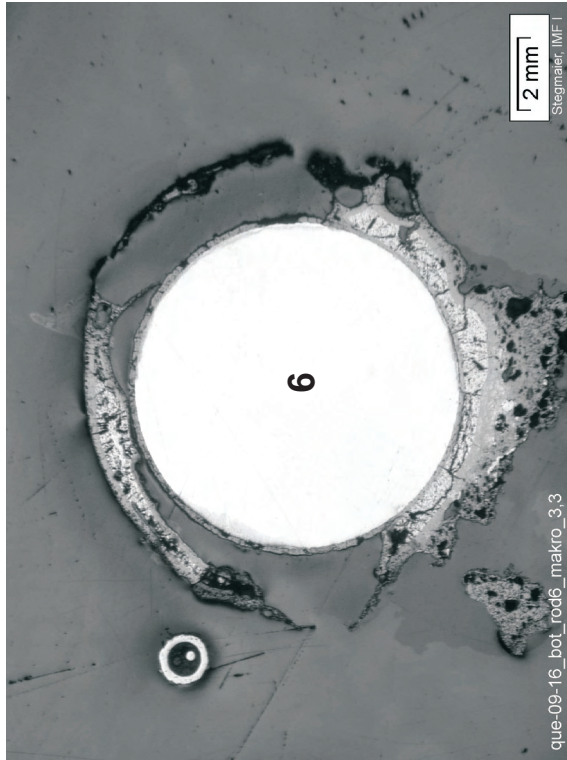
Fig. 84: QUENCH-09; Cross section at 1480 mm elevation (QUE-09-16, bottom); state of selected fuel rod simulators in fair condition



Rod #14, showing loss of cladding and accumulation of melt



Rod #3, showing advanced oxidation and melting of the partly present cladding



Rod #6, showing cladding breach formation and melt redistribution



Rod #4, showing advanced oxidation of residual melt

Fig. 85: QUENCH-09; Cross section at 1480 mm elevation (QUE-09-16, bottom); selected fuel rod simulators with intact molybdenum electrode and zirconia coating, but strongly damaged cladding

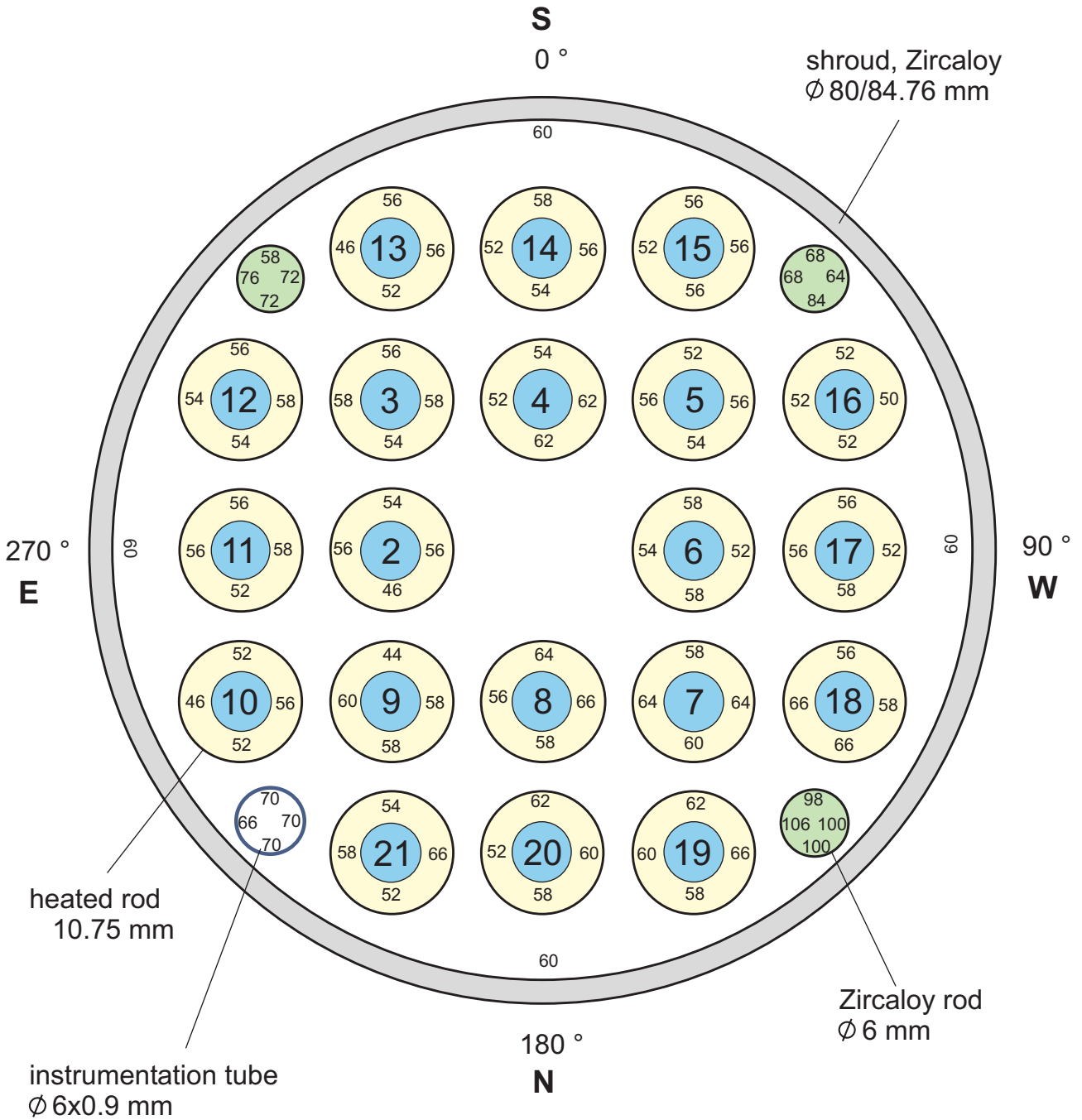


Fig.86-QUE09 cross section 18.cdr
30.08.04 - IMF

Fig. 86: QUENCH-09; Oxide layer thickness at bundle elevation 460 mm (Cross section QUE-09-18)

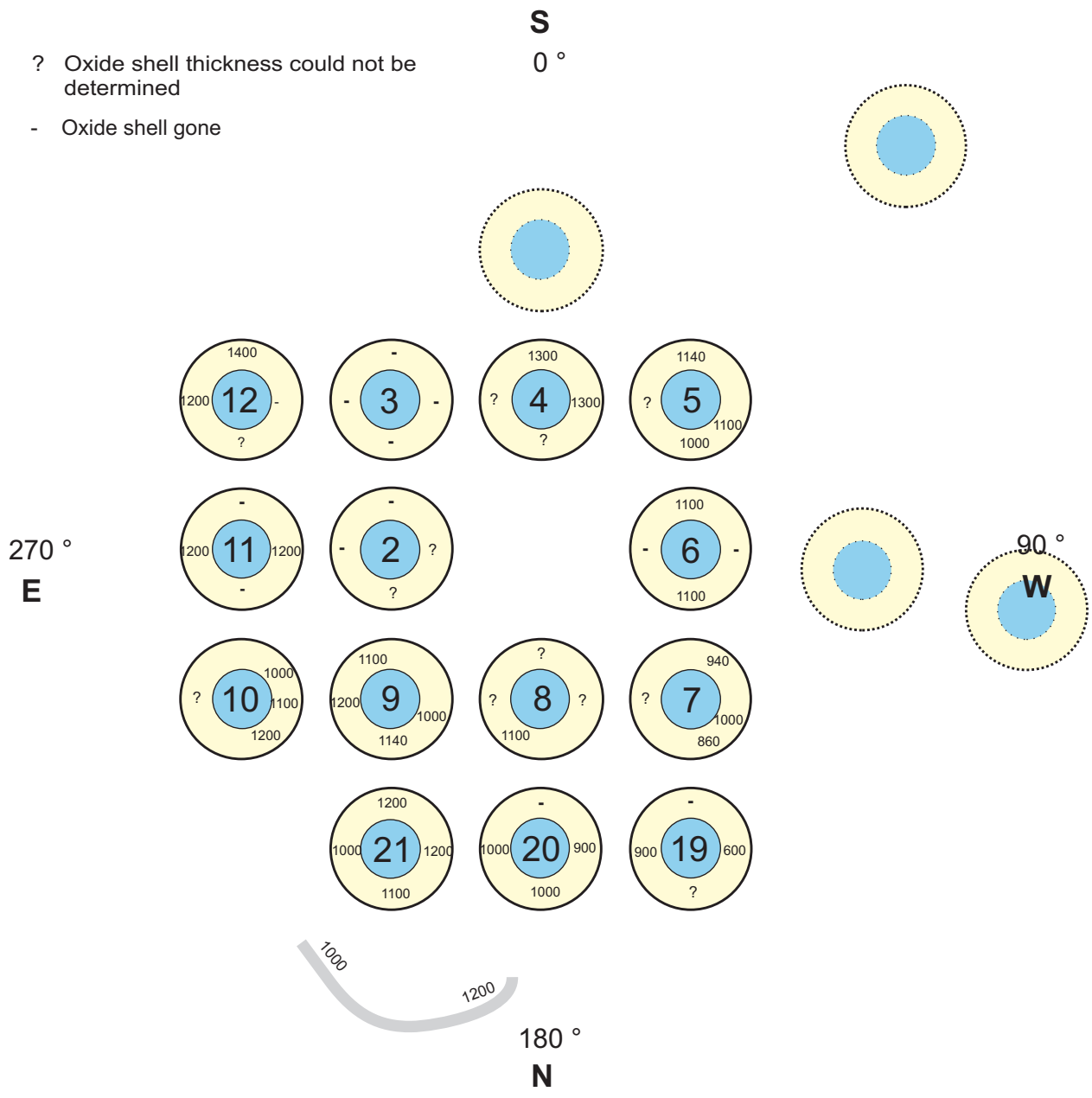


Fig.88-QUE09 cross section 14.cdr
 30.09.04 - IMF

Fig. 88: QUENCH-09; Oxide layer thickness at bundle elevation 950 mm (Cross section QUE-09-14)

- ? Oxide shell thickness could not be determined because of relocated and oxidized melt
- Cladding and oxide shell gone

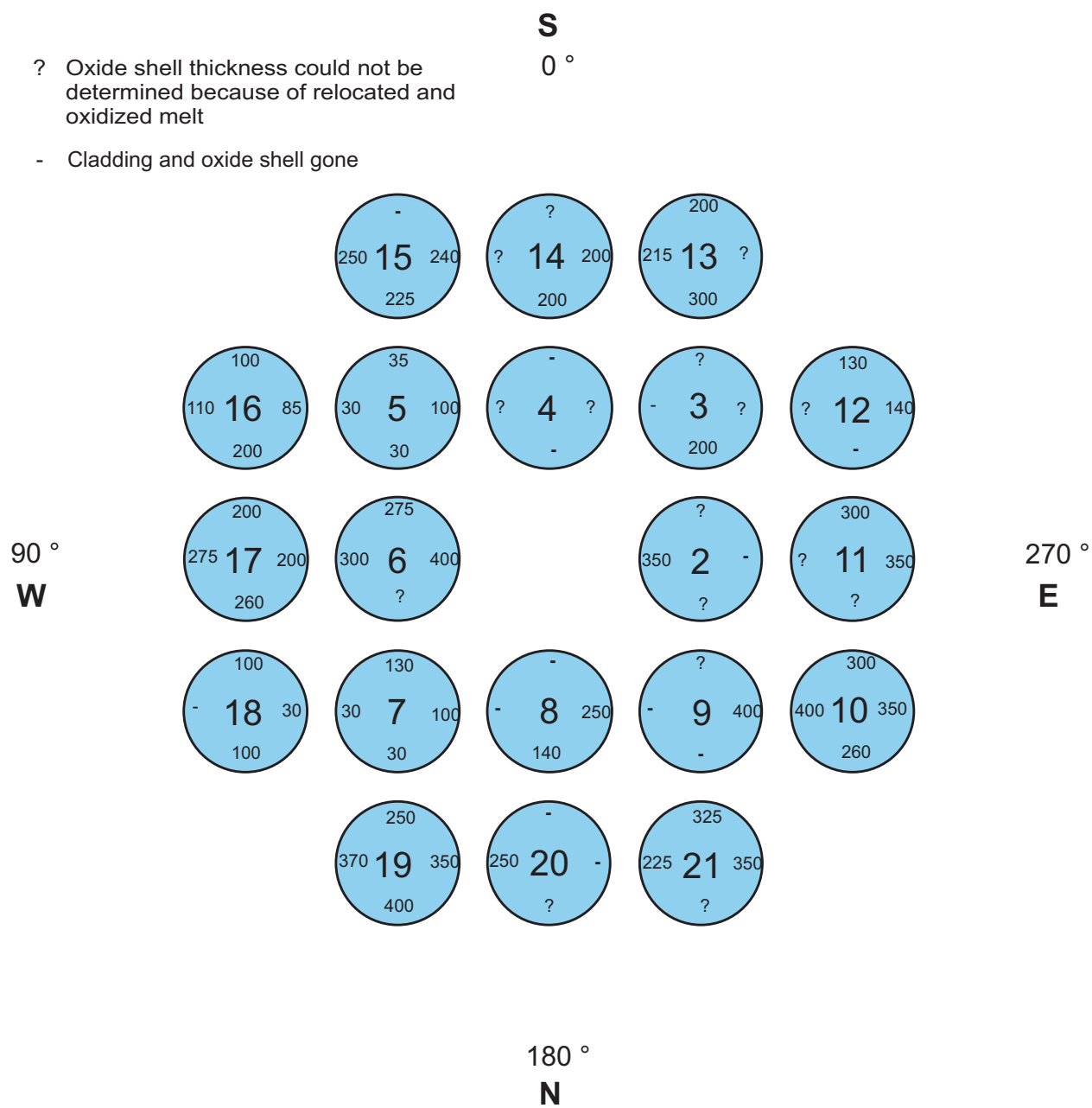


Fig. 89: QUENCH-09; Oxide layer thickness at bundle elevation 1480 mm (Cross section QUE-09-16)

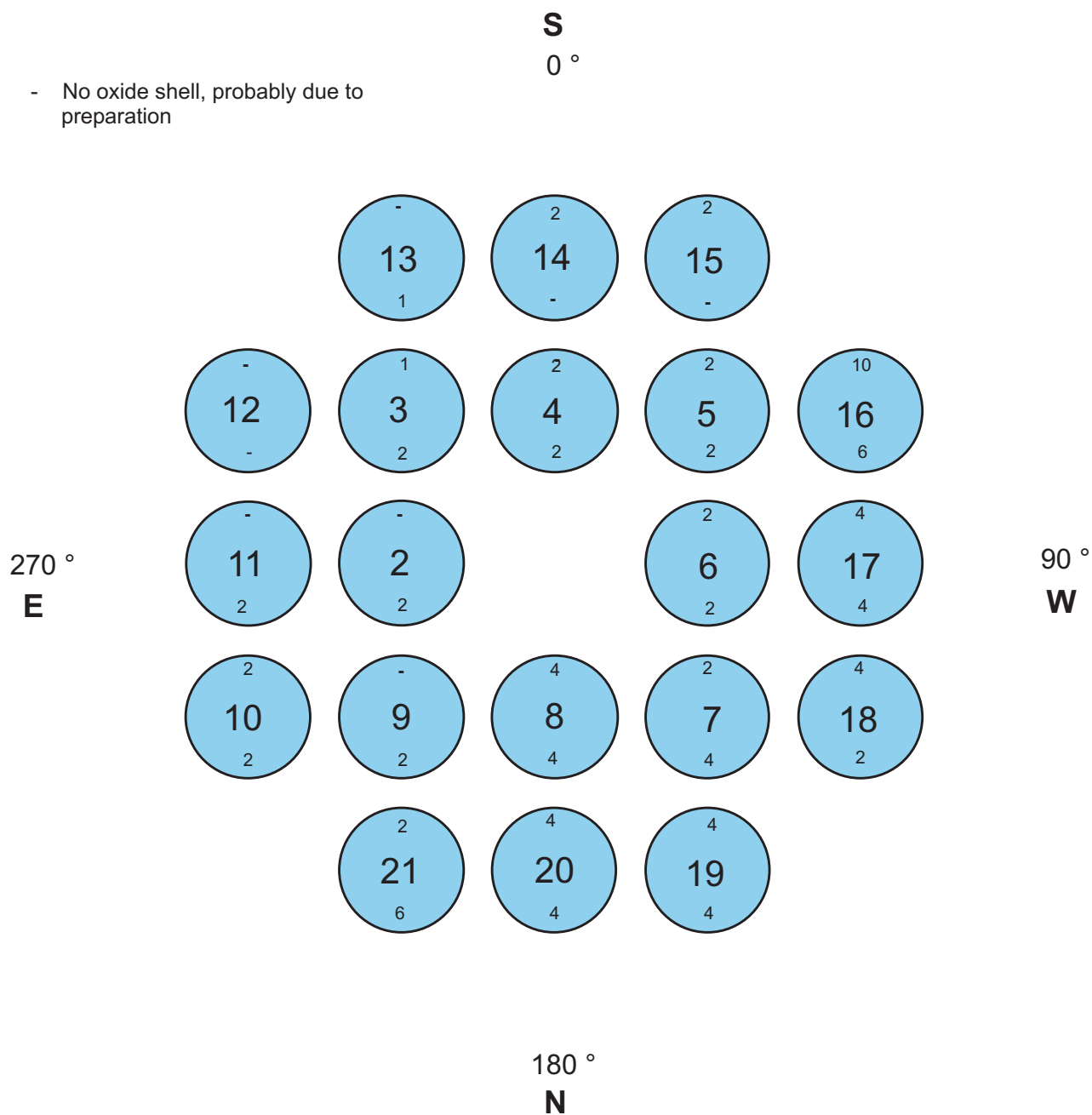


Fig.90-QUE09 cross section 16.cdr
12.10.04 - IMF

Fig. 90: QUENCH-09; Oxide layer thickness at bundle elevation 1510 mm
(Cross section QUE-09-16)

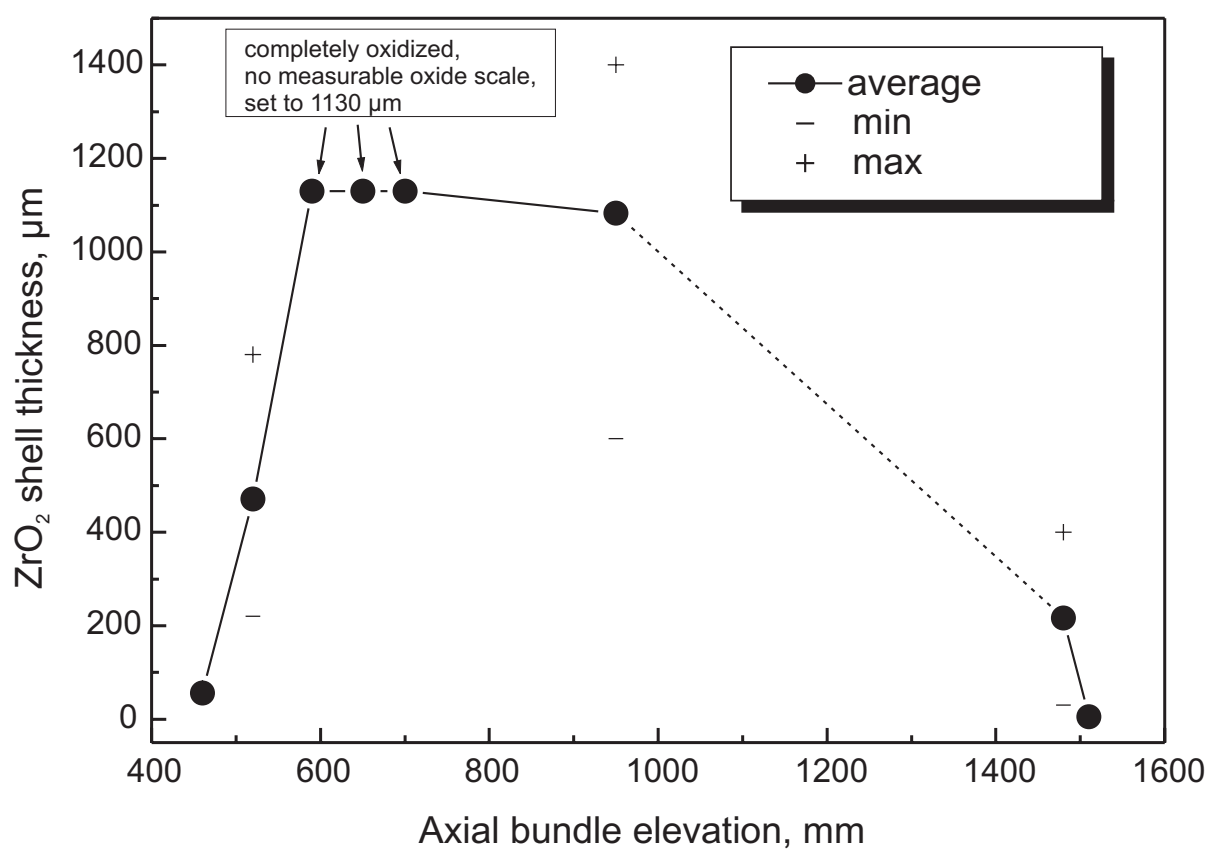
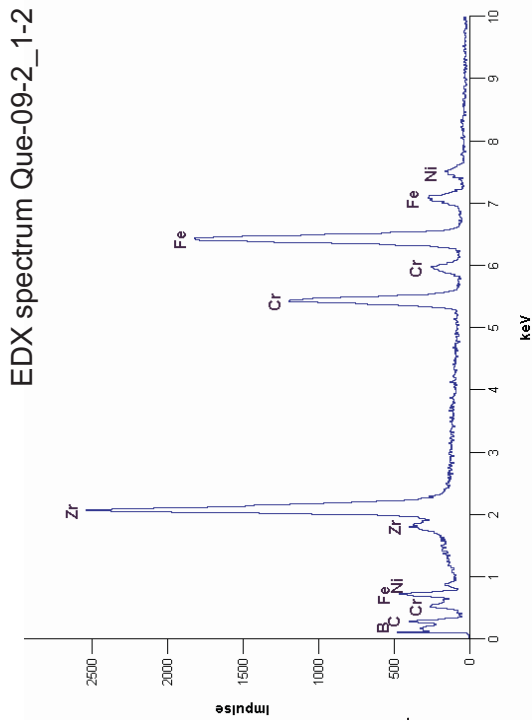
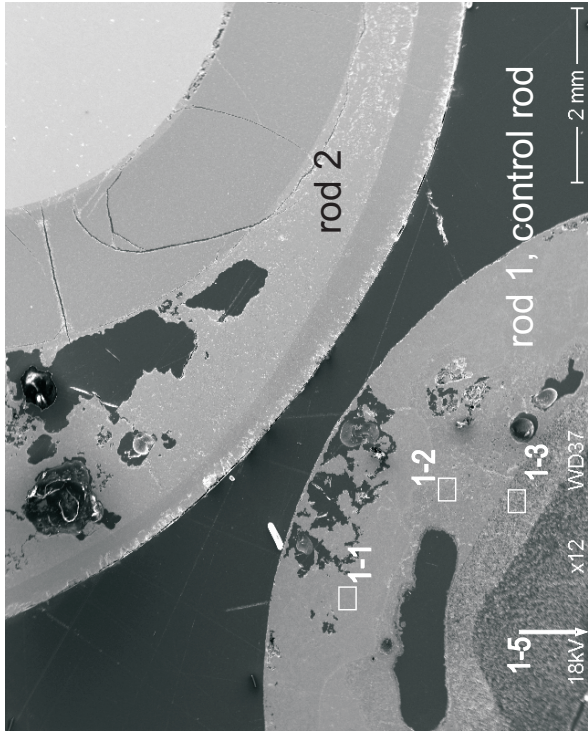


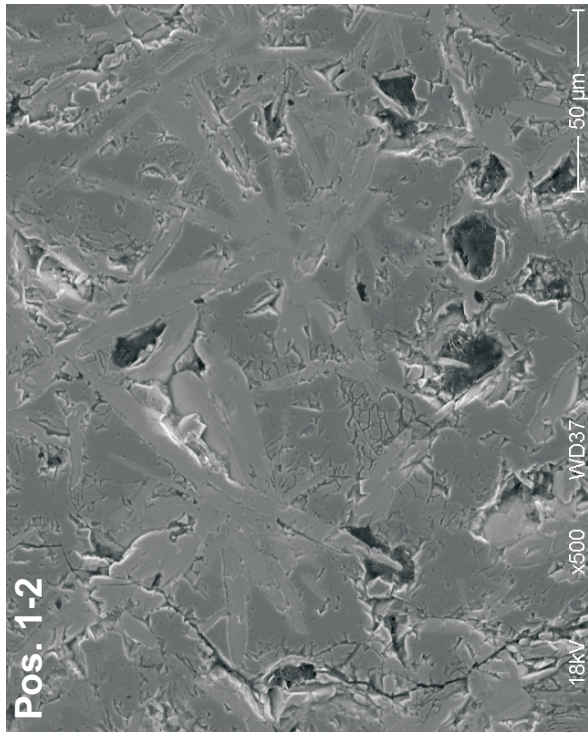
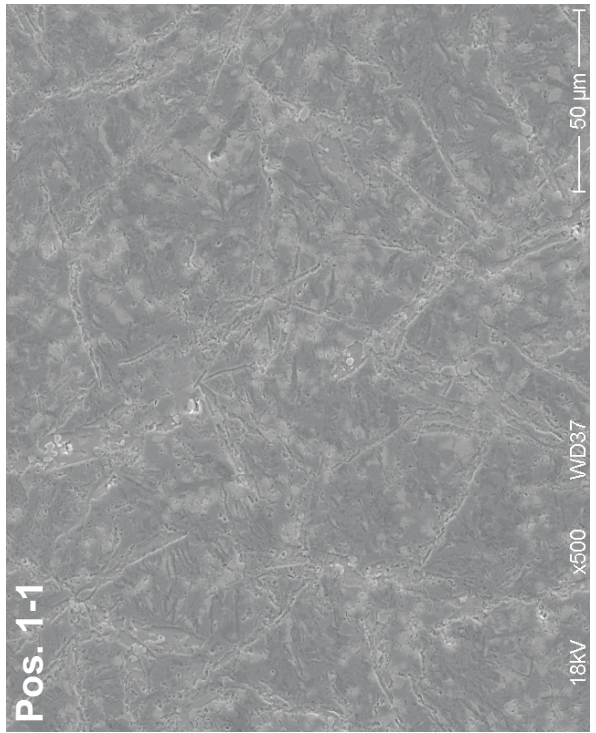
Fig.91-QUE09-oxide scale.cdr
30.09.04 - IMF

Fig. 91: QUENCH-09; Axial distribution of the oxide scale thickness



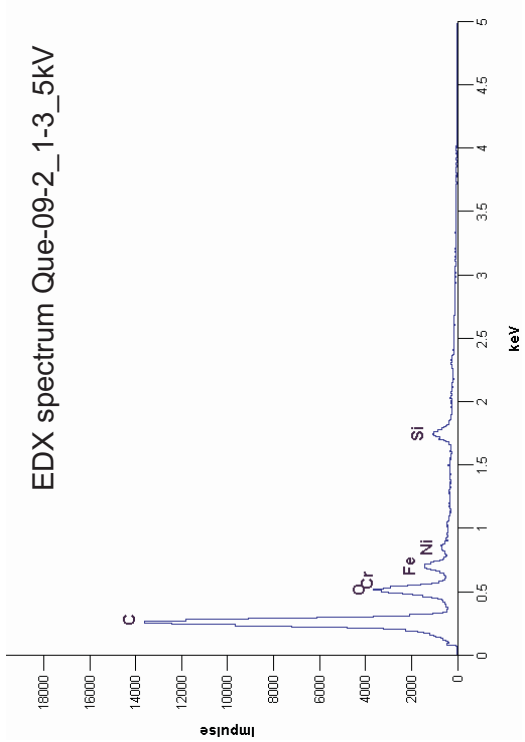
Control rod (left, with indicated EDX analysis positions) and rod #2

EDX spectrum of the below illustrated field of absorber melt; similar spectrum obtained for left field below



SEM images of analysed fields of absorber melt

Fig. 92: QUENCH-09; Cross section at 520 mm elevation (QUE-09-2); SEM/EDX analysis of melt within peripheral zones of the control rod (compare with next figure and Fig. 52)



Left: Spectrum and depicted field of analysis near the absorber pellet
 Right: Same for position within the absorber pellet

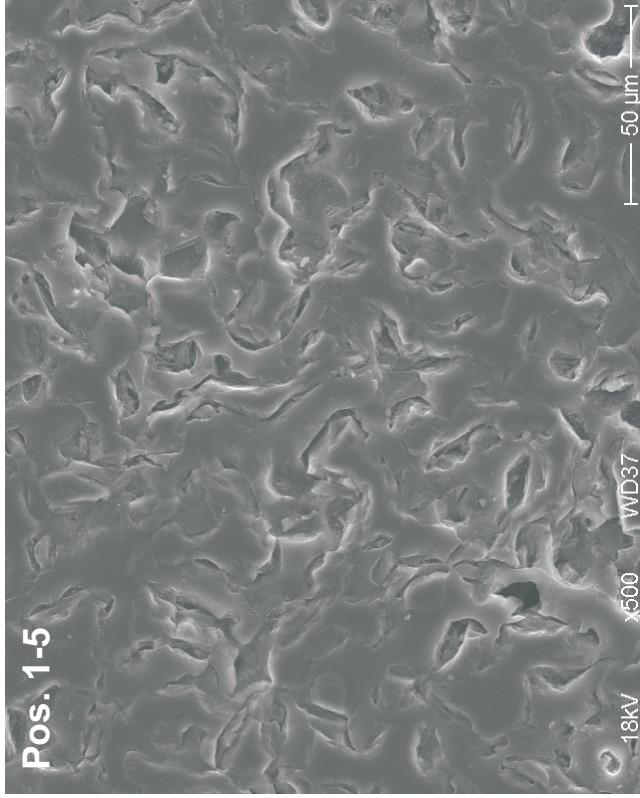
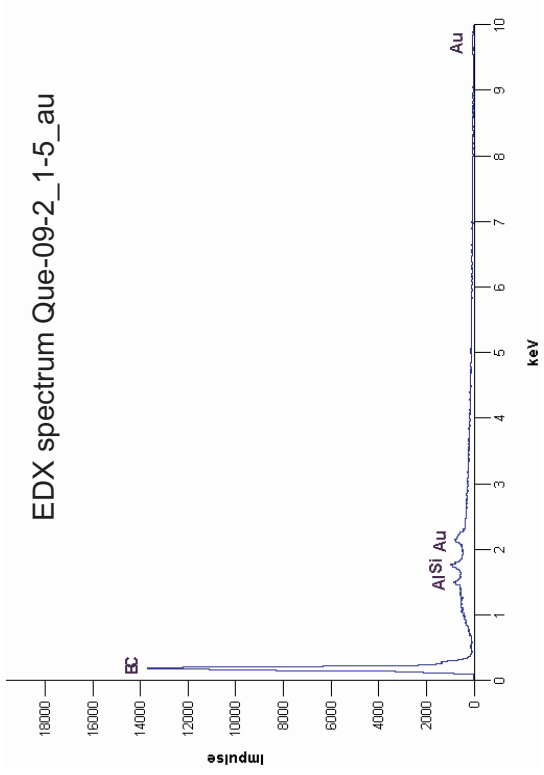
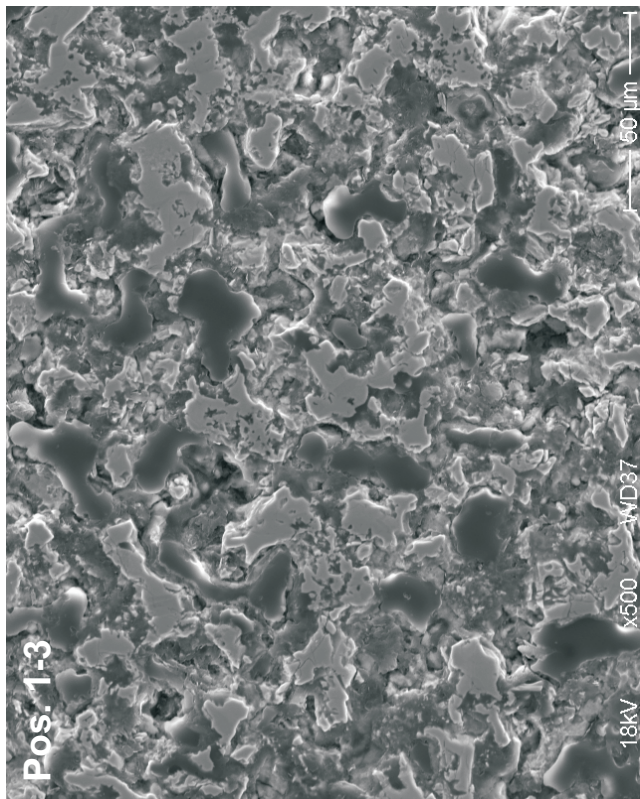
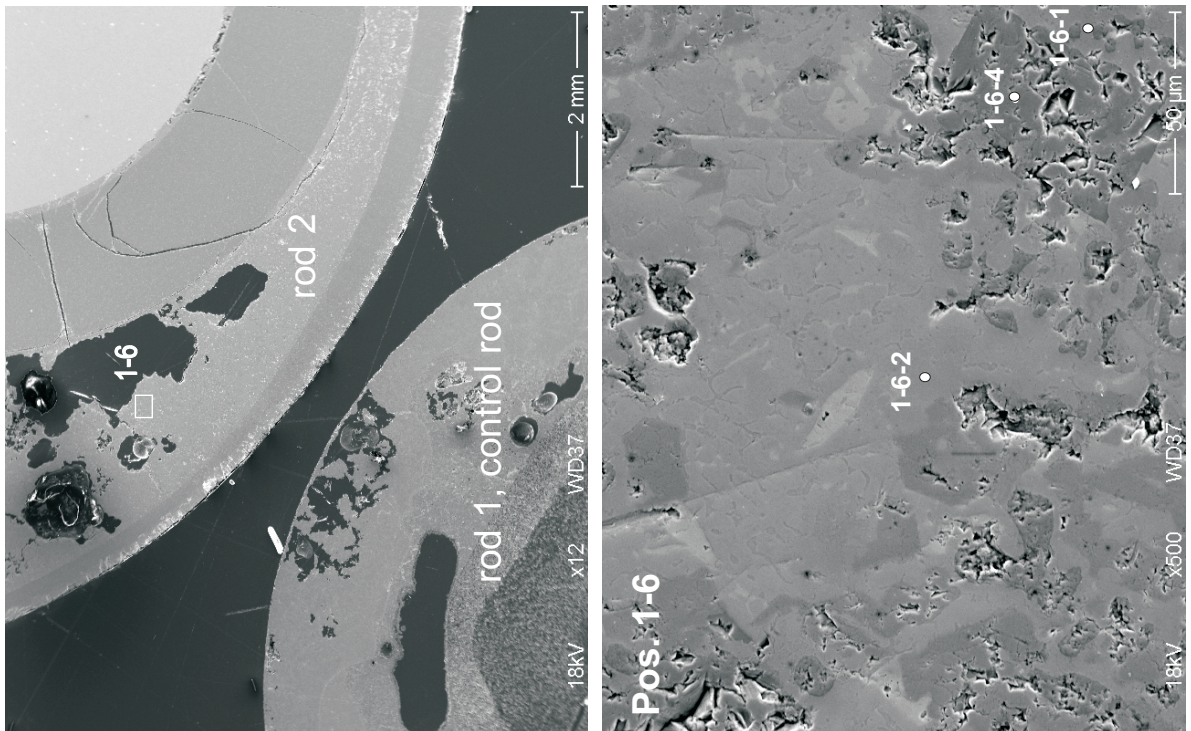


Fig. 93: QUENCH-09; Cross section at 520 mm elevation (QUE-09-2); SEM/EDX analysis of melt, close to and within the absorber pellet (compare with previous figure and Fig. 52)



Rod #2 with indicated SEM/EDX analysis positions

Right: Element spectra of small area analysis:

Zr-Sn phase, typical for residual metallic cladding

Carbon and steel components from absorber melt admixture

Zr-(B,C) phase (minor Ta content from thermocouple sheath)

Fig. 94: QUENCH-09; Cross section at 520 mm elevation (QUE-09-2); SEM/EDX analysis of melt within rod #2, verifying spreading and mixing of CR melt during downward relocation in damaged rods (see Fig. 54)

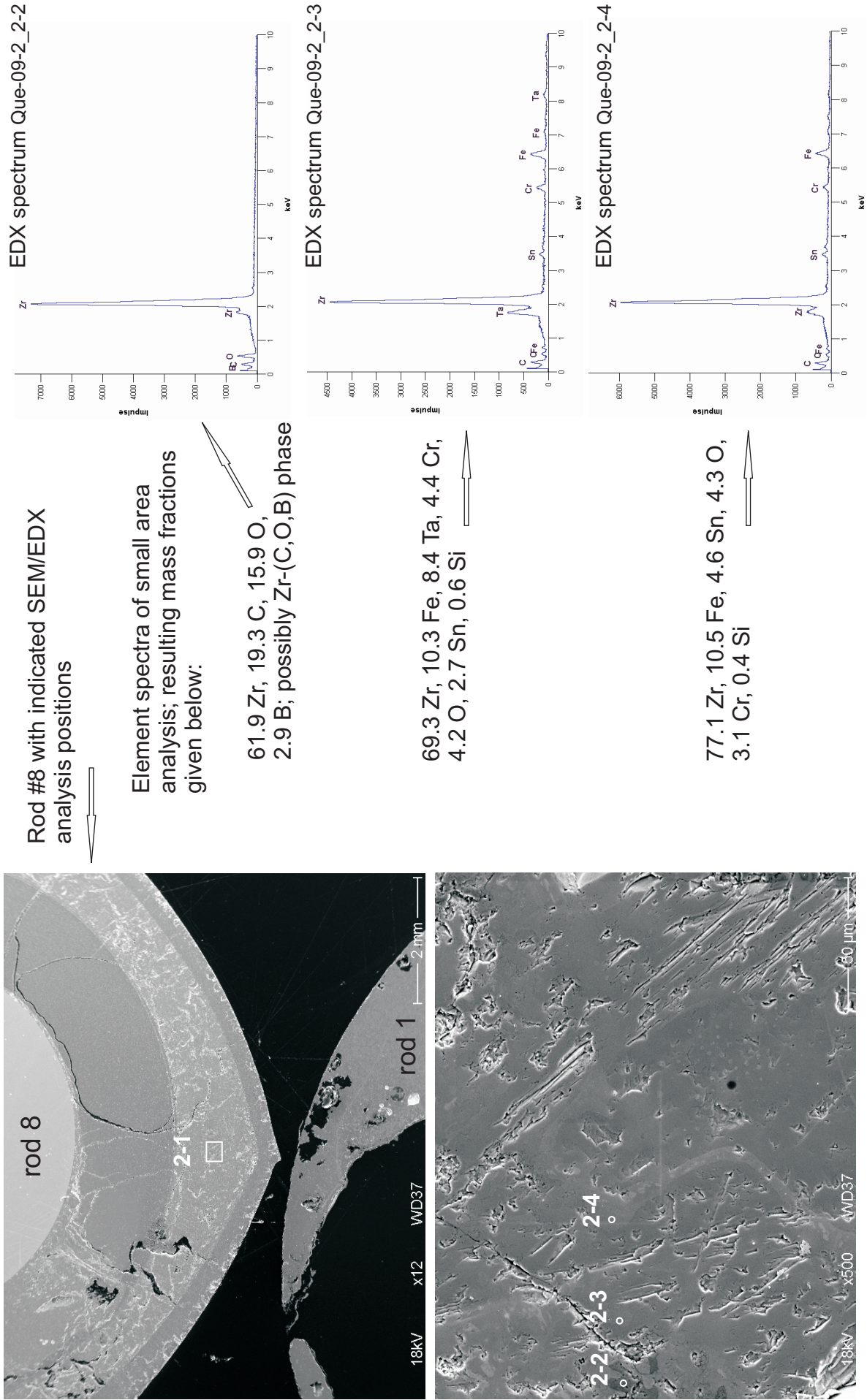
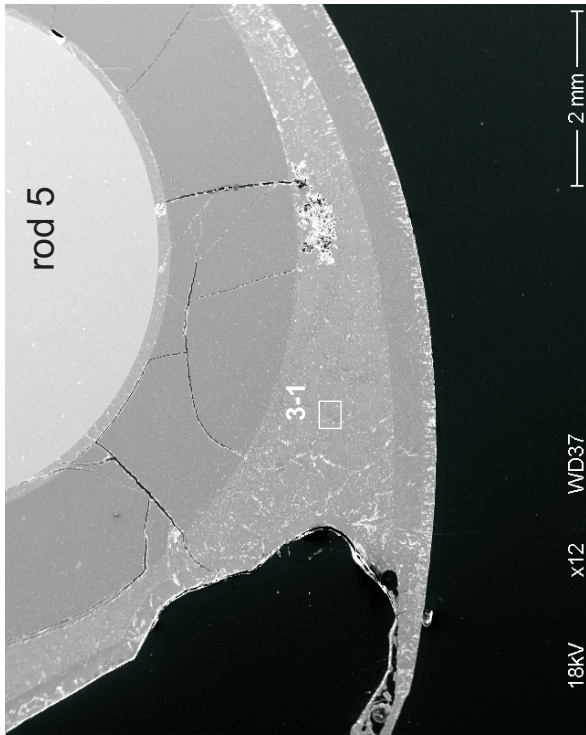
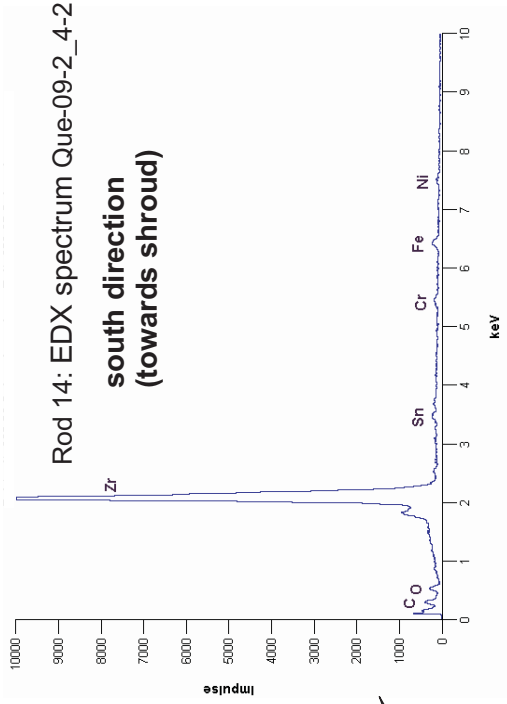


Fig. 95: QUENCH-09; Cross section at 520 mm elevation (QUE-09-2); SEM/EDX analysis of melt within rod #8, indicating presence of control rod degradation products



Rod #5, view indicates position and small area of element analysis (top), element spectrum (bottom)



Rod #14, element spectra obtained within metallic cladding below the closed scale

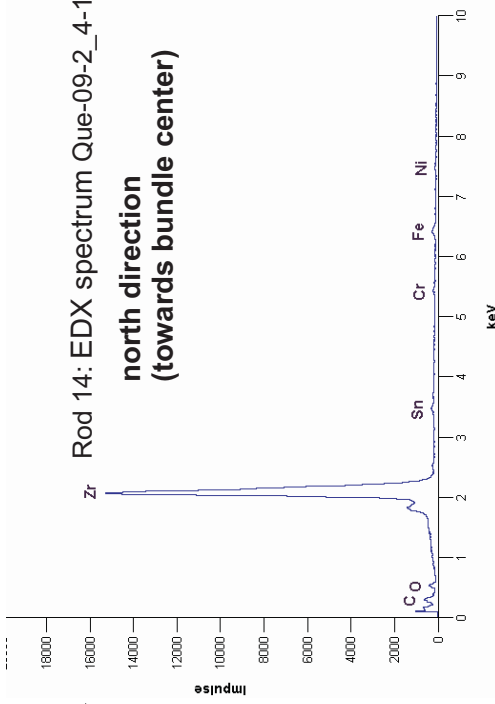
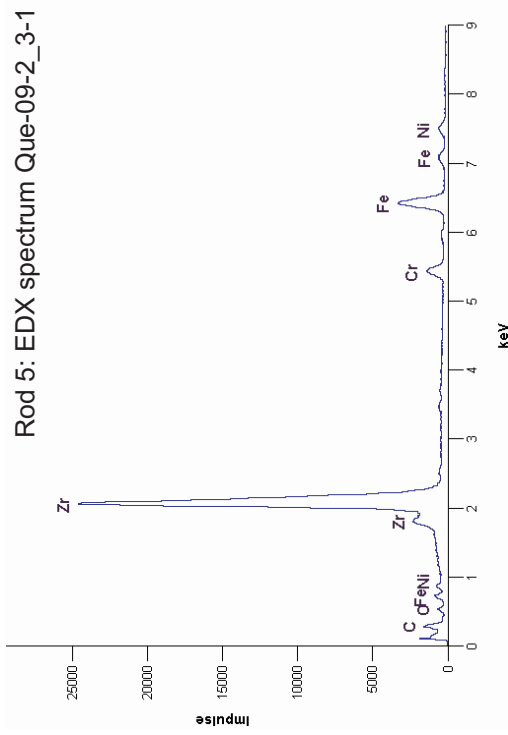
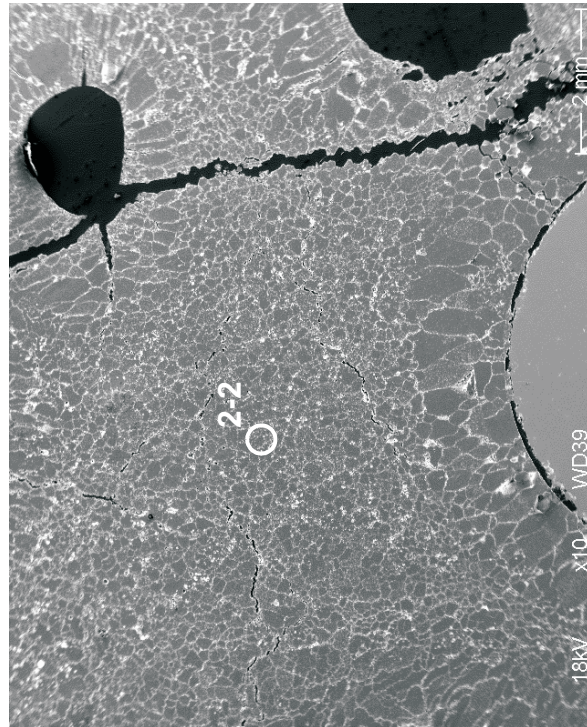
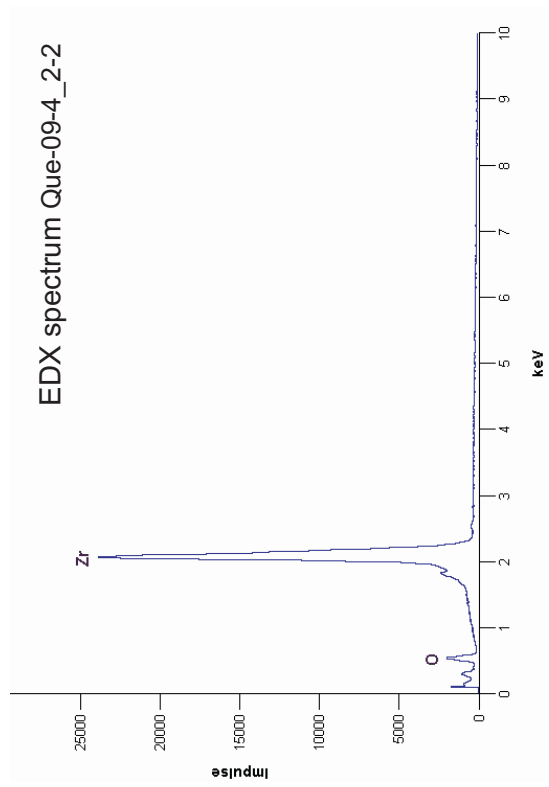


Fig. 96: QUENCH-09; Cross section at 520 mm elevation (QUE-09-2); SEM/EDX analysis of melt within rods #5 and #14, indicating presence of control rod degradation products



Melt, nearby, around a steam flow channel

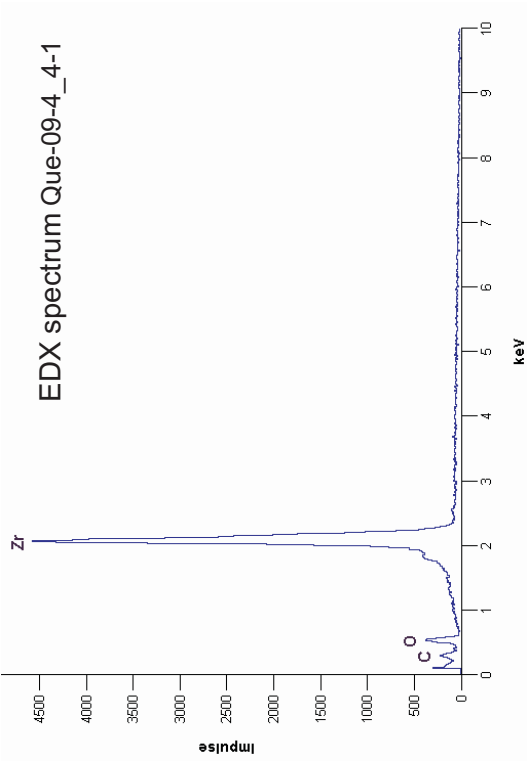
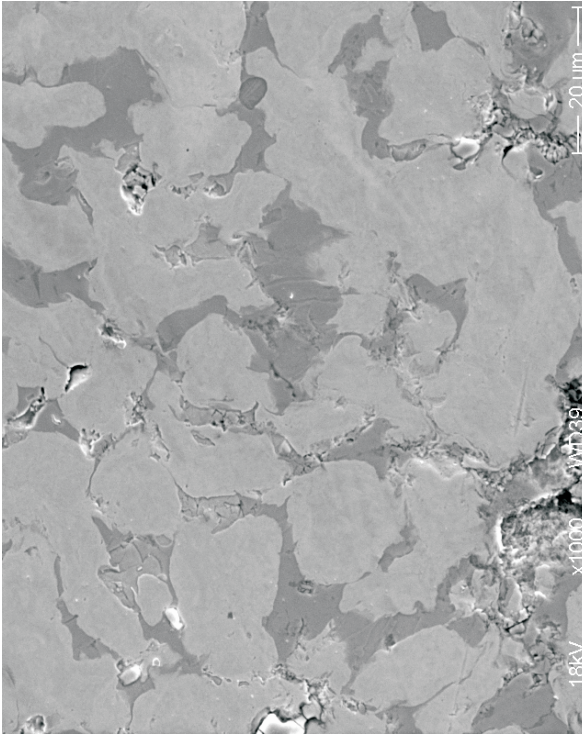
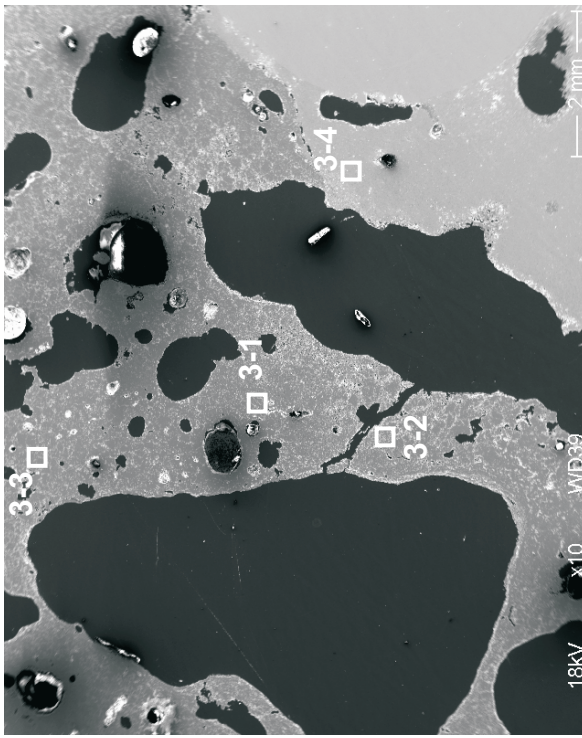
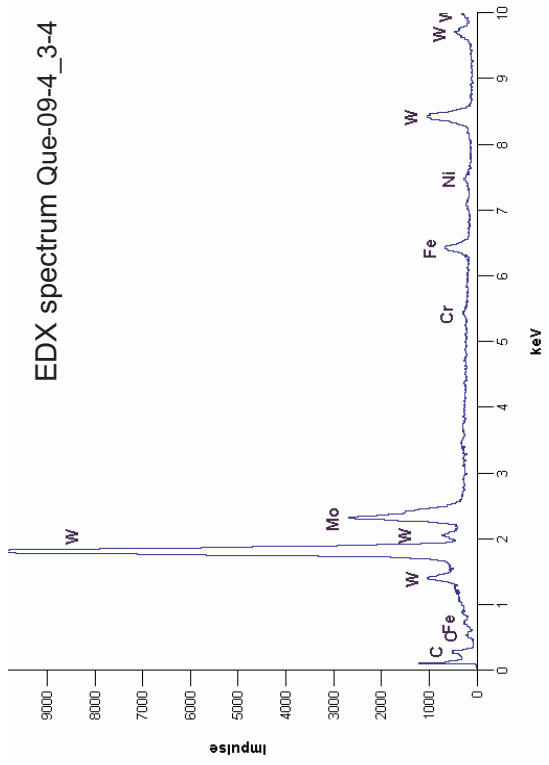
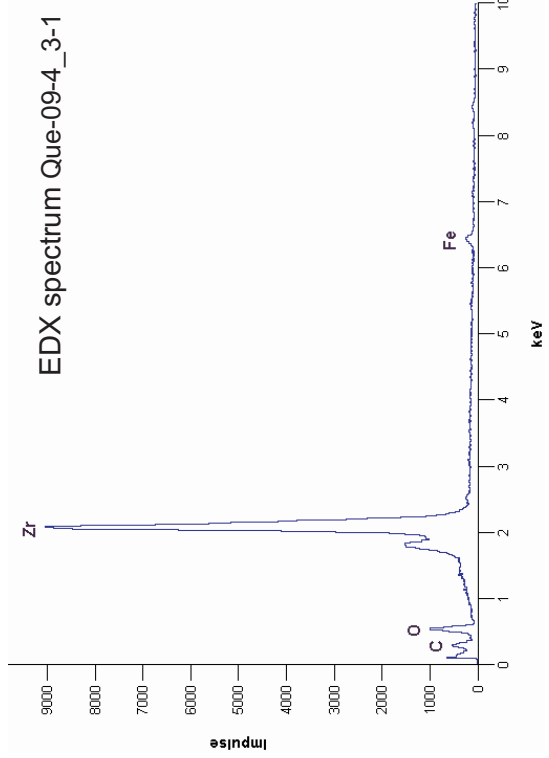


Fig. 97: QUENCH-09; Cross section at 590 mm elevation (QUE-09-4); non-porous melt pool, penetrated by steam flow channels, after complete conversion to ceramic state by pool oxidation mechanism; no control rod components detected in SEM/EDX analysis

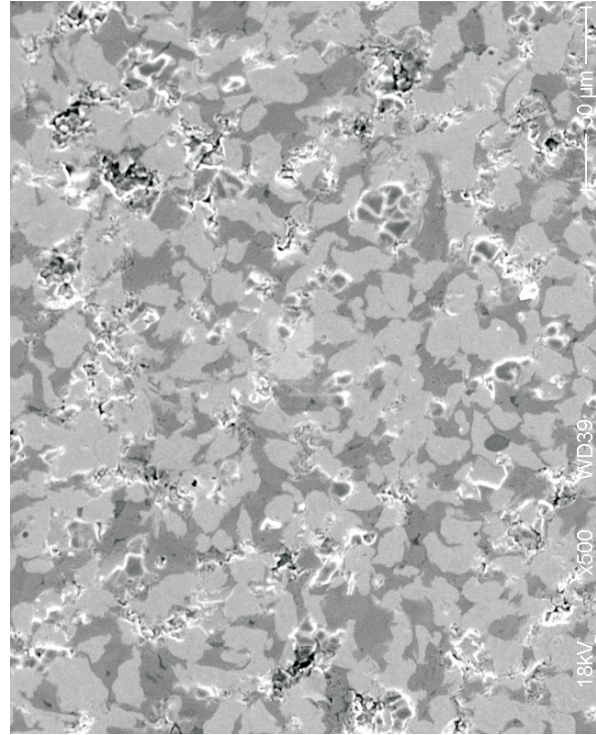
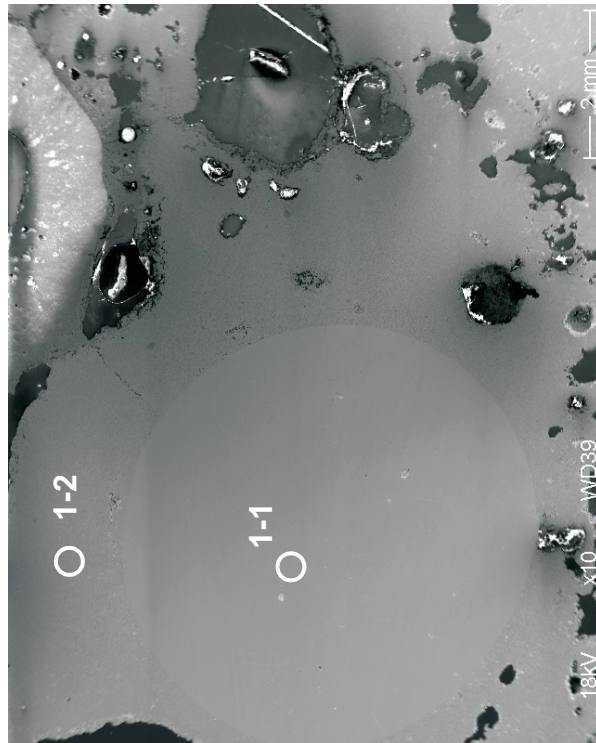
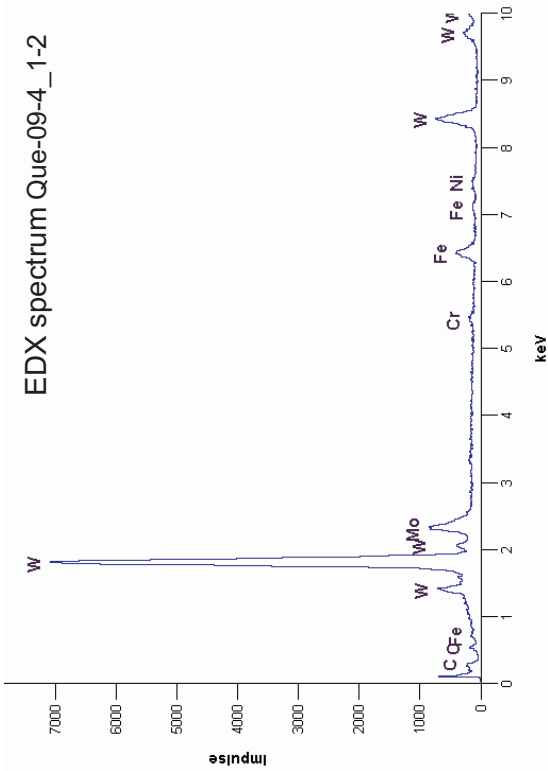
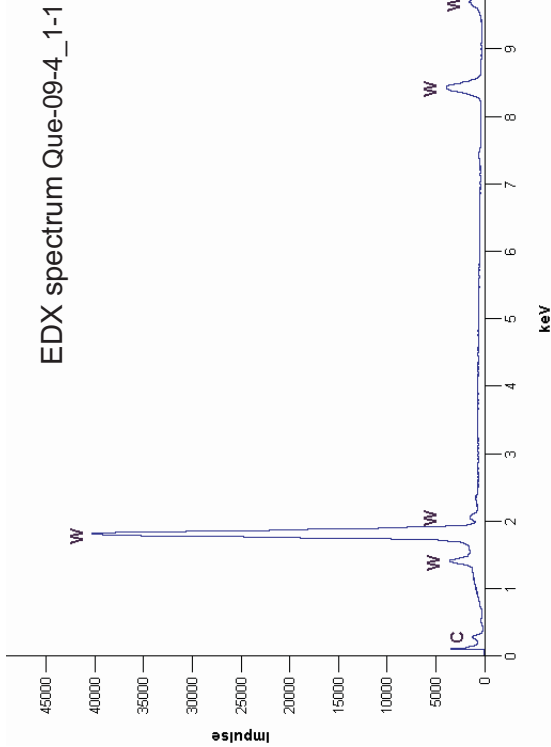


Overview on melt of variable composition; spectrum given for Pos. 3-1, similar composition at Pos. 3-2, no Fe at Pos. 3-3



Micrograph and spectrum of melt around tungsten heater of rod #8, both at Pos. 3-4 (see overview to the left)

Fig. 98: QUENCH-09; Cross section at 590 mm elevation (QUE-09-4); SEM/EDX analysis of porous melt in the bundle centre, resulting from fuel rod dissolution by control rod melt (left), and tungsten-rich melt, formed by dissolution of uncovered heater rod (right); (for W-dissolution see also Fig. 99)

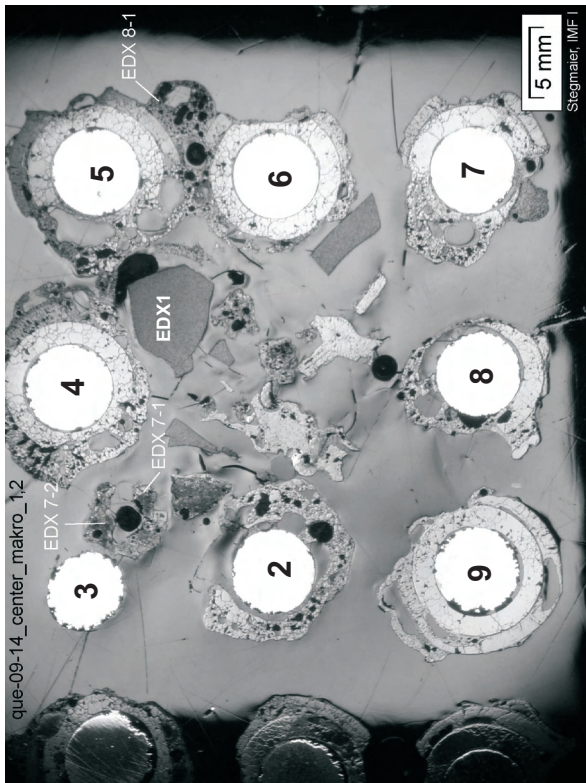


Spectrum from Pos. 1-1
of the overview; tungsten
heater (C from sputter
coating)



Spectrum from Pos. 1-2
of the left overview,
field of analysis depicted by
micrograph; formation of
tungsten-rich melt

Fig. 99: QUENCH-09; Cross section at 590 mm elevation (QUE-09-4); SEM/EDX analysis of the heater rod of fuel rod simulator #2 and of the tungsten-rich melt around; (for dissolution of tungsten see also Fig. 98)



Bundle centre, with EDX analysis positions

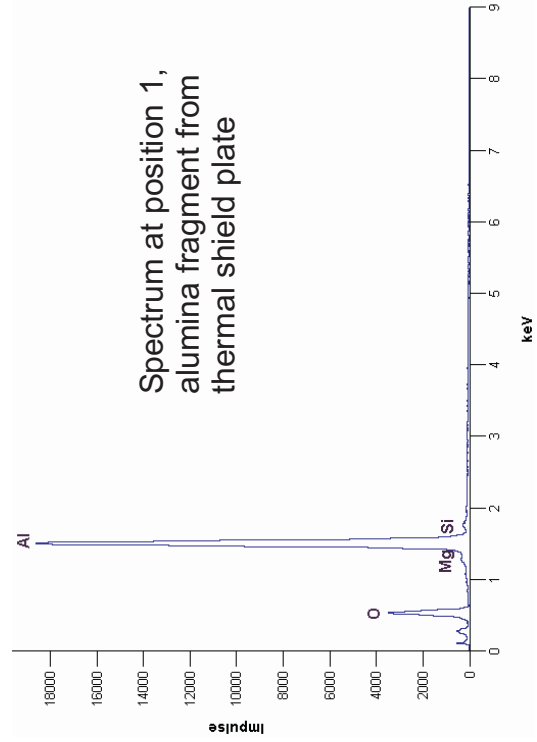
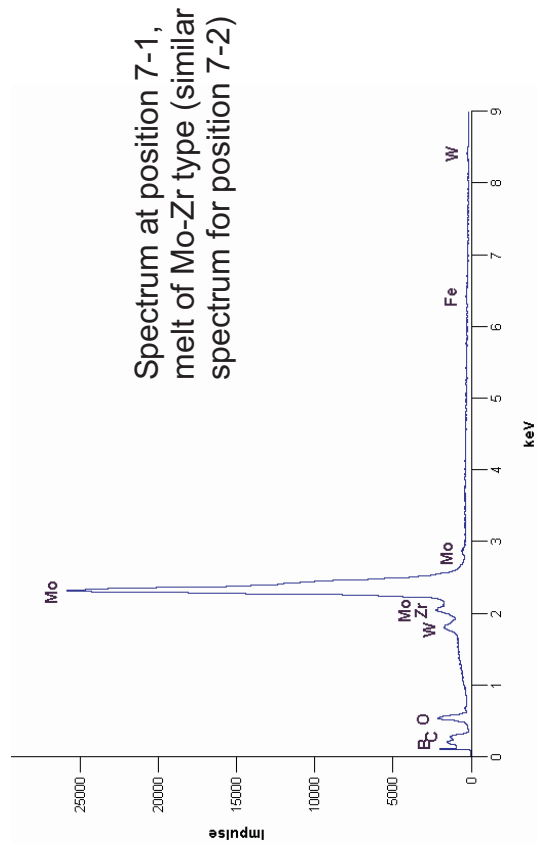
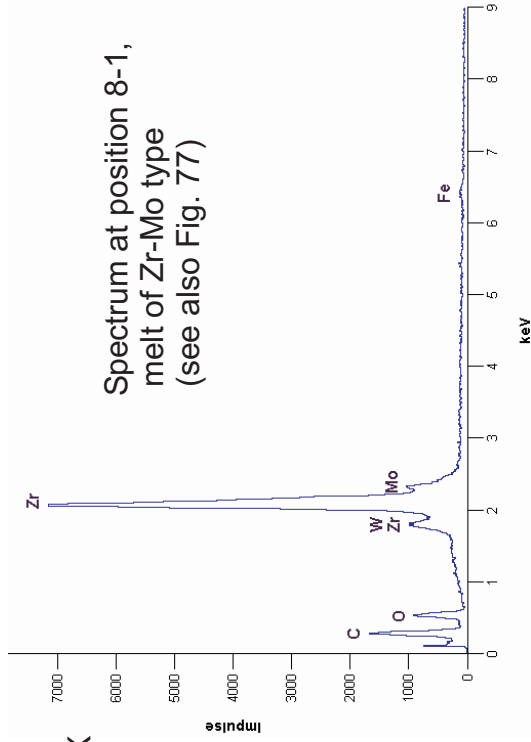
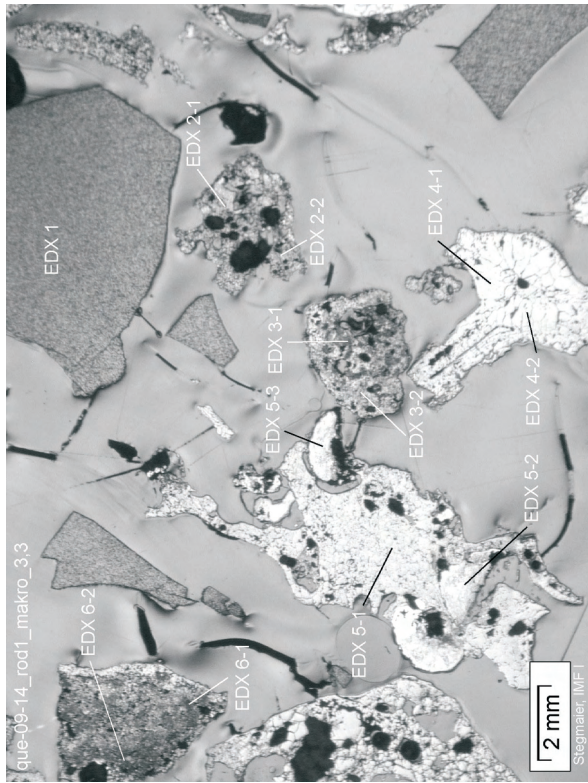


Fig. 100: QUENCH-09; Cross section at 950 mm elevation (QUE-09-14); SEM/EDX analysis positions and element spectra, obtained for melts and rubble fragments



Bundle centre, with EDX analysis positions

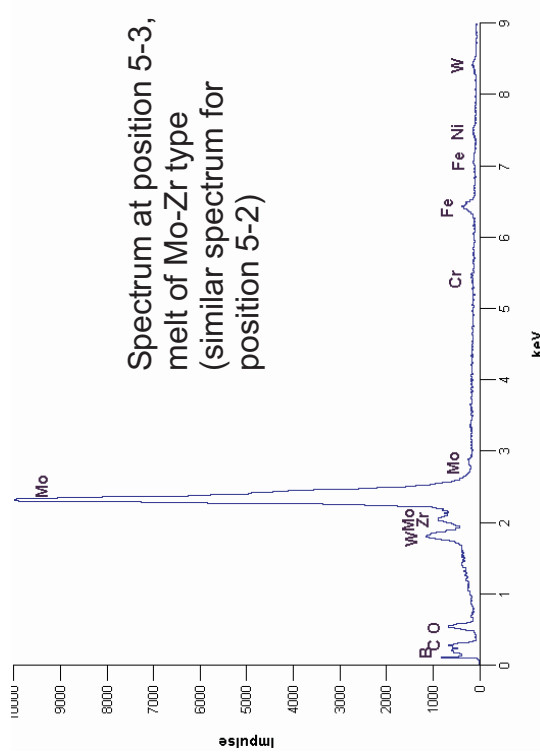
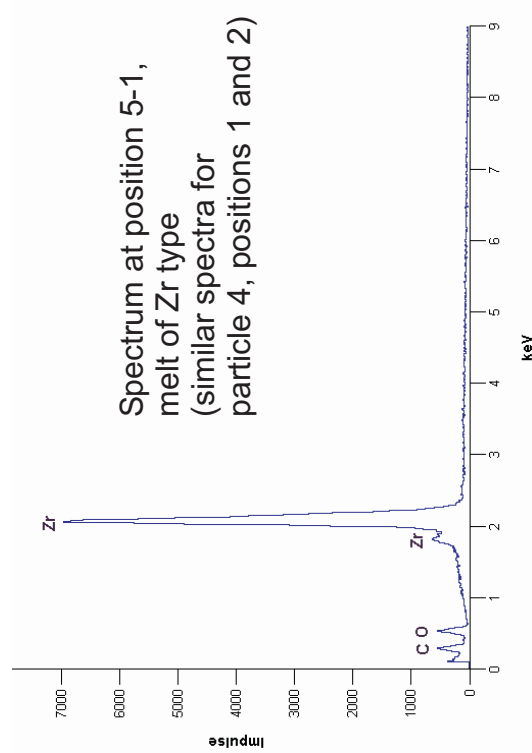
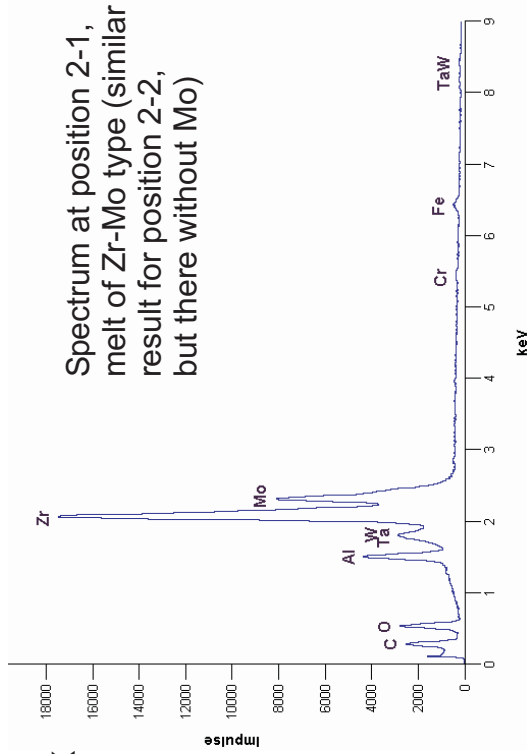


Fig. 101: QUENCH-09; Cross section at 950 mm elevation (QUE-09-14); SEM/EDX analysis positions and element spectra, obtained for melts and rubble fragments in bundle centre

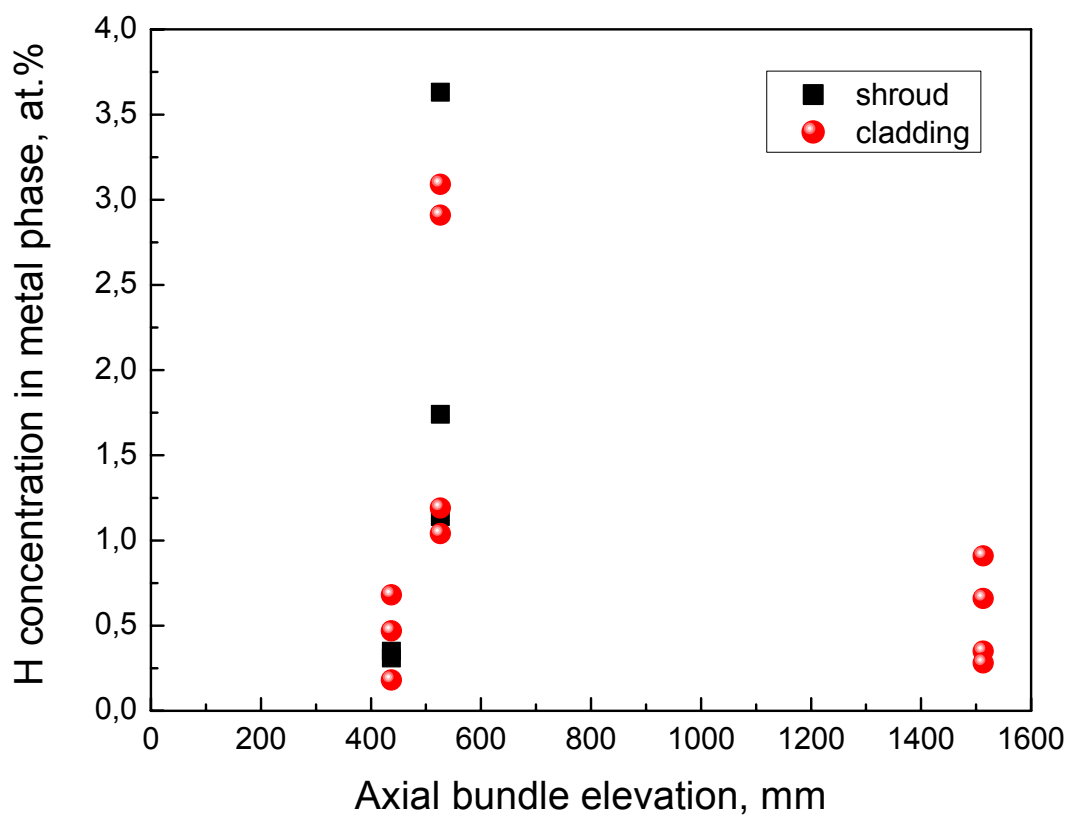


Fig 102-QUE09-hydrogen absorbed.doc
26.02.03 IMF

Fig. 102 QUENCH-09 Analysis of hydrogen absorbed in the residual metallic parts of the rods and shroud.

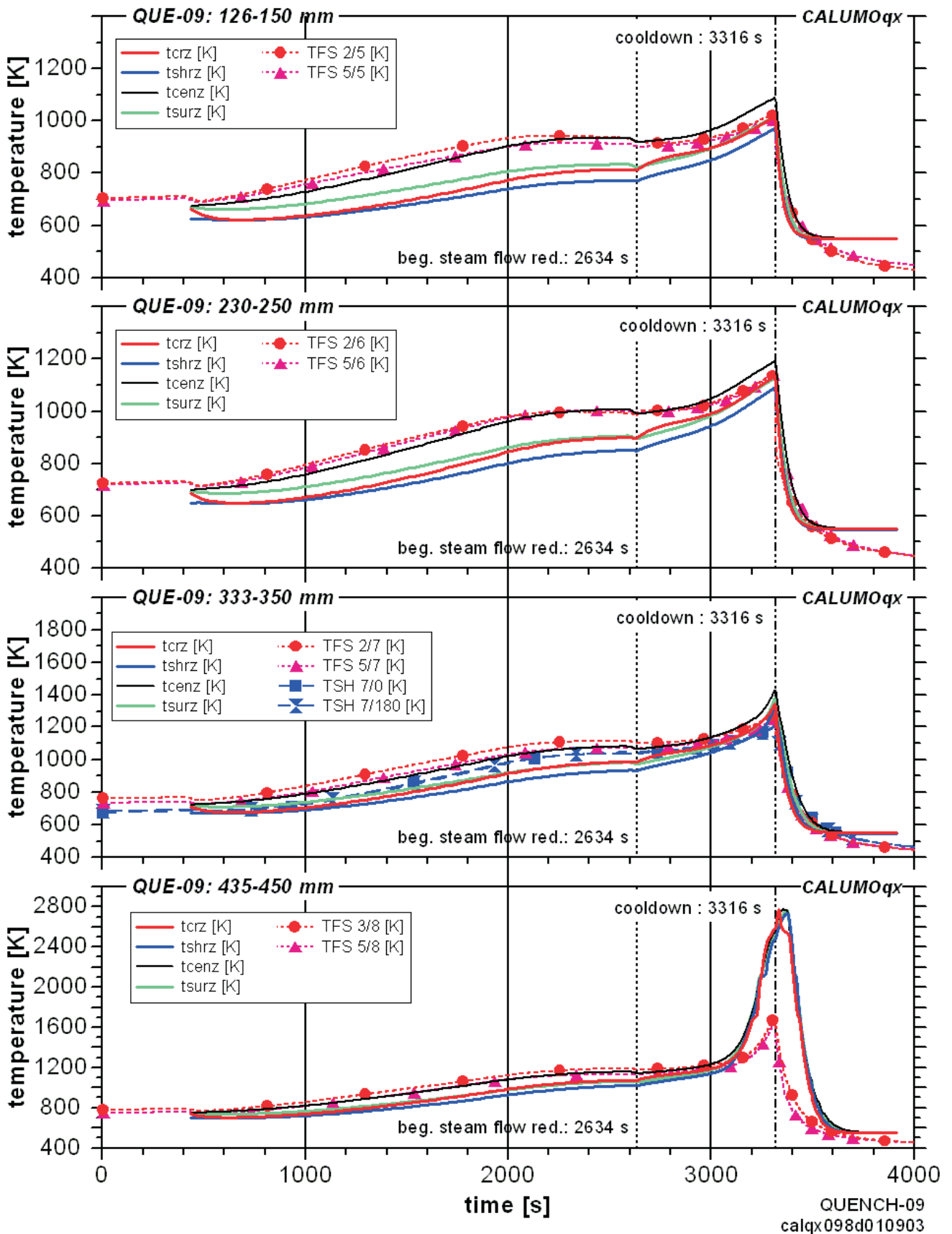
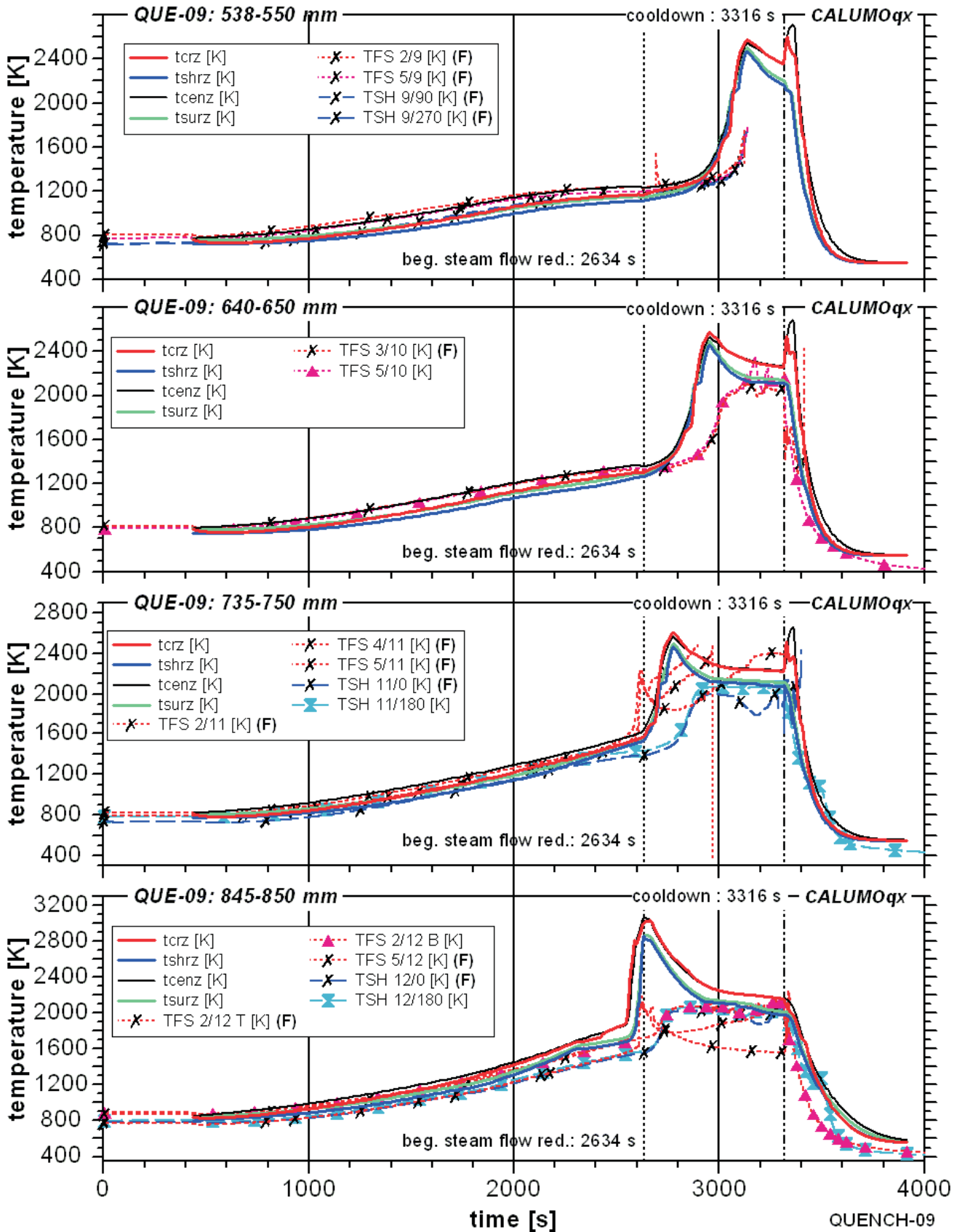


Fig 103-QUE09-Steiner 1.cdr
25.10.04 - IMF

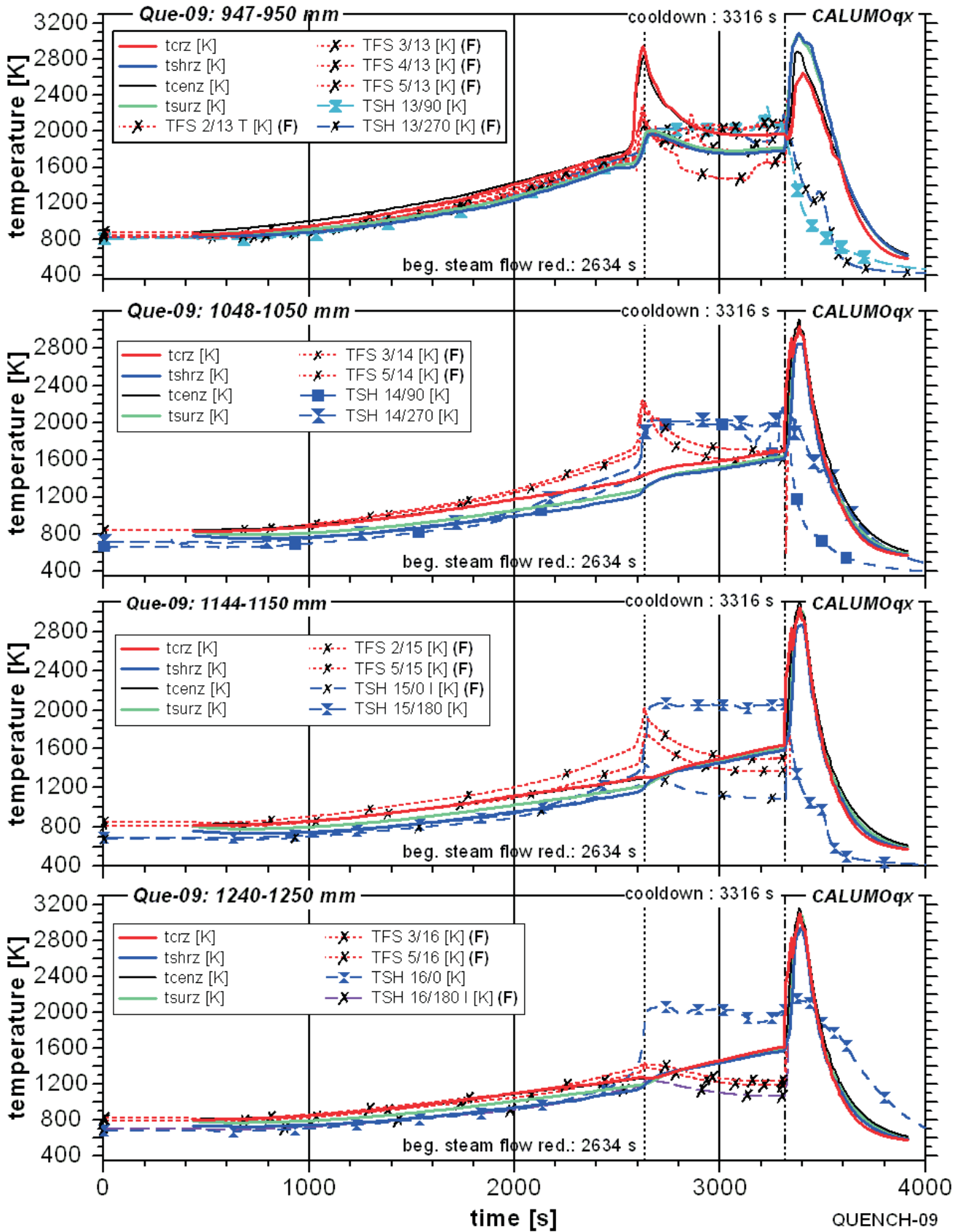
Fig. 103: QUENCH-09; Evolution of rod and shroud temperatures at different axial locations, CALUMO-calculated data in comparison with experimental values.



with \times marked gradients mean: thermocouple failed during experiment

QUENCH-09
calqx098d010903

Fig. 104: QUENCH-09; Evolution of rod and shroud temperatures at different axial locations, CALUMO-calculated data in comparison with experimental values.



with X marked gradients mean: thermocouple failed during experiment

QUENCH-09
calqx098d010903

Fig 105-QUE09-Steiner 3.cdr
25.10.04 - IMF

Fig. 105: QUENCH-09; Evolution of rod and shroud temperatures at different axial locations, CALUMO-calculated data in comparison with experimental values.

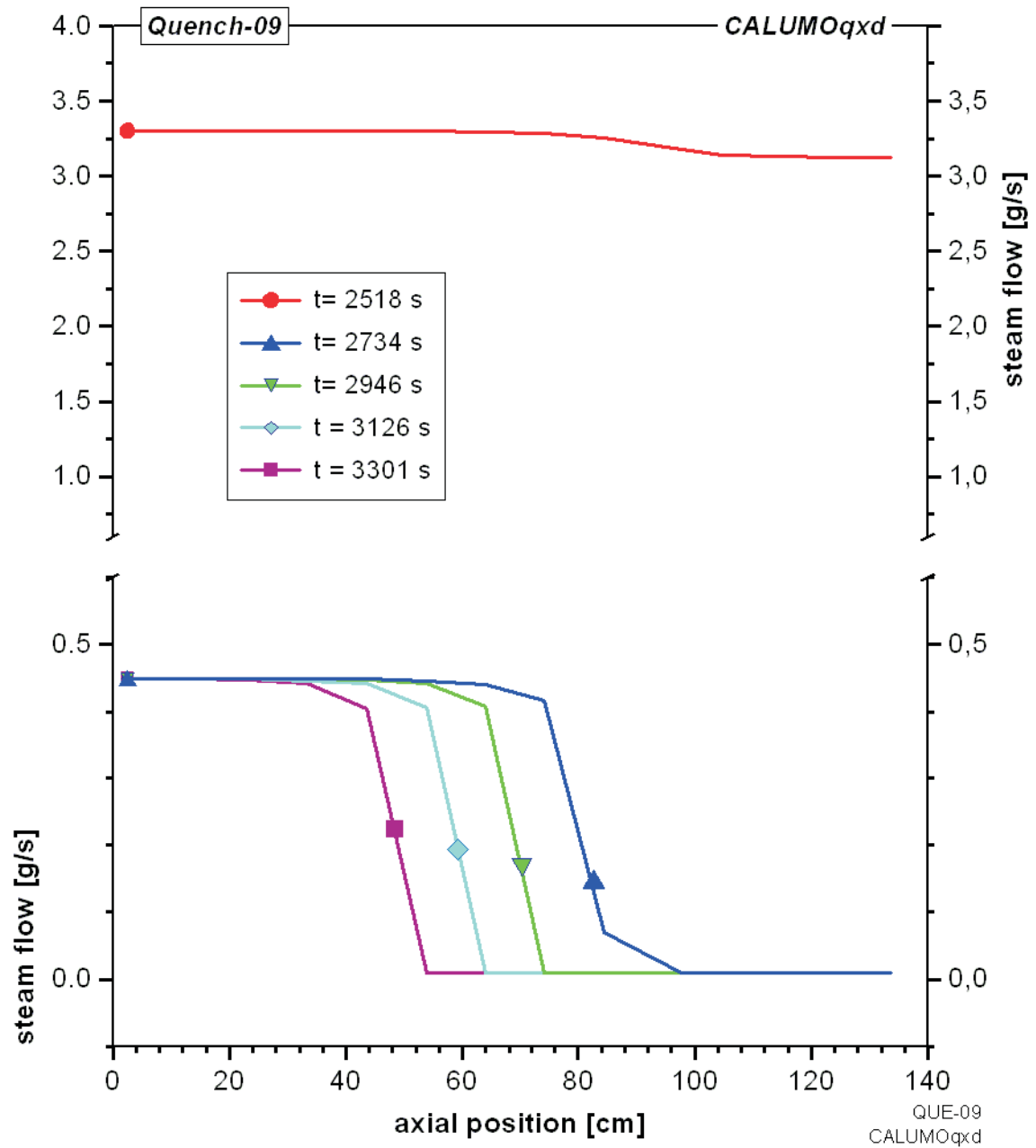


Fig 106-QUE09-Steiner 4.cdr
25.10.04 - IMF

Fig. 106: QUENCH-09; Axial distributions of the steam flow rate at different times during steam reduction.

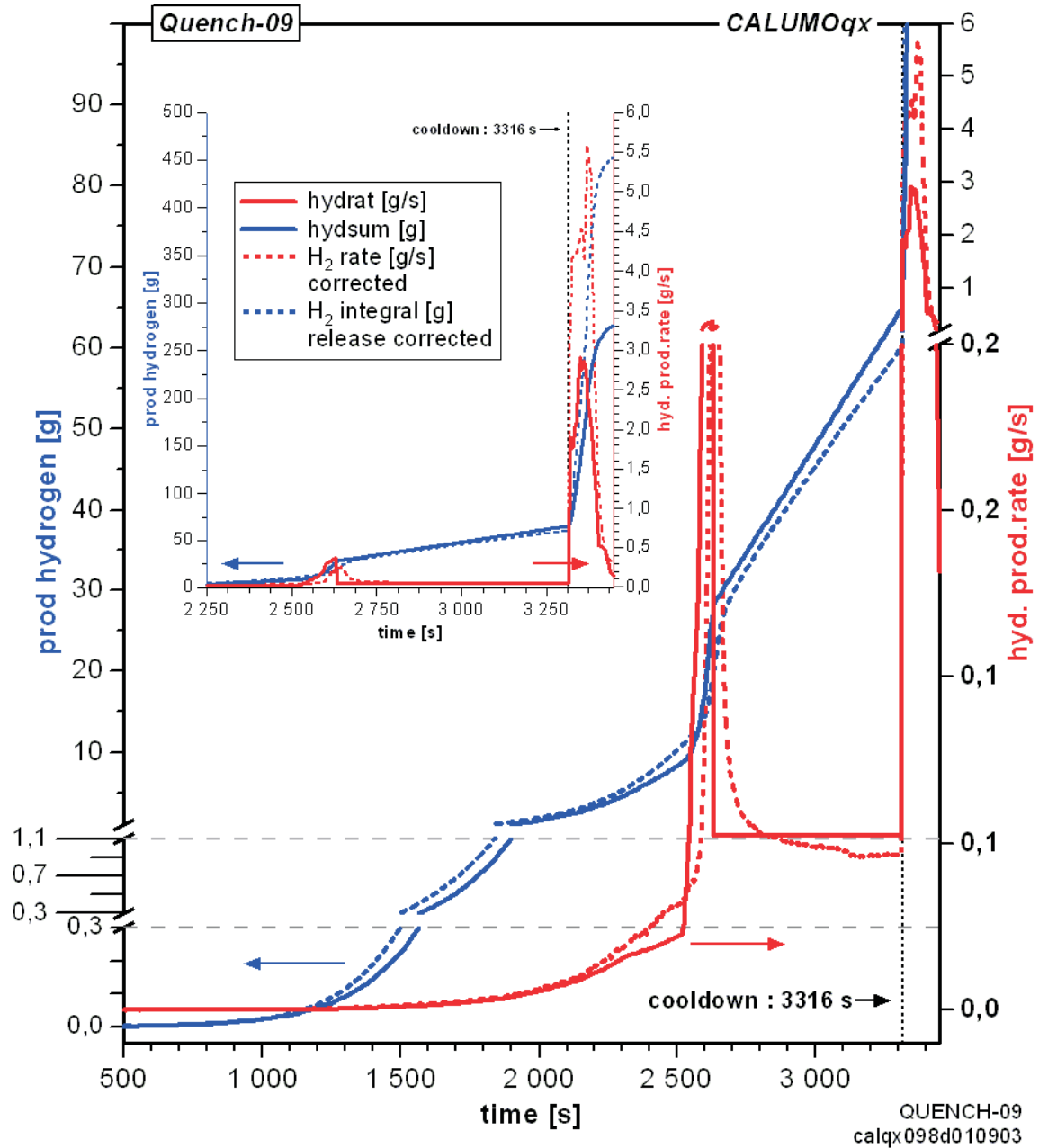


Fig 107-QUE09-Steiner 5.cdr
25.10.04 - IMF

Fig. 107: QUENCH-09; Evolution of the hydrogen production rate and the overall produced hydrogen for QUENCH-09 calculated with CALUMOqx.

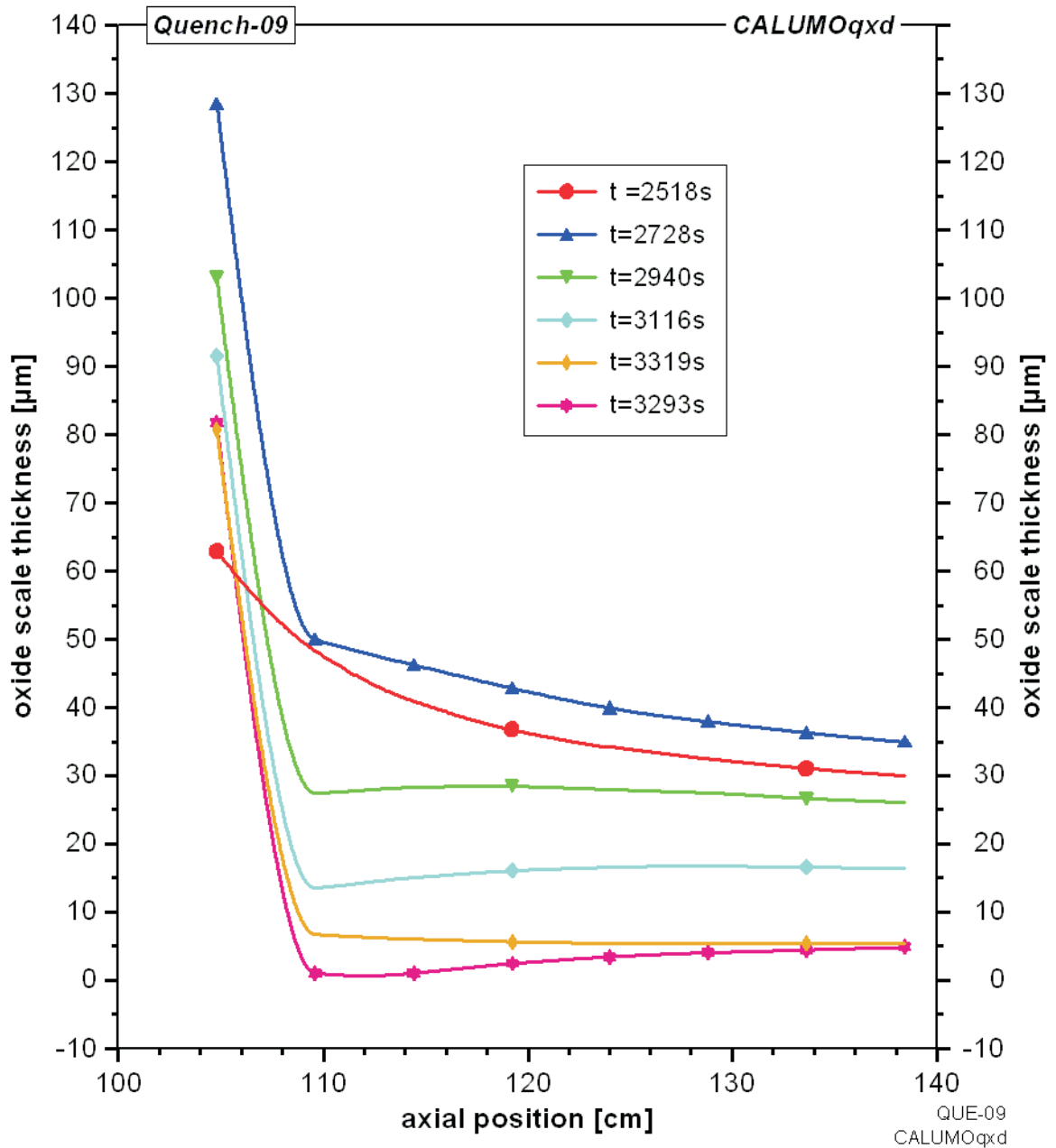


Fig 108-QUE09-Steiner 6.cdr
25.10.04 - IMF

Fig. 108: QUENCH-09; Axial distribution of the oxide scale thickness in the upper part of the test section during steam reduction.

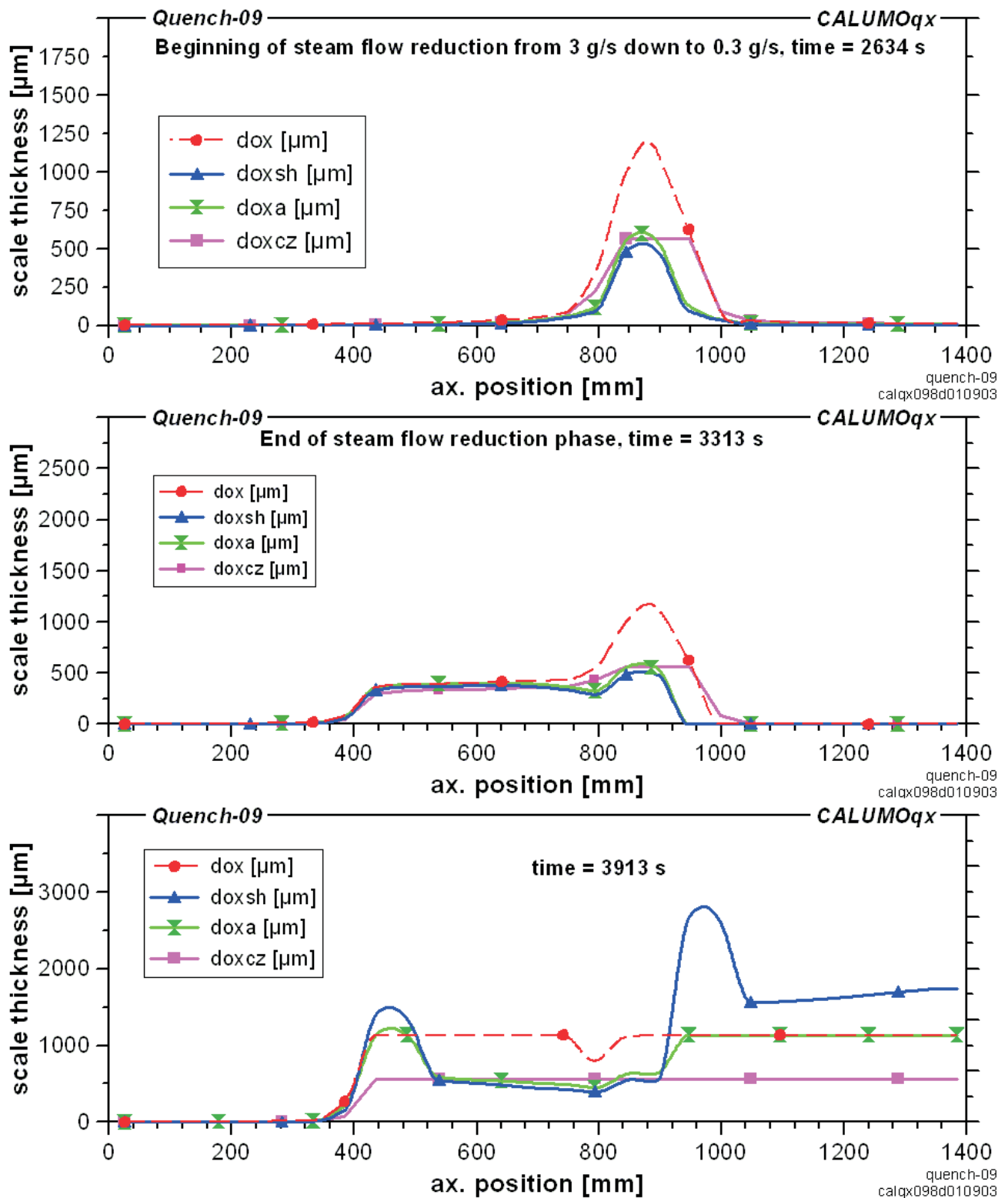


Fig 109-QUE09-Steiner 7.cdr
25.10.04 - IMF

Fig. 109: QUENCH-09; Axial distribution of the oxide scale thickness at the beginning and end of steam flow reduction and the end of QUENCH-09.

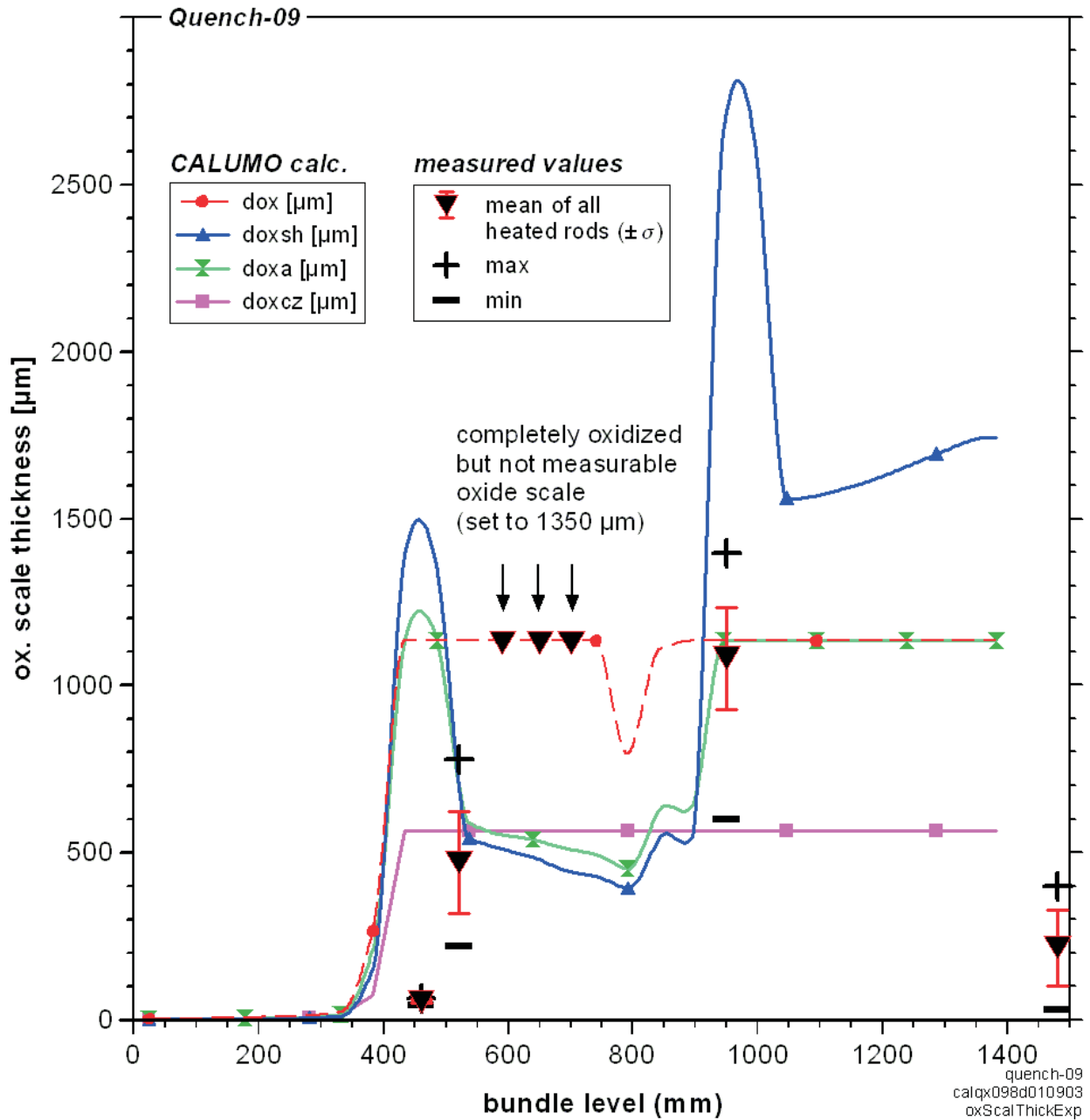


Fig 110-QUE09-Steiner 8.cdr
25.10.04 - IMF

Fig. 110: QUENCH-09; CALUMO calculated data and measured values for the oxide scale thickness of the experiment QUENCH-09 (Prater/Courtright trans. temp 1880 K)

Appendix

Appendix 1

Posttest measurement of the total argon flow through the QUENCH-09 bundle with the perforated inner cooling jacket

According to the P 403 pressure data the cooling jacket was damaged at 3344 s. At this time the shroud of the test bundle was damaged as well. From this time on the argon flow through the bundle consisted of the regular bundle flow of 3 g/s and in addition of a portion of the argon which flows through the annulus of the cooling jacket. The bundle argon flow is measured by FM 401 and the cooling argon by F 403. The latter argon flow, however, could not be measured properly after the break of the annulus because the data exceeded the upper limit of the flow measurement device F 403. So, it was necessary to determine the total argon flow through the test bundle as carrier gas for the analysis of the hydrogen and the various gases.

After the test a bypass tube was set up in parallel to the gas channel (annulus of the cooling jacket) with the aim to measure the total argon flow after the break of the inner cooling jacket (Fig. A1-1). This bypass tube allows the simulation of the undamaged cooling jacket. The diameter of the tube and the diameter of the throttle aperture were calculated to obtain an equal gas flow through the bypass tube and through the gas channel of the cooling jacket. The main formulas are based on the Poiseuille equation for gases, which flowed through a tube with cross-sectional area S and gradient of pressure p (all other parameters see below):

$$Q = - \frac{m \cdot S^2}{8 \cdot p \cdot h \cdot R_g \cdot T} \cdot p \cdot \frac{dp}{dx}$$

The integration of this mass flow over the tube length gives for our two cases the following results:

1) mass flow of the gas with the dynamic viscosity η and mole mass μ between the two coaxial tubes of the cooling jacket (index "c") with the length l and diameters R_c and r .

$$Q_c = \pi \cdot (R_c^4 - r^4 - \frac{(R_c^2 - r^2)^2}{\ln(R_c/r)}) \cdot \mu \cdot \frac{p_1^2 - p_2^2}{16 \cdot \eta \cdot l \cdot R_g \cdot T}$$

with the gas constant $R_g = 8.314 \text{ J/(mole} \cdot \text{K)}$

2) mass flow of the gas with the dynamic viscosity η and mole mass μ through the tube (index "t") with the length l and diameter R_t :

$$Q_t = p \cdot R_t^4 \cdot m \cdot \frac{p_1^2 - p_2^2}{16 \cdot h \cdot l \cdot R_g \cdot T}$$

Before the simulation of the break the argon pressure P 403 and the flow F 403 in the bypass was adjusted to the same values as was the case during the QUENCH-09 test in the cooling jacket, i.e. 0.59 MPa (5.9 bar) and 8.6 Nm³/h, respectively. In addition, the argon mass flow through the bundle before the break simulation was set to 3 g/s. The break was simulated by switching the flow of “cooling” argon (with the help of four valves) from the bypass tube to the cooling jacket of the test train. The total argon flow was measured at the gas outlet of the QUENCH facility, i.e. with the flow meters F 901 and F 902. The flow and pressure data of the bypass tube and the cooling jacket are given in [Fig. A1-2](#). The mass flow data after switching the valves are used as corrected argon bundle flow data ([Fig. A1-3](#)).

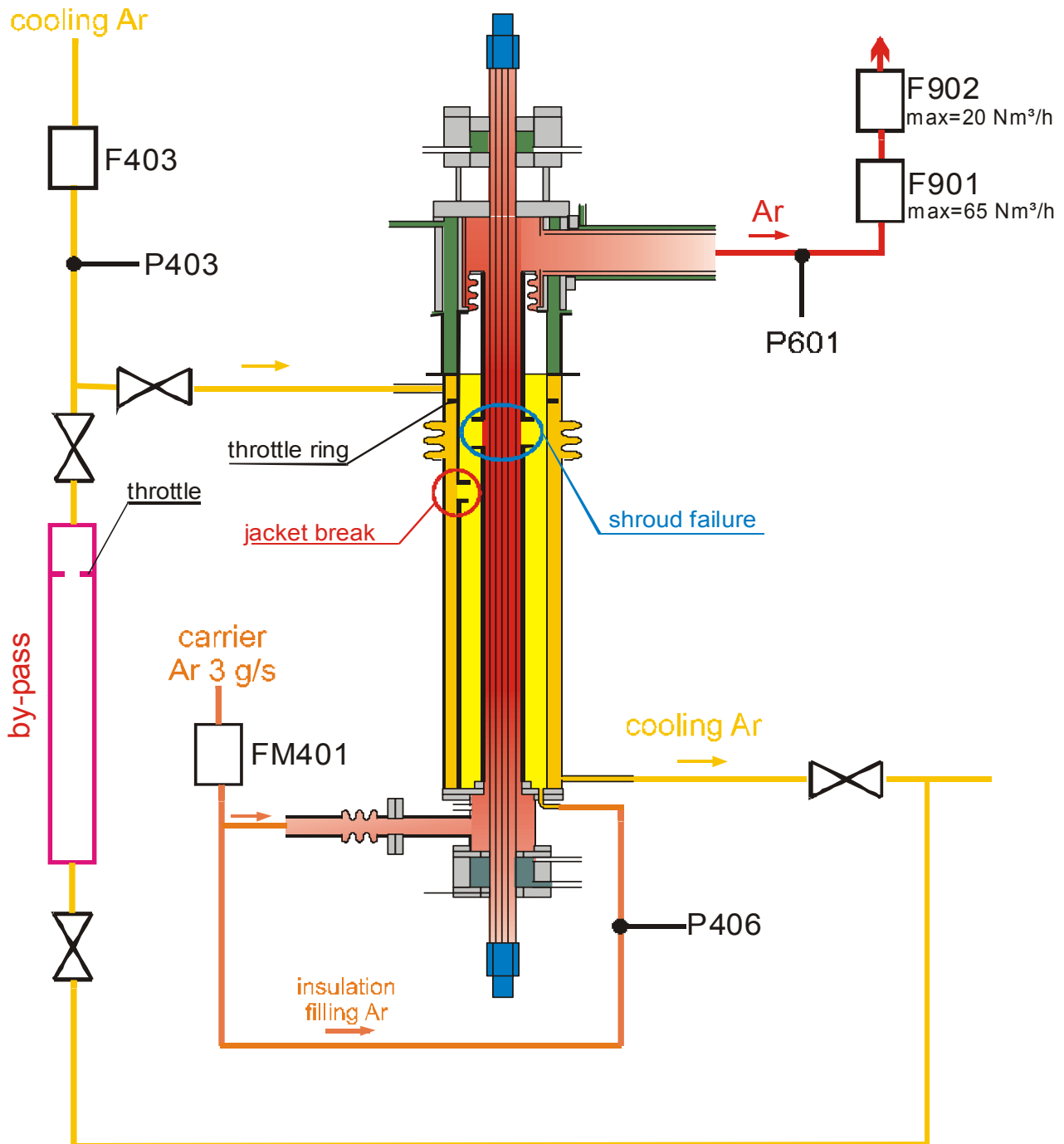


Fig A-1-1 QUE09.doc
26.02.03 IMF

Fig. A1-1 QUENCH-09 Posttest arrangement of the bypass tube to simulate the cooling jacket break

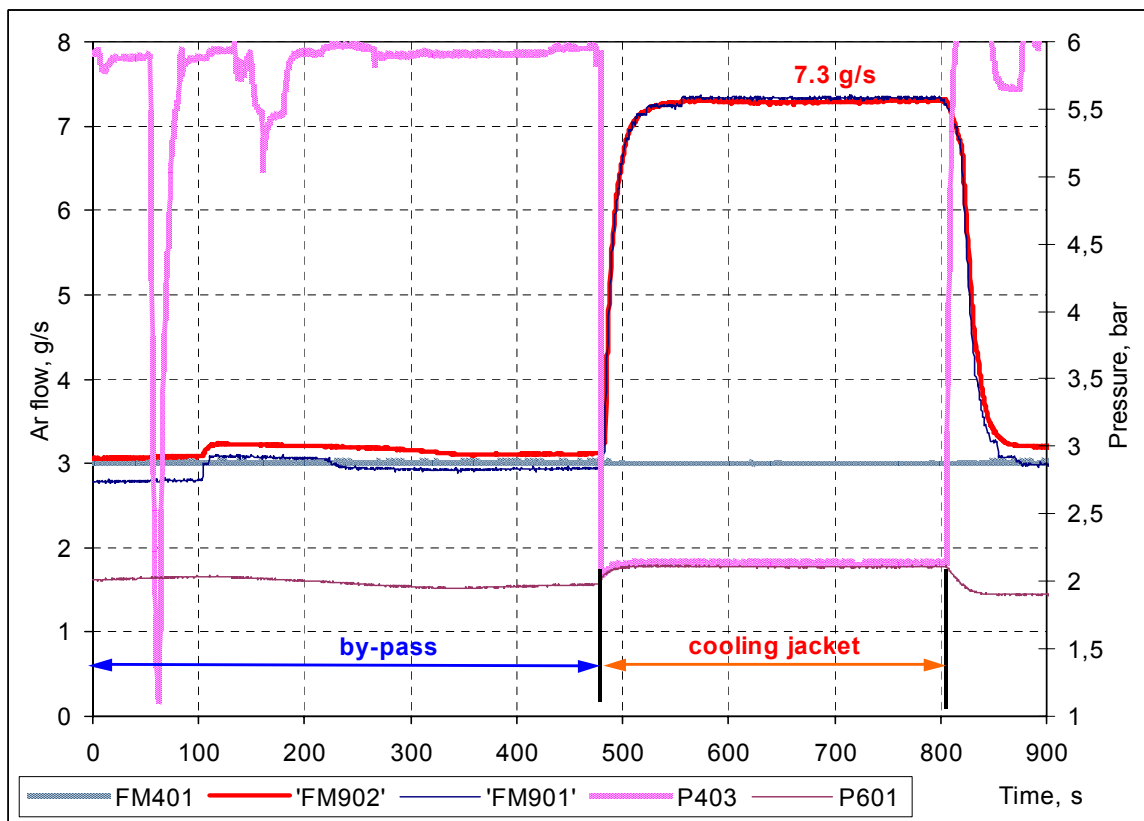


Fig A-1-2 QUE09.doc
26.02.03 IMF

Fig. A1-2: Posttest argon flow and pressure measurements to simulate the break of the inner cooling jacket during the QUENCH-09 test

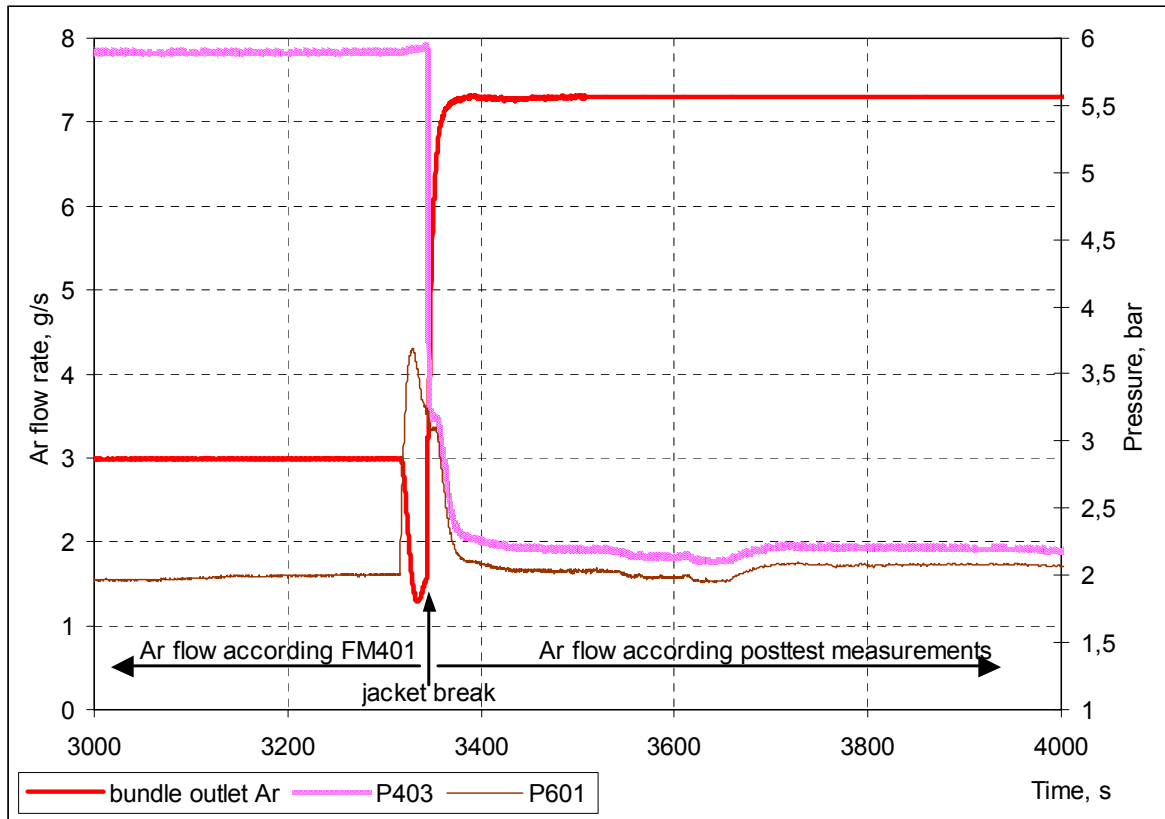


Fig A-1-3 QUE09.doc
26.02.03 IMF

Fig. A1-3: Pressure histories of P 403 (annulus of the cooling jacket) and P 601 (off-gas pipe) during test QUENCH-09 together with the argon bundle flow rate measured posttest (corrected from the time of “jacket break” as indicated)

Appendix 2

Errors in the temperature measurement by the “hot-zone effect”

Results of the oxide layer thickness of the rod claddings of all QUENCH bundles reveal significant discrepancies between the data measured post-test and the calculated ones at some axial levels. The oxide scales have been calculated with the SVECHA-code, using measured temperature histories as input. These calculated data are significantly different from measured data at some axial locations. [Fig. A2-1](#) shows that discrepancies are typical for those levels where thermocouples pass through the hot zone of the QUENCH bundle (shown in red). At 750 mm, e.g., the calculated layer thickness is too high. On the other hand, there is no discrepancy between measured and calculated oxide layer thicknesses for level 13, which is the hottest level, and therefore the thermocouples (shown in blue) from this level can not pass through the hot zone.

The influence of a hot zone on the thermocouple response was investigated in detail in “virtual-junction” tests performed at the Idaho National Engineering Laboratory in the 1980s. In those tests tandem-sheathed thermocouples were used, almost identical to the high-temperature thermocouples used in the QUENCH experiments, with the exception of a BeO insulator instead of HfO₂ ([Fig. A2-2](#)). The “virtual-junction effect”, in which the insulation resistance between the thermoelements (W/Re wires) has become low enough (by elevated temperature) to shunt part of the thermoelectric signal, becomes significant in the 900 – 1100 °C range for thermocouples of 1 mm outer diameter, according to [A2-1].

We supposed, however, a second reason for such differences, namely the axial heat transfer from the hot zone to the TC measuring junction along the TC sheath [A2-2]. Particularly, the inner Ta sheath has a relative high thermal conductivity - twice that of Zircaloy. If the thermocouple cable is at a temperature higher than that at the TC junction, then heat will flow from the hot zone to the junction.

Both phenomena were investigated in hot zone error testing by using a light furnace. In this test two identical thermocouples, routed to opposite directions with TC tips slightly overlapping, were moved along the axis of the furnace KALIO, which was held at 1000 °C. (See Pos. 3 in [Fig. A2-3](#), where both TCs are positioned symmetrically in the center of the furnace.) The largest error is evident at Pos. 1 where both TC tips are at the outside edge of the furnace. TC 2 passing through the hot zone shows a higher temperature than TC 1, which was positioned completely in the cold zone and therefore considered to measure correctly. The results of Pos. 2 show that the “virtual-junction effect” does not play a role at temperatures below 1300 K because both TCs present identical signals. So, it is conjectured that the temperature measurement is affected by heat transfer from the hot zone to the measuring junction. At Pos. 2 heat transfer along the TC sheath is ineffective because the measuring junction of TC 2 is far from the hot zone, i.e. 40 cm from the edge of the furnace.

To verify the influence of TC routing on the temperature reading, TC pairs were mounted at three axial levels in the QUENCH-09 bundle ([Fig. A2-4](#)). One pair was mounted on the rod surface (TFS-type thermocouple) at level 12, the other two pairs on the shroud surface (TSH-type thermocouple) at levels 15 and 16. The TFS-type thermocouple pair consisted of one

TC passing through the hot zone (direction to bundle top) and one TC not passing the hot zone (direction bundle bottom). The cables of the TSH thermocouples were routed to the bundle bottom. The cables of the two “colder” shroud thermocouples were insulated by the ZrO₂ fiber insulation. Fig. A2-4 shows the schematic of TC routing as well as the temperature data of the two TC pairs in the QUENCH-09 experiment.

It is concluded that thermocouples, passing the hot zone, show more higher values, than thermocouples, whose cable located in region with lower temperatures, than temperature at the TC junction. Therefore, hot-zone errors can be avoided by routing the thermocouple cables out of the hot zone (see bottom of Fig. A2-4) and by insulating the shroud TC cable as depicted in the top of Fig. A2-4. This will be done in future tests.

The qualification of questionable thermocouple readings was done for earlier QUENCH tests, and the results of the analysis are summarized in Table A2-1.

References

[A2-1] S.C. Wilkins, Internal report, 1984.

[A2-2] J. Stuckert, “Influence of the temperature gradient along the legs of the thermocouples on their reading,” 8th International QUENCH Workshop, Karlsruhe, October, 2002

**Table A2-1: Questionable thermocouple readings of tests
QUENCH-01 through -09**

TFS thermocouples	Unreliable after time, s	Temperature, K	TSH thermocouples	Unreliable after time, s	Temperature, K	Remarks
QUENCH-01						
TFS 2/11	5000	1317	TSH 14/90	9400	1300	Tmax=1800 K at t=9700 s on level 13 (950 mm)
TFS 4/11	5000	1317	TSH 14/270	9400	1350	
TFS 5/11	5000	1317	TSH 15/0	9300	1184	
TFS 3/12	7750	1430	TSH 15/180	9300	1230	
TFS 5/12	7750	1430	TSH 16/0	5000	1020	
			TSH 16/180	5000	1030	
QUENCH-03						
			TSH 14/90	2500	1230	Tmax=2460 K at t=2560-2600 s on levels 11-13 (750, 850, 950 mm)
			TSH 14/270	2450	1250	
			TSH 15/0	2440	1110	
			TSH 16/0	2420	950	
			TSH 16/180	2500	1130	
QUENCH-04						
TFS 2/11	2030	1560	TSH 14/90	2040	1300	Tmax=2280 K at t= 2065 s on level 13 (950 mm)
TFS 4/11	2030	1560	TSH 14/270	2040	1370	
TFS 5/11	2030	1560	TSH 15/0	1900	1060	
TFS 3/12	2040	1680	TSH 15/180	2040	1150	
TFS 5/12	2040	1680	TSH 16/0	2000	1066	
			TSH 16/180	2000	1066	
QUENCH-05						
TFS 2/11	5500	1360	TSH 14/90	5900	1360	Tmax=2030 K at t= 6012 s on level 13 (950 mm)
TFS 4/11	5500	1360	TSH 14/270	5900	1450	
TFS 5/11	5500	1390	TSH 15/0	5800	1190	
TFS 3/12	5940	1790	TSH 15/180	5800	1230	
TFS 5/12	5960	1740	TSH 16/0	5700	1070	
			TSH 16/180	5700	1120	
QUENCH-06						
TFS 2/11	6600	1400	TSH 14/90	7000	1370	Tmax=1940 K at t= 7188 s on level 13 (TCRC 13, 950 mm)
TFS 4/11	6600	1400	TSH 15/0	6900	1220	
TFS 5/11	6600	1400	TSH 15/180	6900	1220	
TFS 3/12	6900	1650	TSH 16/0	6800	1130	
TFS 5/12	6900	1650	TSH 16/180	6800	1130	
QUENCH-07						
TFS 2/11	3230	1652	TSH 14/90	3100	1390	Tmax=2115 K at t= 3468 s on level 13 (TIT A/13, 950 mm)
TFS 4/11	3100	1570	TSH 14/270	3100	1490	
TFS 5/11	3257	1670	TSH 15/0	2300	1225	
TFS 3/12	3100	1680	TSH 15/180	2300	1190	
TFS 5/12	3100	1650	TSH 16/0	2300	1100	
			TSH 16/180	2300	1100	
QUENCH-09						
TFS 2/11	2500	1510	TSH 14/90	2600	1535	Tmax=2283 K at t= 2629 s on level 13 (TFS 4/13, 950 mm)
TFS 4/11	2500	1450	TSH 14/270	2600	1790	
TFS 5/11	2500	1450	TSH 15/180	2600	1360	
TFS 2/12T	2583	1758	TSH 16/0	2600	1400	
TFS 5/12	2609	1640				

Note: The different colors correspond to different axial levels

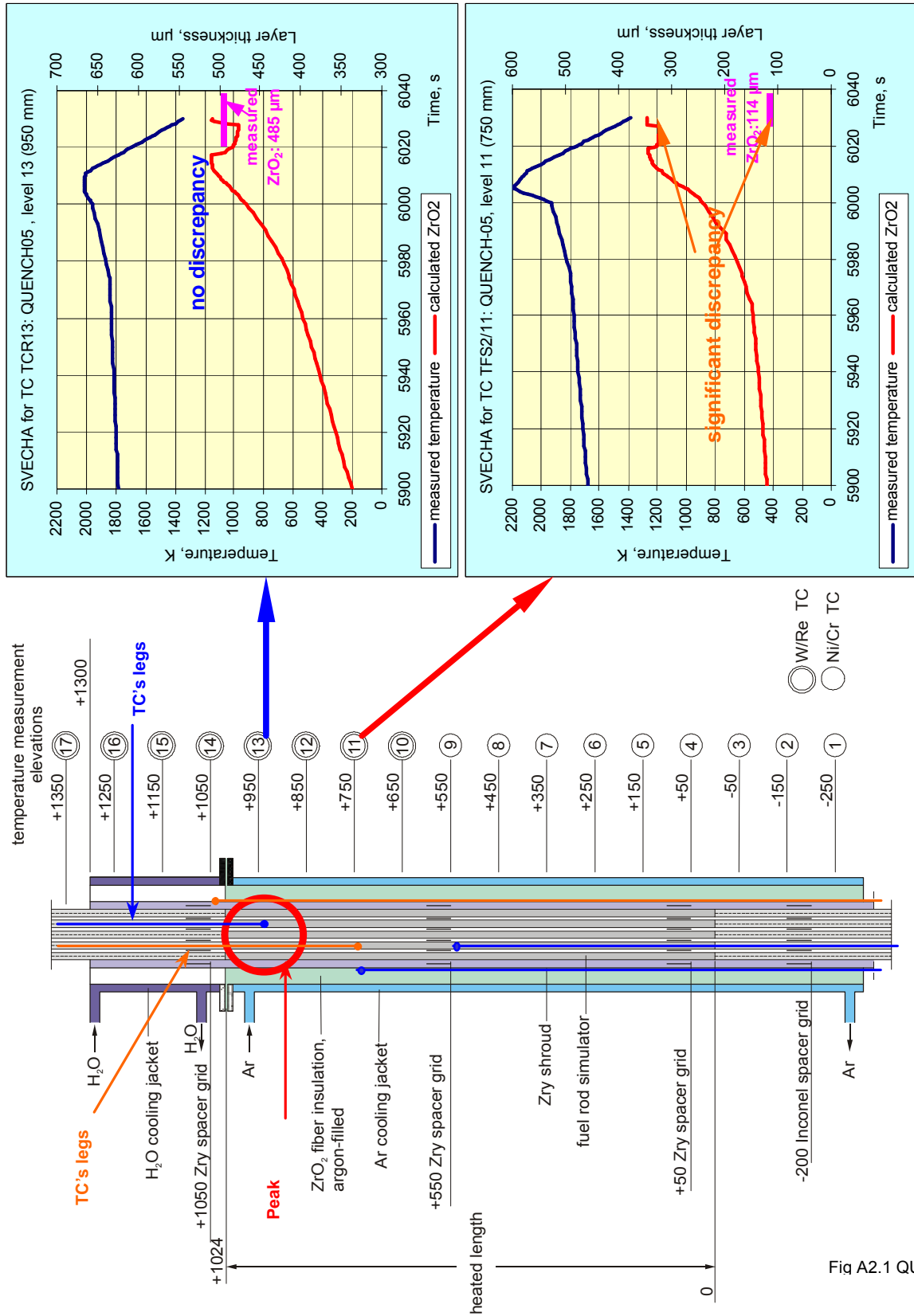


Fig A2.1 QUE09.doc

Fig. A2-1 QUENCH-09; Measured and calculated oxide layer thickness at levels 750 and 950 mm showing significant differences at 750 mm due to uncertainties in the temperature measurement, i.e. hot zone-effect of the rod cladding thermocouples.

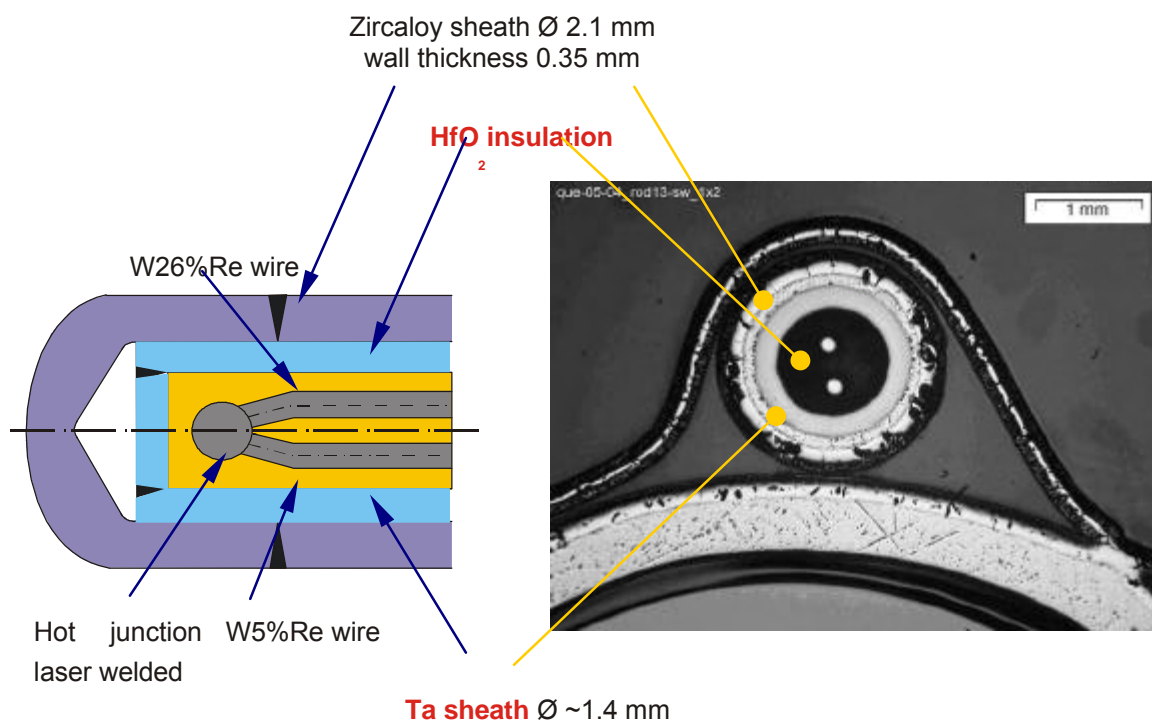


Fig A2-2 QUE09.doc

Fig. A2-2 QUENCH-09; Design of the duplex-sheathed thermocouple, left, and posttest photograph, right.

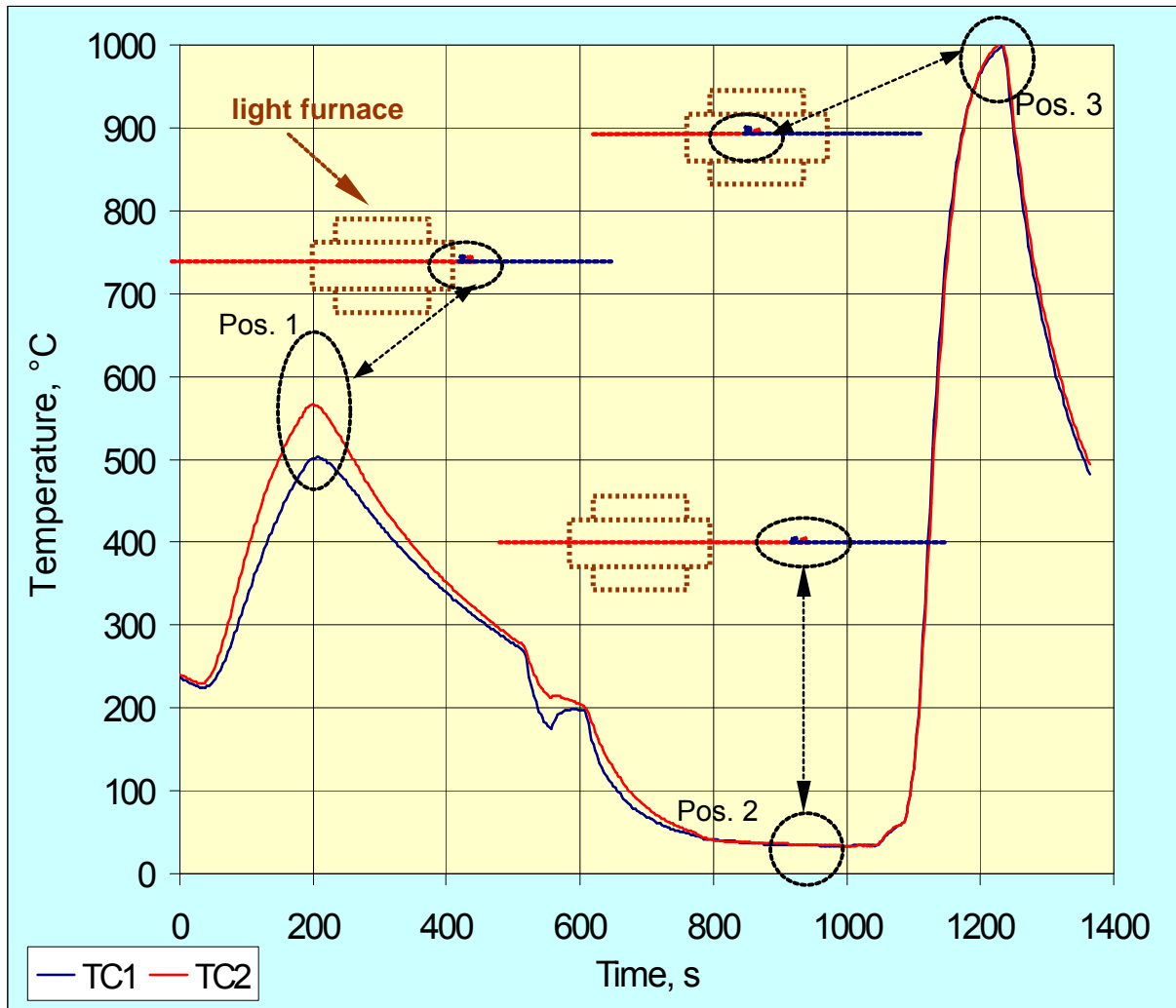


Fig. A2-3 QUENCH-09; Test with two duplex-sheathed thermocouples routed to opposite directions, TC tips slightly overlapping, along the axis of the light furnace KALIO.

Comparison of the TC signals at three positions of both measuring junctions: Pos. 1 – edge of the furnace, i.e. 15 cm from furnace center; Pos. 2 – 40 cm from the furnace edge, Pos. 3 – furnace center.

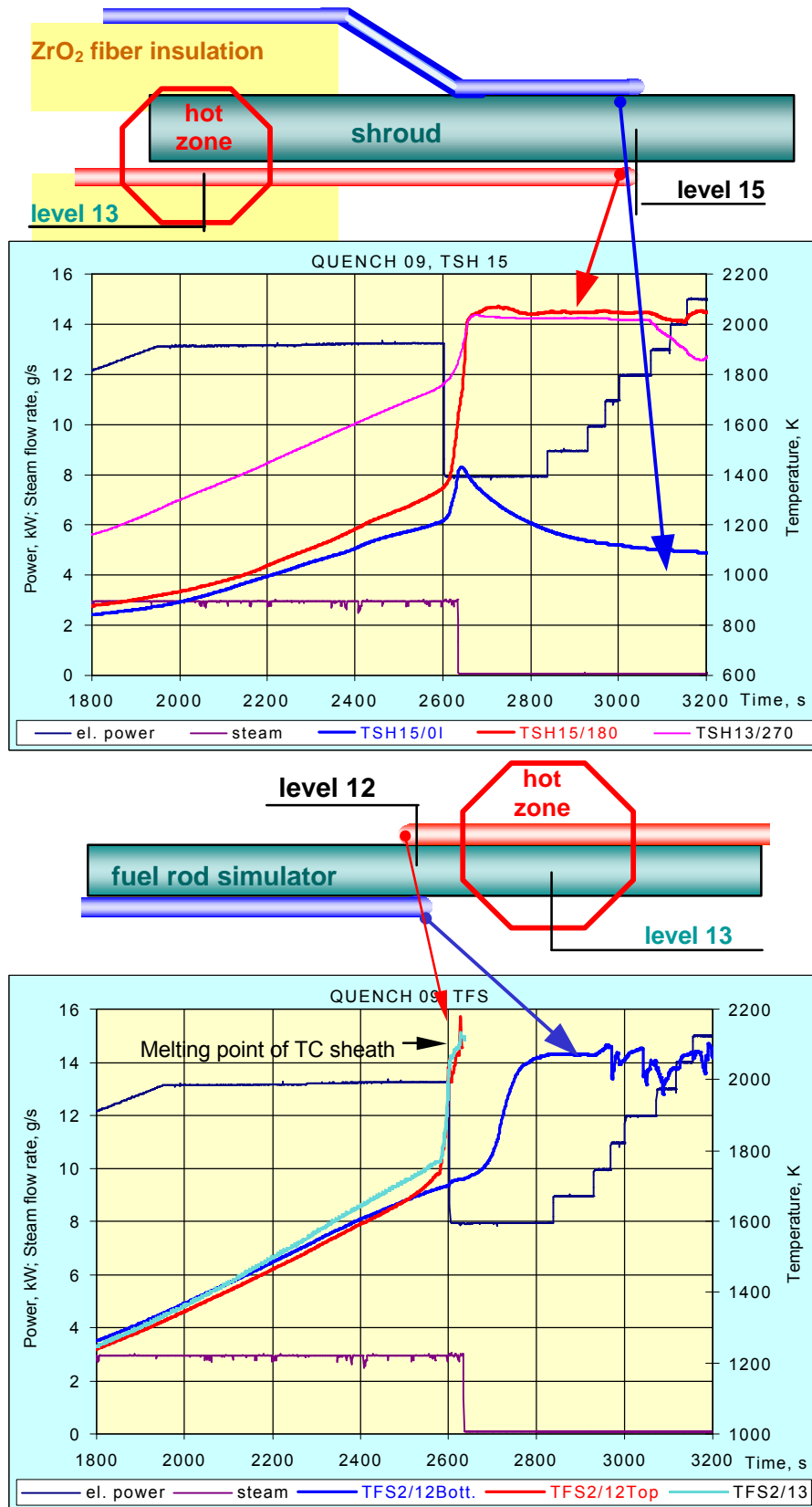


Fig A2-4 QUE09.doc

Fig. A2-4 QUENCH-09; Different temperature readings from thermocouples fastened at the same level on the fuel rod simulator (bottom) and on the shroud surface (top).